Multiphase modeling of as-solidified structure and macrosegregation in continuously cast round billet of large format

A thesis submitted to the Montanuniversität Leoben
for the degree of Doctor of Montanistic Sciences (Dr. mont.)

presented by
Yongjian Zheng
Leoben, March 2018

Supervisor: assoz. Prof. Dr.-Ing. Menghuai Wu
Chair for Simulation and Modeling of Metallurgical Processes
Department of Metallurgy, Montanuniversität Leoben

Eidesstattliche Erklärung

Ich erkläre an Eides statt, dass ich diese Arbeit selbstständig verfasst, andere als die angegebenen Quellen und Hilfsmittel nicht benützt und mich auch sonst keiner unerlaubten Hilfsmittel bedient habe.

Leoben, 12.03.2018

M. Sc. Yongjian Zheng

Affidavit

I declare in lieu of oath, that I wrote this thesis and performed the associated research myself, using only literature cited in this volume.

Leoben, 12.03.2018

M. Sc. Yongjian Zheng

Acknowledgements

First and foremost, I would like to express my sincere gratitude to my supervisor, Prof. Menghuai Wu, for supporting me academically and mentally through his patience, motivation, enthusiasm, and encouragement. This work would not be possible without his supervision. My sincere thanks also go to Prof. Andreas Ludwig for giving me the chance to work in his research group, chair of Simulation and Modeling of metallurgical Process (SMMP). Additionally, I am grateful to Dr. Abdellah Kharica for his help in incorporating magnetic force in the semi-continuous casting (SCC) simulation. My sincere gratitude goes to Prof. Christian Bernhard for his generous help in the lecture about continuous casting process. It is really a fruitful and pleasant experience working with them.

It has been a great pleasure to cooperate with the Primetals Technologies during the thesis preparation. Therefore, I would like to thank those industrial experts Reisenberger Ewald, Guoxin Shan, Franz Wimmer, Heinrich Thoene, Susanne Hahn and Paul Pennerstorfer for generous advice and comments.

I would like to thank my colleagues, Alexander Vakhrushev, Tobias Holzmann, Hadi Barati, Christian Rodrigues, Johann Mogeritsch, Michaela Stefan-Kharicha, Tanja Pfeifer, Samiullah Baig, Georg Nunner, Mahmoud Ahmadein, Lubomir Soukup, Zhongqiu Liu, Haijie Zhang, Veronika Grela, Mehran Abdi, Otto Klaus-Jürgen, Sabine Strassegger, Claudia Heinzl, Nico Baumgartner, Jenny Dorner for their help in the course of my study in Leoben. I would like to specially thank Dr. Jan Bohacek and Dr. Ebrahim Karimi-Sibaki, for their supporting me both in daily life and academic field.

I express a lot of thanks to Prof. Lian Zhou and Prof. Wanqi Jie in Northwestern Polytechnical University. I would like to thank Dr. Yong Feng, Dr. Xianghong Liu, Dr. Baoquan Fu and Dr. Guo Yan in Western Superconducting Technologies Co., Ltd. Without their help and support it would not have been possible for me to reach Montanuniversität Leoben and complete Ph.D study.

I would express many thanks to my parents for their love, support, and encouragement. Finally, I would like to thank my wife, Cun’e Xu, and my daughter, Qiyu Zheng. Without their support and understanding, I could not concentrate on this thesis.

Kurzfassung

Die Vorteile von standardisierten Gießverfahren wie beispielsweise des Blockgusses oder Stranggusses können zusammengeführt werden, um neue Methoden zu entwickeln. Hierzu gehört der Gießprozess, welcher unter dem Akronym SCC (Semi-Continuous Casting) bekannt ist und ein wettbewerbsfähiges Gießverfahren für die moderne Industrie darstellt. Für einen optimalen Abguss müssen jedoch die Entstehungsmechanismen vom Gussgefüge, sowie Makroseigerung und Porositäten verstanden werden. Diesbezüglich wird in dieser Arbeit mithilfe eines 3-Phasen-Modells (mixed columnar-equiaxed) der SCC Prozess numerisch untersucht, um die zuvor genannten Problemstellungen zu analysieren und Verbesserungsvorschläge für die Industrie zu liefern. Das verwendete Modell wurde von Wu und Ludwig (2016) entwickelt, wobei eine Erweiterung des Grundmodells erforderlich war, um den SCC Prozess abzubilden. Zur Verifizierung und Validierung des erweiterten Modelles wurden verschiedene Testszenarien vom Laborexperiment bis zum Industrieversuch herangezogen.

Folgende Modellerweiterungen wurden durchgeführt. 1) Die Betrachtung des Transportes von sogenannten Keimbildungsimpfmitteln (inoculants) in der flüssigen Schmelze; das Impfmittel dient als Keim für das Wachstum des neuen Kristalls. 2) Die Berücksichtigung der unterschiedlichen Phasengebiete, nämlich die Transformation vom Äquiaxial- zum Stängelkristallgefüge (Equiaxed-to-Columnar, ECT). 3) Eine neue Formulierung für die Kristallfragmentierung wurde auf Grundlage der Flemings Theorie entwickelt und implementiert.

Die verwendeten Validierungsfälle sind experimenteller Natur. Das erste Experiment stellt einen plattenförmigen Abguss dar [Hachani et al., Int. J. Heat Mass Transfer, 85 (2015), p.438], welches mit einer Legierung aus Zinn und Blei umgesetzt wurde. Die Abkühlung der Schmelze wird kontrolliert, indem nur eine Seite des Abgusses abgekühlt wird. Das zweite Experiment, welches zur Validierung herangezogen worden ist, modelliert die Erstarrung einer Amoniumchloridlösung [Gao et al. MCWASP VIII, 1998, p.425]. Auch hier erfolgt die Erstarrung gerichtet, wodurch gezielte Aussagen über die Erstarrungsphasengebiete getroffen werden können. Die numerischen Ergebnisse ergaben eine gute Übereinstimmung mit den Experimenten, sowohl qualitativ als auch quantitativ.

Das numerische Modell wurde verwendet, um industrielle Prozesse abzubilden. Hierbei wurde eine vertikale Stranggießanlage betrachtet (Vertical continuous casting – VCC). Die numerische Vorhersage des Makroseigerungsprofils entlang des Durchmessers stimmt gut mit den experimentell erhaltenen Werten überein. Zudem wurden der elektromagnetische Rührer (EMS: electromagnetic stirrer) im Modell implementiert und für den SCC Prozess herangezogen. Des Weiteren wird hier die Funktion der Kristallfragmentierung im Modell berücksichtigt. Plausible Ergebnisse wurden erhalten.

Zusammenfassend kann das 3-Phasen Modell (mixed columnar-equiaxed) mit erweiterten Funktionen für Erstarrungsvorgänge herangezogen werden, um die Industrieprozess (SCC und VCC) besser zu verstehen. Das Modell wurde mit Laborexperimenten, und einem Industrieversuch validiert. Weitere Validierungen sind wünschenswert.

Abstract

The demand for large format round steel billet has been increasing in past decades. As a new casting method, semi-continuous casting (SCC) process, which attempts to combine the merits of ingot casting and continuous casting techniques, is becoming a competitive technique in modern steel plants to produce large round. However, understanding to the process regarding to the formation of as-solidified structure, macrosegregation, porosity, and so on is not very clear. The objective of this thesis is to use a three-phase columnar-equiaxed solidification model to simulate solidification process of SCC, evaluating the aforementioned issues and supplying instructive suggestions to the industry. This numerical model is originally developed by Wu and Ludwig [Metall. Mater. Trans. A, 2006, p.1613]. In order to model the SCC process, the numerical model was extended. Verifications of the extended model were made in several cases at different scales from laboratory benchmark to practical SCC strand.

Following major numerical model extensions were made. 1) Consideration of transport of inoculants (embryos) in the melt. The inoculants serve as heterogeneous nucleation sites for the equiaxed crystals. The numbers of inoculants and equiaxed crystals are conserved. Inoculants move with liquid phase, while equiaxed crystals move with different velocity. 2) Consideration of the equiaxed-to-columnar transition (ECT) in the volume average model. The remaining melt can fully solidify as columnar structure when the available inoculants are consumed, resulting in ECT. 3) A new formula for crystal fragmentation. Based on the Flemings local remelting theory, it is the interdendritic flow in the columnar growth direction that promotes the solute enrichment of the local interdendritic melt, leading to the solute-driven remelting of the dendrite arms and the formation of crystal fragments.

The extended model is validated against laboratory experiments. Validation of the fragmentation formula was made through the comparison with two benchmark experiments. The first one was based on a plate casting benchmark [Hachani et al., Int. J. Heat Mass Transfer, 85 (2015), p.438], as cast with Sn-10 wt.%Pb alloy and cooled laterally. The second one was an aqueous ammonium chloride (NH_4Cl-H_2O) experiment as cooled from top unidirectionally [Gao et al. in conf. MCWASP VIII, 1998, p.425]. Simulation results agreed quantitatively and qualitatively with observations from experiments.

The extended model was implemented into industrial-scale casting processes. The model with extended features for inoculant-equiaxed crystal conservation and ECT was implemented into a simulation case of vertical continuous casting (VCC). The predicted macrosegregation along the diameter agrees well with the experimental measurement from the plant trial. The model with extended features for fragmentation and magnetic stirring (EMS) was incorporated into the semi-continuous casting (SCC) process. Reasonable results were obtained.

It can be concluded that the extended three-phase mixed columnar-equiaxed solidification model can be used to study the casting process of industry scale, such as SCC and VCC. The model was partially validated against laboratory experiments and limited industry trial. Further validations are desirable.

List of abbreviations

2/3 D	2/3 Dimensional
CBN	Carlson-Beckermann-Niyama criterion
CC	continuous casting
CET	columnar-to-equiaxed transition
ECT	equiaxed-to-columnar transition
EMS	electromagnetic stirring
GMI	global macrosegregation intensity
ICP	inductively coupled plasma
LICC	large ingot continuous caster
M-EMS	mold electromagnetic stirring
RHS	right hand side
SC	segment solidification
SCC	semi-continuous casting
SCN	succinonitrile
S-EMS	strand electromagnetic stirring
SEN	submerged entry nozzle
VCC	vertical continuous casting

Contents

Part I

1 Introduction

1.1 Background

With the surging demand for final wrought products such as large rotor shafts, bearing rings, thread rolling dies or similar components with large formats, the thirst for large steel rounds has been more and more intensive in the past decades [1-3]. The conventional ingot casting can produce large round products, but it has expensive operation costs and substantially lower yields. Continuous casting (CC) also can make the round strand effectively. However, the cross-section of continuous casting is usually small. Semi-continuous casting (SCC), which attempts to combine the high productivity and quality of continuous casting (CC) and the ability to produce large cross-section products of conventional ingot casting, is an alternative option to produce large steel round.

As-solidified structure is usually composed of a thin equiaxed chill zone near the outside surface, a columnar zone based on the chill zone and another equiaxed zone in the center. A typical macrostructure in continuous casting round is show in Figure 1.1 (a). The macrosegregation in large steel strands by SCC is suspected to be sensitive to strand size. The intensity of macrosegregation increases with the size of the casting. A well-configured as-cast columnar and equiaxed structure in the casting is beneficial to relieve the macrosegregation. With the increase of the length of the casting, centerline porosity is also an issue of concern.

With conventional solidification methods, in which melt is with a certain amount of impurities and cooling rate is usually smaller than 1000 K/s, equiaxed crystals can originate from heterogeneous nucleation and/or fragmentation. Subsequently, the equiaxed crystals are transported away in the melt and they can settle down or floating up through the balance of drag force and buoyancy. The equiaxed crystals will grow or remelt during the movement. When the volume fraction of equiaxed crystals exceeds a so-called blocking criterion at the columnar tip front, the columnar-to-equiaxed transition (CET) occurs. It is well accepted that equiaxed structure in metal castings can promote mechanical performance for the as-cast component. Additionally, the probability of porosity is relatively low in equiaxed region. The equiaxed zone in the casting can be manipulated by adding inoculants in the melt, implementing electromagnetic stirring, etc.

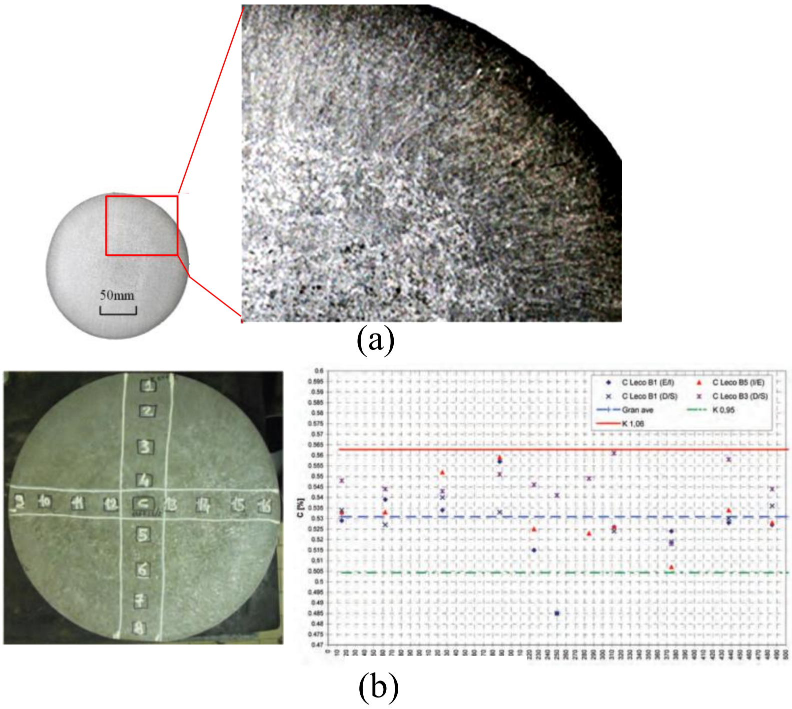

Figure 1.1 Examples of continuously-cast round billet. a) Macrostructure of a round steel strand (ϕ 200 mm) [4]; b) as-cast structure and macrosegregation of carbon along the diameter (ϕ 500 mm) [5].

Macrosegregation is the inhomogeneous solute distribution observed at the scale of a casting. Due to the solutal partition, in which the partition coefficient is usually considered smaller than unit, equiaxed and columnar have negative microsegregation, while the liquid has increasing positive microsegregation. Relative motion between liquid, equiaxed and columnar can redistribute those solutal elements, result in macrosegregation. The sedimentation of early stage formed equiaxed crystals may result in negative macrosegregation (Fig 1.1 (b)). However, in some continuous casting a positive macrosegregation can be witnessed in the center by decreasing the diameter of the strand or using of electromagnetic stirring. In the portion of end solidification it usually has positive macrosegregation.

1.2 Objectives

Semi-continuous casting (SCC) process is a very promising method to produce large format round steel billet. In comparison with the experimental study for the SCC process, simulation is of great advantage for its high flexibility and low cost. Volume average method [6, 7] is an available tool to simulate as-solidified structure and the macrosegregation. However, due to the complexity of solidification process, direct numerical predictions of the as-cast structure and macrosegregation are still difficult. The target of this thesis is to extend a three-phase columnar-equiaxed solidification model, so that it can capture the key features of solidification for SCC, e.g. the formation of the as-solidified structure and macrosegregation.

(1) Test the original numerical model. Try to understand three-phase mixed columnar-equiaxed solidification model, which considers a variety of phenomena as such as (a) the growth of columnar trunks, (b) the tracking of the columnar tips, (c) the origination and transport of crystals, (d) the thermal-solutal buoyancy flow and it interaction with the sedimentation of crystals and (e) columnar-to-equiaxed transition (CET).

(2) Extend the multiphase solidification model by including following new features. (a) Take inoculant-equiaxed crystal conservation into account. The inoculants serve as heterogeneous nucleation sites for the equiaxed crystals. b) Try to realize equiaxed-to-columnar transition (ECT) in volume average model. The remaining melt can fully solidify as columnar structure when the available inoculants are consumed, resulting in

ECT. (c) Propose a fragmentation formula based on a remelting-driven fragmentation theory. (d) Incorporate electromagnetic stirring (EMS) into multiphase solidification model for VCC and SCC process.

(3) Validate the extended model by comparison of simulation results with published experimental measurements [6, 8, 9].
(4) Implement the extended model into the casting process of industrial scale, such as VCC and SCC.

This thesis consists of two parts. Part I describes the motivation, the state-of-the-art of the field, and an executive summary of the Ph.D work. Part II presents the main results of the thesis, in the form of paper collection. 5 peer reviewed journal articles are included.

2 State of the art

2.1 Steel ingot of large format

In the last decades, a rising demand for the manufacture of large size casting (above 600 mm equivalent circle diameter) is witnessed for the medium- and high-alloyed steel grade production [2, 3]. The industrial-scale steel castings of large format can be generally manufactured by following processes: conventional ingot casting， continuous casting, semi-continuous casting or segment casting. The distinctive attribute of those process are briefly described in this section.

2.1.1 Conventional ingot casting

The production of conventional steel ingot casting can date back to 1870's. Before 1970's this casting route dominated the entire steel production. Due to the dramatically development of continuous casting process in the last decades, the occupation of conventional ingot steel casting in the market shrinks to about 10% [2]. Nowadays, ingot casting is still the optimum choice for some low-alloy steel grades and steels for special purposes. Those include high carbon chromium bearing steel, thick seamless tube and large format forgings [3, 10, 11].

Top pouring for ingot casting is an easy-to-implement method, but it has a high probability to have defects both on the surface and inside the ingot. Bottom pouring (teeming) is better to produce a high quality ingot, especially when the melt has high super heat or the casting speed is low. A typical bottom-poured ingot casting is shown in Figure 2.1. The ingot mold is filled directly from the ladle via trumpet (central runner) and further in the heavy molding shells from bottom (Figure 2.1(a)) [12-13].

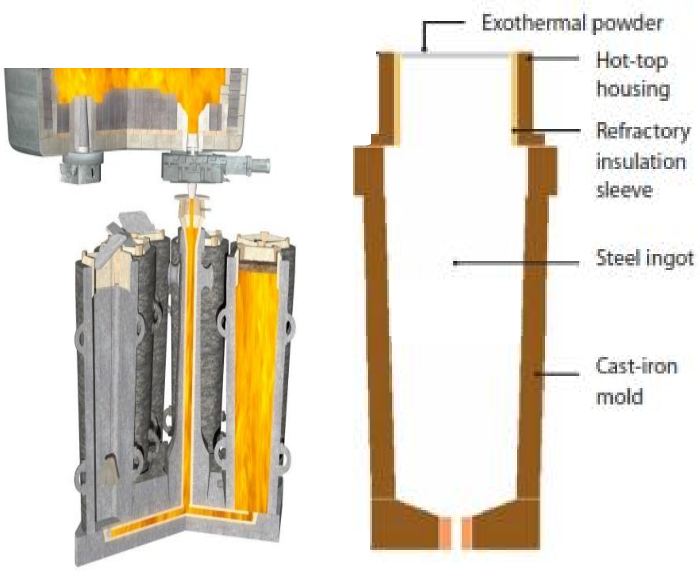

(a) (b)

Figure 2.1. Ingot casting: (a) ingot production by bottom pouring [13] and (b) a tyipical casting mold with a trapeze form wall [14].

The filling is very quick and usually takes just several minutes. The ingot shell is solidified quickly by the cold mold. Afterwards, the thick iron mold wall, which has low heat conductivity, limit the extraction of heat from the liquid pool through solid shell during the solidification. The mold and solid shell keep the inner part of the ingot in a liquid status for a long time of couple of hours, even several days, resulting in a very slow solidification.

In order to avoid strong shrinkage porosity in the center, the mold usually have a trapeze form of mold (Figure 2.1(b)) [14]. The bigger dimension on the top side can get a large portion of liquid pool on upper part, as is beneficial to reduce the center porosity. Additionally, the top of the ingot is kept in a liquid condition as long as possible by hot topping, similar to the insulations laterally on the top by slag (powder) covering. Thus the center area of the ingot can get new liquid from the top for shrinkage compensation until the end of solidification. The ingot usually has an equiaxed zone in the bottom part and mostly columnar zone in the upper part. Generally, the ingot has negative macrosegregation at the equiaxed zone, while it has positive macrosegregation in the hot top position as well as the center part of columnar zone, where the ingot has high probability of porosity [15]. Additionally, the ingot casting may have issues related to non-metallic inclusions, et al.

2.1.2 Vertical continuous casting

Even as early as the nineteenth century the advantage of solidifying steel using a more continuous method was recognized. These methods are firstly not used in steel production due to the higher temperatures and the low thermal conductivity of steel. In 1946, one of the first continuous casting machines for steel was a vertical caster installed for the production of steel billets at Low Moor, Great Britain. After that, scientists and engineers in UK, USA, Austria and Germany gave valuable contributions to the development of modern steel continuous casters, from fixed mold to a spring suspended mold, till mold with oscillation systems [16]. From 1950 onwards, the development of the technology for the continuous casting of steel at a large scale accelerated [17]. Nowadays, there are different continuous casting installations in use, such as vertical, curved, horizontal, strip, etc. [18]. In order to reduce crack defects on round billet surfaces, the vertical caster is considered as a feasible method to produce large format blooms [19-22].

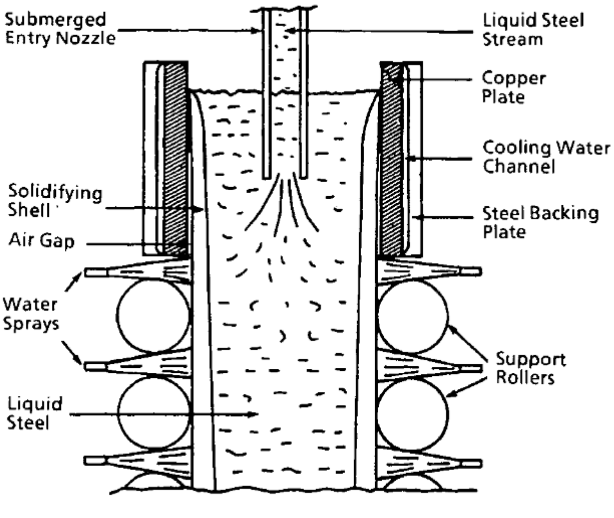

Figure 2.2. Basic principles of vertical continuous casting process near the mold [17].

The schematic of vertical continuous casting near the mold is shown in Figure 2.2. At continuous casting pouring is done under full protection against oxygen by using submerged entry nozzle and casting powder covering. The synthetic covering powder is used on the top (meniscus) of the melt in the mold. The powder in contact with the liquid steel melts to form a slag flux infiltrates into the gap between steel and copper mold at the meniscus to provide lubrication. The powder can clean the steel melt since inclusions in the liquid pool can float up and are entrapped into the slag layer which is carried away continuously via the surface of the strand shell [2]. The strand then is formed continuously to an expected shape with good surface by an oscillating copper mold.

As soon as the solidified skin is sufficiently thick to contain the liquid steel the strand leaves the mold and is further cooled by water sprays. Due to the skin cooling and contracting, the mold becomes less efficient in heat transfer due to the 'air' gap forming between the copper wall and the outer side of the solidified skin. Therefore, copper mold does not help further solidification. It is more efficient to use direct water spraying from high pressure nozzles. However, the hot solidified skin cannot withstand the pressure arising from the liquid steel within the solidified skin and, if unconstrained, would bulge outwards. Thus it is necessary to support the continuously solidifying shell by rollers or some other mechanical systems [17].

A schematic of a recent vertical continuous casting machine targeting at steel strand of large format is shown in Figure 2.3. The vertical continuous casting machine was constructed of concrete, with a total height of 52 m (ground height 25 m and underground depth 27 m), the machine was designed to produce three round billet sizes: 800 mm, 3.6 t/m (large); 600 mm, 2 t/m (medium); and 400 mm, 0.9 t/m (small). The top of the mold was at 22 m. During withdrawing, the strand is surrounded by mold electromagnetic stirrer (M-EMS), secondary cooling system, strand electromagnetic stirrer (S-EMS), and torch cutting machine. The billet was guided by elevator into an inclined transport car. Maximum casting speed was 0.40 and 0.10 m/min for small and large billet section, respectively [23]. Due to the strong water spray, the solid may grow along the thermal gradient, and form a deep melt pool, resulting in porosity (Figure 2.4) due to insufficient melt compensation in the late stage of solidification [24]. Similar casters can be found in some other publications [19-22].

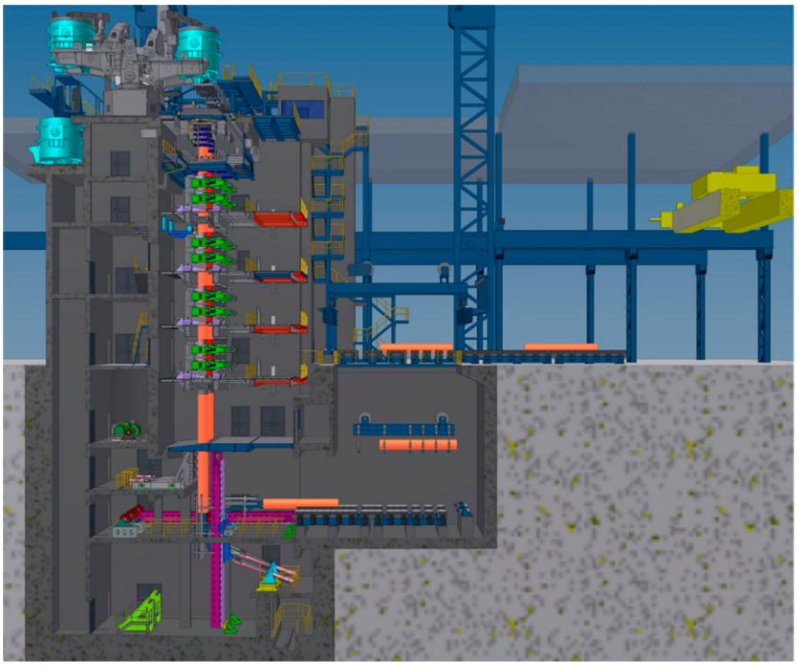

Figure 2.3. Schematic of vertical continuous casting process [23].

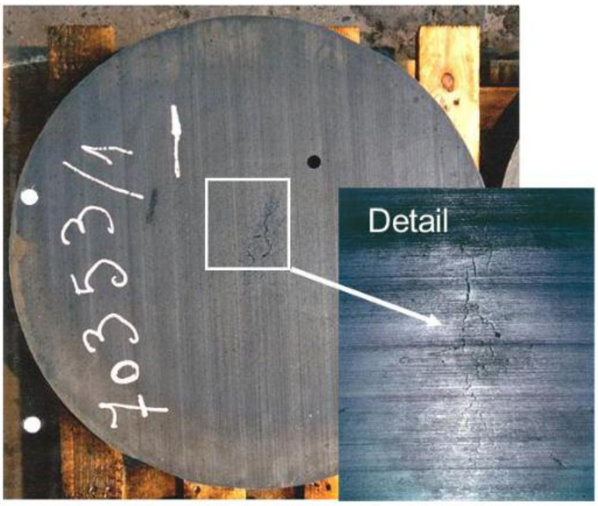

Figure 2.4. Porosity in the vertical continuous casting strand [24].

Compared to the ingot casting, the benefits of continuous casting process are: 1) higher yield; 2) lower operation cost; 3) better surface finish and 4) the ability to improve melt cleanness. But it cannot cope with high alloyed steel grades and it is handicapped in costs at very low volume production due to its expensive initial investment [2, 25].

2.1.3 Semi-continuous casting

Semi-continuous casting (SCC) is a derivation of the vertical continuous casting process. The difference is that the strand in SCC is withdrawn to a specified length, and then the strand undergoes a hot toping stage till it is fully solidified. There is a similar process called segment casting (Figure 2.5). This process can be decomposed into 2 steps [3, 26]. 1) Casting step. The casting step starts with the insertion of the dummy bar head into the machine; the dummy bar acts as a withdrawing device of the solidified strand from the mold; casting process can be started upon the opening of a ladle; melt flow into the tundish through a protective refractory shroud in order to prevent re-oxidation; steel stream flowing from tundish to mold will also be protected by a submerged entry nozzle. 2) Solidification step. The strand is stationary and the solidification continues; a hot feeding (hot topping) operation is carried out to avoid the formation of shrinkage piping; magnetic stirring can be applied around the strand to improve the strand quality.

High cooling rates in conventional/vertical continuous casting cause pronounced radial orientation of the crystallization front in the strand. Thus the strand center, where the crystallization front is closing from all sides, gets sensitive for porosity and shrinkage crack. In semi-continuous casting only bloom shell is solidified quickly like at continuous casting. The inner strand is solidified very slowly similar to ingot casting. In order to improve the performance of strand quality, another caster called semi-continuous casting with the possibility to control the cooling condition is set up (Figure 2.6). A dynamic heat shielding, which can adjust the heat transfer condition, is placed around the strand in solidification step. This assists to enhance the hot toping and prevent a long final solidification range in the strand center [2, 20].

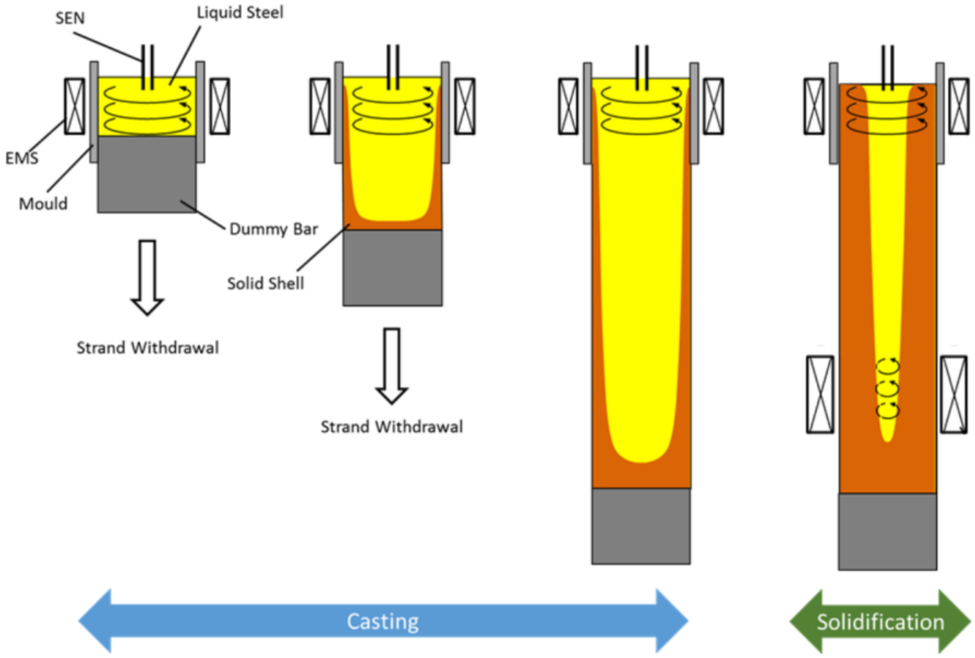

Figure 2.5. Schematic of segment casting process [26].

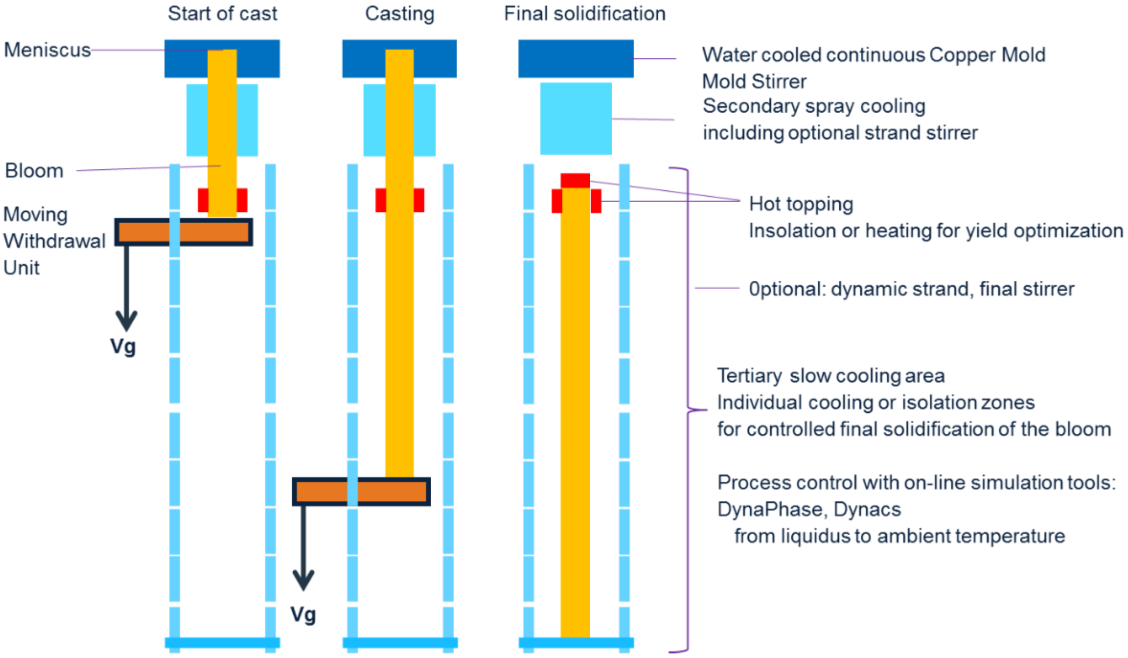

Figure 2.6. Schematic of semi-continuous casting process with cooling control system [2].

Semi-continuous casting is a quite mature process for producing copper and aluminum alloys in the non-ferrous industry [27-33]. It is not easy to transfer the technology into steel strand manufacturing due to high temperature involved and the low thermal conductivity of steel [17], as would result in the tendency of crack/hot tearing both on the surface and inside the strand. Nowadays, the large format casting production technology resorting to vertical continuous casting or semi-continuous casting is still in the evolving progress. Quite a few companies, including both equipment producers and steel manufactures, take part in this vigorous field, as are listed in Table 2.1. They are trying to produce bigger format steel strand with higher efficiency, higher yielding, as well as lower cost.

Table 2.1. Concept/techniques under development for large steel strand.

Company	Technical means	Ref.
Primetals	Semi-continuous casting (SCC)	[2, 20, 23, 24, 34]
Inteco TBR	Segment casting (SC)	[3, 26]
SMS	VERSCON	[1, 35]
Posco	Large ingot continuous caster (LICC)	[19, 36]

Conventional ingot casting has limitations due to several reasons, such as the fixed process procedure, low controllability of cooling, low yield and production efficiency [2, 3, 17]. By using copper mold and oscillating technology, continuous casting strand production has higher production efficiency and the strands have a good surface quality. Semi-continuous casting, which attempts to combine the advantages of ingot casting and continuous casting, is aimed to replace ingot casting with improved yield and quality for the production of special grades like tool- , die- and stainless steel. It can manipulate the cooling condition of the strand during solidification process [2, 21]. The hot feeding would take effect during the whole solidification stage and will substantially decrease the formation of cavities and avoid undesired piping in the large blooms and thereby increasing the yield of the process [22-24] . Thus, the formation of cavities, pores and segregation patterns can be reduced significantly. The entire casting process becomes more reliable and reproducible. The distinctive attribution of the aforementioned processes are briefly described and compared with other processes in Table 2.2. The advantages of semi-continuous casting can be easily highlighted.

Table 2.2. The pros and cons of different casting processes.

	Steel ingot	Continuous casting	Semi CC
Initial investment cost	+++	++	++
Operation cost	+	+++	+++
Yield	--	+++	++
Production capacity	+	+++	++
Process controllability	+	++	+++
Equiaxed zone control	---	+	+++
Risk of centerline porosity	-	+	+++
Surface quality	-	+++	+++
Macrosegregation	++	++	+
Diameter (thickness) limitation	+++	--	++

Note: '-' '--', '---', indicate low, middle, and high disadvantages, respectively; '+', '++', '+++' indicate low, middle, and high advantages, respectively.

2.2 Numerical model – volume average method

There are two types of averaging methods which were used to calculate solidification. Assemble averaged (statistical) approach is consistent with the random nature of the germination process as well as the behavior of the equiaxed grains. The ensemble averaging technique can treat various types of solidification, i.e. columnar or/and equiaxed solidification [37, 38]. However, within this method the melt flow and equiaxed movement are not included. Another method is called volume average method. It is a powerful tool to cope with the prediction of the as-cast structure and macrosegregation. It can couple the transport phenomena during solidification at the macroscopic scale with the phenomena at the microscopic scale. The volume average method has been widely used in numerical simulation of solidification. It greatly promotes the understanding of the multi-scale coupling in solidification process. Beckermann and Viskanta [39] proposed a volume average model to simulate solidification, and predict the double-diffusive convection during dendritic solidification of ammonium chloride (NH4Cl) solution. It pointed out that the solidification and melting of the solid are closely related to the convection and solutal distribution. This model was extended by J. NI and C. Beckermann [40, 41] to consider the relative movement between liquid, equiaxed phases to predict the macrosegregation in a wide range of casting process. M. Bellet [42] developed a similar two-phase model, which considers the motion of solid in the solidification end, to predict the centerline macrosegregation in the steel slab. Wu et al. extended the multiphase model and enable it to analyze effectively the mechanism of macrosegregation in conventional steel ingot [7, 43, 44] and centerline macrosegregation in continuous casting process [45, 46]. For dendrite solidification envelope, a concept of the dendritic crystal envelope can be taken into account in this statistical approach. However, it needs dramatically high computation resource if interdendritic flow is considered [37, 38, 47, 48]. The volume average method with a simple dendrite model is computationally more efficient and the simulation in this thesis adopt the volume average multiphase model with simple dendrite assumption [49]. The introduction of volume average model and its derivation into a three-phase mixed columnar-equiaxed solidification model are shown in the coming sections.

2.2.1 Theorems of volume average

The objectives of the averaging methods are twofold [50]: (1) to define the average properties for the multiphase system and correlate the experimental data, and (2) to obtain solvable governing equations that can be used to predict the macroscopic properties of the multiphase system.

Consider a representative elementary volume ΔV as shown in Figure 2.7, we have the following definitions and theorems [50-52]. Eulerian volumetric averaging is usually performed over a volume element, ΔV, around a point (x, y, z) in the flow. For a multiphase system that includes N different phases, the total volume equals the summation of the individual phase volumes:

$$\Delta V = \sum_{\mathrm{k}=1}^{\mathrm{N}} \Delta V_{\mathrm{k}} . \tag{2.1}$$

ΔV_{k}, indicates the volume of phase *k* in the represitive volume.

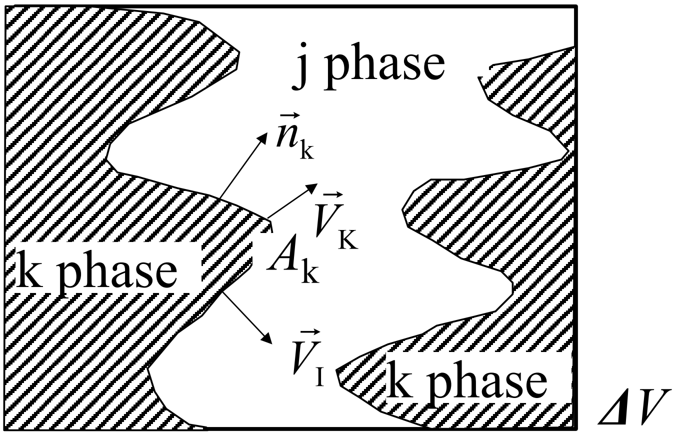

Figure 2.7. Representative volume used to average the conservation equation. $\vec{n}_{\mathrm{k}}$, A_{k}, $\vec{V}_{\mathrm{K}}$, $\vec{V}_{\mathrm{I}}$ indicate the normal direction of k phase, surface area of k phase, absolute advancing velocity of k phase surface, and the relative velocity between k and j phases without considering mass transfer, respectively.

The phase-average value of any variable or property for a certain phase Φ_{k} is obtained with the following equations by intrinsic phase average,

$$\left\langle \Phi_{\mathrm{k}} \right\rangle^{\mathrm{k}} = \frac{1}{\Delta V_{\mathrm{k}}} \int_{\Delta V_{\mathrm{k}}} \Phi_{\mathrm{k}} dV , \tag{2.2}$$

and extrinsic phase average,

$$\left\langle \Phi_{\mathrm{k}} \right\rangle^{\mathrm{k}} = \frac{1}{\Delta V} \int_{\Delta V_{\mathrm{k}}} \Phi_{\mathrm{k}} dV . \tag{2.3}$$

These two phase-averages are related through the phase volume fraction f_{k} by

$$\left\langle \Phi_{\mathrm{k}} \right\rangle = f_{\mathrm{k}} \left\langle \Phi_{\mathrm{k}} \right\rangle^{\mathrm{k}} . \tag{2.4}$$

They are related to the volume averaged value by

$$\langle\Phi\rangle = \sum_{k=1}^{N}\langle\Phi_k\rangle = \sum_{k=1}^{N} f_k\langle\Phi_k\rangle^k . \tag{2.5}$$

The deviation of Φ_k from a respective intrinsic phase average value is

$$\hat{\Phi}_k = \Phi_k - \langle\Phi_k\rangle^k . \tag{2.6}$$

When the products of two variables are phase averaged, the following relations are needed:

$$\langle\Phi_k\Psi_k\rangle^k = \langle\Phi_k\rangle^k\langle\Psi_k\rangle^k + \langle\hat{\Phi}_k\hat{\Psi}_k\rangle^k \tag{2.7}$$

$$\langle\Phi_k\Psi_k\rangle = f_k\langle\Phi_k\rangle^k\langle\Psi_k\rangle^k + \langle\hat{\Phi}_k\hat{\Psi}_k\rangle . \tag{2.8}$$

For the control volume ΔV shown in Figure 2.7, the volume averaging of the partial derivate with respect to time is obtained by the following general transport theorem:

$$\left\langle\frac{\partial\Omega_k}{\partial t}\right\rangle = \frac{\partial\langle\Omega_k\rangle}{\partial t} + \frac{1}{\Delta V}\int_{A_k}\Omega_k\vec{V}_I\cdot\vec{n}_k dA_k . \tag{2.9}$$

The volume average of the gradient is

$$\langle\nabla\Omega_k\rangle = \nabla\langle\Omega_k\rangle - \frac{1}{\Delta V}\int_{A_k}\Omega_k\cdot\vec{n}_k dA_k . \tag{2.10}$$

Volume average of a divergence is

$$\langle\nabla\cdot\Omega_k\rangle = \nabla\cdot\langle\Omega_k\rangle - \frac{1}{\Delta V}\int_{A_k}\Omega_k\cdot\vec{n}_k dA_k . \tag{2.11}$$

2.2.2 Conservative equations by volume average method

Now let us deduce the macroscopic mass conservation equation for the solidification system by using the definitions and the theorems. Let's consider the following microscopic mass conservation Equation (2.12) for the liquid phase:

$$\frac{\partial\rho_k}{\partial t} + \nabla\cdot(\rho_k\vec{v}_k) = 0 \tag{2.12}$$

$$\left\langle\frac{\partial\rho_k}{\partial t}\right\rangle + \langle\nabla\cdot(\rho_k\vec{v}_k)\rangle = 0 . \tag{2.13}$$

The two terms on the left-hand side can be obtained by using Equation (2.9) and Equation (2.11). Substituting the above expressions into Equation (2.13) the volume averaged continuity equation becomes

$$\frac{\partial\langle \rho_{\mathrm{k}}\rangle}{\partial \mathrm{t}}+\nabla\cdot\langle \rho_{\mathrm{k}}\vec{v}_{\mathrm{k}}\rangle=-\frac{1}{\Delta V}\int_{A_{\mathrm{k}}}\rho_{\mathrm{k}}(\vec{V}_{\mathrm{K}}-\vec{V}_{\mathrm{I}})\cdot\vec{n}_{\mathrm{k}}dA_{\mathrm{k}} \tag{2.14}$$

The right-hand side of Equation (2.14) can be rewritten as

$$\frac{1}{\Delta V}\int_{A_{\mathrm{k}}}\rho_{\mathrm{k}}(\vec{V}_{\mathrm{K}}-\vec{V}_{\mathrm{I}})\cdot n_{\mathrm{k}}dA_{\mathrm{k}}=\sum_{\mathrm{j=1\,(j\neq k)}}^{\mathrm{N}}\dot{m}_{\mathrm{jk}}\ , \tag{2.15}$$

where $\dot{m}_{\mathrm{jk}}$ represents mass transfer from the j^{th} to the k^{th} phase due to phase change. The value of $\dot{m}_{\mathrm{jk}}$ depends on the phase change process that takes place in the multiphase system, and the conservation of mass requires $\dot{m}_{\mathrm{jk}}=-\dot{m}_{\mathrm{kj}}$. For solid - liquid two phase system (k = s, ℓ), we can deduce

$$\frac{\partial\langle \rho_{\ell}\rangle}{\partial t}+\nabla\cdot\langle \rho_{\ell}\vec{u}_{\ell}\rangle=M_{\mathrm{s}\ell} \tag{2.16}$$

$$\frac{\partial\langle \rho_{\mathrm{s}}\rangle}{\partial t}+\nabla\cdot\langle \rho_{\mathrm{s}}\vec{u}_{\mathrm{s}}\rangle=M_{\ell\mathrm{s}}\,. \tag{2.17}$$

We can simply take the instinct liquid (or solid) density as a constant. For solid-liquid two phase system with stationary solid $\vec{u}_{\mathrm{s}}=0$, we can rewrite $\langle \rho_{\ell}\rangle$ into $f_{\ell}\rho_{\ell}$, and $\langle \rho_{\ell}\vec{u}_{\ell}\rangle$ into $f_{\ell}\rho_{\ell}\vec{u}_{\ell}$ for simplification in the continuity equations as

$$\frac{\partial}{\partial t}(f_{\ell}\rho_{\ell})+\nabla\cdot(f_{\ell}\rho_{\ell}\vec{u}_{\ell})=M_{\mathrm{s}\ell} \tag{2.18}$$

$$\frac{\partial}{\partial t}(f_{\mathrm{s}}\rho_{\mathrm{s}})=-M_{\mathrm{s}\ell}\,. \tag{2.19}$$

If three phases, i.e. liquid, equiaxed and columnar, are considered, in the system then we can get

$$\frac{\partial}{\partial t}(f_{\ell}\rho_{\ell})+\nabla\cdot(f_{\ell}\rho_{\ell}\vec{u}_{\ell})=M_{\mathrm{e}\ell}+M_{\mathrm{c}\ell} \tag{2.20}$$

$$\frac{\partial}{\partial t}(f_{\mathrm{e}}\rho_{\mathrm{e}})+\nabla\cdot(f_{\mathrm{e}}\rho_{\mathrm{e}}\vec{u}_{\mathrm{e}})=M_{\ell\mathrm{e}} \tag{2.21}$$

$$\frac{\partial}{\partial t}(f_{\mathrm{c}}\rho_{\mathrm{c}})=M_{\ell\mathrm{c}}\ . \tag{2.22}$$

Similarly, the momentum conservation equations can be derived as

$$\frac{\partial}{\partial t}(f_\ell\rho_\ell\vec{u}_\ell)+\nabla\cdot(f_\ell\rho_\ell\vec{u}_\ell\otimes\vec{u}_\ell)=-f_\ell\nabla p+\nabla\cdot\bar{\bar{\tau}}_\ell+f_\ell\rho_\ell\vec{g}_\ell'-\vec{U}_{\ell\mathrm{e}}-\vec{U}_{\ell\mathrm{c}} \tag{2.23}$$

with $\vec{g}_\ell' =\frac{\rho_\ell^{\mathrm{b}}(T,c)-\rho_\ell}{\rho_\ell}\vec{g}$, $\rho_\ell^{\mathrm{b}}(T,c)=\rho_\ell\cdot\left[1+\beta_{\mathrm{T}}\cdot(T^{\mathrm{ref}}-T_\ell)+\beta_{\mathrm{c}}\cdot(c^{\mathrm{ref}}-c_\ell)\right]$, $\vec{U}_{\ell\mathrm{e}}=\vec{U}_{\ell\mathrm{e}}^{\mathrm{p}}+\vec{U}_{\ell\mathrm{e}}^{\mathrm{d}}$,

$\vec{U}_{\ell\mathrm{c}}=\vec{U}_{\ell\mathrm{c}}^{\mathrm{p}}+\vec{U}_{\ell\mathrm{c}}^{\mathrm{d}}$. Similarly, we can get

$$\frac{\partial}{\partial t}(f_{\mathrm{e}}\rho_{\mathrm{e}}\vec{u}_{\mathrm{e}})+\nabla\cdot(f_{\mathrm{e}}\rho_{\mathrm{e}}\vec{u}_{\mathrm{e}}\otimes\vec{u}_{\mathrm{e}})=-f_{\mathrm{e}}\nabla p+\nabla\cdot\bar{\bar{\tau}}_{\mathrm{e}}+f_{\mathrm{e}}\rho_{\mathrm{e}}\vec{g}_{\mathrm{e}}'+\vec{U}_{\ell\mathrm{e}}+\vec{U}_{\mathrm{ce}} \tag{2.24}$$

with $\vec{g}_{\mathrm{e}}'=\frac{\Delta\rho}{\rho_{\mathrm{e}}}\vec{g}$, $\vec{U}_{\mathrm{ce}}=\vec{U}_{\mathrm{ce}}^{\mathrm{p}}+\vec{U}_{\mathrm{ce}}^{\mathrm{d}}$, $\Delta\rho=\rho_{\mathrm{e}}-\rho_\ell$.

Similarly, the enthalpy equations can be written as

$$\frac{\partial}{\partial t}(f_\ell\rho_\ell c_\ell)+\nabla\cdot(f_\ell\rho_\ell\vec{u}_\ell c_\ell)=\nabla\cdot(f_\ell\rho_\ell D_\ell\nabla c_\ell)-C_{\ell\mathrm{c}}^{\mathrm{p}}-C_{\ell\mathrm{e}}^{\mathrm{p}} \tag{2.25}$$

$$\frac{\partial}{\partial t}(f_{\mathrm{e}}\rho_{\mathrm{e}}h_{\mathrm{e}})+\nabla\cdot(f_{\mathrm{e}}\rho_{\mathrm{e}}\vec{u}_{\mathrm{e}}h_{\mathrm{e}})=\nabla\cdot(f_{\mathrm{e}}k_{\mathrm{e}}\nabla\cdot T_{\mathrm{e}})+Q_{\ell\mathrm{e}}+Q_{\mathrm{ce}} \tag{2.26}$$

$$\frac{\partial}{\partial t}(f_{\mathrm{c}}\rho_{\mathrm{c}}h_{\mathrm{c}})=\nabla\cdot(f_{\mathrm{c}}k_{\mathrm{c}}\nabla\cdot T_{\mathrm{c}})+Q_{\ell\mathrm{c}}-Q_{\mathrm{ce}} \tag{2.27}$$

with $Q_{\ell\mathrm{e}}=Q_{\ell\mathrm{e}}^{\mathrm{p}}+Q_{\ell\mathrm{e}}^{\mathrm{d}}$, $Q_{\mathrm{ce}}=Q_{\mathrm{ce}}^{\mathrm{p}}+Q_{\mathrm{ce}}^{\mathrm{d}}$, $Q_{\mathrm{ce}}^{\mathrm{d}}=0$, $Q_{\ell\mathrm{c}}=Q_{\ell\mathrm{c}}^{\mathrm{p}}+Q_{\ell\mathrm{c}}^{\mathrm{d}}$, $h_\ell=\int_{T_{\mathrm{ref}}}^{T_\ell}c_{\mathrm{p}}^{\ell}dT+h_\ell^{\mathrm{ref}}$, $h_{\mathrm{e}}=h_c=\int_{T_{\mathrm{ref}}}^{T_{\mathrm{e}}}c_{\mathrm{p}}^{\mathrm{e}}dT+h_{\mathrm{e}}^{\mathrm{ref}}$ and Δh_{f}

$=h_\ell^{\mathrm{ref}}-h_{\mathrm{e}}^{\mathrm{ref}}$.

Species equations can be written as follows.

$$\frac{\partial}{\partial t}(f_\ell\rho_\ell c_\ell)+\nabla\cdot(f_\ell\rho_\ell\vec{u}_\ell c_\ell)=\nabla\cdot(f_\ell\rho_\ell D_\ell\nabla c_\ell)-C_{\ell\mathrm{c}}^{\mathrm{p}}-C_{\ell\mathrm{e}}^{\mathrm{p}} \tag{2.28}$$

$$\frac{\partial}{\partial t}(f_{\mathrm{e}}\rho_{\mathrm{e}}c_{\mathrm{e}})+\nabla\cdot(f_{\mathrm{e}}\rho_{\mathrm{e}}\vec{u}_{\mathrm{e}}c_{\mathrm{e}})=\nabla\cdot(f_{\mathrm{e}}\rho_{\mathrm{e}}D_{\mathrm{e}}\nabla c_{\mathrm{e}})+C_{\ell\mathrm{e}}^{\mathrm{p}} \tag{2.29}$$

$$\frac{\partial}{\partial t}(f_{\mathrm{c}}\rho_{\mathrm{c}}c_{\mathrm{c}})=\nabla\cdot(f_{\mathrm{c}}\rho_{\mathrm{c}}D_{\mathrm{c}}\nabla c_{\mathrm{c}})+C_{\ell\mathrm{c}}^{\mathrm{p}}\ . \tag{2.30}$$

The meanings of symbols above can be found in Paper II of Part II. The above mentioned conservation equations are used and the simulations conducted are based on the three-phase mixed columnar-equiaxed solidification model. They solved are based on the platform of commercial software ANSYS Fluent version 14.5.

2.2.3 Incorporate EMS into volume average method

The flow in the mushy zone during solidification can be intensively manipulated by electromagnetic stirring (EMS) [53] or other mechanical stirring. It is feasible to regulate the mass transformation from columnar phase to equiaxed phase by EMS [8, 54, 55]. The following Maxwell equations need to be solved [56]:

$$\nabla \times \vec{E} = \mu_0 \varepsilon_0 \frac{\partial \vec{E}}{\partial t} + \mu_0 \vec{J} \tag{2.31}$$

$$\nabla \cdot \vec{E} = -\frac{\rho}{\varepsilon_0} \tag{2.32}$$

$$\nabla \cdot \vec{B} = 0 \tag{2.33}$$

$$\nabla \times \vec{E} = -\frac{\partial \vec{B}}{\partial t} . \tag{2.34}$$

The equations introduce the electric field, $\vec{E}$ [kgmA^{-1}s^{-3}], a vector field, and the magnetic induction, $\vec{B}$ [kgs^{-2}A^{-1}], a pseudo-vector field, each generally having a time and location dependence. The sources are the total electric charge density, ρ [C/m^3], and the total electric current density, $\vec{J}$ [A/m^2], a vector. The universal constants appearing in the equations are the permittivity of free space, ε_0 [kg^{-1}m^{-3}A^{2}s^4], and the permeability of free space, μ_0 [kgms^{-2}A^{-2}]. Then we can get the magnetic force through

$$\nabla \cdot \vec{J} = -\nabla \cdot \frac{\partial \rho}{\partial t} \tag{2.35}$$

$$\vec{F} = \vec{J} \times \vec{B} . \tag{2.36}$$

$\vec{F}$ is with the unit N/m^3. Finally, as source term (vector), the magnetic force can be calculated for specific phases according to their own volume fraction:

$$\vec{S}_\ell = f_\ell \vec{F} \tag{2.37}$$

$$\vec{S}_\mathrm{e} = f_\mathrm{e} \vec{F}\,. \tag{2.38}$$

Above magnetic forces are calculated by software ANSYS Maxwell, then the force are averaged and interpolated into ANSYS Fluent. For the round strand with the length greatly larger than the height of the EMS, we can calculate the force analytically. Based on the results of experiments, the magnetic force has an typical variation that can be approximated by a Gaussian distribution as follows [57]:

$$\vec{F} = \frac{1}{2}\sigma B_0^2 |\omega r| \exp\left(-2\left(\frac{x - x_{\mathbf{mid}}}{x_{\mathbf{width}}}\right)^2\right) \cdot \left(1 - \frac{v_\theta}{\omega r}\right) \cdot \vec{\theta} \tag{2.39}$$

where ω is the line frequency and B_0 , z_{mid} and z_{width} indicate the maximal magnetic induction, the middle position of the magnetic and the width of the magnetic, respectively; r is the distance between the local reference point and the axial on the radial direction; $\vec{\theta}$ is the directional unit vector in cylindrical coordinate. The region near the surface and the middle point of the magnet stirrer has the biggest magnetic force. The magnetic force in the center of the strand is zero.

2.3 Special aspects in simulation of solidification process

2.3.1 Heterogeneous nucleation

Nucleation is of great importance to formation of microstructure and macroscopic transport phenomena. Although the importance of those transport phenomena in the as-cast structure formation was since long recognized [58], there is no mature theory to describe the relationship between the crystal transport and the resulting structural and compositional heterogeneities until some numerical models were developed in 1990s [41, 59]. Mechanisms for the origin of equiaxed crystals, considering the transport phenomenon of inoculants and equiaxed crystals [60-62], are not fully understood. For most models considering solidification, the origin of the equiaxed crystals was simply treated as a continuous undercooling-dependent heterogeneous nucleation event [7, 63] or a simultaneous nucleation event at a certain undercooling [14]. The nucleation prefers to be activated on foreign particles. Heterogeneous nucleation as function of undercooling according to a Gaussian distribution law was usually assumed [63]: $\dot{n} = K_1[n_0 - n(t)]\exp(-K_2/T(\Delta T)^2)$, $\dot{n}$ [m^{-3} s^{-1}] is the nucleation rate at a given undercooling ΔT . n_t [m^{-3}] the nucleation number density while n_0 [m^{-3}] is saturation limit of nucleation number density. K_1 [s^{-1}] and K_2 [K^3] are two constants, K_1 is proportional to the collision frequency of the atoms of the melt with the nucleation sites of the heterogeneous particles and K_2 is related to the interfacial energy balance between the nucleus, the liquid, and the foreign substrate on which nucleation occurs.

The equiaxed crystals can be treated as a pseudo liquid phase (secondary fluid phase), interpenetrating and incorporating with the parent melt (primary fluid phase). The morphology of the solid particles can be treated as globular equiaxed [64-67] and dendritic equiaxed solidification [37, 68-71].

Heterogeneous nucleation is a traditional topic to estimate the origination of equiaxed crystals and it can be connected to the presence of inoculants [72-74]. Inoculants, i.e. nucleation embryos, exist in the parent melt. Those inoculants will be activated by undercooling as new sites for equiaxed grains to grow. The undercooling needed to activate an inoculant depends on the size of the inoculant. Empirically, it was found that the nucleation event follows a Gaussian function of undercooling [63], and it is widely used in different solidification models. The roles of inoculants on the heterogeneous nucleation behavior of metallic melt have been investigated for a long time [75-77]. As shown in Figure 2.8, The including of inoculants can refine the structure of the casting [78], as is expected to improve the mechannical properties.

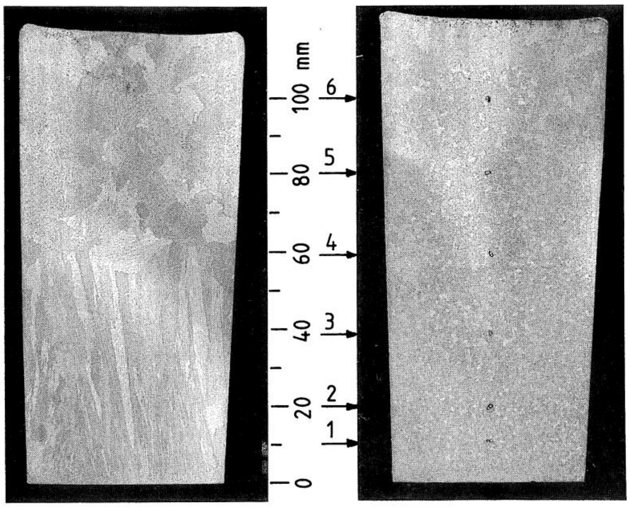

(a) (b)

Figure 2.8. Al-7Si ingot solidified under same 1-dimensional heat flow conditions: (a): pure alloy; (b): alloy inoculated with 50 ppm of Ti [63].

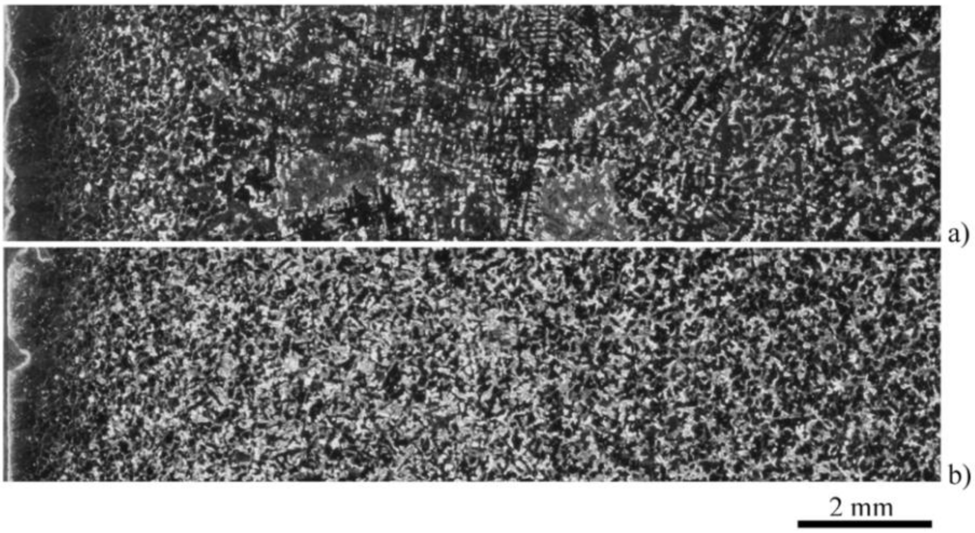

Figure 2.9. Microstructure of high Mn steel casting. Micrographs are taken close to the surface of the casting, a) reference casting without Ce, b) casting with 0.05 wt% Ce and 0.02 wt% Al [79] .

Eijk et al. made CeS inoculation in carbon steel by melting and quenching the mixture of FeS and Ce chip [79]. There are significant differences in the microstructure after inoculants additions, as shown in Figure 2.9. The steel without Ce addition shows a chill zone close to the surface of the casting and a coarse dendritic structure some distance (*ca.* 2 mm) from the surface. After addition of 0.02 % Al and 0.05% Ce, the steel has a much finer dendritic microstructure close to the surface of the block, as well as, in the center of the block. Steel with Ce additions contain Ce-oxides and Ce-Al-oxides.

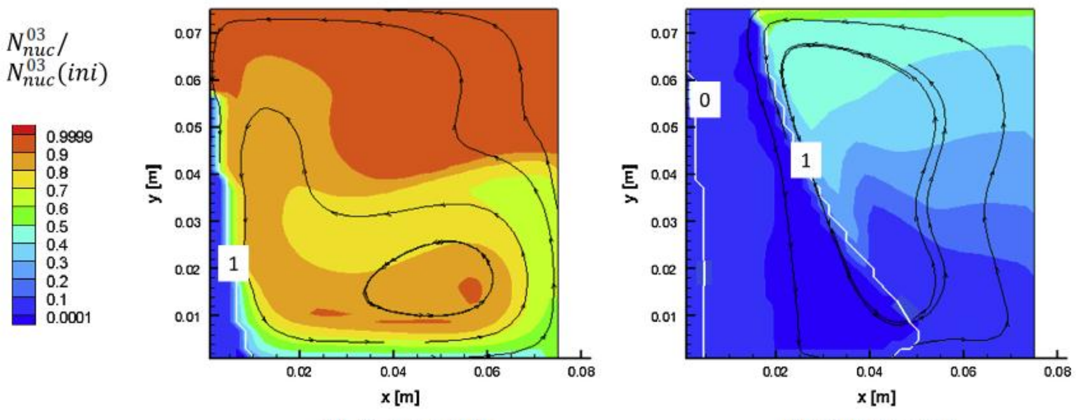

(a) 3rd class, t = 10 s (b) 3rd class, t = 50 s

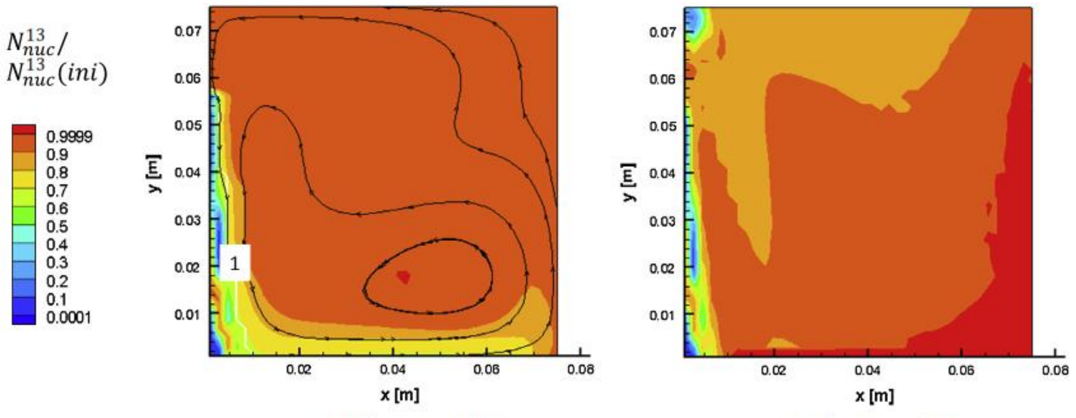

(c) 13th class, t = 10 s (d) 13th class, t = 720 s

Figure 2.10. Maps of relative inoculant density (normalized by the initial density of the respective class), streamlines of intrinsic liquid velocity in black and liquidus and solidus isolines in white (shown by liuqid volume fraction), for the 3rd and the 13th inoculant classes, at different times [60].

Bedel et al [60] carry out numerical simulations of a casting experiment, considering the solidification of an Al-22 wt.% Cu alloy inoculated with Al-Ti-B in a side-cooled 76 ×76 × 254 mm sand mold. Different size groups of inoculants are considered and transport of each size group has to be calculated individually. Different group of inoculants need their own undercooling conditions. A portion of inoculants could be embedded in the solid, having no chance to be activated (Figure 2.10). The transport of the inoculant particles considerably increases the heterogeneities of the microstructure and reduces the average grain size. Zheng et al. extended this idea to a three-phase columnar-equiaxed solidification model, considering the morphology of equiaxed dendrite morphology. Transport equation for inoculants and equiaxed grains are solved. Statistically, nucleation rate is estimated to be proportional to inoculants number density [62].

2.3.2 Fragmentation

The number of equiaxed crystals created through fragmentation was ignored or simplified by most numerical models, although many laboratory experiments [55, 80, 81] and industry practices [82] have confirmed its importance. Fragmentation has been understood through two main mechanisms: the mechanism of the mechanical fracture of the crystal dendrites, and mechanism of dendrite remelting.

As early as the 1960s, Chalmers and Williamson [83] observed the formation of ice crystals in the flowing and undercooled waters and determined that mechanical rupture (fracture) was responsible for their origin. By submerging bulk ice in flowing and slightly-undercooled (−0.2 °C) water, new ice crystals in the shape of small discs were observed to grow immediately from the ice substrate. As the connection of the ice discs with the substrate of the bulk ice was very weak, they were washed away from it by the flow. Based on these experimental observation, Chalmers and Williamson [83] anticipated that this type of “crystal multiplication” mechanism through mechanical rupturing would occur in metal castings by the agitation of the melt during freezing. However, a later experiment conducted by Garabedian et al. [84] with the same type of water showed that it was very difficult to produce the “crystal breeding,” that is, crystal multiplication by pure fluid sheering. A growing ice crystal was rotated in the undercooled water to create a sheer force on the ice dendrites. By sheering the water with a velocity as high as 1.5 m/s, the ice crystals could not be broken.

In the late 1990s, Pilling and Hellawell [85] performed a theoretical calculation for the metal alloy, and determined that the maximum stress of a dendrite arm at its weakest point (connection with the primary dendrite) under the sheer flow would only reach approximately 1% of the estimated yield strength of the material at its melting point. They concluded that the interdendritic flow does not contribute directly to the crystal multiplication because of dendrite fracturing. This conclusion was confirmed by Mullis et al. [86] with a recent calculation, for which they stated that "under most conditions, the likelihood of dendrites experiencing mechanical damage due to flow of the parent melt is remote." Usually, geometric model of a dendrite for the calcualtion is consisered to be very simple (Figure 2.11).

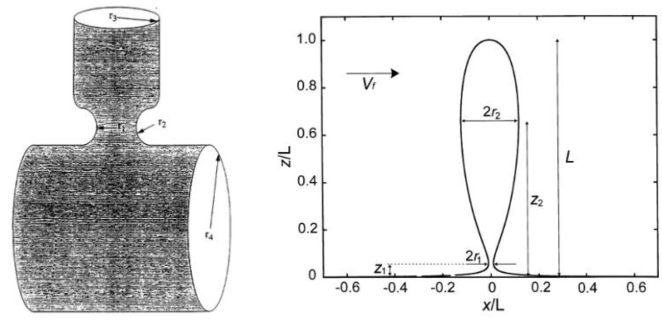

(a) (b)

Figure 2.11. Geometric model of a dendrite as to estmate the maximum stress of a dendrite arm at its weakest point (connection with the primary dendrite) under the sheer flow: (a) in referrence [85] and (b) in referrence [86].

The fragmentation caused by remelting the dendrite stem was first proposed by Jackson et al. through an NH_4Cl-H_2O solidification experiment [87]. Forced flow during solidification was introduced by stirring the melt by using a motor-driven propeller. It was suggested that fragmentation resulted from solute rejection during dendrite growth, producing favorable conditions for the remelting of a side branch at its base and leading to subsequent "pinch off." The heat and solute generated by the growth of side branches increases the local temperature and solute concentration; this is experienced by the base of the side branches leading to the occurrence of “constitutional” remelting. Stirring was performed to create or enhance the interdendritic flow necessary for transporting the fragments out of the mushy zone. This remelting-induced fragmentation theory was later supported by many follow-up experiments, for example, by using similar NH_4Cl-H_2O solutions [54, 88, 89], other model alloys (succinonitrile-acetone) [90], and even metal alloys (Figure 2.12) [81, 91-93]. The method of synchrotron X-ray radiography provided an opportunity to perform *in situ* observation of the fragmentation process of metal alloys during solidification at the elevated temperature. Solute-driven remelting seems to be the dominant mechanism for fragmentation. The importance of the flow is confirmed by almost all the above-mentioned studies: (1) the flow influences the transport of the fragments and (2) the flow also promotes or retards the remelting of the dendrite stems through solute transportation.

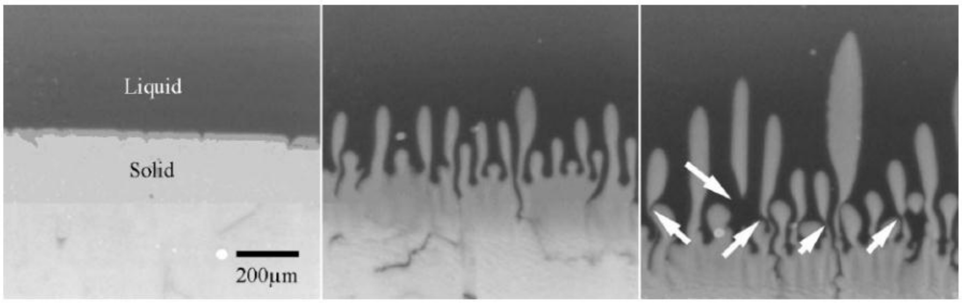

Figure 2.12 Fragmentation at root of dendrite arms in Sn- 13at.%Bi alloy [81].

According to Hellawell et al. [80], five steps are necessarily considered for evaluating the fragmentation event and its consequence on the as-cast structure formation (Figure 2.13): (1) dendrite arms are first fragmented/detached from the columnar dendrites; (2) fragments are transported through the mushy zone by interdendritic flow; (3) fragments during transport through the mushy zone survive the superheat; (4) fragments continue to grow in the bulk melt; and (5) equiaxed grains grow from those fragment sediments and interact with the columnar structure, and they might be entrapped into and block the columnar structure, leading to CET. In reality, some multiphase volume average models [94, 95] have already considered steps (2)–(5). This information is needed for defining the source term for the transport equation of the number density of equiaxed crystals. It is necessary to figure out mass and energy transfers between the columnar structure phase and the newly formed fragments. In the multiphase transport system, "fragmentation" implies that a certain number of detached dendrite arms from the columnar structure will be converted into equiaxed structure, and correspondingly a certain amount of mass and energy will be transferred into the equiaxed phase.

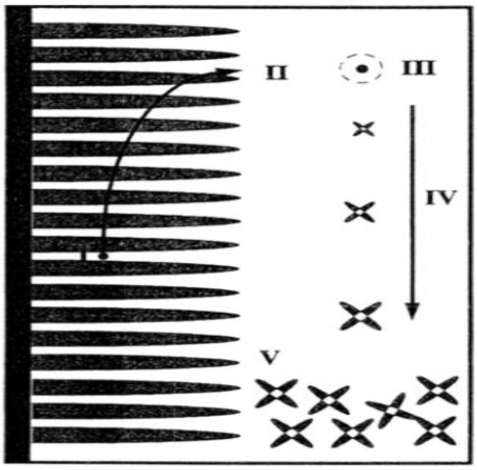

Figure 2.13. Schematic of formation and transport of fragments. The grain-evolutionary cycle and transition in castings from intrinsic source [80]. Five steps are necessarily considered: (I) fragment detaching; (II) fragments moving out of the mushy zone; (III) fragments surviving through superheat; (IV) fragments growing in the bulk melt; and (V) equiaxed grains grown from fragment settling.

Experiments were also conducted for performing fragment count. For example, Paradies et al. [90] performed a solidification experiment under forced flow condition based on a model alloy, that is, succinonitrile (SCN)-acetone. They attempted to count the number of detached fragments at the front of the mushy zone. Fragments that cannot be transported out of the mushy zone (fully remelted or locked into the dendrite network) were ignored. Based on this fragment count, they estimated the fragment production rate. Montgomery et al. [54] performed another fragment count experiment based on the solidification of NH_4Cl-H_2O solutions under natural convection conditions. The fragments were counted ahead of the mushy zone, and both the number and volume fraction of fragments were measured (from which average size of fragments can be estimated). By using the synchrotron X-ray radiography, Liotti et al. attempted to count the fragmentation rate during solidification of metal alloys (Al-15 wt.%Cu) [93]. In this study a pulsed electromagnetic field was introduced to create a pulse flow in the interdendritic region, and the following valuable information was obtained. Solidification would oscillate in the liquid induced by pulsed electromagnetic field (Figure 2.14). The introduced pulse flow enhances the fragmentation through the remelting mechanism; fragmentation is not a phenomenon confined to the front mushy region but is spread throughout a wide range of the mushy zone with high solid fraction. Fragments created in the deep mushy zone are not necessarily counted as active nuclei of equiaxed crystals because they cannot be transported into the bulk melt [80].

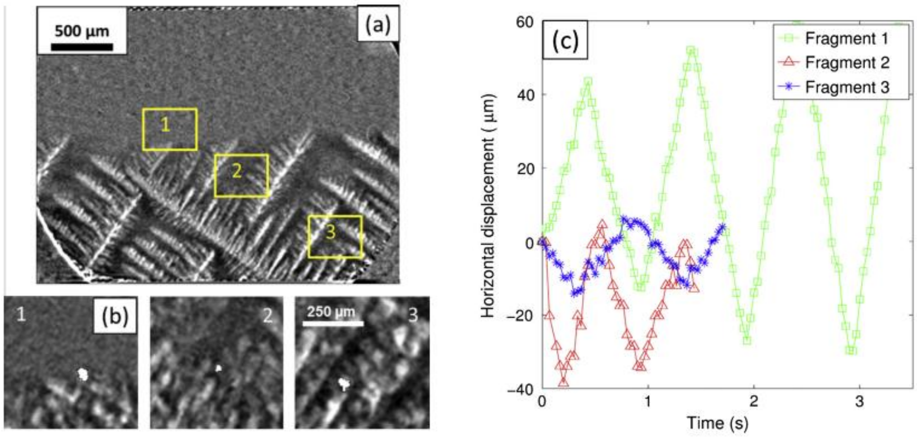

Figure 2.14. Fragment oscillations in the liquid induced by the pulse electromagnetic force (PEMF) during the solidification sequence of Al-15 wt.%Cu: (a) the general arrangement of the dendritic network indicating the approximate location of fragments 1, 2 and 3 at time t = 23 s, 32 s, 41 s; (b) higher magnification views of the fragments in white; and (c) the horizontal position of each fragment identified by image analysis over consecutive frames as a function of time [93].

Lesoult [82] reported a very valuable study for steel based on a hypothesis that stirring of molten steel before the solidification of the front would result in seeding of the liquid with dendritic fragments. Presumably, those fragments were eroded from the columnar tip front. He determined that the fragment flux quantified by the number of crystals eroded per unit time and area of the columnar solidification front (cm^{-2}s^{-1}) correlated with the tangential velocity of the liquid along the solidification front. This concept was later implemented into a multiphase solidification model to calculate the fragmentation phenomenon during a mixed columnar-equiaxed solidification of steel [96]. The predicted final equiaxed grain fraction g_{grain}^{eqx} for increasing fragmentation fluxes at the columnar front is shown in Figure 2.15. According to the classical interdendritic flow induced remelting theory [97], it is the flow in the growth direction of the primary columnar dendrites, rather than the tangential liquid velocity, that may promote the remelting of the dendrites.

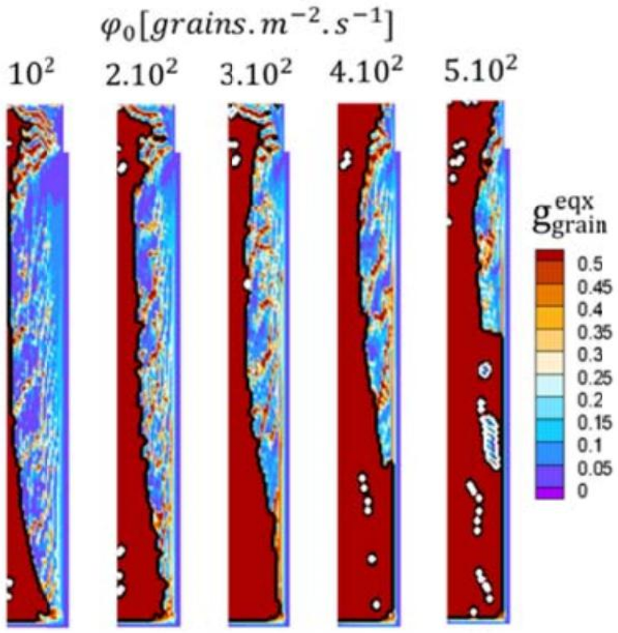

Figure 2.15. A modeling result of fragmentation affected structure for a cylindrical casting of steel. Predicted final equiaxed grain fraction g_{grain}^{eqx} as well as CET (Columnar-to-equiaxed transition) and ECT (Equiaxed-to-columnar transition)for increasing fragmentation fluxes at the columnar front [96]. A increasing Fragment flux, φ_0, quantified by the number of crystals eroded per unit time and area of the columnar solidification front ($cm^{-2}s^{-1}$), is related to a increasing equiaxed zone.

Based on the Flemings' theory for local remelting of the mushy zone [97], Campanella et al. derived an onset criterion for remelting-induced fragmentation [98]. That is, fragmentation occurs when the component of the fluid flow velocity in the thermal gradient direction, presumably coinciding with the growth direction of the primary columnar dendrites, becomes larger than the speed of the isotherms at a depth of 6–8 λ_2 (secondary dendrite arm space) in the mushy zone. This implies that the flow transports a solute-enriched melt from the deep interdendritic region into the front region of the mushy zone, reducing the melting point, and hence promoting the remelting of dendrite arms in that region. Additionally, the flow in the columnar growth direction is necessary for transporting fragments out of the mushy zone. The shortcoming of this onset criterion is that no quantitative information is provided about the production rate and size of the fragments.

2.3.3 Structure transition (ECT & CET)

Equiaxed crystals can coagulate with each other. When the local solid volume fraction (f_{e}) becomes larger than a critical volume fraction ($f_{\mathrm{e}}^{\mathrm{c}}$), the equiaxed phase builds a rigid network. Here $f_{\mathrm{e}}^{\mathrm{c}}$ is called as packing limit, usually taking 0.637. As the equiaxed phase is arrested by the mold wall (stationary), the motion of the equiaxed phase vanishes, then the equiaxed phase is considered as rigid and stationary. Columnar primary dendrite tips are allowed to initiate and grow from this marked zone (volume element). The numerical algorithm, as described by Wu et al. [99] to track the columnar tip front, is valid here as well. The growth velocity of the columnar primary dendrite tip is modeled according to LGK [100]. The growth of columnar phase competes always with the growth of equiaxed phase. If the tracked columnar primary dendrite tip front can grow out of the considered volume element before f_{e} reaches a so-called blocking limit ($f_{\mathrm{e,CET}}$), the growth of columnar primary tip front can continue into the neighboring cell or cells. If the tracked columnar primary dendrite tip front cannot grow out of the considered volume element before f_{e} reaches $f_{\mathrm{e,CET}}$, CET occurs. $f_{\mathrm{e,CET}}$ was suggested by Hunt to be 0.49 [101], but recently modified as 0.2 [102]. Criterion for free moving equiaxed phase in columnar zone, $f_{\mathrm{c}}^{\mathrm{free}}$, is can also influence the position of CET. The equiaxed crystals would be fixed in the dendrite if the columnar fraction is bigger then $f_{\mathrm{c}}^{\mathrm{free}}$. Case with a bigger $f_{\mathrm{c}}^{\mathrm{free}}$ can get a larger equiaxed zone (Figure 2.16) [99].

On the one hand, new equiaxed crystals can block the growth of columnar phase; on the other hand, columnar trunks can develop from the packed rigid equiaxed networks. Firstly, when the liquid has a very large cooling rate, the liquid would have large undercooling very soon. The nucleation rate in the bulk melt is very large with this undercooling. The solidification of equiaxed phase dominates the mass transfer from liquid to solid phase. This situation is common for the surface part chill zone of a solidifying ingot [103]. Secondly, for those cases with the inhomogeneous nucleation, the nuclear embryos (or inoculant) may exhaust in the later age of the solidification. Generally, condition of homogeneous nucleation is not attained yet at this moment. After that the growth of columnar phase will overweigh that of equiaxed phase. When the equiaxed crystals are arrested by any obstacle, e.g. the mold wall, columnar structure develops from the stationary equiaxed crystals. Additionally, the equiaxed-to-columnar transition (ECT) occurs when no sufficient equiaxed crystals ahead of the columnar tip front blocks the growth of columnar dendrite tips [96, 99].

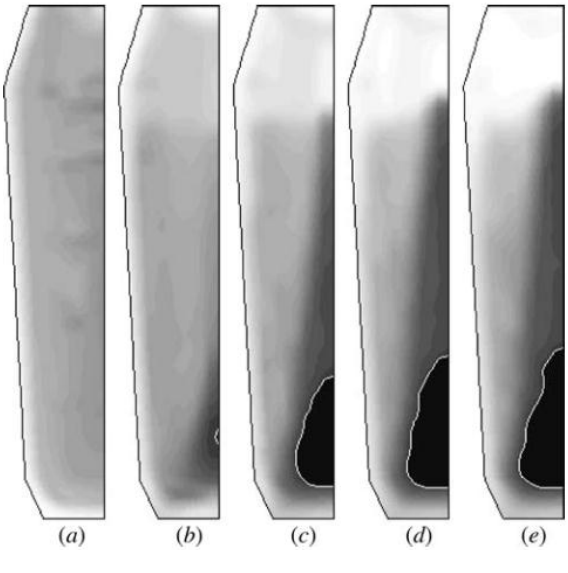

Figure 2.16. Predicted CET by varying f_c^{free} from 0 to 0.4. The term f_c is shown in gray scale with dark for 1 and bright for 0.

When the initially-formed equiaxed crystals sediment in the casting bottom and no further equiaxed crystals is supplied, e.g. exhaust of inoculants, columnar would grow from the as-packed equiaxed crystals. Thus, the growth of columnar will overweigh that of the equiaxed during the late stage of solidification [62, 104]. Coexistence of CET and ECT is common in a solidifying ingot [103, 105], as shown in Figure 2.17. Either CET or ECT is the result of growth competition between columnar and equiaxed structures, even under some circumstance they coexist. Studies on CET were carried to improve understanding of the blocking mechanism of the columnar growth by the equiaxed crystals [7, 101, 106]. Within the volume average method a special treatment is necessarily made for the ECT [62, 104, 107].

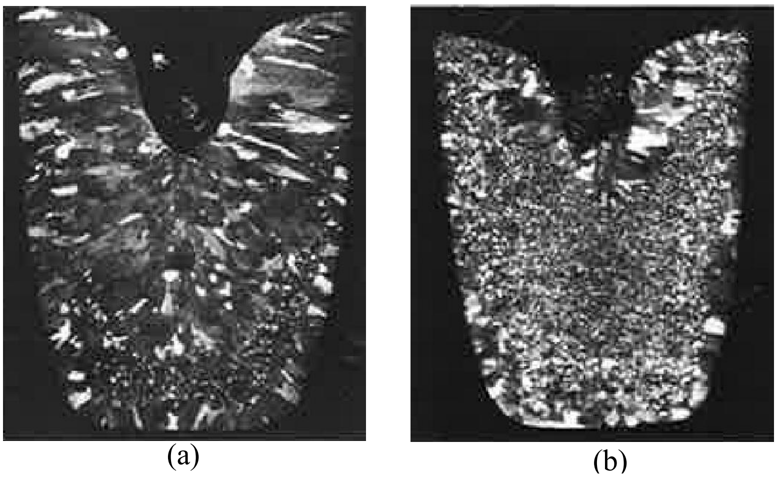
(a) (b)

Figure 2.17. Examples of as-cast structures of Al-0.2%Cu (a) and Al-0.3%Be (b) ingots [105].

2.3.4 Macrosegregation

In the last decades numerous investigations have been carried for the macrosegregation in alloy casting, which are reviewed by several publications [15, 108-110]. Formation of almost all types of macrosegregation in castings is related to the density variation under gravity condition, which can result in relative motion between solid (equiaxed or columnar) and liquid during solidification [111]. For example, the flow due to thermal-solutal buoyancy of melt can cause channel segregation (A-segregates) in steel ingots [112], freckles in unidirectionally solidified casting components [113], centerline positive/negative (depending on flow pattern) segregation in steel ingots [14, 108, 114] and continuous castings [32, 108]. Density change due to solidification shrinkage can lead to centerline segregation in continuous castings [45, 46, 115]. Sedimentation of equiaxed crystals due to the density difference between liquid and solid can lead to typical bottom cone-shape negative segregation in heavy ingots [112, 114].

In order to figure out the mechanisms of macrosegregation during solidification in the presence of thermal solutal convection and crystal sedimentation, we assume that solidification shrinkage and global species transport by diffusion is ignored [116], i.e. $D_{\mathrm{e}} = 0$, $D_{\ell} = 0$ and $D_c = 0$, the sum of the volume average species conservations can be written as

$$\frac{\partial}{\partial t}\bar{\rho} = -\nabla\cdot\left(f_{\ell}\rho_{\ell}\vec{u}_{\ell}\right) - \nabla\cdot\left(f_{\mathrm{e}}\rho_{\mathrm{e}}\vec{u}_{\mathrm{e}}\right) \tag{2.40}$$

$$\frac{\partial}{\partial t}(\bar{\rho}c_{\mathrm{mix}}) = -\nabla\cdot\left(f_{\ell}c_{\ell}\rho_{\ell}\vec{u}_{\ell}\right) - \nabla\cdot\left(f_{\mathrm{e}}c_{\mathrm{e}}\rho_{\mathrm{e}}\vec{u}_{\mathrm{e}}\right). \tag{2.41}$$

According to the mass conservation equations, it yields that $\nabla\cdot\left(f_{\mathrm{e}}\vec{u}_{\mathrm{e}}\right) = -\nabla\cdot\left(f_{\ell}\vec{u}_{\ell}\right)$, together with the assumption that three phases share an identical density, i.e. $\bar{\rho} = \rho_{\ell} = \rho_{\mathrm{e}}$, thus the above equations give

$$\frac{\partial}{\partial t}(c_{\mathrm{mix}}) = (c_{\ell} - c_{\mathrm{e}})\cdot\nabla\cdot\left(f_{\mathrm{e}}\vec{u}_{\mathrm{e}}\right) - f_{\ell}\vec{u}_{\ell}\nabla c_{\ell} - f_{\mathrm{e}}\vec{u}_{\mathrm{e}}\nabla c_{\mathrm{e}}. \tag{2.42}$$

It means that the variation of the local mixture concentration, c_{mix}, is caused by three RHS terms in Equation (2.42). The first RHS term '$(c_{\ell} - c_{\mathrm{e}})\cdot\nabla(f_{\mathrm{e}}\vec{u}_{\mathrm{e}})$' represents the influence of equiaxed crystal sedimentation on the macrosegregation change rate. The term '$c_{\ell} - c_{\mathrm{e}}$' is generally positive during the solidification when the alloy partitioning coefficient *k* less than one. The sedimentation term, $\nabla\cdot(f_{\mathrm{e}}\vec{u}_{\mathrm{e}})$, gives an indication about the local depletion or accumulation of equiaxed crystals. According to Equation (2.42), the accumulation of equiaxed crystals would lead to a negative value of $\partial c_{\mathrm{mix}}/\partial t$, i.e. the decrease of c_{mix}, and result in more negative segregation. Liquid-flow-interaction term (second RHS term),

$-f_\ell \vec{u}_\ell \nabla c_\ell$, and equiaxed-flow-interaction term (third RHS term), $-f_\mathrm{e} \vec{u}_\mathrm{e} \nabla c_\mathrm{e}$, are the influences of liquid flow and equiaxed movement on the macrosegregation change rate, respectively. If the dot product of velocity of liquid (equiaxed) and liquid (equiaxed) concentration gradient is positive, it would result in a more negative macrosegregation and vice versa.

2.3.5 Porosity

Porosity/shrinkage is a typical metallurgical defect in the casting. According to the appearance of the shrinkage defects in the casting and the existing knowledge about their formation mechanisms, three types of shrinkage defects can be categorized [117] :

(i) Micro porosity. It occurs in the deep interdendritic mushy zone, where it is hard for the melt to feed the solidification shrinkage. When the shrinkage-induced pressure drop reaches a threshold, pores would initiate and grow in the interdendritic space. This kind of porosity was initially modeled analytically with the solution of the pressure drop in the mushy zone [118], then investigated with more advanced numerical method [119]. As the nucleation and growth of the micro pores are closely related to the gas content, rejection of the gas element by solidification becomes an important issue for the pore formation. Therefore, a diffusion-governed growth model was also proposed to analyze the pore growth kinetics [120].

(ii) Open pipe-shrinkage. This kind of defect can be observed in the hot top region of the ingot. The sinking of the melt level due to the accumulated volume shrinkage in the connected bulk melt region leads to the formation of a funnel-shape pipe.

(iii) Macro porosity. It is similar to the open pipe shrinkage but inside the casting. The difference is that it forms in a closed melt region which is disconnected (surrounded by the already-solidified region). Also, the numerical treatment of these two types of macroscopic shrinkage cavities is similar: calculation and relocation of the accumulated volume shrinkage based on thermal and gravity fields [121].

Nevertheless, it is difficult to use above mechanisms to predict the pore formation quantitatively. For simplicity, some criterion functions purely based on the thermal field, e.g. the Niyama criterion [122], were derived to predict the occurrence probability of the shrinkage porosity and the most likely position of the shrinkage porosity in engineering castings. Niyama criterion is written as

$$Ny = G / \sqrt{\dot{T}} \tag{2.43}$$

where G is the temperature gradient and $\dot{T}$ is the cooling rate, both of which are evaluated at a specified temperature at a critical temperature T_{cr}. Later on, researchers extended this idea by considering the effect of mush zone morphology and permeability [123].

In the present study a modified Niyama criterion, i.e. CBN (Carlson-Beckermann-Niyama) criterion [43, 122, 124] is used to predict the probability of shrinkage porosity:

$$\mathrm{CBN} = C_\lambda \frac{G}{\dot{T}^{5/6}} \sqrt{\frac{\Delta P_{\mathrm{cr}}}{\mu_\ell \beta (T_{\mathrm{Liquidus}} - T_{\mathrm{Eutectic}})}} \, , \tag{2.44}$$

where C_λ is a material constant, 1.44×10^{-4} [m $(\mathrm{K/s})^{1/3}$]; G and $\dot{T}$ are the temperature gradient and cooling rate, which are evaluated at a critical temperature of T_{cr} ($= 0.1 \cdot T_{\mathrm{liquidus}} + 0.9 T_{\mathrm{Eutectic}}$), assuming solidification ends at T_{Eutectic}; β is the solidification shrinkage, $(\rho_{\mathrm{s}} - \rho_{\mathrm{s}}) / \rho_\ell$; ΔP_{cr} is the critical pressure drop when a pore-nucleus with a critical radius of r_{pore} in the deep mushy zone can overcome capillary force ($2\sigma / r_{\mathrm{pore}}$). There is no threshold of CBN for the occurrence of pores can be determined in advance; this criterion is only used qualitatively.

A smaller CBN criterion indicates a higher probability of shrinkage porosity. The porosity in equiaxed zone is truncated in present simulation since the CBN criterion is unable to predict porosity in equiaxed phase. It is also worthy to mention that, the porosity probabilities in equiaxed are much less than that in columnar phase. The occurrence possibility of shrinkage porosity and the amount of pores (volume fraction of voids) decrease with increasing local CBN value. In another word, the smaller the CBN value, the more probably the shrinkage porosity would occur, and the more amounts of pores might be. Although Eulerian approach offers the possibility to calculate the interdendritic flow, it is extremely hard to solve the feeding flow in the deep mush near the end of solidification due to the convergence difficulty. Therefore, a so-called 'simplified porosity model' is introduced. Aforementioned numerical models can incorporate with multiphase transport phenomena, and their interaction with the formation of macrosegregation is available to be taken into account. Wu et al. [43, 125] adopted this formula in a multiphase solidification model to calculate the solidification of a 10.5 tons ingot. The position with high probability of porosity locates in the center part of the columnar region (Figure 2. 18).

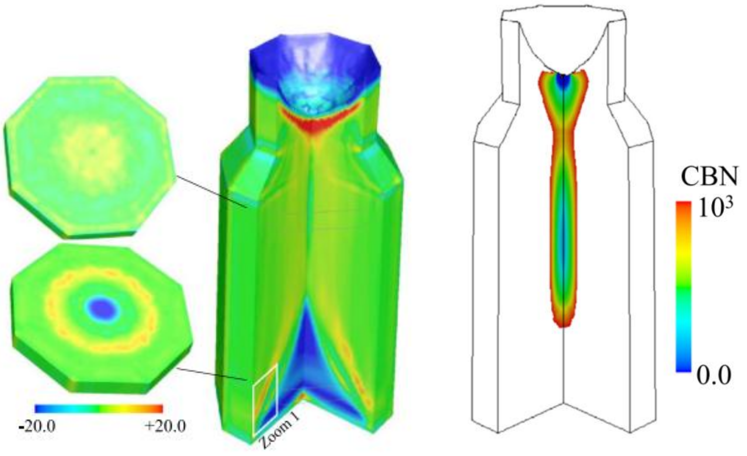

(a) (b)

Figure 2.18. Simulation result: (a) Macrosegregation; and (b) CBN criterion for microscopic shrinkage porosity [125].

3 Modeling examples

6 examples will be presented in this section. Examples 1 to 4 show the extension of the numerical model study and they are corresponding to the publications in the Part II. Examples 5 and 6 are related to the application of the model in the analysis of vertical continuous casting (VCC) and semi-continuous casting (SCC) processes. The application part is published due to the commercial reason. The general background, numerical method, and some demonstration results are presented here, while the details of the industrial process are omitted.

3.1 Example I: Test case of columnar solidification

In order to get basic understanding of the formation mechanisms of structure and macrosegregation, 8 simple cases of a 2D benchmark (50 × 60 mm^2) with unidirectional cooling from either top or bottom (Figure 3.1) were configured and calculated [7]. Two different alloys were considered: Sn-10 wt.%Pb with solute element Pb heavier than the solvent Sn; Pb-18 wt.%Sn with solute element Sn lighter than the solvent Pb. This section includes 4 cases of pure columnar solidification. Other 4 cases with equiaxed solidification are described in section 3.2. Direction of the thermal-solutal buoyancy force of the interdendritic melt can be estimated according to the alloy (Sn-10 wt.%Pb or Pb-18 wt.%Sn); and the possible flow pattern can also be estimated when the solidification direction (upwards or downwards) is known. As consequence, the macrosegregation tendency should be empirically estimated as well. However, the modeling results show that complicated details of macrosegregation distribution can develop due to the complexity of the transient flow. This work can be used as reference stuff for the "Solidification Course", as held annually in Les Diablerets, EPFL Switzerland.

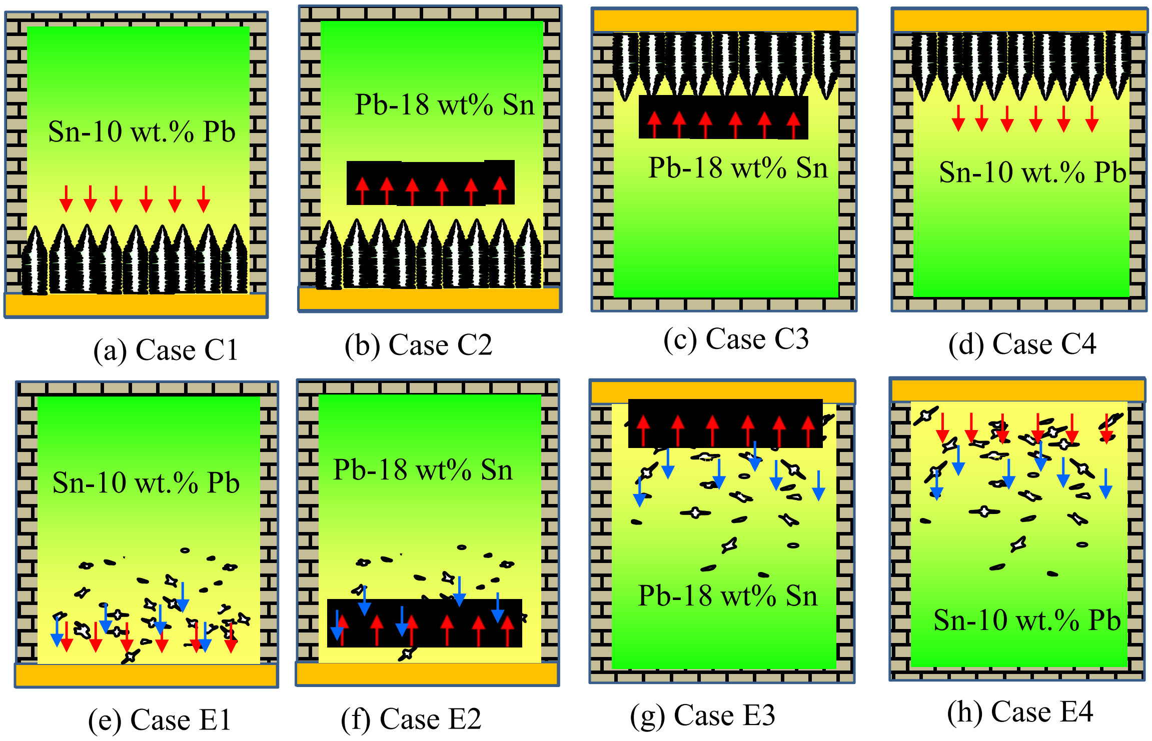

(a) Case C1 (b) Case C2 (c) Case C3 (d) Case C4

(e) Case E1 (f) Case E2 (g) Case E3 (h) Case E4

Figure 3.1. Schematics of columnar (upper row) and equiaxed (lower row) solidification, solutal buoyancy force direction (red arrows) of the interdendritic/intergranular melt, and crystal sedimentation direction (blue arrows) of the equiaxed grains. 8 cases are defined. Two different alloys were considered: Sn-10 wt.%Pb with solute element Pb heavier than the solvent Sn; Pb-18 wt.%Sn with solute element Sn lighter than the solvent Pb. Color gradient indicates the distribution of solute element in the melt: yellow for enrichment, green as the nominal composition. Cases C1, C2, E1 and E2 are cooled from bottom, while other 4 cases are cooled from top.

The configuration of the 2D benchmark is shown in Figure 3.2. Model details can be found in several publications [7, 94, 95, 99]. Here only two phases, liquid and columnar, are considered. The functionalities of the model for the nucleation and growth of equiaxed phase are "switched off", i.e. no equiaxed can nucleate.

For a simple case of pure columnar solidification, when its solidification direction is unidirectional, either upwards (Figure 3.2(a)) or downwards (Figure 3.2(b)), the final macrosegregation tendency should be empirically predictable according to the alloy and the predefined solidification direction. For example, a solute lighter alloy (Pb-18 wt.%Sn) solidifies upwards would lead to a positive segregation (enrichment of Sn) in top and negative segregation (poor in Sn) in the bottom region. However, the modeling results show that more complicated details of macrosegregation distribution can develop due to the complexity of the transient flow.

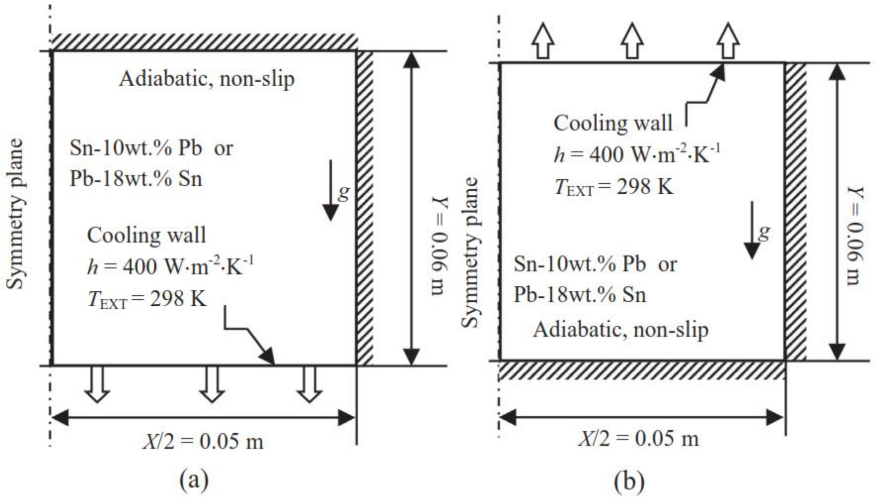

Figure 3.2. Benchmark geometry with boundary and initial conditions: (a) test case solidified from bottom to top and (b) test case solidifed from top to bottom.

3 mechanisms operate for the macrosegregation: thermal buoyancy flow, solutal buoyancy flow and solute diffusion in interdendritic melt. Solidification shrinkage is ignored here. Diffusion-induced macrosegregation occurs only at the bottom and top surfaces, and it is ignorable if the mechanism of thermo-solutal buoyancy flow operates. Solutal buoyancy dominates over the thermal buoyancy in this benchmark when both of them operate at the same time; hence solutal buoyancy represents the dominant mechanism for the macrosegregation. Calculated macrosegregation results of 4 cases are compared in Figure 3.3. The segregation distribution is shown in color scale, but its intensity is analyzed by the c^{index} distribution range as labelled in the figures and by the so-called global macrosegregation intensity (GMI). This part of study is publishend in Paper I of Part II.

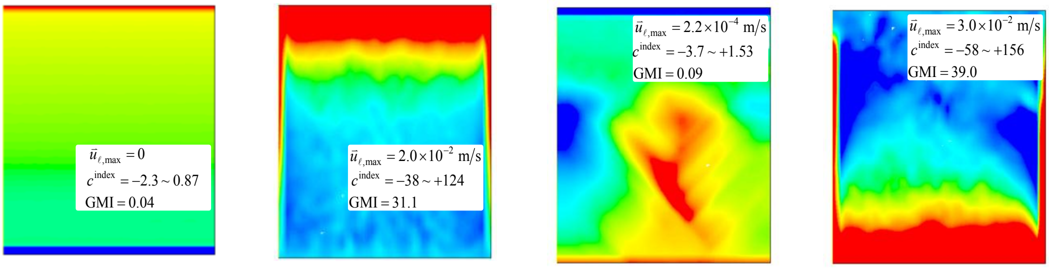

(a) Case C1 (b) Case C2 (c) Case C3 (d) Case C4

Figure 3.3. Comparison of the macrosegregation patterns among 4 cases of columnar solidification. The segregation index (c^{index}) contours are shown in color scale, and they have different distribution ranges, as labelled in the figure. The maximum flow velocity during solidification and the global macrosegregation intensity (GMI), as defined by $\text{GMI}=\frac{1}{\text{V}_{\text{domain}}}\cdot\iiint_{V_{\text{domain}}}|c^{\text{index}}|dV$, are also given [104].

3.2 Example II: Test case of equiaxed solidification

This section will present other 4 cases of equiaxed solidification, i.e. the scenarios as shown schematically in cases of E1 through E4 of Figure 3.1. Equiaxed structure, one of the most common as-cast structures, is often pursued by industries to promote (or it is believed to promote) the structural and compositional homogeneities in metal castings. Understanding to the solidification fundamentals of equiaxed crystal growth was significantly developed in last decades [126, 127], but most part of knowledge about the crystal transport phenomena, which is closely correlated to macrosegregation (compositional heterogeneity), was missing [108]. The volume-average based three-phase mixed columnar-equiaxed solidification model [7, 99] with several modifications is used. One modification is to consider the transport of inoculants (embryos), similarly to Bedel et al [60]. The inoculants serve as heterogeneous nucleation sites for the equiaxed crystals. Another modification is to include the equiaxed-to-columnar transition (ECT). During equiaxed solidification under gravity condition, the rest melt can fully solidify as columnar structure when the available inoculants are consumed.

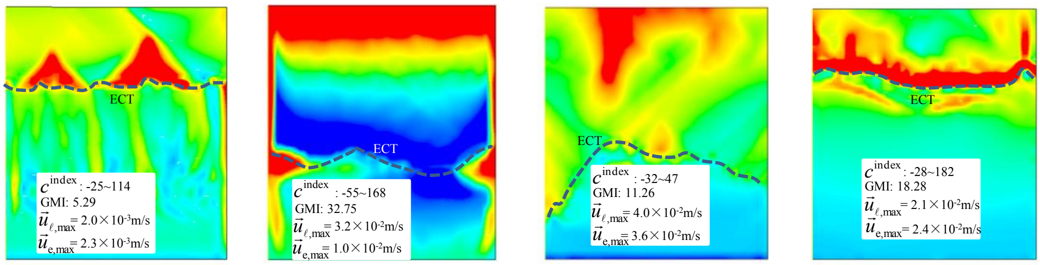

(a) Case E1 (b) Case E2 (c) Case E3 (d) Case E4

Figure 3.4. Comparison of the macrosegregation patterns among 4 cases of equiaxed solidification. The segregation (c^{index}) contours are shown in color scale, and they have different distribution ranges, as labeled in the figure. The maximum flow velocity and crystal sedimentation velocity during solidification and the global macrosegregation intensity (GMI), as defined by $\text{GMI} = \frac{1}{\text{V}_{\text{domain}}} \cdot \iiint_{V_{\text{domain}}} |c^{\text{index}}| dV$ are also given.

According to the classical heterogeneous nucleation theory [60] that equiaxed nuclei originate from exogenous particles/inoculants, it is difficult to get pure equiaxed structure in technical alloys by gravity casting technique. The modeling results show that ECT event occurs during late stage of solidification when all inoculants are consumed.

The geometry and boundary condition settings are same as those shown in Figure 3.2. Calculated macrosegregation results of 4 cases considering equiaxed solidification are compared in Figure 3.4. Even for a simple case of equiaxed solidification, when its cooling direction is unidirectional, either upwards or downwards, it is not easy to predict the final macrosegregation tendency. The main difficulty arises from the ECT. During the early stage of equiaxed solidification before ECT, the macrosegregation tendency is predictable: equiaxed sedimentation, i.e. the dominant macrosegregation mechanism, induces negative segregation in the bottom region; while solute-enriched melt is distributed in the upper region. When the inoculants in the melt are exhausted, the growth of columnar trunks would overweight equiaxed growth, result in ECT. After the ECT during the late stage of columnar solidification, the thermo-solutal convection becomes the dominant macrosegregation mechanism. The redistribution of the positive macrosegregation pattern in the upper region, by the mechanism of thermo-solutal convection, depends on the alloy and cooling direction [104]. The details of this part are included in Paper II of Part II.

3.3 Example III: Formulation of fragmentation

It is known that the transport of the solute-enriched melt by the interdendritic flow in the columnar-growth direction would lead to remelting [97, 98]. Under normal diffusion-governed solidification/remelting condition, the driving force for the remelting is the constitutional supersaturation $\left(c_\ell - c_\ell^*\right)$, where c_ℓ is the volume-averaged concentration of interdendritic melt; c_ℓ^* is the thermodynamic equilibrium concentration of the melt at the liquid–solid interface. A positive value of $\left(c_\ell - c_\ell^*\right)$ is a driving force for remelting, or a process leading to an increase of c_ℓ promotes remelting. The influence of the interdendritic flow on c_ℓ^* is very limited. Furthermore, the curvature of the dendrite stem is independent from the flow, whose influence on the local temperature *T* is ignorable compared with its influence on solute concentration. Note that Lewis number, ratio of thermal diffusivity to mass diffusivity, is relatively large for metal alloys. The interdendritic melt usually has a concentration gradient (∇c_ℓ) contradictory to the columnar growth direction of alloys with the solute partition coefficient (*k*) less than one. An interdendritic flow in the columnar growth direction indicates $-(\vec{u}_\ell - \vec{u}_\mathrm{c})\cdot \nabla c_\ell > 0$; therefore, the flow leads to a local increase in c_ℓ, promoting the remelting. Actually, the rate of remelting should be proportional to the value of $-(\vec{u}_\ell - \vec{u}_\mathrm{c})\cdot \nabla c_\ell$. Even if the local capillary effect, that is, the coarsening or ripening phenomenon is ignored, fragments can be produced by the "homogenous" remelting. Based on the large number of experimental facts on the remelting-induced fragmentation [54, 87-93] and the above-mentioned theoretical analysis, we assume that the rate of fragmentation is proportional to the value of $-(\vec{u}_\ell - \vec{u}_\mathrm{c})\cdot \nabla c_\ell$ by suggesting the following formulation for the fragmentation-induced mass transfer rate from the columnar to equiaxed phase:

$$M_\mathbf{ce} = -\gamma \cdot \left(\vec{u}_\ell - \vec{u}_\mathrm{c}\right)\cdot \nabla c_\ell \cdot \rho_\mathbf{e}. \tag{3.1}$$

Note that fragmentation occurs only with remelting, that is, when $M_{\mathrm{ce}} > 0.0$. When the calculated M_{ce} has a negative value, we set $M_{\mathrm{ce}} = 0.0$, i.e. the fragmentation would not be possible. The mass integral of all fragments as produced per time ($\mathrm{kg \cdot m^{-3} \cdot s^{-1}}$) is proportional to the increase rate of constitutional supersaturation caused by the interdendritic flow. Here, a fragmentation coefficient γ was assigned to bridge the unknown correlation between M_{ce} and the increase rate of constitutional supersaturation. In other words, all other unknown contributing factors, such as the curvature effect of the dendrites, latent heat-induced thermal fluctuation, and diffusion in the interdendritic melt, for the remelting-induced fragmentation are included in the single coefficient γ. The coefficient must be determined experimentally, or estimated reversely from some available experimental information.

As shown in Figure 3.5, we assume that the shape of fragment is globular (spherical). The diameter of the fragment is proportional to the secondary dendrite arm (λ_2) and volume fraction of the columnar phase (f_{c}):

$$d^{0}_{\mathrm{e,frag}} = \lambda_2 f_{\mathrm{c}} \,. \tag{3.2}$$

Hence, the rate of the fragment production can be calculated as follows:

$$N_{\mathrm{frag}} = \frac{M_{\mathrm{ce}}}{\rho_{\mathrm{e}} \cdot \frac{\pi}{6} \left(d^{0}_{\mathrm{e,frag}} \right)^3} \,. \tag{3.3}$$

Correspondingly, the fragmentation-induced momentum transfer ($\vec{U}^{\mathrm{p}}_{\mathrm{ce}}$), energy transfer ($Q^{\mathrm{p}}_{\mathrm{ce}}$), and species transfer ($C^{\mathrm{p}}_{\mathrm{ce}}$) from the columnar to equiaxed phases are defined as follows:

$$\vec{U}^{\mathbf{p}}_{\mathbf{ce}} = \vec{u}_c \cdot M_{\mathbf{ce}} \tag{3.4}$$

$$Q^{\mathrm{p}}_{\mathrm{ce}} = h_{\mathrm{c}} \cdot M_{\mathrm{ce}} \tag{3.5}$$

$$C^{\mathrm{p}}_{\mathrm{ce}} = c_{\mathrm{c}} \cdot M_{\mathrm{ce}} \tag{3.6}$$

where $\vec{u}_c$, h_{c} , and c_{c} are respectively the moving velocity, enthalpy, and concentration of the columnar phase.

(a) (b)

Figure 3.5. Schematic description of remelting-induced fragmentation: (a) transport of solute-enriched interdendritic melt through the flow, and (b) formation of a fragment by remelting of the side arm.

Figure 3.6 shows the configuration of a 2D test case. The geometry is adapted from the benchmark as defined by Bellet et al. [128]; however, in this study, only half of the benchmark is calculated by setting a symmetry plane at the left boundary. Heat is only extracted through the top wall with a heat transfer coefficient h = 400 $\mathrm{W \cdot m^{-2} \cdot K^{-1}}$, while other walls are set as adiabatic boundaries. Moreover, an alloy of Sn-10 wt.%Pb is considered. The solute element Pb is heavier than the solvent Sn, and the solidified equiaxed crystal is assumed to always be heavier than the melt. As a closed domain is calculated and no volume shrinkage is considered, the Boussinesq approximation is conducted for the thermo-solutal convection and crystal sedimentation. The test-case domain is initially filled with the stationary melt of its liquidus temperature, that is, no superheat and motion. Solidification with a columnar structure initiates from the top unidirectionally. Equiaxed crystals could be produced near the columnar region through fragmentation. The parts due to the heterogeneous nucleation N_{nucl} and the death by dissolution (remelting) N_{remelt} were ignored.

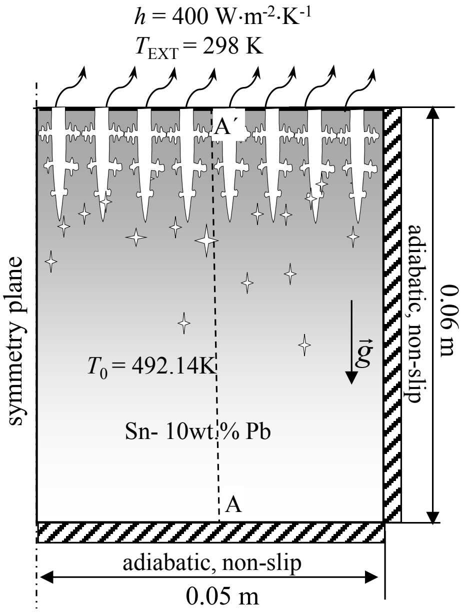

Figure 3.6. Configuration of the calculation domain for the test of formation of fragment.

Figure 3.7 shows the solidification sequence of the test case. For this calculation, a constant fragmentation coefficient (γ = 0.1) was assumed. With the initiation of cooling, the growth of columnar trunks and thermo-solutal convection begin from the top. The velocity magnitude is calculated as 1.4 cm/s. At 5 s, as shown in Figure 3.7(a.1), a columnar-liquid two-phase region (mush) is developed. Some melt convection cells can penetrate into the mushy zone. Furthermore, fragmentation shown by the N_{frag} contour in Figure 3.7(c.1) occurs in the mushy zone. The formation of the fragments seems non-uniform. Some “islands” with local high fragmentation rate are found near the columnar tip front in the mushy zone; these fragments serve as nuclei for the equiaxed crystals. The number density N_{eq} achieves a magnitude of 10^9 m^{-3}. Moreover, the equiaxed crystals start growing and sinking; however, their motion is influenced by the melt flowing through the drag force. Figure 3.7(b.1) shows the motion of the equiaxed crystals, with similar velocity magnitude to the liquid flow.

At 75 s, the top mushy zone (columnar) extends to approximately 1/3 of the domain (Figure 3.7(a.2)). A large vortex of melt flow and some small convection cells form in the bulk and near the columnar tip front regions, penetrating into the mushy zone (till $f_e \sim 0.3$). The melt flow has a significant impact on the velocity field of the equiaxed crystals (Figure 3.7(b.2)). Both the melt flow and motion of equiaxed crystals have similar velocity magnitude: 1.7 and 1.6×10^{-2} m/s. The equiaxed crystals finally settle at the bottom of the domain. As f_e reaches the packing limit, the equiaxed phase stops moving. This phenomenon is known as equiaxed settlement or sedimentation. A second mushy zone with packed equiaxed crystals develops from the bottom. The fragmentation continues near the columnar tip front (Figure 3.7(c.2)), supplying equiaxed nuclei continuously. The maximum number density can reach a magnitude of 10^{11} m^{-3}.

At 320 s, the extension of the columnar mushy zone and the pile-up of the equiaxed mushy zone meet at approximately one-third height of the domain, Figure 3.7(a.3)–(b.3). The growth of the columnar tip front is blocked by the equiaxed grain envelope mechanically, that is, CET occurs, as represented by the blue dash line. The melt flow is confined in the mushy zone, and its velocity magnitude is reduced to 10−5 m/s. This slow interdendritic flow still causes fragmentation in the columnar mushy zone above the CET line (Figure 3.7 (c.3)). The motion of equiaxed crystals is ignorable. These newly formed fragments cannot be transported out of the columnar mushy region but they will grow as equiaxed phase, competing with the growth of the columnar phase. In addition, a mixed columnar-equiaxed phase region is obtained. Figure 3.7(a.4)–(c.4) shows the solidification results at 420 s. The entire solidification sequence ends at 580 s, and the remaining melt in the mushy zone solidifies as a eutectic phase below temperature T_{eu}.

Figure 3.7(d.1)-(d.4) presents the evolution of macrosegregation during solidification. At 5 s, the macrosegregation is weak, and a negative segregation occurs in the columnar mushy zone. A slightly positive segregation, following the pattern of the melt convection cells, is obtained before the columnar tip front.

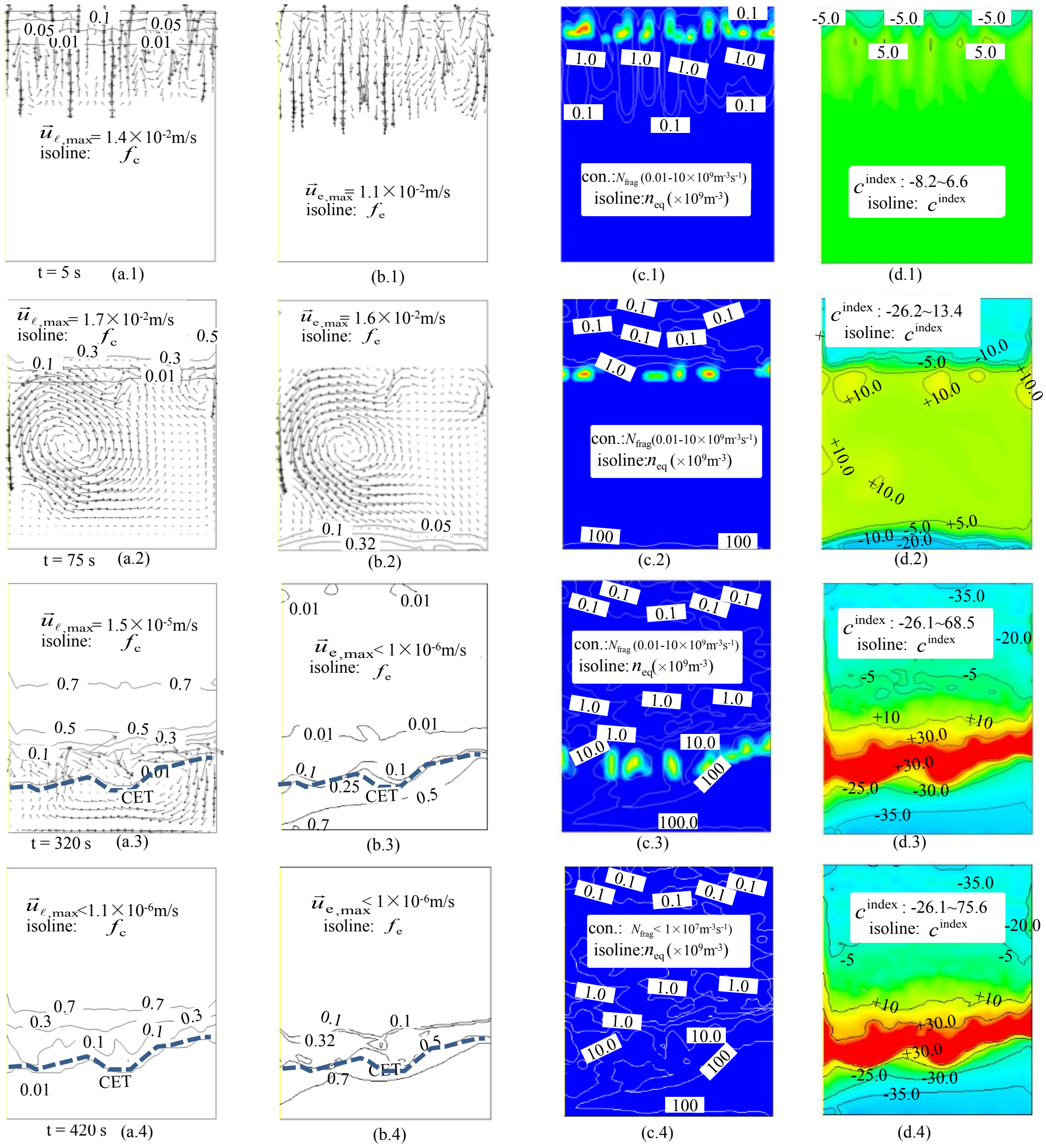

Figure 3.7. Solidification sequence of the test case for fragmentation: a.x show liquid velocity overlaid with f_c isoline; b.x show equiaxed velocity overlaid with f_e isoline; c.x show N_{frag} contour overlaid with n_{eq} isoline; and d.x show the contour of macrosegregation index (c^{index}). N_{frag} and c^{index} are represented in the color scales with blue for the minimum (or negative extreme), and red for the maximum (or positive extreme).

At 75 s, with the extension of the columnar mushy zone, the negative segregation (both the strength and area) increases. The positive segregation in the bulk melt region due to the mixing effect of the melt flow and crystals sedimentation becomes relatively homogenous. The equiaxed mushy zone near the bottom bears negative segregation. This process continues until the CET occurs at 320 s. The region of the middle positive segregation is gradually reduced to a relatively narrow region between the top negatively-segregated columnar mushy zone and the bottom negatively-segregated equiaxed mushy zone. The positive segregation intensity is very strong. After the CET event, the global segregation distribution patterns remain. The intensity of positive segregation (c^{index}) increases from 67% to 76% because of the slow interdendritic flow.

A experiment taken the similar configuration of the current test case was performed by Cao et al. [9]. A 2D cavity, as initially filled with aqueous ammonium chloride (NH_4Cl-H_2O), is cooled from top unidirectionally. The columnar structure grows from the top; the thermal-solutal convection causes the fragmentation; equiaxed crystals as grown from the fragments sediment at the bottom; finally a mixed columnar (top region) and equiaxed (bottom region) structure is developed. The simulation agrees qualitatively with the experiment observation. This part of study is published in Paper III and Paper V of Part II.

3.4 Example IV: Simulation of a Sn-Pb benchmark

The laboratory solidification experiments with Pb based alloys, following the configuration of Hebditch and Hunt [129], were widely used to investigate the formation of as-cast structure and macrosegregation [130-132]. Recently, a sophisticated AFRODITE setup for this experiment with precise control of cooling rate and temperature gradient was designed, and a series of solidification experiments and post-mortem metallographic and compositional analyses of as-solidified samples were performed at the SIMAP Laboratory in Grenoble France [6, 8]. Figure 3.8 shows the configuration of the AFRODITE setup. Hachani et al [8] presented the comprehensive results regarding to the temperature evolution, as-cast structure, and macro- and mesosegregation. Sn-10 wt.%Pb alloy was considered. The simulation of this benchmark is made by a multiphase solidification model, as developed by the authors [7]. In the original experiments of Hachani et al [8], both solidification experiments under forced convection (with electromagnetic stirring) and under natural convection (gravity) were performed. In this thesis, however, only the experiment under natural convection is numerically studied. The simulation results agree well with the experiment measurement comprehensively.

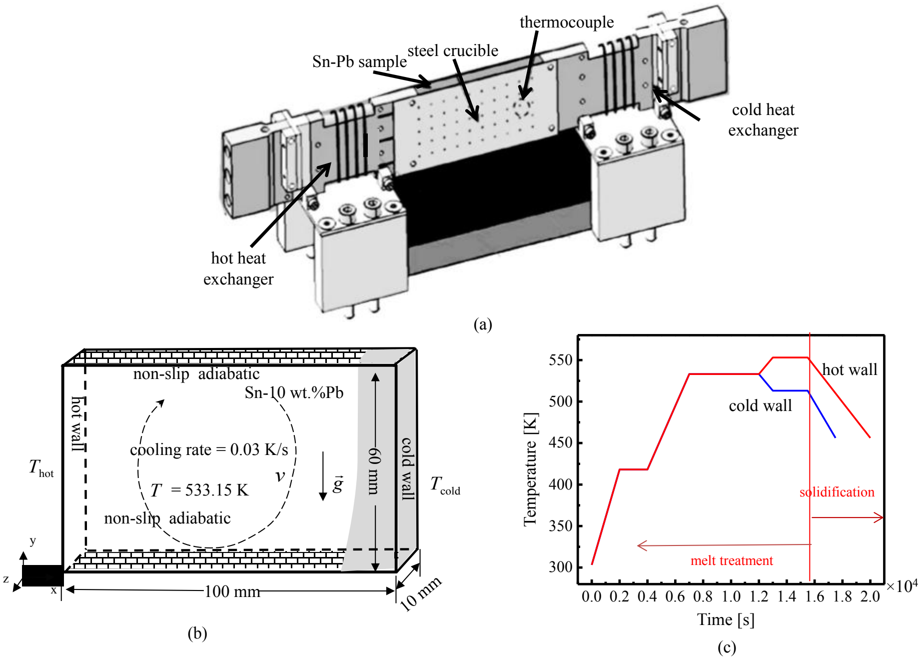

Figure 3.8. Configuration of the AFRODITE setup [8]: (a) schematic view of the experimental facility; (b) geometry and boundary conditions of Sn-Pb sample (benchmark casting); (c) temperature history experimentally applied at the boundaries of hot and cold walls.

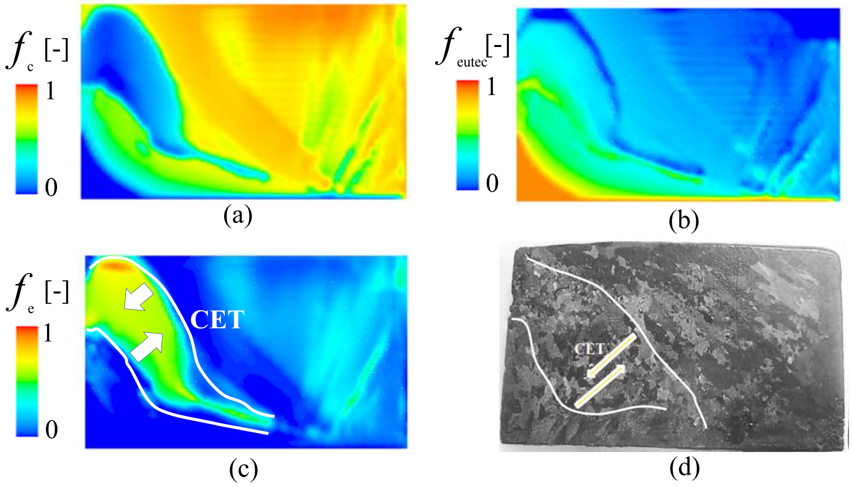

Figure 3.9. As-cast structure: simulation results of volume fractions of (a) columnar; (b) rest eutectic; (c) equiaxed; (d) metallography of as-cast structure.

Comparison of the as-cast structure between simulation and experiment is made in Figure 3.9. The general appearance of them is quite similar. The upwind tiled columnar structure region locates in the left side. A small second columnar structure region is observed in the lower left corner, where the volume fraction of rest eutectic is predicted quite high by the simulation. Equiaxed structure locates in the upper left region, which extends to the middle bottom. The equiaxed zone is enclosed between two lines, which indicate the columnar-to-equiaxed transition (CET).

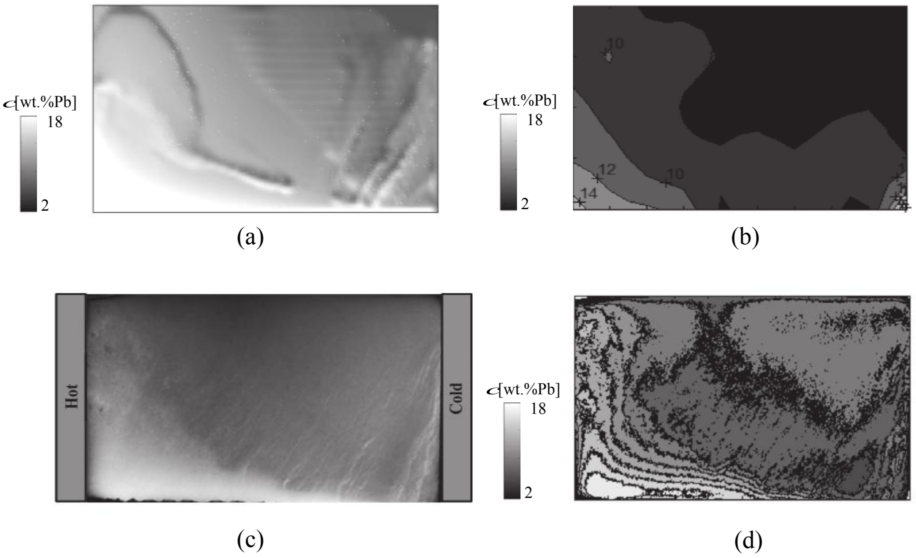

Figure 3.10. Macrosegregation: (a) simulated macrosegregation (wt.%Pb) on the center plane of the casting; (b) Pb concentration map measured by chemical method coupled with technical ICP (Inductively Coupled Plasma); (c) X-radiography of as-solidified benchmark; (d) Pb concentration map digitally processed from (c), and calibrated by the concentration value in (b).

The macrosegregation between simulation and experiment is compared in Figure 3.10. Numerically, the most positive macrosegregation (up to 25 wt.%Pb) locates near the left side wall where the melt solidifies at the late stage and the negative macrosegregation locates in the upper right side of the benchmark. Near the lower right corner, several segregation channels are witnessed Figure 3.10(a). Pb concentration in the segregation channels reaches about 16 wt.%. The numerically predicted segregation map (Figure 3.10(a)) agrees qualitatively with the experimental results, as measured by two different methods. Figure 3.10(b) shows Pb distribution as measured by chemical analysis with technical ICP (Inductively Coupled Plasma). It is mapped based on 50 discrete measurements over the longitudinal section of the benchmark. Figure 3.10(c) shows X-radiography of as-solidified benchmark. Mesosegregation (channel segregates) can be clearly observed. The contrast of the X-radiography can only give the qualitatively evaluation of relative Pb concentration. A quantitative segregation map (Figure 3.10(d)) is made through the digital processing of the X-radiography, and then calibrated by the chemically-analyzed quantities from Figure 3.10(b).

A 3D view of segregation channels is presented by the iso-surface of 12 wt.%Pb (Figure 3.11). The channels form preferably along the mold walls. Only some small discontinuous channel pieces in the casting center are found. Most channels are in form of tubular structures. There are also some lamellar-structured channels, which connect the bottom Pb-enriched zone. This part is published in Paper IV of Part II.

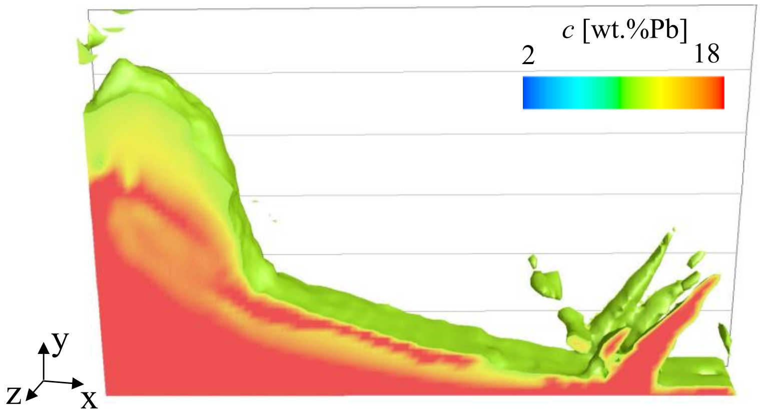

Figure 3.11. 3D view of iso-surface of 12 wt.%Pb, colored by Pb-concentration from 2 wt.% (blue) to 18 wt.% (red).

3.5 Example V: Simulation of vertical continuous casting

The vertical continuous casting (VCC) technique is recently applied to produce large round steel strands aiming to replace some of conventional ingot castings with high yields and low cost [24, 36, 133, 134]. The large format VCC strand usually has an equiaxed zone in the center, as is expected by the industry. The center equiaxed zone on the one hand can improve the mechanical properties of the final steel products; on the other hand can minimize the probability of porosity. In this section, the equiaxed crystals come from heterogeneous nucleation of inoculates in the undercooling melt. The conservation of inoculants and equiaxed crystals are taken into account. ECT and CET are also included in the study. Through the predefined inoculants the structure and macrosegregation can be manipulated.

The schematic of vertical continuous casting is shown in Figure 3.12. The molten steel is conducted into the mold through a submerged entry nozzle (SEN) and the melt solidifies against the water-cooled copper mold. Below the copper mold, water mist sprays cool the strand continuously to maintain the solidification of melt in the strand until it is fully solidified. A special numerical procedure is taken to mimic the continuous casting process based on a stationary numerical grid (Eulerian approach). The calculation domain is in 2D axial symmetry with 0.3 m radius and 36 m height, which is long enough to get a steady state of continuous casting process. We assume that the whole calculation domain (ϕ 0.6 m × 36 m) is initially filled with hot melt of pouring temperature, and the melt is stationary (no flow). As opposed to the real casting process where the mold is stationary and the hot melt is filled through the SEN into the mold when the solidified strand is withdrawn downwards continuously with a casting speed V_{pull}, we set the whole calculation domain as stationary while the mold is moving upwards with a velocity of $-V_{\mathrm{pull}}$. The so-called pseudo slag-SEN region is also set as a rigid material with the same temperature of liquid melt, and it also moves in parallel with the mold in the same magnitude of pull velocity ($-V_{\mathrm{pull}}$). As the whole domain of calculation is closed, the upward motion of the pseudo slag-SEN region leads to the upper part of liquid melt flowing through the SEN into the lower part of the mold region. This kind of configuration can mimic the real process of VCC withdrawing process.

Metallurgical quality of continuous casting strand is influenced by the physical properties of constituent elements, composition, strand size, and other practical conditions [135-138]. There is no experience that can be referred to control the macrosegregation in the vertical continuous casting strand of large format. Transport phenomena in the continuous casting were investigated by numerical simulations [139-144]. Some parameters studies were also made, such as casting speed, steel grade, and so on.

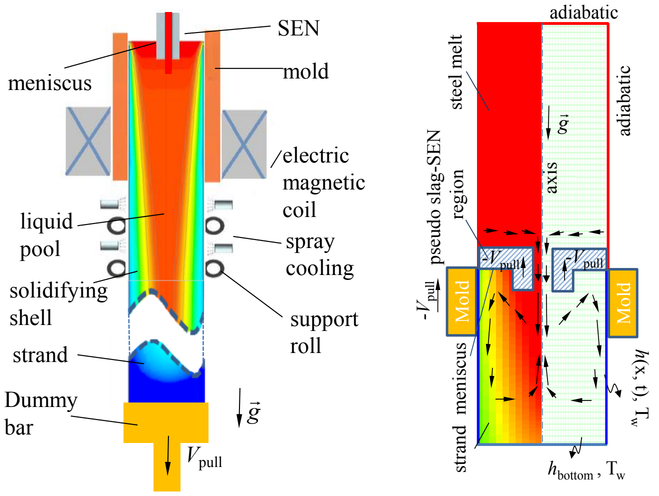

(a) (b)

Figure 3.12. Schematic of vertical continuous casting and simulation settings: (a) Schematic of vertical continuous casting process. (b) Numerical configuration of vertical continuous casting steel strand. The calculation domain is in 2D axial symmetry with 0.3 m radius and 36 m height. Left half of the figure shows schematically the construction of the calculation domain; while the right half shows thermal boundary conditions.

It is known both from experiment and simulation that mixed columnar-equiaxed as-cast structure is typical for the strand with large format. However, equiaxed phase can be absent in the slab casting or small round strand due to the existed high thermal gradient, which gives no sufficient conditions for the growth of equiaxed crystals. As a matter of fact, the appearance of equiaxed phase as well as its movement in the solidification process in the strand can play a very important role for the formation of macrosegregation. A comparative simulation in which the growth of equiaxed phase had been suppressed was carried out to evaluate the function of equiaxed phase in the formation of macrosegregation. Figure 3.13 shows the comparative analysis of two cases with and without considering the presence of equiaxed crystals. The case that does not include the growth of equiaxed phase bears positive macrosegregation in the center, while the case with equiaxed crystals has negative macrosegregation there. Both of them have positive macrosegregation in the mid-radius region (Figure 3.13(a)) in form of quasi channels. The quantitative analyses of the macrosegregation along the axis show that the center macrosegregation index is about c^{index} = 3.0, when the equiaxed crystals are not taken into account. However, when the equiaxed phase is introduced in the solidification, it bears about -12 of the negative macrosegregation index (Figure 3.13(b)). From the macrosegregation distribution curves along radius direction, Figure 3.13(c), it can be seen that near the surface two cases have similar macrosegregation distribution, but in the center they have opposite macrosegregation. In the mid-radius region the case with equiaxed has more severe positive macrosegregation, corresponding to the quasi-channels. Generally, a larger fluctuation of macrosegregation is witnessed in the case considering equiaxed phase. However, when the equiaxed crystals are included in the case, there is an equiaxed zone in the center of the strand. In the equiaxed zone, the probability of porosity would decrease effectively, improving the quality of the strand. For the case without equiaxed crystals, the strand has high probability of porosity in the center part, as is unacceptable even it has a relative small macrosegregation fluctuation. Through adjusting impurities (inoculants), we can change the size of equiaxed zone and the position of CET.

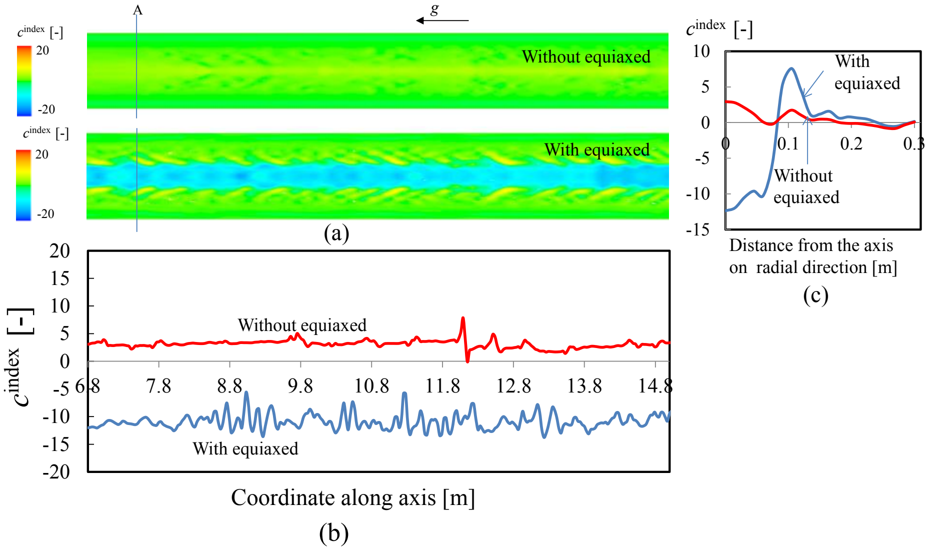

Figure 3.13. Comparison of two cases, with or without considering the exist of equiaxed phase: (a) macrosegregation index contours in the steady-state section, (b) the macrosegregation index along the axis, and (c) macrosegregation distribution along the radius at cross-section A in (a).

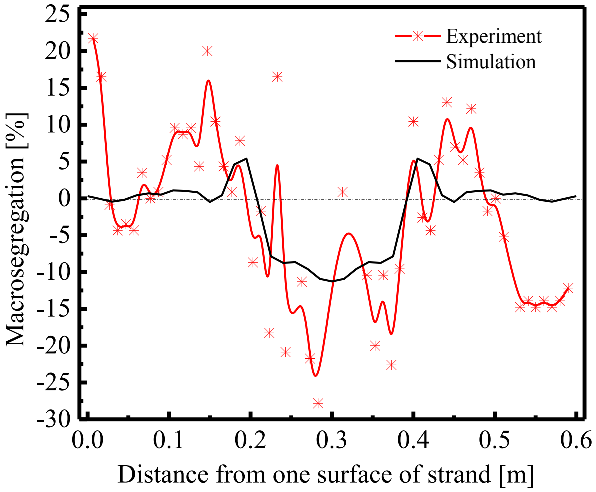

Figure 3.14**.** Comparison of predicted macrosegregation (blue line) with experiment (red line) in a trans-diameter sample. The experiment result courtesy of Primetals Technologies.

The measurement of macrosegregation across the strand diameter of as-cast strand was conducted to evaluate the numerical model, as is shown in Figure 3.14. The red line is the result of measurement for macrosegregation while the blue one is its counterpart from the simulation. The tendency is the same for both of them: in the center the strand bears negative segregation and in the mid-radius part it has positive segregation. However, the simulation cannot ideally fit the experiment result. The variation of macrosegregation from the simulation is slightly smaller than that from the experimental measurement. For the commercial reason, no technical detail is presented here.

3.6 Example VI: Simulation of semi-continuous casting

The semi-continuous casting (SCC), thanks to high flexibility of manipulation, as well as high productivity and low operation cost, might be considered as an alternative option for ingot casting. SCC, as schematically shown in Figure 3.15, is a derivation of the vertical continuous casting process. The difference is that the strand in SCC is withdrawn to a specified length (casting), and then the strand undergoes a hot toping stage till it is fully solidified (solidification). Fragmentation is an important origin of equiaxed crystals during steel casting process, especially when the steel melt is relatively clean. In this section, the formulation of fragment is taken into account and the equiaxed crystals originate from the remelting-induced fragmentation. During hot top stage in the SCC process, the thermal shielding around the strand and electromagnetic stirring (EMS) are expected to improve internal quality. In this section, both of them are also modeled and analyzed numerically.

A SCC strand of the format up to 0.8 m even larger with the model alloy Fe-C with composition larger than 1.0 wt% was calculated (Figure 3.12(b)). The calculation domain (the volume of the final strand) in 3D is enmeshed in 0.3 million hexahedral volume elements (Figure 3.12(b)). In the subsequent solidification stage, the controlled cooling (e.g. thermal shielding) and the electromagnetic stirring (EMS) are implemented and the stirrer would move upwards from the bottom to the top according to the predefined movement scheme. With above mentioned measures, it is expected to avoid surface crack, promote the equiaxed zone in the center, minimize porosity in the center, and so on.

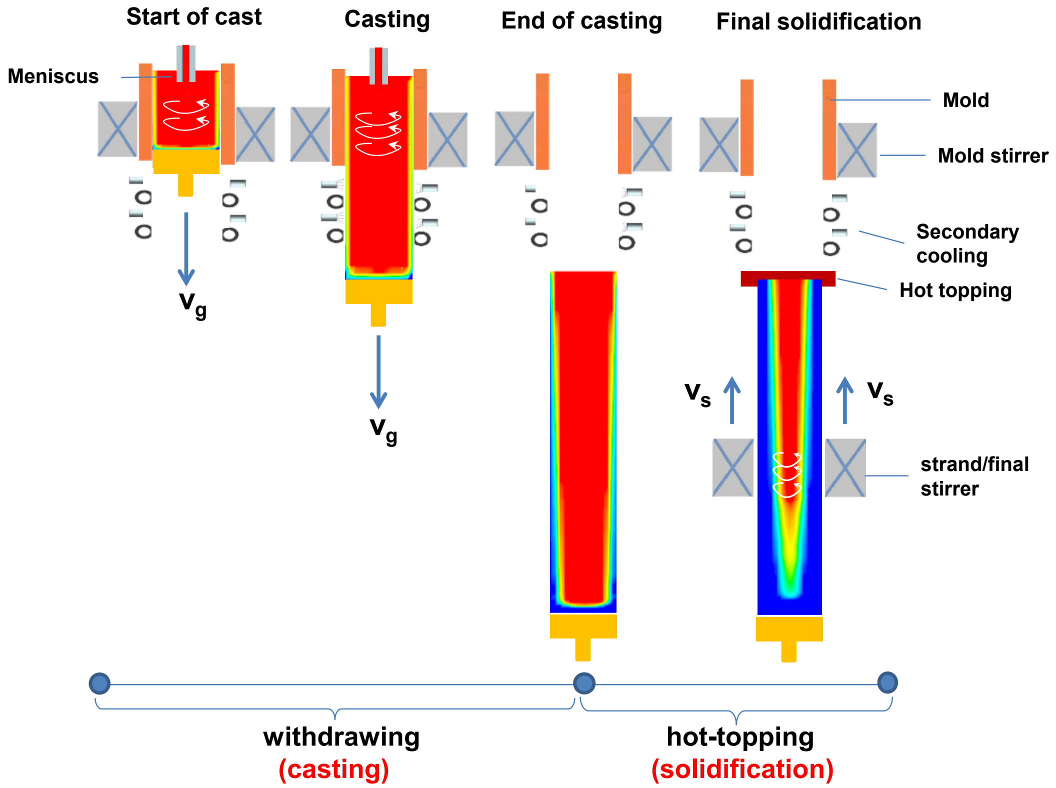

Figure 3.15. Schematic of semi-continuous casting process.

In order to demonstrate the solidification and liquid convention during the withdrawing period, contour of columnar phase volume fraction overlaid with liquid velocity at 600 s are shown in Figure 3.16. At the early stage, solid shell is formed gradually. As the strand is continuously withdrawn to a certain length, the flow pattern in the liquid pool includes two large circulations. Generally, the melt in front of the solid shell flows downwards, and the melt in the center region tends to rise (Figure 3.16(a)). Convection rolls develop in the liquid pool dynamically. The convection rolls are non-axisymmetric and rotational. The flow in the upper part of the mold region is strongly influenced by the jet flow coming from the inlet (SEN). There are strong convections near the nozzle and they are induced by the joint effect of thermo-solutal convection and SEN jet flow (Figure 3.16 (b)).

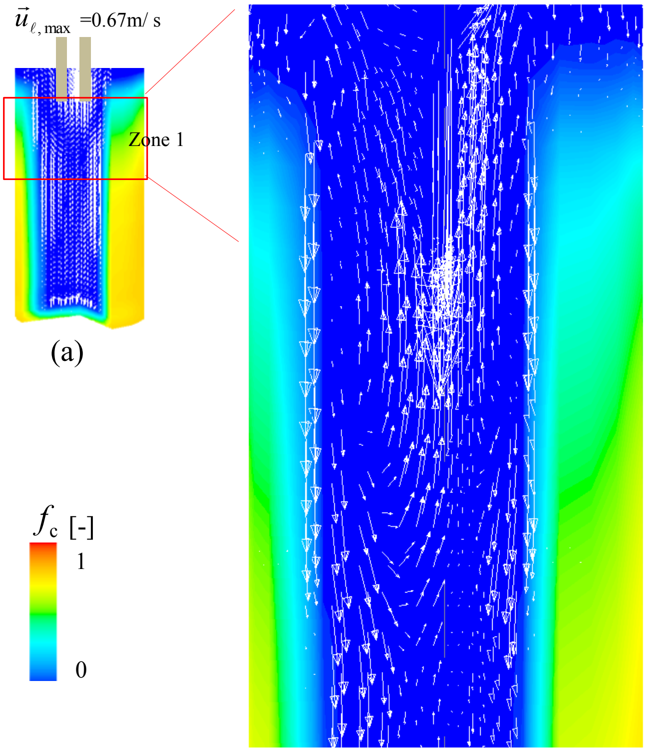

(a)

(b)

Figure 3.16. Contour of columnar phase volume fraction overlaid with liquid velocity (white arrow) during the withdrawing period: (a) global view; (b) zoom-in of Zone 1 in (a).

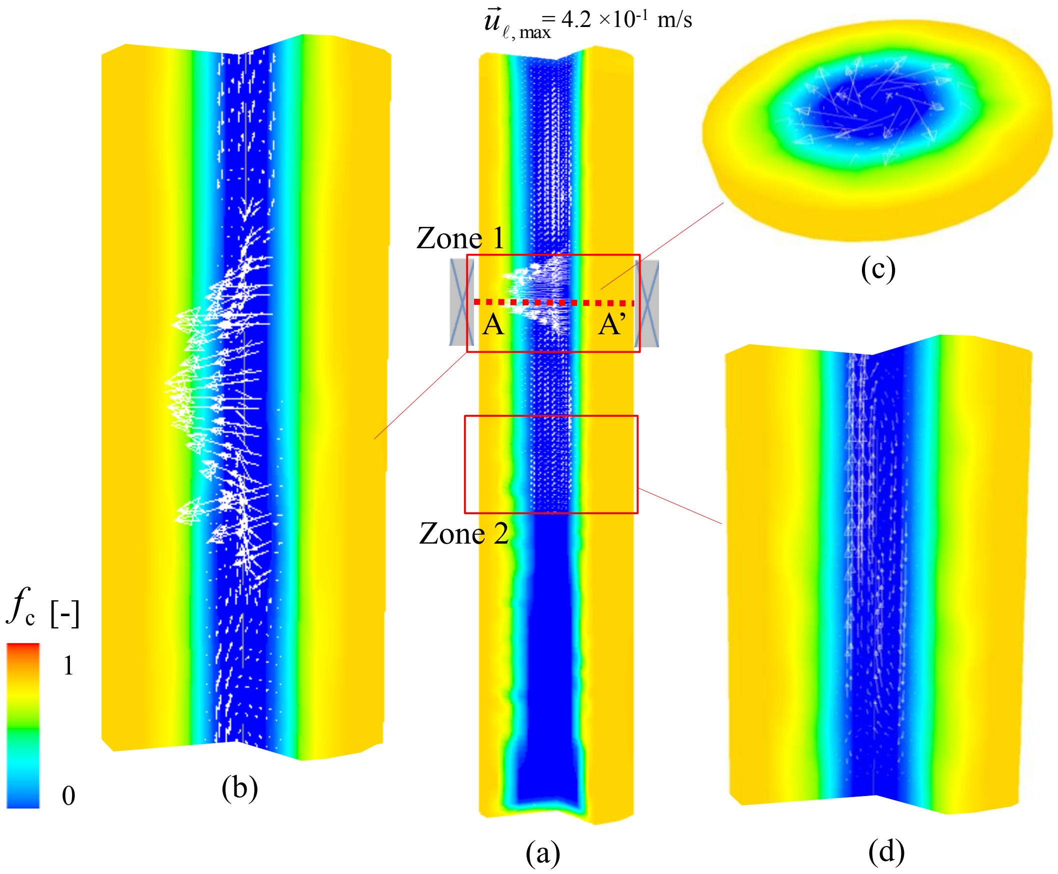

Figure 3.17. Contour of columnar phase volume fraction overlaid with liquid velocity (white arrow) during hot topping period (3900 s): (a) global view; (b) zoom-in of Zone 1 in (a) in the region of the electromagnetic stirrer; (c) the cross-section view through AA'; (d) zoom-in view of Zone 2 in (a).

During the hot-topping process the meniscus is set as adiabatic condition, while the side wall is set as convection heat transfer boundary condition, taking the thermal shielding into account. The f_c and liquid velocity at the moment of 3900 s are shown in Figure 3.17. The solid shell (columnar phase) grows. The flow pattern with convection cells remains, but the intensity of convection cells decrease. The motion of equiaxed crystals and the melt flow are fully coupled. The driving force for the flow at this moment is due to the thermo-solutal convection and its interaction with the crystal sedimentation. Liquid velocity under the EMS is significantly influenced by the electromagnetic force. It is with maximum flow velocity 0.42 m/s, which is slightly smaller than the jet flow from the SEN (0.67 m/s) during the withdrawing period.

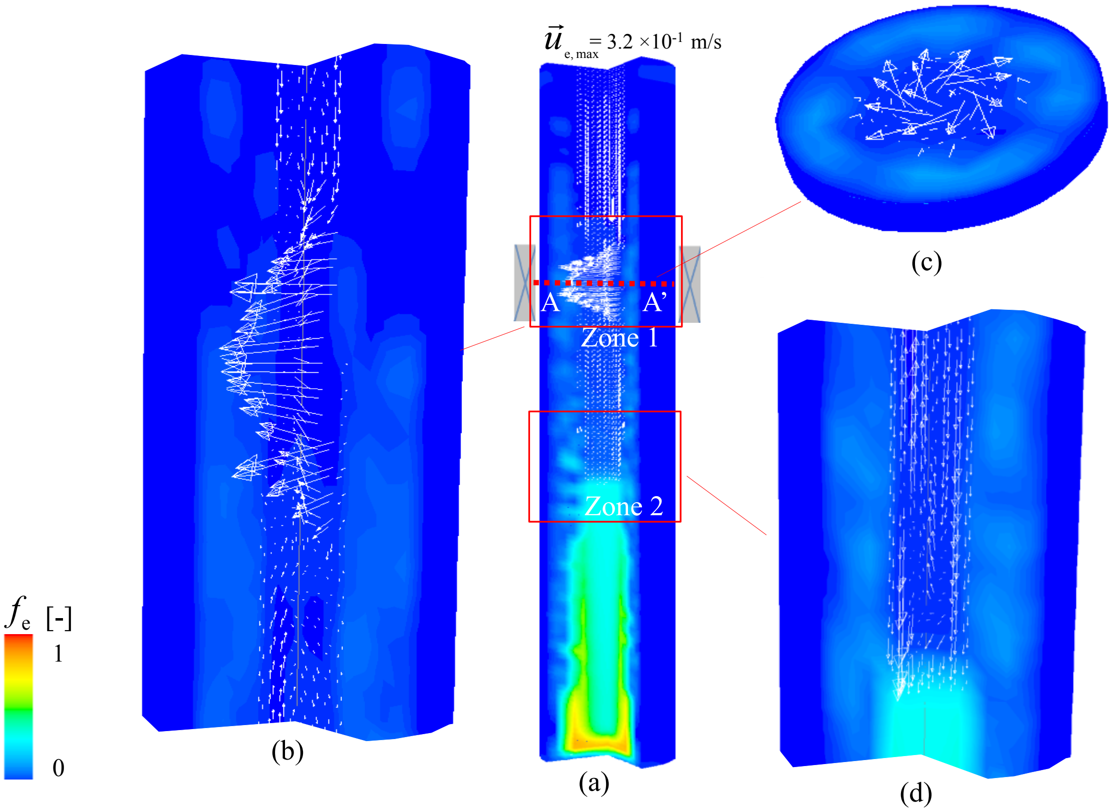

Figure 3.18. Contour of equiaxed phase volume fraction overlaid with liquid velocity (white arrow) (3900 s): (a) global view; (b) zoom-in of Zone 1 in (a) in the region of the electromagnetic stirrer; (c) the cross-section view through AA'; (d) zoom-in view of Zone 2 in (a) near the bottom of the melt pool.

In order to show the settling of equiaxed crystals during hot topping period, contour of equiaxed phase volume fraction overlaid with equiaxed velocity are shown in Figure 3.18. The equiaxed crystals mainly located in the lower part of the strand. Obviously, equiaxed crystals move in the melt pool corresponding to the similar flow pattern of liquid phase. A small amount of equiaxed crystals are captured in-between of the columnar dendrites, while the solid shell of the strand consists of a mainly columnar structure (Figure 3.18(a)). The electromagnetic stirring (EMS) is applied during the hot topping stage. Crystals with large equiaxed velocity are located in the region of the EMS. Crystals in the strand near the middle of the EMS have the largest velocity, which is with a magnitude of 10^{-1} m/s (Figure 3.18(b)). From the cross section, we can observe an obvious equiaxed crystal circulation (Figure 3.18(c)). This kind of circulation is coupled with liquid convections, through the drag force between different phases. In the lower part of the melt pool, an equiaxed convection is witnessed. Specifically, near the bottom of the melt pool, the crystals tend to settle down, attaching to the equiaxed network below (Figure 3.18(d)).

Accumulation of the equiaxed crystals in the lower part of the strand would result in negative macrosegregation. This phenomenon would last from the beginning of solidification (withdrawing stage) till the very late stage of solidification. The solute-rich liquid pool would shrink gradually, resulting in a positive macrosegregation zone in the hot-top region at the end of solidification.

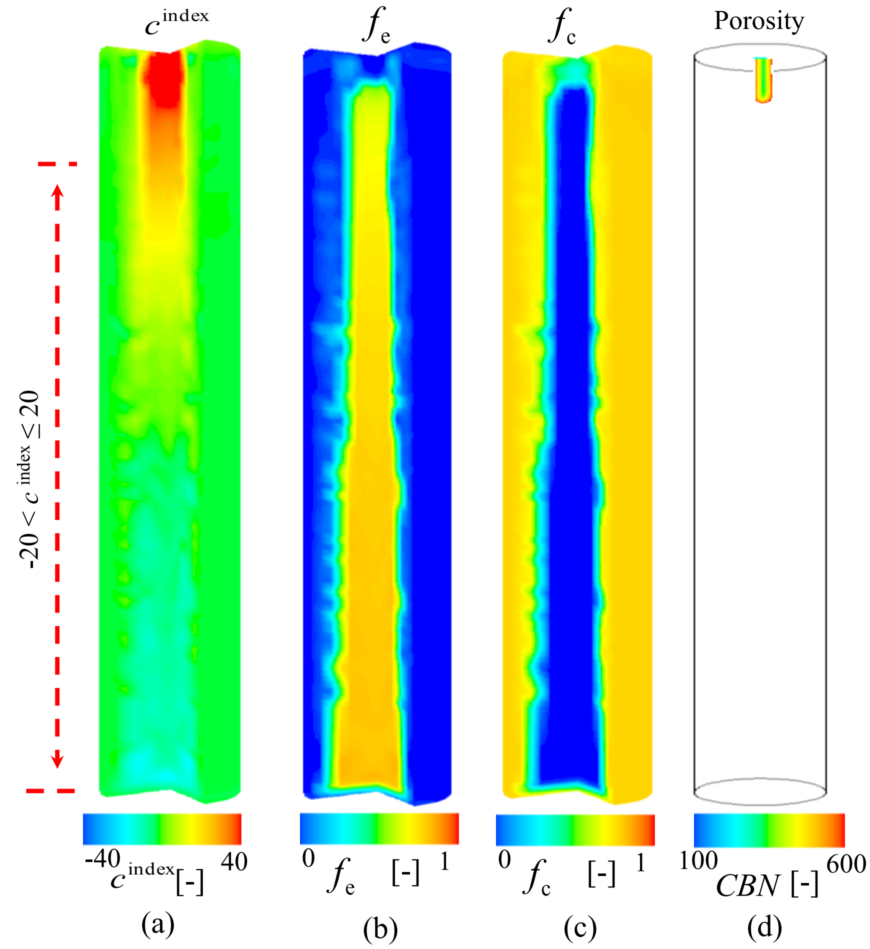

Figure 3.19. Final results of the simulation of semi-continuous casting process: (a) macrosegregation index c^{index}; (b) equiaxed phase distribution, (c) columnar phase distribution, (d) probability of shrinkage/porosity by the CBN criterion. The geometry in vertical direction is under-scaled for the purpose of visualization.

The distribution range of c^{index} over the whole strand is from -18 to 35% (Figure 3.19(a)). The strand has negative macrosegregation in the bottom equiaxed zone and positive macrosegregation in the top columnar zone. The part with c^{index} larger than 20% is only located in the very top region of the strand, less than 2 m from the top.

The density of equiaxed crystals is bigger than that of liquid phase. Equiaxed crystals have the potential to move downwards. The global as-cast structure in the strand is characterized by the center equiaxed zone and the outer radius columnar zone, as shown in Figure 3.19(b)-(c). The center equiaxed zone is separated from the outer columnar zone by the so-called CET. It is also seen that a small portion of equiaxed crystals are entrapped in the columnar zone. The bottom part of the strand, which is mainly formed during the start stage of the withdrawing, is mostly occupied by the equiaxed phase. In the top part of the strand columnar dominates the region. The reason for the bottom equiaxed zone is mainly due to equiaxed crystal sedimentation.

A modified Niyama criterion, i.e. CBN [43, 122, 124], is used to predict the probability of shrinkage porosity in the columnar structure zone. The smaller CBN criterion indicates the higher probability of shrinkage porosity. Figure 3.19(d) shows that the greatest probability of shrinkage porosity is predicted in a very small region in the upper part of the strand center, less than 1 m. The pore formation in the lower part of the strand, where the equiaxed phase occupies the strand center (Figure 3.19(b)), cannot be properly predicted by the current model. For commercial reason, no technical details are presented in this thesis.

4 Summary

Volume-average based multiphase solidification model is an effective tool to calculate the formation of as-solidified structure and macrosegregation during solidification. The model used is based on the three-phase mixed columnar-equiaxed model [7]. In order to realize the multiphase modeling of structure and macrosegregation in round steel billet of large format, some improvements are made and new features are extended.

Firstly, three-phase mixed columnar-equiaxed model were extended.

- Consideration of the transport of inoculants (embryos). The inoculants serve as heterogeneous nucleation sites for the equiaxed crystals. The total numbers (volume integral) of inoculants and equiaxed crystals are conserved: a certain number of inoculants consumed are identical to the number of newly-nucleated equiaxed crystals.
- Realization of the equiaxed-to-columnar transition (ECT). During equiaxed solidification, when all inoculants are consumed and the equiaxed crystals settle down in the bottom region, the remaining melt in the upper part can solidify as columnar.
- Implementation of fragmentation formula. We assume that the rate of fragmentation is proportional to the value of $-(\vec{u}_\ell - \vec{u}_\mathrm{c}) \cdot \nabla c_\ell$ by suggesting the following formulation for the fragmentation-induced mass transfer rate from the columnar to equiaxed phase: $M_\mathrm{ce} = -\gamma \cdot (\vec{u}_\ell - \vec{u}_\mathrm{c}) \cdot \nabla c_\ell \cdot \rho_\mathrm{e}$. Note that fragmentation occurs only with remelting, that is, when $M_\mathrm{ce} > 0.0$. For solidification (calculated M_ce has a negative value), we set $M_\mathrm{ce} = 0.0$ to prevent the occurrence of fragmentation. The mass integral of all fragments produced per time ($\mathrm{kg} \cdot \mathrm{m}^{-3} \cdot \mathrm{s}^{-1}$) is proportional to the increase rate of constitutional supersaturation as caused by the solute transport due to interdendritic

flow. A fragmentation coefficient γ was assigned to bridge the unknown correlation between M_{ce} and the increase rate of constitutional supersaturation.

- Adoption of electromagnetic stirring (EMS). EMS is calculated by the commercial software ANSYS Maxwell, then averaged and interpolated into the software ANSYS Fluent.

Secondly, the features of the extended three-phase mixed columnar-equiaxed solidification model were tested. A 2D cavity (50×60 mm^2) with Pb-Sn alloy solidified from top or bottom is considered.

- Columnar solidification. 1) Three macrosegregation formation mechanisms operate: thermal buoyancy flow, solutal buoyancy flow and diffusion of interdendritic flow. Solidification shrinkage is ignored here. Diffusion-induced macrosegregation occurs only at the bottom and top surfaces, and it is ignorable if the mechanism of thermo-solutal buoyancy flow operates. 2) Solutal buoyancy dominates over the thermal buoyancy in Pb-18 wt.%Sn and Sn-10 wt.%Pb benchmarks when both of them operate at the same time; hence solutal buoyancy represents the dominant mechanism for the macrosegregation. 3) Global macrosegregation intensity increases with the magnitude of the flow velocity. Details of the macrosegregation can be analyzed by thermo-solutal convections during columnar solidification.
- Equiaxed solidification. 1) During the early stage of equiaxed solidification before ECT, the macrosegregation tendency is predictable: equiaxed sedimentation, i.e. the dominant macrosegregation mechanism, induces negative segregation in the bottom region; while solute-enriched melt is distributed in the upper region. 2) As equiaxed solidification proceeds, the rest melt can only fully solidify as columnar structure when the available inoculants are consumed. 3) After the ECT during the late stage of columnar solidification, the thermo-solutal convection becomes the dominant

macrosegregation mechanism. The redistribution of the positive macrosegregation pattern in the upper region, by the mechanism of thermo-solutal convection, depends on the alloy and cooling direction. 4) In order to understand the macrosegregation mechanisms, the solidification process must be analyzed in two steps. During the early stage of equiaxed solidification before ECT, the equiaxed crystal sedimentation induced macrosegregation can be analyzed by the relation of $\partial c_{\mathrm{mix}} / \partial t \approx (c_\ell - c_{\mathrm{e}}) \cdot \nabla \cdot \left(f_{\mathrm{e}} \vec{u}_{\mathrm{e}} \right)$. During the late stage of columnar solidification, the macrosegregation as induced by thermo-solutal convection can be analyzed by the relation of $\partial c_{\mathrm{mix}} / \partial t = -f_\ell \vec{u}_\ell \cdot \nabla c_\ell$.

- Fragmentation formula. 1) The columnar structure, growing from the top, and the pile-up of equiaxed crystals from the bottom finally led to a mixed columnar-equiaxed structure and the occurrence of a CET. A special macrosegregation pattern was predicted, according to which negative segregation occurred in both columnar and equiaxed regions, and a relatively strong positive segregation occurred near the CET line. 2) The current formulation for the fragmentation considers that transport of a solute-enriched melt through interdendritic flow in the columnar growth direction is in favor of the solute-driven remelting, and hence in favor of fragmentation. One modeling parameter was required to be introduced: the fragmentation coefficient γ. For the fragmentation, the unknown contributing factors, such as the curvature effect of the dendrites, latent heat-induced thermal fluctuation, and diffusion in the interdendritic melt, were included in γ . This parameter must be determined experimentally or requires the development of another theoretical model. Bigger the γ is, larger is the equiaxed zone in the as-solidified structure.

Thirdly, evaluations were made by comparison with laboratory experiments.

- Comparison against a Sn-10 wt.%Pb laterally solidified benchmark [8]. 1) The crystals can be swept away by the liquid with higher lead concentration. The equiaxed crystals even can move upward with the liquid near the solidification front. The equiaxed crystals are concentrated in the upper left corner extending to the middle bottom of the benchmark. Position of equiaxed region is sensitive to the difference of density between liquid and equiaxed crystals. The right side of the benchmark is dominantly occupied by columnar phase, and some eutectic phase is located in the final solidification region near hot wall. There is also little fraction of eutectic phase embedded in columnar phase. The CET is obvious between columnar and equiaxed phase. 2) The most positive macrosegregation locates in the left hot wall where the liquid finally solidifies and the negative macrosegregation locates in the upper right side of the bench-mark. Solute element rejection starts from the right cold wall. As a result, a lead-enriched area locates at the left bottom in the finial solidification end. 3) Near the cold wall, several segregated channels are witnessed. Segregated channels form near the cold wall of the benchmark, and extend obliquely downwards to the center bottom position. Channels prefer to locate along the walls while a small portion of discrete channels are seen in the center of the benchmark. The channels are mainly in form of tubular or lamellar structures. The simulation results agree with the experimental measurements satisfactorily.
- Comparison against a top solidified aqueous ammonium chloride (NH_4Cl-H_2O) cavity [9]. The alloy used in the simulation is Sn-10 wt.%Pb alloy. The columnar structure grows from the top; the thermal-solutal convection causes the fragmentation; equiaxed crystals as grown from the fragments sediment at the bottom; finally a mixed columnar (top region) and equiaxed (bottom region) structure is developed. Although the alloy in the simulation is different from the experiment, the predicted results fit the experiment observation qualitatively.

Finally, we applied the extended model in the simulation of vertical continuous casting (VCC) and semi-continuous casting (SCC) process, and following summaries can be drawn:

- Simulation of a large vertical continuous casting (VCC) steel round. 1) An equiaxed zone locates in the center of the strand, and a columnar zone occupies the outer part of the strand. They are separated by the CET. The calculated segregation pattern shows a negative segregation in the center equiaxed zone, surrounded by a middle-radius positive segregation ring near the CET region. 2) The macrosegregation originates from relative motion between different phases, as can be theoretically expressed by the combined effect the liquid flow-solidification interaction, equiaxed flow-solidification interaction and the equiaxed sedimentation. 3) A plant trial of vertical continuous casting was conducted to validate the model. The predicted macrosegregation distribution along radius direction agrees well with the measurements.
- Numerical analysis of macrosegregation in a semi-continuously casting steel (SCC) strand. 1) The key features of industry semi-continuous casting strand, such as the as-cast structure, CET, macrosegregation, porosity, etc., are reproduced. 2) The motion of equiaxed crystals and the melt flow are fully coupled. The driving force for the flow is the thermo-solutal convection and its interaction with the crystal sedimentation. Liquid velocity in the region of EMS is significantly influenced by the electromagnetic force when the EMS is applied. It is with the maximum flow velocity of 4.2×10^{-1} m/s. 3) the equiaxed crystals are confined in the center of the strand, while the remaining part is mainly occupied by columnar phase. The center part of the strand near the top in the columnar structure region has the highest porosity possibility. The bottom has negative macrosegregation and the upper center part of the strand has positive macrosegregation.

As can be conclude that the extended three-phase mixed equiaxed-columnar solidification model can be used to study the casting process of industry scale, such as SCC and VCC. The model was partially validated against laboratory experiments and limited industry trial. Further validations are desirable.

5 References

[1] T. Meier, B. Kundig, S. Feldhaus, C. Tercelli, F. Zani, Y. Lim, Y. Park, Continuous casting machine for oversized blooms, in: 9th European continuous casting conference, Austria center Vienna, 2017, p. 257-266.

[2] A. Eichinger, H.P. Kogler, A. Puhringer, G. Hrazeder, S. Hahn, F. Wimmer, Semi-continuous casting technology combining technological advantages of two different casting practices, in: 9th European continuous casting conference, Austria center Vienna, 2017, p. 267-276.

[3] S. Michelic, M. Riedler, Production of Jumbo Blooms by Semi-continuous Casting: Challenges, Feasibility, and Future Potential, BHM Berg-und Hüttenmännische Monatshefte, 2016, vol. 161, p. 39-44.

[4] J. Zhang, D.-F. Chen, C.-Q. Zhang, S.-G. Wang, W.-S. Hwang, M.-R. Han, Effects of an even secondary cooling mode on the temperature and stress fields of round billet continuous casting steel, J. Mater. Process. Tech, 2015, vol. 222, p. 315-326.

[5] S. Buoro, G. Romanelli, Ladle Metallurgy & Continuous Casting-Technological Review of the Start-Up of a New Jumbo Bloom Continuous Caster for Specialty Steels, Iron and Steel Technology, 2012, vol. 9, p. 39.

[6] R. Boussaa, L. Hachani, O. Budenkova, V. Botton, D. Henry, K. Zaidat, H.B. Hadid, Y. Fautrelle, Macrosegregations in Sn-3wt% Pb alloy solidification: Experimental and 3D numerical simulation investigations, Int. J. Heat Mass Transfer, 2016, vol. 100, p. 680-690.

[7] M. Wu, A. Ludwig, A three-phase model for mixed columnar-equiaxed solidification, Metall. Mater. Trans. A, 2006, vol. 37A, p. 1613-1631.

[8] L. Hachani, K. Zaidat, Y. Fautrelle, Experimental study of the solidification of Sn–10 wt.%Pb alloy under different forced convection in benchmark experiment, Int. J. Heat Mass Transfer, 2015, vol. 85, p. 438-454.

[9] J.W. Gao, C.Y. Wang, Effects of grain transport on columnar to equiaxed transition in dendritic alloy solidification, in: Modeling of Casting, Welding and Advanced Solidification Processes VIII, 1998, p. 425-432.

[10] K. Sumitomo, M. Hashio, T. Kishida, A. Kawami, Bottom Pouring and Ingot Quality of Sumitomo Metal Industries, Iron Steel Eng., 1985, vol. 62, p. 54-61.

[11] E. Fuchs, P. Jonsson, Inclusion characteristics in bearing steel before and during ingot casting, High Temp. Mat. Pr-isr, 2000, vol. 19, p. 333-344.

[12] T. Sjökvist, M. Göransson, P. Jönsson, P. Cowx, Influence of ferromanganese additions on microalloyed engineering steel, Ironmak. Steelmak., 2003, vol. 30, p. 73-80.

[13] Solutions for ingot casting, retrieved from https://www.vesuvius.com/en/our-solutions/international/iron-and-steel/ingot-casting.html in 2018.

[14] H. Combeau, M. Založnik, S. Hans, P.E. Richy, Prediction of macrosegregation in steel ingots: influence of the motion and the morphology of equiaxed grains, Metall. Mater. Trans. B, 2009, vol. 40, p. 289-304.

[15] M. Wu, A. Ludwig, A. Kharicha, Simulation of As-Cast Steel Ingots, Steel Res. Int., 2017, vol. 87, p. 1700037.

[16] Committee on technology of international iron and steel institute, Continuous casting of steel 1985: a second study, 1986.

[17] W.R. Irving, Continuous casting of steel, Cambridge The University Press, 1993.

[18] B.G. Thomas, Continuous Casting of Steel, in: O. Yu, M. Dekker (Eds.) Chapter 15 in Modeling for casting and solidification processing, New York, 2001, p. 499-540.

[19] K. Shikoh, J. Lee, C.K. Jeong, U.K. Cho, S. Lee, H. Kim, Initial solidification behavior in an extra largeCC mold at ultra low casting speed, in: 9th European continuous casting conference, Austria center Vienna, 2017, p. 1079-1090.

[20] J. Penn, P. Pennerstofer, A. Junbauer, New generation of continuous casting plants with intelligent manufacturing strategy, in: 9th European continuous casting conference, Austria center Vienna, 2017, p. 28-37.

[21] L. Lorenzo, M. Li, Y. Han, 800mm round blooms in special engineering steel cast on a 5 strand caster ar Laowu steel Co., in: 8th European continuous casting conference, Congress Graz, Austria, 2014, p. 451-458.

[22] S. Antonil, R. Macro, K. Siebo, Y. Dominique, Recent Danieli experiences for eletromagnetic stirrer optimisation in round blooms continuous casting, in: 8th European continuous casting conference, Congress Graz, Austria, 2014, p. 1456-1463.

[23] L. Zhang, Z. Wang, C. Xu, S. Li, X. Ai, J. Li, A vertical continuous casting machine for large blooms, Ironmak. Steelmak., 2017, vol. 12, p. 1-5.

[24] F. Wimmer, H. Thöne, P. Pennerstorfer, New vertical bloom caster, Metallu rgical Research & Technology, 2015, vol. 112, p. 101-103.

[25] P. Du, Numerical modeling of porosity and macrosegregation in continuous casting of steel, Doctor thesis, University of Iowa, 2013.

[26] S. Michelic, M. Riedler, Production of jumbo blooms by semi-continuous casting: challenges, feasibility and future potential in: Proceedings of the 2015 international symposium on liquid metal processing and casting, 2015, p. 471-478.

[27] D.G.Eskin, A.Jafari, L.Katgerman, Contribution of forced centreline convection during direct chill casting of round billets to macrosegregation and structure of binary Al-Cu aluminium alloy, Mater. Sci. Tech-lond., 2011, vol. 27, p. 890-896.

[28] H. Zhang, H. Nagaumi, Y. Zuo, J. Cui, Coupled modeling of electromagnetic field, fluid flow, heat transfer and solidification during low frequency electromagnetic casting of 7XXX aluminum alloys: Part 1: Development of a mathematical model and comparison with experimental results, Mater. Sci. Eng. A, 2007, vol. 448, p. 189-203.

[29] A. Ludwig, M. Gruber-Pretzler, F. Mayer, A. Ishmurzin, M. Wu, A way of coupling ternary phase diagram information with multiphase solidification simulations, Mater. Sci. Eng. A, 2005, vol. 413, p. 485-489.

[30] C. Xu, M. Zheng, Y. Chi, X. Chen, K. Wu, E. Wang, G. Fan, P. Yang, G. Wang, X. Lv, Microstructure and mechanical properties of the Mg–Gd–Y–Zn–Zr alloy fabricated by semi-continuous casting, Mater. Sci. Eng. A, 2012, vol. 549, p. 128-135.

[31] R. Nadella, D. Eskin, L. Katgerman, Effect of Grain Refinement on Structure Evolution,“Floating” Grains, and Centerline Macrosegregation in Direct-Chill Cast AA2024 Alloy Billets, Metall. Mater. Trans. A, 2008, vol. 39, p. 450-461.

[32] J. Hao, M. Grasser, M. Wu, A. Ludwig, Numerical study and experimental investigation of solidification phenomena in semi-continuous casting of Bronze, 2010 International Conference on Advances in Materials and Manufacturing Processes, ICAMMP 2010, November 6, 2010 - November 8, 2010, 2011, vol. 154-155, p. 1401-1404.

[33] M. Zaloznik, A. Kumar, H. Combeau, M. Bedel, P. Jarry, E. Waz, The Coupling of Macrosegregation with Grain Nucleation, Growth and Motion in DC Cast Aluminum Alloy Ingots, in: Essential Readings in Light Metals. Springer, Cham, 2011, p. 848-853.

[34] P. Johann, A. David, What's next for continuous casting, in: 8th European continuous casting conference, Congress Graz, Austria, 2014, p. 394-405.

[35] A.-G. Nicholas, Y. Mansur, F. Stephan, Design and firs operation results from 5 strand billet, bloom and beam blank combicaster at kademir, Turkey, in: 8th European continuous casting conference, Congress Graz, Austria, 2014, p. 406-415.

[36] K. Oh, J. Lee, S. Kim, J. Choi, Development of a large ingot continuous caster, Metallurgical Research & Technology, 2015, vol. 112, p. 203-212.

[37] A. Ciobanas, Y. Fautrelle, Ensemble averaged multiphase Eulerian model for columnar/equiaxed solidification of a binary alloy: I. The mathematical model, J. Phys. D: Appl. Phys., 2007, vol. 40, p. 3733-3741.

[38] A. Ciobanas, Y. Fautrelle, Ensemble averaged multi-phase Eulerian model for columnar/equiaxed solidification of a binary alloy: II. Simulation of the columnar-to-equiaxed transition (CET), J. Phys. D: Appl. Phys., 2007, vol. 40, p. 4310.

[39] C. Beckermann, R. Viskanta, Double-diffusive convection during dendritic solidification of a binary mixture, PhysicoChemical Hydrodynamics, 1988, vol. 10, p. 195-213.

[40] J. Ni, C. Beckermann, A two-phase model for mass, momentum, heat, and species transport during solidification, Transport phenomena in material processing, New York. ASME HTD, 1990, vol. 132, p. 45-56.

[41] J. Ni, C. Beckermann, A volume-averaged two-phase model for transport phenomena during solidification, Metall. Mater. Trans. B, 1991, vol. 22, p. 349-361.

[42] M. Bellet, Two-phase multiscale FEM modelling of macrosegregation formation in steel slabs, in: AIP Conference Proceedings, 2007, p. pages 1369-1374.

[43] M. Wu, A. Kharicha, A. Ludwig, Using four-phase Eulerian volume averaging approach to model macrosegregation and shrinkage cavity, IOP Conf. Series: Mate. Sci. Eng., 2015, vol. 84, p. 012006.

[44] J. Li, M. Wu, A. Ludwig, A. Kharicha, Simulation of macrosegregation in a 2.45-ton steel ingot using a three-phase mixed columnar-equiaxed model, Int. J. Heat Mass Transfer, 2014, vol. 72, p. 668-679.

[45] F. Mayer, M. Wu, A. Ludwig, On the formation of centreline segregation in continuous slab casting of steel due to bulging and/or feeding, Steel Res. Int., 2010, vol. 81, p. 660-667.

[46] M. Wu, J. Domitner, A. Ludwig, Using a two-phase columnar solidification model to study the principle of mechanical soft reduction in slab casting, Metall. Mater. Trans. A, 2012, vol. 43, p. 945-964.

[47] M. Wu, A. Fjeld, A. Ludwig, Modelling mixed columnar-equiaxed solidification with melt convection and grain sedimentation–Part I: Model description, Comp. Mater. Sci., 2010, vol. 50, p. 32-42.

[48] M. Wu, A. Ludwig, A. Fjeld, Modelling mixed columnar-equiaxed solidification with melt convection and grain sedimentation–Part II: Illustrative modelling results and parameter studies, Comp. Mater. Sci., 2010, vol. 50, p. 43-58.

[49] J. Li, M.H. Wu, A. Ludwig, A. Kharicha, P. Schumacher, Influence of dendritic morphology on the calculation of macrosegregation in steel ingot, Mater. Sci. Forum., 2014, vol. 790, p. 121-126.

[50] A. Faghri, Y. Zhang, J.R. Howell, Advanced heat and mass transfer, Global Digital Press, 2010.

[51] W. Liu, Finite elemrnt modelling of macrosegregation and thermomechanical phenomenain solidification processes, Doctor thesis, Ecole Des Mines de Paris, Nacy, 2005.

[52] C. Beckermann, R. Viskanta, Natural convection solid/liquid phase change in porous media, Int. J. Heat Mass Transfer, 1988, vol. 31, p. 35-46.

[53] C. Vivѐs, Solidification of tin in the presence of electric and magnetic fields, J. Cryst. Growth, 1986, vol. 76, p. 170-184.

[54] W. Montgomery, F. Incropera, Fragmentation of dendritic crystals during solidification of aqueous ammonium chloride, Exp. Heat Transfer, 1998, vol. 11, p. 59-86.

[55] Z.J. Su, J. Chen, K. Nakajima, J.C. He, Criterion for Dendrite Fragmentation of Carbon Steel under Imposition of Linear Travelling EMS, Steel Res. Int., 2009, vol. 80, p. 824-833.

[56] P.A. Davidson, An introduction to magnetohydrodynamics, Cambridge university press, 2001.

[57] J.K. Roplekar, J.A. Dantzig, A study of solidification with a rotating magnetic field, Int. J. Casting metals research, 2001, vol. 14, p. 79-95.

[58] A. Ohno, Solidification: the separation theory and its practical applications, Springer Science & Business Media, 1987.

[59] C. Beckermann, R. Viskanta, Mathematical modeling of transport phenomena during alloy solidification, Appl. Mech. Rev., 1993, vol. 46, p. 1-27.

[60] M. Bedel, K. Tveito, M. Založnik, H. Combeau, M. M'Hamdi, A model study of the impact of the transport of inoculant particles on microstructure formation during solidification, Comp. Mater. Sci., 2015, vol. 102, p. 95-109.

[61] M. Bedel, M. Založnik, A. Kumar, H. Combeau, P. Jarry, E. Waz, Influence of transport mechanisms on nucleation and grain structure formation in DC cast aluminium alloy ingots, in: IOP Conf. Series: Mate. Sci. Eng., IOP Publishing, 2012, p. 012070.

[62] Y. Zheng, M. Wu, A. Kharicha, A. Ludwig, Numerical analysis of macrosegregation in vertically solidified Pb-Sn test castings–Part II: Equiaxed solidification, Comp. Mater. Sci., 2016, vol. 124, p. 456-470.

[63] M. Rappaz, Modelling of microstructure formation in solidification processes, Int. Mater. Rev., 1989, vol. 34, p. 93-124.

[64] J. Ni, C. Beckermann, Modeling of Globulitic Alloy Solidification with Melt Convection, J. Mater. Process. Manuf. Sci., 1993, vol. 2, p. 217-231.

[65] M. Wu, A. Ludwig, J. Luo, Numerical Study of the Thermal-Solute! Convection and Grain Sedimentation during Globular Equiaxed Solidification, Mater. Sci. Forum., 2005, vol. 475-479, p. 2725-2730.

[66] M. Wu, A. Ludwig, L. Ratke, Modelling the solidification of hypermonotectic alloys, Model. Simul. Mater. Sci. Eng., 2003, vol. 11, p. 755-769.

[67] R. Nadella, D. Eskin, Q. Du, L. Katgerman, Macrosegregation in direct-chill casting of aluminium alloys, Prog. Mater. Sci., 2008, vol. 53, p. 421-480.

[68] C. Wang, C. Beckermann, Equiaxed dendritic solidification with convection: Part I. Multiscale/multiphase modeling, Metall. Mater. Trans. A, 1996, vol. 27, p. 2754-2764.

[69] M. Wu, A. Ludwig, Modeling equiaxed solidification with melt convection and grain sedimentation—I: Model description, Acta Mater., 2009, vol. 57, p. 5621-5631.

[70] M. Wu, A. Ludwig, Modeling equiaxed solidification with melt convection and grain sedimentation—II. Model verification, Acta Mater., 2009, vol. 57, p. 5632-5644.

[71] Ø. Nielsen, A. Mo, B. Appolaire, H. Combeau, Measurements and modeling of the microstructural morphology during equiaxed solidification of Al-Cu alloys, Metall. Mater. Trans. A, 2001, vol. 32, p. 2049-2060.

[72] A. Greer, Grain refinement in rapidly solidified alloys, Mater. Sci. Eng. A, 1991, vol. 133, p. 16-21.

[73] T. Quested, A. Greer, The effect of the size distribution of inoculant particles on as-cast grain size in aluminium alloys, Acta Mater., 2004, vol. 52, p. 3859-3868.

[74] A. Greer, A. Bunn, A. Tronche, P. Evans, D. Bristow, Modelling of inoculation of metallic melts: application to grain refinement of aluminium by Al–Ti–B, Acta Mater., 2000, vol. 48, p. 2823-2835.

[75] K. Nakajima, H. Hasegawa, S. Khumkoa, S. Mizoguchi, Effect of a catalyst on heterogeneous nucleation in pure and Fe-Ni alloys, Metall. Mater. Trans. B, 2003, vol. 34, p. 539-547.

[76] B.L. Bramfitt, The effect of carbide and nitride additions on the heterogeneous nucleation behavior of liquid iron, Metall. Mater. Trans. B, 1970, vol. 1, p. 1987-1995.

[77] S.-B. Kim, S.-Y. Lee, J.-S. Lee, J.-W. Cho, Grain refinement of solidification structure by direct inoculation, in: 9th European continuous casting conference, Austria center Vienna, 2017, p. 277-282.

[78] H. Fredriksson, E.M.R.S. Meeting, State of the art of computer simulation of casting and solidification processes, 1986: June 17th-20th, 1986, Strasbourg (France), in, Editions de physique, 1986, p. 255-266.

[79] C. Van Der Eijk, Ø. Grong, F. Haakonsen, L. Kolbeinsen, G. Tranell, Progress in the development and use of grain refiner based on cerium sulfide or titanium compound for carbon steel, ISIJ Int., 2009, vol. 49, p. 1046-1050.

[80] A. Hellawell, S. Liu, S. Lu, Dendrite fragmentation and the effects of fluid flow in castings, JOM, 1997, vol. 49, p. 18-20.

[81] H. Yasuda, Y. Yamamoto, N. Nakatsuka, T. Nagira, M. Yoshiya, A. Sugiyama, I. Ohnaka, K. Umetani, K. Uesugi, In situ observation of nucleation, fragmentation and microstructure evolution in Sn–Bi and Al–Cu alloys, Int. J. Cast. Metal. Res, 2008, vol. 21, p. 125-128.

[82] G. Lesoult, Macrosegregation in steel strands and ingots: Characterisation, formation and consequences, Mater. Sci. Eng. A, 2005, vol. 413–414, p. 19-29.

[83] B. Chalmers, R. Williamson, Crystal multiplication without nucleation, Science, 1965, vol. 148, p. 1717-1718.

[84] H. Garabedian, R. Strickland-Constable, Collision breeding of ice crystals, J. Cryst. Growth, 1974, vol. 22, p. 188-192.

[85] J. Pilling, A. Hellawell, Mechanical deformation of dendrites by fluid flow, Metall. Mater. Trans. A, 1996, vol. 27, p. 229-232.

[86] A.M. Mullis, D.J. Walker, S.E. Battersby, R.F. Cochrane, Deformation of dendrites by fluid flow during rapid solidification, Mater. Sci. Eng. A, 2001, vol. 304, p. 245-249.

[87] K. Jackson, J. Hunt, D. Uhlmann, T. Seward, On the origin of the equiaxed zone in castings, Trans. Metall. Soc. Aime, 1966, vol. 236, p. 149-158.

[88] M. Christenson, F. Incropera, Solidification of an aqueous ammonium chloride solution in a rectangular cavity—I. Experimental study, Int. J. Heat Mass Transfer, 1989, vol. 32, p. 47-68.

[89] M. Christenson, W. Bennon, F. Incropera, Solidification of an aqueous ammonium chloride solution in a rectangular cavity—II. Comparison of predicted and measured results, Int. J. Heat Mass Transfer, 1989, vol. 32, p. 69-79.

[90] C. Paradies, R. Smith, M. Glicksman, The influence of convection during solidification on fragmentation of the mushy zone of a model alloy, Metall. Mater. Trans. A, 1997, vol. 28, p. 875-883.

[91] R. Mathiesen, L. Arnberg, P. Bleuet, A. Somogyi, Crystal fragmentation and columnar-to-equiaxed transitions in Al-Cu studied by synchrotron X-ray video microscopy, Metall. Mater. Trans. A, 2006, vol. 37, p. 2515-2524.

[92] H. Jung, N. Mangelinck-Noel, H. Nguyen-Thi, N. Bergeon, B. Billia, A. Buffet, G. Reinhart, T. Schenk, J. Baruchel, Fragmentation in an Al–7 wt-% Si alloy studied in real time by X-ray synchrotron techniques, Int. J. Cast. Metal. Res, 2009, vol. 22, p. 208-211.

[93] E. Liotti, A. Lui, R. Vincent, S. Kumar, Z. Guo, T. Connolley, I. Dolbnya, M. Hart, L. Arnberg, R. Mathiesen, A synchrotron X-ray radiography study of dendrite

fragmentation induced by a pulsed electromagnetic field in an Al–15Cu alloy, Acta Mater., 2014, vol. 70, p. 228-239.

[94] M. Wu, J. Li, A. Ludwig, A. Kharicha, Modeling diffusion-governed solidification of ternary alloys–Part 2: Macroscopic transport phenomena and macrosegregation, Comp. Mater. Sci., 2014, vol. 92, p. 267-285.

[95] M. Wu, J. Li, A. Ludwig, A. Kharicha, Modeling diffusion-governed solidification of ternary alloys–Part 1: Coupling solidification kinetics with thermodynamics, Comp. Mater. Sci., 2013, vol. 79, p. 830-840.

[96] N. Leriche, H. Combeau, C.-A. Gandin, M. Založnik, Modelling of Columnar-to-Equiaxed and Equiaxed-to-Columnar Transitions in Ingots Using a Multiphase Model, in: IOP Conf. Series: Mate. Sci. Eng., IOP Publishing, 2015, p. 012087.

[97] M.C. Flemings, G.E. Nereo, Macrosegregation : Part I, Trans. Metall. Soc. Aime, 1967, vol. 239, p. 1449-1462.

[98] T. Campanella, C. Charbon, M. Rappaz, Grain refinement induced by electromagnetic stirring: A dendrite fragmentation criterion, Metall. Mater. Trans. A, 2004, vol. 35, p. 3201-3210.

[99] M. Wu, A. Ludwig, Using a three-phase deterministic model for the columnar-to-equiaxed transition, Metall. Mater. Trans. A, 2007, vol. 38A, p. 1465-1475.

[100] J. Lipton, M.E. Glicksman, W. Kurz, Dendritic growth into undercooled alloy metals, Mater. Sci. Eng., 1984, vol. 65, p. 57-63.

[101] J. Hunt, Steady state columnar and equiaxed growth of dendrites and eutectic, Mater. Sci. Eng., 1984, vol. 65, p. 75-83.

[102] V. Biscuola, M. Martorano, Mechanical blocking mechanism for the columnar to equiaxed transition, Metall. Mater. Trans. A, 2008, vol. 39, p. 2885-2895.

[103] W. Kurz, D.J. Fisher, Fundamentals of solidification, Trans Tech Publications, 1984.

[104] M. Wu, Y. Zheng, A. Kharicha, A. Ludwig, Numerical analysis of macrosegregation in vertically solidified Pb-Sn test castings–Part I: Columnar solidification, Comp. Mater. Sci., 2016, vol. 124, p. 444-455.

[105] A. Ohno, Solidification: the Separation Theory and Its Practical Applications, Springer-Verlag, 1987.

[106] M. Martorano, V. Biscuola, Predicting the columnar-to-equiaxed transition for a distribution of nucleation undercoolings, Acta Mater., 2009, vol. 57, p. 607-615.

[107] N. Leriche, H. Combeau, C.-A. Gandin, M. Založnik, Modelling of Columnar-to-Equiaxed and Equiaxed-to-Columnar Transitions in Ingots Using a Multiphase Model, IOP Conf. Series: Mate. Sci. Eng., 2015, vol. 84, p. 012087.

[108] M.C. Flemings, Our understanding of macrosegregation: past and present, ISIJ Int., 2000, vol. 40, p. 833-841.

[109] C. Beckermann, Modelling of macrosegregation: applications and future needs, Int. Mater. Rev., 2002, vol. 47, p. 243-261.

[110] A. Ludwig, M. Wu, A. Kharicha, On Macrosegregation, Metall. Mater. Trans. A, 2015, vol. 46A, p. 4854-4867.

[111] J.A. Dantzig, M. Rappaz, Solidification, EPFL Press, 2009.

[112] J. Moore, N. Shah, Mechanisms of formation of A-and V-segregation in cast steel, International metals reviews, 1983, vol. 28, p. 336-356.

[113] D. Ma, Q. Wu, A. Bührig -Polaczek, Some new observations on freckle formation in directionally solidified superalloy components, Metall. Mater. Trans. B, 2012, vol. 43, p. 344-353.

[114] M. Wu, L. Könözsy, A. Ludwig, W. Schützenhöfer, R. Tanzer, On the formation of macrosegregations in steel ingot castings, Steel Res. Int., 2008, vol. 79, p. 637-646.

[115] J. Moore, Review of axial segregation in continuously cast steel, Iron and Steelmaker, 1980, vol. 10, p. 8-16.

[116] M. Wu, L. Konozsy, A. Ludwig, W. Schutzenhofer, R. Tanzer, On the formation of macrosegregations in steel ingot castings, Steel Res. Int., 2008, vol. 79, p. 637-644.

[117] C. Pequet, M. Rappaz, M. Gremaud, Modeling of microporosity, macroporosity, and pipe-shrinkage formation during the solidification of alloys using a mushy-zone refinement method: applications to aluminum alloys, Metall. Mater. Trans. A, 2002, vol. 33, p. 2095-2106.

[118] T. Piwonka, M. Flemings, Pore formation in solidification, Aime Met Soc Trans, 1966, vol. 236, p. 1157-1165.

[119] K. Kubo, R.D. Pehlke, Mathematical modeling of porosity formation in solidification, Metallurgical Transactions B, 1985, vol. 16, p. 359-366.

[120] R. Atwood, P. Lee, Simulation of the three-dimensional morphology of solidification porosity in an aluminium–silicon alloy, Acta Mater., 2003, vol. 51, p. 5447-5466.

[121] I. Imafuku, K. Chijiiwa, A Mathematical Model for Shrinkage Cavity Prediction in Steel Castings.(Retroactive Coverage), Transactions of the American Foundrymen's Society., 1983, vol. 91, p. 527-540.

[122] E. Niyama, T. Uchida, M. Morikawa, S. Saito, A method of shrinkage prediction and its application to steel casting practice, Int. Cast Met. J., 1982, vol. 7, p. 52-63.

[123] K.D. Carlson, C. Beckermann, Prediction of shrinkage pore volume fraction using a dimensionless Niyama criterion, Metall. Mater. Trans. A, 2009, vol. 40, p. 163-175.

[124] K.D. Carlson, C. Beckermann, Prediction of shrinkage pore volume fraction using a dimensionless Niyama criterion, Metall. Mater. Trans. A, 2009, vol. 40A, p. 163-175.

[125] M. Wu, A. Ludwig, A. Kharicha, A four phase model for the macrosegregation and shrinkage cavity during solidification of steel ingot, Appl. Math. Model., 2017, vol. 41, p. 102-120.

[126] W. Kurz, D.J. Fisher, Fundamentals of Solidification, 3rd ed., Trans Tech Pub, Aedermannsdorf, Switzerland, 1992.

[127] M.C. Flemings, Solidification Processing, McGraw-Hill, 1974.

[128] M. Bellet, H. Combeau, Y. Fautrelle, D. Gobin, M. Rady, E. Arquis, O. Budenkova, B. Dussoubs, Y. Duterrail, A. Kumar, Call for contributions to a numerical benchmark problem for 2D columnar solidification of binary alloys, Int. J. Therm. Sci., 2009, vol. 48, p. 2013-2016.

[129] D. Hebditch, J. Hunt, Observations of ingot macrosegregation on model systems, Metall. Mater. Trans., 1974, vol. 5, p. 1557-1564.

[130] C. Gau, R. Viskanta, Melting and solidification of a metal system in a rectangular cavity, Int. J. Heat Mass Transfer, 1984, vol. 27, p. 113-123.

[131] J. Sarazin, A. Hellawell, Channel formation in Pb-Sn, Pb-Sb, and Pb-Sn-Sb alloy ingots and comparison with the system NH4Cl-H2O, Metall. Mater. Trans. A, 1988, vol. 19, p. 1861-1871.

[132] M.I. Bergman, D.R. Fearn, J. Bloxham, M.C. Shannon, Convection and channel formation in solidifying Pb-Sn alloys, Metall. Mater. Trans. A, 1997, vol. 28, p. 859-866.

[133] H. Cherukuri, R. Johnson, Modelling vertical continuous casting with temperature-dependent material properties, Int. J. Mech. Sci., 2001, vol. 43, p. 1243-1257.

[134] P.E.R. Lopez, P.N. Jalali, J. Björkvall, U. Sjöström, C. Nilsson, Recent developments of a numerical model for continuous casting of steel: model theory, setup and comparison to physical modelling with liquid metal, ISIJ Int., 2014, vol. 54, p. 342-350.

[135] K. Timmel, X. Miao, T. Wondrak, F. Stefani, D. Lucas, S. Eckert, G. Gerbeth, Experimental and numerical modelling of the fluid flow in the continuous casting of steel, The European Physical Journal Special Topics, 2013, vol. 220, p. 151-166.

[136] R. Kalter, B. Righolt, S. Kenjereš, C. Kleijn, M. Tummers, Experimental modeling of heat transfer in a continuous casting mould model, in: ASME 2014 4th Joint US-European fluids engineering division summer meeting collocated with the ASME 2014 12th International conference on nanochannels, microchannels, and minichannels, American Society of Mechanical Engineers, Illinois, USA, 2014, p. 1-8.

[137] B.G. Thomas, Modeling of the continuous casting of steel—past, present, and future, Metall. Mater. Trans. B, 2002, vol. 33, p. 795-812.

[138] A.A. Tzavaras, H. Brody, Electromagnetic stirring and continuous casting—Achievements, problems, and goals, JOM, 1984, vol. 36, p. 31-37.

[139] H. Henein, J. Brimacombe, A. Watkinson, The modeling of transverse solids motion in rotary kilns, Metallurgical transactions B, 1983, vol. 14, p. 207-220.

[140] B. Thomas, L. Mika, F. Najjar, Simulation of fluid flow inside a continuous slab-casting machine, Metallurgical Transactions B, 1990, vol. 21, p. 387-400.

[141] B. Thomas, I. Samarasekera, J. Brimacombe, Comparison of numerical modeling techniques for complex, two-dimensional, transient heat-conduction problems, Metallurgical Transactions B, 1984, vol. 15, p. 307-318.

[142] J. Domitner, M. Wu, A. Ludwig, Numerical study about the influence of small casting speed variations on the metallurgical length in continuous casting of steel slabs, Steel Res. Int., 2014, vol. 85, p. 1-5.

[143] A. Jonayat, B.G. Thomas, Transient thermo-fluid model of meniscus behavior and slag consumption in steel continuous casting, Metall. Mater. Trans. B, 2014, vol. 45, p. 1842-1864.

[144] K. Timmel, T. Wondrak, M. Röder, F. Stefani, S. Eckert, G. Gerbeth, Use of cold liquid metal models for investigations of the fluid flow in the continuous casting process, Steel Res. Int., 2014, vol. 85, p. 1283-1290.

Part II

Papers included in this thesis:

1) Menghuai Wu, Yongjian Zheng, Abdellah Kharicha, Andreas Ludwig, Numerical analysis of macrosegregation in vertically solidified Pb-Sn test castings – Part I: Columnar solidification, Computational Materials Science, 2016, 124: 444-455.
2) Yongjian Zheng, Menghuai Wu, Abdellah Kharicha, Andreas Ludwig, Numerical analysis of macrosegregation in vertically solidified Pb-Sn test castings – Part II: Equiaxed solidification, Computational Materials Science, 2016, 124: 456-470.
3) Yongjian Zheng, Menghuai Wu, Abdellah Kharicha, Andreas Ludwig, Incorporation of fragmentation into a volume average solidification model, Modelling and Simulation in Materials Science and Engineering, 2018(26): 015004.
4) Yongjian Zheng, Menghuai Wu, Ebrahim Karimi-sibaki, Abdellah Kharicha, Andreas Ludwig, Use of a mixed columnar-equiaxed solidification model to analyse the formation of as-cast structure and macrosegregation in a Sn-10 wt% Pb benchmark experiment, International Journal of Heat and Mass Transfer, 2018, 122: 939-953.
5) Yongjian Zheng, Menghuai Wu, Abdellah Kharicha, Andreas Ludwig, Role of fragmentation in as-cast structure: numerical study and experimental validation, China Foundry, 2017(14): 321-326.

Other scientific publications not included in this thesis:

1) Yongjian Zheng, Menghuai Wu, Abdellah Kharicha, Andreas Ludwig, Volume average Nodelling of equiaxed-to-columnar transition in a vertically solidified Pb-18 wt.%Sn cavity, 6th Decennial International Conference Solidification Processing (SP17), (2017): 312-316.
2) Menghuai Wu, Yongjian Zheng, Abdellah Kharicha, Andreas Ludwig, Numerical analysis of as-cast structure, macrosegregation and shrinkage cavity in steel ingots: case study of a 36 ton ingot, 7^{rd} STEELSIM, Aug. 16-18, 2017, Qingdao, China, Proceedings in CD-ROM: 129-132.
3) Yongjian Zheng, Menghuai Wu, Abdellah Kharicha, Andreas Ludwig, Simulation of thermo-solutal convection induced macrosegregation in a Sn-10% Pb alloy benchmark during columnar solidification, IOP Conference Series: Material Science and Engineering (MPPE), 119 (2016): 012004.
4) Yongjian Zheng, Menghuai Wu, Abdellah Kharicha, Andreas Ludwig, Simulation of macrosegregation in a large vertical continuous casting of steel, IOP Conference Series: Material Science and Engineering (LMPC), 143 (2016): 012032.
5) Yongjian Zheng, Menghuai Wu, Abdellah Kharicha, Andreas Ludwig, Transport phenomena during solidification of a vertical casting of steel: a multiphase numerical study, 6th. Int. Conf. "SteelSim 2015", proceedings on data storage device.

Paper I

Numerical-analysis of macrosegregation in vertically solidified Pb-Sn test castings – Part I: Columnar solidification

Menghuai Wu, Yongjian Zheng, Abdellah Kharicha, Andreas Ludwig

Computational Materials Science, 2016, 124: 444-455.

Computational Materials Science 124 (2016) 444–455

Contents lists available at ScienceDirect

Computational Materials Science

journal homepage: www.elsevier.com/locate/commatsci

Numerical analysis of macrosegregation in vertically solidified Pb-Sn test castings – Part I: Columnar solidification

M. Wu [a,b,*], Y. Zheng [a], A. Kharicha [a,b], A. Ludwig [a]

[a] Chair of Modelling and Simulation of Metallurgical Processes, Montanuniversitaet Leoben, Austria
[b] Christian Doppler Lab for Advanced Simulation of Solidification and Melting, Montanuniversitaet Leoben, Austria

ARTICLE INFO

Article history:
Received 22 April 2016
Received in revised form 14 July 2016
Accepted 16 July 2016
Available online 6 August 2016

Keywords:
Macrosegregation
Columnar solidification
Thermo-solutal convection

ABSTRACT

Macrosegregation in a casting is caused by different flow and crystal movement phenomena during solidification. In order to get basic understanding of the macrosegregation mechanisms, 8 simple test cases of a 2D casting ($50 \times 60\ \mathrm{mm}^2$) with unidirectional cooling from either top or bottom were configured and calculated by using a volume-average based three-phase solidification model (Wu and Ludwig, 2006). Two different alloys were considered: Sn-10 wt.%Pb with solute element Pb heavier than the solvent Sn; Pb-18 wt.%Sn with solute element Sn lighter than the solvent Pb. The work is presented in two parts. Part I (this paper) presents 4 cases of pure columnar solidification. Direction of the thermal-solutal buoyancy force of the interdendritic melt can be estimated according to the alloy (Sn-10 wt.%Pb or Pb-18 wt.% Sn); and the possible flow pattern can also be estimated when the solidification direction (upwards or downwards) is known. As consequence, the macrosegregation tendency should be estimated as well. However, the modelling results show that complicated details of macrosegregation distribution can develop due to the complexity of the transient flow. Other 4 cases of equiaxed solidification will be presented as Part II in next paper.

1. Introduction

Understanding the formation of macrosegregation in castings has been, and it remains to be, an important topic in the solidification researches [1,2]. It is also one of the key topics in the annual "solidification course", as held in Les Diablerets, Swiss Federal Institute of Technology of Lausanne (EPFL), Switzerland. The one-week course is designed for engineers and scientists who wish to improve their knowledge in the field of solidification. 8 simple test cases of a 2D casting with unidirectional cooling from either top or bottom, as shown in Fig. 1 [3,4], were taken as exercises for the course-participants to test their knowledge about macrosegregation. In principle, if the directions of buoyancy force and crystal sedimentation are known, one can estimate the possible macrosegregation tendency. The current work is to simulate these 8 cases numerically. One purpose is to confirm the knowledge. A more important purpose is to demonstrate the potential complexity of the macrosegregation phenomena. Macrosegregation occurring in these simple test cases are sometimes beyond the knowledge.

Macrosegregation is mainly caused by different melt flow [1,2,5–9] and crystal sedimentation [10–13] phenomena. In some cases the solid dendrite deformation in the mush region [6,14], the exudation of interdendritic melt close to the casting surface [15,16], and even the macroscopic solute diffusion in the interdendritic melt can also cause macrosegregation [17,18]. The macroscopic diffusion induced macrosegregation is very weak [19]. In order to simulate macrosegregation different solidification models by considering the above multiphase transport phenomena were developed. The continuum model [20–24] was the earliest one. It treats the mushy zone as a solid-liquid mixture, and conservation equations (mass, momentum, energy and species) for both liquid and solid phases are merged to form a set of mixture conservation equations, i.e. the concerned liquid and solid phases are simplified as one phase mixture. In the early 1990s the group of Beckermann developed multiphase solidification models based on Eulerian-Eulerian volume-average approach [10,25,26]. Conservation of mass, momentum, energy and species for each phase (liquid, equiaxed and/or columnar) are considered separately. Interactions between the phases are treated and the conservation equations are solved in a coupled manner. This work was recently extended by Wu et al. [11,12,27–38] and Leriche et al. [39]. A series of multiphase volume-average solidification models were proposed.

---

* Corresponding author at: Chair of Modelling and Simulation of Metallurgical Processes, Montanuniversitaet Leoben, Austria.

E-mail address: menghuai.wu@unileoben.ac.at (M. Wu).

http://dx.doi.org/10.1016/j.commatsci.2016.07.017

Nomenclature

c_0	initial concentration, (1)
c_ℓ, c_c	species concentration, (1)
c^{ref}	reference concentration, (1)
c_{eu}	eutectic concentration, (1)
c_ℓ^*, c_c^*	equilibrium concentration at interface, (1)
$C_{\ell c}^{p}$	species exchange between liquid and columnar, ($kg{\cdot}m^{-3}{\cdot}s^{-1}$)
c^{index}	macrosegregation index, (%)
c_{mix}	mix concentration, (1)
c_p^ℓ, c_p^c	specific heat, ($J{\cdot}kg^{-1}{\cdot}K^{-1}$)
D_ℓ, D_c	diffusion coefficient, ($m^2{\cdot}s^{-1}$)
d_c	columnar trunk diameter, (m)
f_ℓ, f_c	volume fraction of different phases, (1)
$\vec{g}$	gravity, ($m{\cdot}s^{-2}$)
$\vec{g}'_\ell$	reduced gravity, ($m{\cdot}s^{-2}$)
h	heat transfer coefficient, ($W{\cdot}m^{-2}{\cdot}K^{-1}$)
H^*	volume heat transfer coefficient between phases, ($W{\cdot}m^{-3}{\cdot}K^{-1}$)
h_ℓ, h_c	enthalpy, ($J{\cdot}kg^{-1}$)
h_ℓ^{ref}, h_c^{ref}	reference enthalpy, ($J{\cdot}kg^{-1}$)
Δh	latent heat, ($J{\cdot}kg^{-1}$)
K	permeability of liquid in porous medium, (m^2)
k	solute partitioning coefficient at the liquid solid interface, (1)
k_ℓ, k_c	thermal conductivity, ($W{\cdot}m^{-1}{\cdot}K^{-1}$)
l	actual columnar length in tip cell, (m)
$M_{\ell c}(= -M_{c\ell})$	liquid-columnar net mass transfer rate, ($kg{\cdot}m^{-3}{\cdot}s^{-1}$)
m	slope of liquidus in phase diagram, (K)
p	pressure, ($N{\cdot}m^{-2}$)
$Q_{\ell c}(= -Q_{c\ell})$	total energy exchange between liquid and columnar phases, ($J{\cdot}m^{-3}{\cdot}s^{-1}$)
$Q_{\ell c}^{d}(= -Q_{c\ell}^{d})$	energy transfer between liquid and columnar phases, ($J{\cdot}m^{-3}{\cdot}s^{-1}$)
$Q_{\ell c}^{p}(= -Q_{c\ell}^{p})$	energy exchange due to phase change between liquid and columnar phases, ($J{\cdot}m^{-3}{\cdot}s^{-1}$)
R_{tip}	primary dendrite tip radius, (m)

R_c	columnar radius, (m)
$R_{f,c}$	maximum radius of columnar trunk, (m)
T_0	initial temperature, (K)
T, T_ℓ, T_c	temperature, (K)
T_f	melting point of solvent at $c_0 = 0$, (K)
T_{ref}	reference temperature for enthalpy definition, (K)
T_{eu}	eutectic temperature, (K)
T_{liq}	liquidus temperature, (K)
T_{EXT}	external temperature, (K)
ΔT	constitutional undercooling, (K)
t	time, (s)
Δt	time step, (s)
$\vec{U}_{\ell c}(= -\vec{U}_{c\ell})$	total liquid-columnar momentum exchange rate, ($kg\ m^{-2}s^{-2}$)
$\vec{U}_{\ell c}^{d}(= -\vec{U}_{c\ell}^{d})$	liquid-columnar momentum change due to drag force, ($kg{\cdot}m^{-2}{\cdot}s^{-2}$)
$\vec{U}_{\ell c}^{p}(= -\vec{U}_{c\ell}^{p})$	liquid-columnar momentum exchange due to phase change, ($kg{\cdot}m^{-2}{\cdot}s^{-2}$)
$\vec{u}_\ell$	velocity vector, ($m{\cdot}s^{-1}$)
v_{Rc}	growth speed in radius direction for columnar, ($m{\cdot}s^{-1}$)
v_{tip}	growth speed in tip direction, ($m{\cdot}s^{-1}$)
V_{domain}	volume of the calculated domain, (m^3)
β_T	thermal expansion coefficient, (K^{-1})
β_c	solutal expansion coefficient, (1)
Γ	Gibbs Thomson coefficient, ($m{\cdot}K$)
λ_1	primary columnar arm space, (m)
μ_ℓ	viscosity, ($kg{\cdot}m^{-1}{\cdot}s^{-1}$)
ρ_ℓ, ρ_c	density, ($kg{\cdot}m^{-3}$)
ρ_{ref}	reference density, ($kg{\cdot}m^{-3}$)
ρ_ℓ^{b}	density for buoyancy force, ($kg{\cdot}m^{-3}$)
$\bar{\bar{\tau}}_\ell$	stress-strain tensors, ($kg{\cdot}m^{-1}{\cdot}s^{-1}$)

Subscripts

ℓ	mark liquid
c	columnar phases

The numerical model used for the current work is based on a three phase mixed columnar-equiaxed solidification model as developed by Wu and Ludwig [28,29,37,38]. Conception of test cases of Fig. 1 comes from the exercises of the "solidification course" at EPFL [3,4]. The geometry, alloys and most of material properties are taken from a numerical benchmark as suggested by Bellet et al. [40], but the thermal boundary conditions are set differently. The test cases of Fig. 1 are cooled either from bottom or from top, while the benchmark of the Ref. [40] is cooled from a side wall. Studies, based on the similar benchmark as cooled from a side wall, are many, both numerically [35,36,41,42] and experimentally [43,44], but they focused on the formation of channel segregation. The simple design of the test cases (Fig. 1) is to minimize the complexity of macrosegregation for a learning purpose. The current work is presented in two parts. Part I (this paper) presents the 4 cases of pure columnar solidification. The other 4 cases of equiaxed solidification will be presented as Part II in next paper.

2. Numerical model and simulation settings

Model details can be found in previous publications [28,29,37,38]. Here, only two phases, liquid and columnar, are considered. The functionalities of the model for the nucleation and growth of equiaxed phase are "switched off". A brief outline of the model and main assumptions are described below. Conservation equations, source and exchange terms, and some auxiliary equations are summarized in Table 1.

(1) The two phases are the liquid melt and the solid columnar dendrite trunks.
(2) The morphology of the columnar dendrite trunks is approximated by step-wise growing cylinders positioned in a staggered arrangement with constant primary dendritic arm spacing, λ_1.
(3) The columnar trunks grow from the casting surface when constitutional undercooling develops and the columnar tip is tracked applying the LGK model [45,46].
(4) The liquid-to-solid mass transfer (solidification/melting) rate, $M_{\ell c}$, is calculated as a function of the growth velocity of the columnar trunks, v_{R_c}, which is governed by diffusion of the solute in the interdendritic melt around each cylindrical trunk.
(5) Thermodynamic equilibrium is assumed at the liquid-solid interface, which determines the interface concentrations (c_ℓ^*, c_c^*). Back diffusion in solid is neglected ($D_c = 0$). The concentration difference ($c_\ell^* - c_\ell$) is the driving force for the growth of columnar trunks.

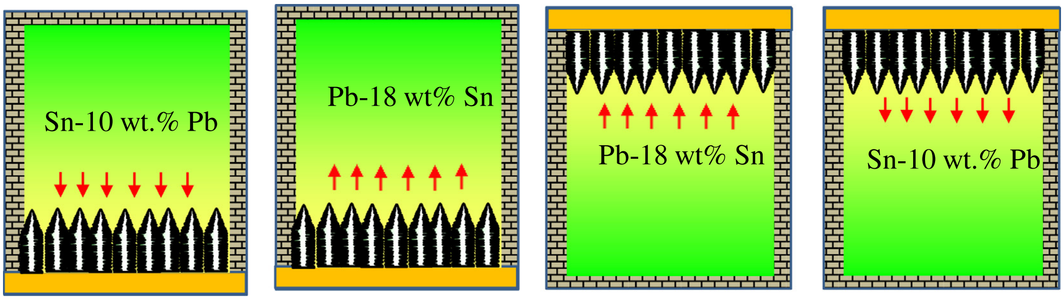

(a) Case C1 (b) Case C2 (c) Case C3 (d) Case C4

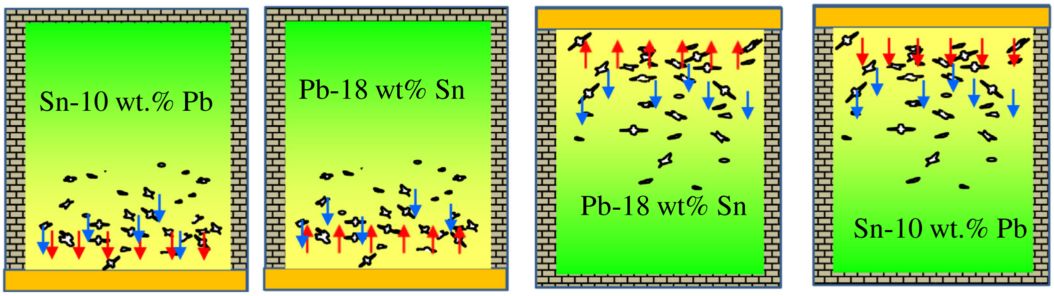

(e) Case E1 (f) Case E2 (g) Case E3 (h) Case E4

Fig. 1. Schematics of columnar (upper row) and equiaxed (lower row) solidification, solutal buoyancy force direction (red arrows) of the interdendritic/intergranular melt, and crystal sedimentation direction (blue arrows) of the equiaxed grains. 8 cases are defined. Two different alloys were considered: Sn-10 wt.%Pb with solute element Pb heavier than the solvent Sn; Pb-18 wt.%Sn with solute element Sn lighter than the solvent Pb. Color gradient indicates the distribution of solute element in the melt: yellow for enrichment, green as the nominal composition. The yellow walls indicate chilled walls, while the hatched ones are adiabatic. Cases C1, C2, E1 and E2 are cooled from bottom, while other 4 cases are cooled from top. (For interpretation of the references to color in this figure legend, the reader is referred to the web version of this article.)

(6) Volume-averaged concentrations for each phase (c_ℓ, c_c) are solved by global species conservation equations. A macrosegregation index (c^{index}) based on the phase-mixture concentration (c_{mix}) is defined by Eqs. (14) and (15). The quantity of c^{index} is presented in %. Additionally, a global macrosegregation intensity (GMI) is defined by Eq. (16) to evaluate the global segregation severity.

(7) A linearized binary Sn-Pb phase diagram with a constant solute partitioning coefficient k and a constant liquidus slope m is used.

(8) Interdendritic flow resistance in the mushy zone is calculated via a permeability law according to the Blake-Kozeny approach [47].

(9) Solidification shrinkage is not accounted for and we assume $\rho_\ell = \rho_c$. Thermo-solutal convection of the liquid melt is modelled with the Boussinesq approximation. The solid columnar phase is considered to be rigid and stationary.

The configuration of the test cases in 2D is shown in Fig. 2. The geometry, alloys and most of material properties are taken from a numerical benchmark as suggested by Bellet et al. [40]. Only half of the casting domain is calculated by setting a symmetry plane at the left boundary. Two different alloys (Fig. 3) were considered: one is Sn-10 wt.%Pb with solute element Pb heavier than the solvent Sn; the other is Pb-18 wt.%Sn with solute element Sn lighter than the solvent Pb. The materials chosen for these simulations have advantages of relatively simple phase diagram and well known properties, as well as a large temperature interval in the two-phase region during solidification and a large density difference between components. Both of the latter two characteristics enhance macrosegregation [19]. Thermodynamic data and thermal physical properties of both alloys are available, as listed in Table 2. The benchmark is cooled unidirectionally, either from bottom or from top. Therefore, 4 cases of calculations are defined and they are correspondent to the 4 cases in the upper row of Fig. 1.

The model is implemented in ANSYS FLUENT, version 14.5 [51]. Although FLUENT formulation is implicit and theoretically there is no stability criterion to be met in determining the time step Δt, the time steps used impact the accuracy of the numerical results. Due to the complexity of the coupling, there is no formulation to determine the optimal Δt. For each time step, 60 iterations are adopted to decrease the scaled residual of concentration, flow quantities and pressure below 10^{-4} and enthalpy quantities below 10^{-7}. The scaled residual [51] is the sum of the imbalance in the discretized conservation equations over all computational cells (volume elements), $\sum_{\text{cells},P}|\sum_{\text{nb}} a_{\text{nb}}\phi_{\text{nb}} + b - a_P\phi_P|$, being normalized by a scaling factor, $\sum_{\text{cells},P}|a_P\phi_P|$. Here ϕ_P and ϕ_{nb} are values of a general variable ϕ at a cell P and neighbor cells nb, a_P is the center coefficient, a_{nb} are the influence coefficients for the neighboring cells, and b is the contribution of the constant part of the source term. Mesh size is 10^{-3} m, and initial Δt is 10^{-3} s. In order to enhance the calculation efficiency, Δt can be gradually and manually increased to 0.01 s during the late stage of solidification. One case simulation takes 2 days to complete on a high performance cluster (2.6 GHz, 8 Cores).

3. Modelling results

3.1. Case C1

This case (Fig. 1(a)) considers the solidification of Sn-10 wt.%Pb alloy from the bottom. A solidification sequence, as indicated by isolines of f_c, and the evolution of macrosegregation (c^{index}) in color are shown in Fig. 4. The solidification progresses smoothly and unidirectionally. Both the thermal and solutal buoyancy forces of the liquid melt act in the direction against the solidification direction, hence no flow occurs. However, a very weak macrosegregation still occurs at the bottom and top surface. At the bottom the maximum negative segregation (c^{index}) is −3.5%, while at the top positive

Table 1
Conservation equations, source and exchange terms, auxiliary equations.

Conservation equations			
Mass	$\frac{\partial}{\partial t}(f_\ell \rho_\ell) + \nabla \cdot (f_\ell \rho_\ell \vec{u}_\ell) = -M_{\ell c}$ $\frac{\partial}{\partial t}(f_c \rho_c) = M_{\ell c}$		(1)
Momentum	$\frac{\partial}{\partial t}(f_\ell \rho_\ell \vec{u}_\ell) + \nabla \cdot (f_\ell \rho_\ell \vec{u}_\ell \otimes \vec{u}_\ell) = -f_\ell \nabla p + \nabla \cdot \bar{\bar{\tau}}_\ell + f_\ell \rho_\ell \vec{g}'_\ell - \vec{U}_{\ell c}$ with $\vec{g}'_\ell = \frac{\rho^b_\ell(T,c) - \rho_\ell}{\rho_\ell} \vec{g}$, $\rho^b_\ell(T,c) = \rho_\ell \cdot [1 + \beta_T \cdot (T^{ref} - T_\ell) + \beta_c \cdot (c^{ref} - c_\ell)]$, where $\vec{U}_{\ell c} = \vec{U}^p_{\ell c} + \vec{U}^d_{\ell c}$		(2)
Species	$\frac{\partial}{\partial t}(f_\ell \rho_\ell c_\ell) + \nabla \cdot (f_\ell \rho_\ell \vec{u}_\ell c_\ell) = \nabla \cdot (f_\ell \rho_\ell D_\ell \nabla c_\ell) - C^p_{\ell c}$ $\frac{\partial}{\partial t}(f_c \rho_c c_c) = \nabla \cdot (f_c \rho_c D_c \nabla c_\ell) + C^p_{\ell c}$		(3)
Enthalpy	$\frac{\partial}{\partial t}(f_\ell \rho_\ell h_\ell) + \nabla \cdot (f_\ell \rho_\ell \vec{u}_\ell h_\ell) = \nabla \cdot (f_\ell k_\ell \nabla \cdot T_\ell) - Q_{\ell c}$ $\frac{\partial}{\partial t}(f_c \rho_c h_c) = \nabla \cdot (f_c k_c \nabla \cdot T_c) + Q_{\ell c}$ with $Q_{\ell c} = Q^p_{\ell c} + Q^d_{\ell c}$, $h_\ell = \int_{T_{ref}}^{T_\ell} c^\ell_p dT + h^{ref}_\ell$, $h_c = \int_{T_{ref}}^{T_e} c^c_p dT + h^{ref}_c$, $L = h^{ref}_\ell - h^{ref}_c$		(4)
Solidification net mass transfer			
Mass transfer	$M_{\ell c} = v_{R_c} \cdot S_A \cdot \rho_c \cdot \Phi_{imp}$ for trunks $M_{\ell c} = v_{R_c} \cdot n_c \cdot (\pi d_c \cdot l) \cdot \rho_\ell \cdot \Phi_{imp} + v_{tip} \cdot n_c \cdot (\pi R^2_{tip}) \cdot \rho_\ell \cdot \Phi_{imp}$ for trunks incl. col. tip		(5)
Col. trunk growth velocity	$v_{R_c} = \frac{dR_c}{dt} = \frac{D_\ell}{R_c} \cdot \frac{(c^*_\ell - c_\ell)}{(c^*_\ell - c^*_c)} \cdot \ln^{-1}\left(\frac{R_{f,c}}{R_c}\right)$		(6)
Diameter of col. trunks	$d_c (= 2R_c) = \lambda_1 \cdot \sqrt{\frac{\sqrt{12} \cdot f_c}{\pi}}$		(7)
Far field radius of col. trunks	$R_f = \frac{1}{\sqrt{3}} \cdot \lambda_1$		(8)
Col. surface concentration	$S_A = \frac{d_c \cdot \pi}{\lambda_1^2}$		(9)
Growing surface impingement	$\Phi_{imp} = \begin{cases} 1 & d_c \leqslant \lambda_1 \\ 2\sqrt{3} \cdot f_\ell / (2\sqrt{3} - \pi) & d_c > \lambda_1 \end{cases}$		(10)
Source and exchange terms			
Momentum transfer	$\vec{U}^p_{\ell c} = \vec{u}_\ell \cdot M_{\ell c}$	$\vec{U}^d_{\ell c} = \frac{f_\ell^2 \cdot \mu_\ell}{K} \cdot \vec{u}_\ell$ where $K = 6 \times 10^{-4} \cdot \lambda_1^2 \cdot \frac{f_\ell^3}{(1-f_\ell)^2}$	(11)
Species transfer	$C^p_{\ell c} = k \cdot c^*_\ell \cdot M_{\ell c}$		(12)
Enthalpy transfer and latent heat	$Q^p_{\ell c} = h_\ell \cdot M_{\ell c}$	$Q^d_{\ell c} = H^* \cdot (T_\ell - T_c)$ where $H^* = 10^9 \text{ W m}^{-2} \text{ K}^{-1}$	(13)
Auxiliary equation			
Mixture concentration	$c_{mix} = (c_\ell \cdot \rho_\ell \cdot f_\ell + c_c \cdot \rho_c \cdot f_c)/(\rho_\ell \cdot f_\ell + \rho_c \cdot f_c)$		(14)
Macrosegregation index	$c^{index} = \frac{c_{mix} - c_0}{c_0} \times 100$		(15)
Global macroseg. intensity (GMI)	$GMI = \frac{1}{V_{domain}} \cdot \iiint_{V_{domain}} \lvert c^{index} \rvert dV$		(16)

segregation (c^{index}) reaches a maximum of 0.64%. The reason for this is due to macroscopic interdendritic solute diffusion. As the schematic (insert) of Fig. 1(a) shows, the interdendritic melt is enriched with solute element (Pb), and there exists a relatively strong concentration gradient in the mushy zone. This solute concentration gradient invokes solute diffusion from the surface towards inner regions, causing a mini layer of negative segregation at the bottom surface where solidification starts. The same mechanism operates at the end of solidification when the solidification front reaches the top surface, and the solute diffusion towards the top surface leads to the formation of a positive segregation layer there. In order to prove this hypothesis an additional numerical calculation is made for the same case C1, but the solute diffusion coefficient is intentionally chosen as a very small value, $D_\ell = 1.0 \times 10^{20} \text{m}^2 \cdot \text{s}^{-1}$, instead of the physical value of $4.5 \times 10^{-9} \text{m}^2 \cdot \text{s}^{-1}$. As expected these mini surface segregation layers vanish.

This segregation mechanism was firstly reported by Schneider and Beckermann [17], and further verified by Thevik and Mo [18]. The surface segregation layer is extremely narrow, in a magnitude of 100 μm, and the segregation in this layer is very weak. If other flow mechanisms, e.g. shrinkage induced flow and thermo-solutal convection, are involved, this macroscopic diffusion induced surface segregation will be easily overwelmed by other flow effects [19].

3.2. Case C2

This case (Fig. 1(b)) considers an alloy of Pb-18 wt.%Sn, where the solute element Sn is lighter than the solvent Pb. Although thermal buoyancy is always in the same direction as gravity, i.e. against the solidification direction to keep the melt in the mushy zone, the solute enriched interdendritic melt tends to rise, and provokes melt flow. The solutal buoyancy overweighs the thermal buoyancy when solidification starts. A solidification sequence, with melt flow and induced macrosegregation are shown in Fig. 5. Although the global solidification sequence is unidirectional, the temperature field and the contour of fraction solid f_c are obviously disturbed by the flow. The flow pattern is very transient, some vortex develops dynamically. The flow velocities are in the order of 10^{-3} m/s, but it can reach a maximum of 10^{-2} m/s occationally. This kind of flow pattern continuously brings solute enriched melt out of the interdendritic region, and mixed with bulk melt. The bulk melt in the upper part is gradually enriched with the solute, and it leads to the formation of a large positive segregation zone in the upper region. As balance, a large negative segregation zone forms in the lower part. At 300 s, the local macrosegregation index falls in a range of −39.0 to 62.0%. This range is adapted to −38.0 to 124.0% at the end of solidification. The diffusion induced surface segregation at the top and bottom surfaces should occur as well, but its

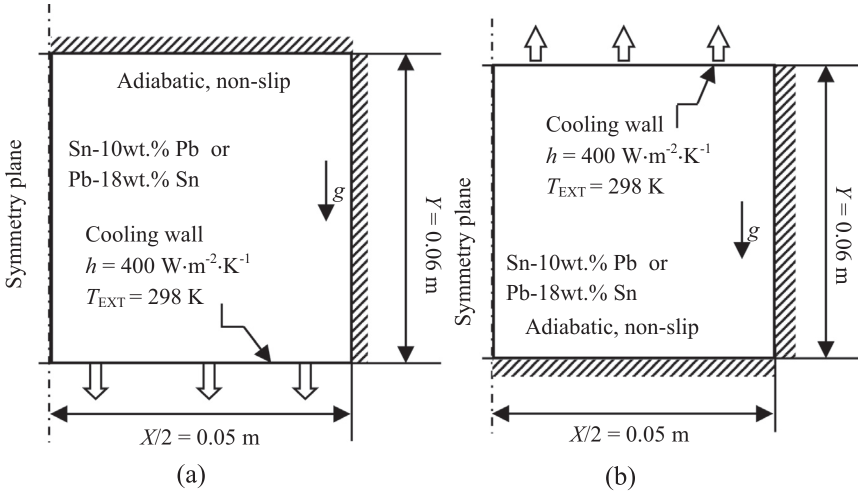

(a) (b)

Fig. 2. Geometry of test cases with boundary and initial conditions.

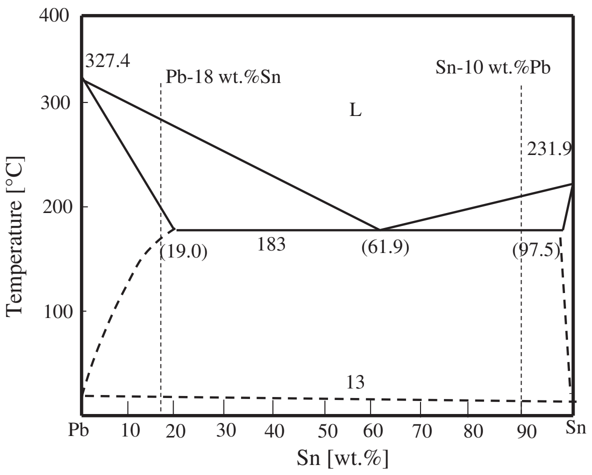

Fig. 3. Phase diagram of Pb-Sn binary alloy system.

magnitude is so small that it is almost undetectable in the presence of convection-induced segregation.

One interesting phenomenon is that positive segregation channels are developed along both side boundaries, i.e. symmetry plane (left) and adiabatic and non-slop wall (right). The segregation intensity and patterns along both left and right boundaries are similar. The symmetry plane here is actually consistent with an adiabatic and free-slip wall. It seems that non-slip and free-slip boundary conditions play a similar role. By analyzing the flow fields of Fig. 5(c.1)–(c.4), we find that the flow pattern is largely confined by the domain boundaries. The interdendritic melt near the side boundaries is difficult to be brought out of the mushy region, and the solidification is retarded, hence channels form there.

It is observed that the dynamic flow pattern tends to build some local compositional heterogeneity (strip-like structure, or mini channel segregates) in the inner part of the benchmark, as seen in Fig. 5(d.1)–(d.4). Those segregation structures are not stable, and they survive only temporarily. Depending on the change of

Table 2
Material properties and other parameters.

	Symbol	Units	Sn-10 wt.%Pb	Pb-18 wt.%Sn	Ref.
Nominal concentration	c_0	–	10.0 wt.% Pb	18.0 wt.% Sn	
Liquidus temperature	T_{liq}	K	492.14	558.63	[40]
Melting point of solvent at $c_0 = 0$	T_{f}	K	505	600.65	[40]
Eutectic composition	c_{eu}	wt.%	38.1	61.9	[40]
Eutectic temperature	T_{eu}	K	456	456	[41]
Liquidus slope	m	K (wt.%)$^{-1}$	-1.286	-2.334	[40]
Equilibrium partition coefficient	k	–	0.0656	0.310	[40]
Reference density	ρ_{ref}	kg·m^{-3}	7000	9250	[40]
Specific heat	c_{p}^{ℓ}, $c_{\mathrm{p}}^{\mathrm{c}}$	J·kg^{-1}·K^{-1}	260	176	[40]
Thermal conductivity	k_{ℓ}, k_{c}	W·m^{-1}·K^{-1}	55.0	17.9	[40]
Latent heat	Δh_{f}	J·kg^{-1}	6.1×10^{4}	3.76×10^{4}	[40]
Viscosity	μ_{ℓ}	kg·m^{-1} s^{-1}	1.0×10^{-3}	1.1×10^{-3}	[40]
Liquid thermal expansion coefficient	β_{T}	K^{-1}	6.0×10^{-5}	1.16×10^{-4}	[40]
Liquid solutal expansion coefficient	β_{C}	wt.%$^{-1}$	-5.3×10^{-3}	4.9×10^{-3}	[40]
Primary dendritic arm spacing	λ_1	m	1.3×10^{-3}	1.85×10^{-3}	[40]
Diffusion coefficient (solid)	D_c	m^2·s^{-1}	1.0×10^{-12}	1.0×10^{-12}	[48]
Diffusion coefficient (liquid)	D_{ℓ}	m^2·s^{-1}	4.5×10^{-9}	4.5×10^{-9}	[48]
Initial temperature	$T_0 = \mathrm{T}_{\mathrm{liq}}$	K	492.14	558.64	[40]
Heat transfer coefficient	h	W·m^{-2}·K^{-1}	400	400	[40]
External temperature	T_{EXT}	K	298	298	[40]
Density difference of solid and liquid	$\Delta\rho$	kg·m^{-3}	304	420	[49]
Gibbs Thomson coefficient	Γ	m·K	6.5×10^{-8}	7.9×10^{-8}	[50]

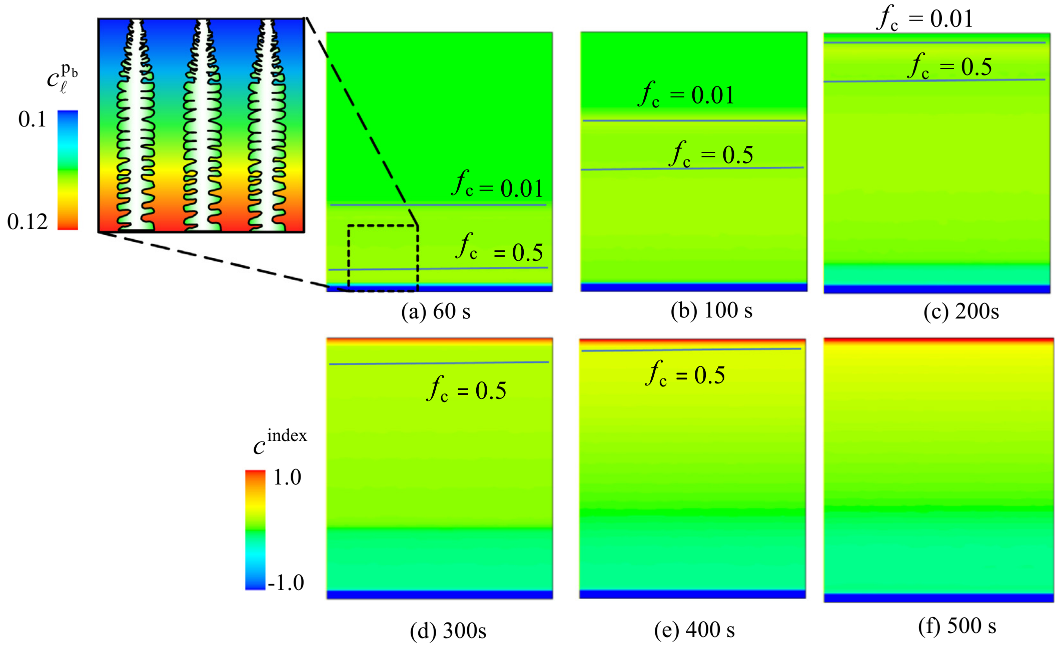

(a) 60 s (b) 100 s (c) 200s

(d) 300s (e) 400 s (f) 500 s

Fig. 4. Solidification process and macrosegregation evolution of Case C1. The contour of c^{index} (%) in color scale is overlaied with isolines $f_\ell = 0.99$ and $f_\ell = 0.5$. Alloy is Sn-10 wt.%Pb. Columnar tip front position is represented by $f_c = 0.01$. (For interpretation of the references to color in this figure legend, the reader is referred to the web version of this article.)

local flow direction, some structures appear while some others vanish. Consequence of this dynamics is that a non-uniform c^{index} distribution develops.

3.3. Case C3

In this case (Fig. 1(c)) we consider Pb-18 wt.%Sn alloy, which is unidirectionally cooled from the top. As shown in Fig. 6, solidification starts from the top surface and the solidification front moves downwards. Thermal buoyancy drives the flow initially downwards, while solute (lighter) buoyancy is in the direction against the solidification direction and tends to stabilize the flow. Although the solute buoyancy overweighs the thermal buoyancy, there still exists a weak flow (magnitude of 10^{-5} m/s) in the bulk region. At the beginning of cooling before solidification starts, the thermal buoyancy flow reaches its maximum of 10^{-3} m/s, but this flow is to a great extent suppressed by solutal buoyancy as solidification begins. Obviously, the weak flow disturbs the solidification front slightly, and it can induce a quite special pattern of macrosegregation. In the center part a positive segregation region develops, while at the right side and left side of this area depletion in solutal element and negative macrosegregation occur. The final macrosegregation intensity falls in the range of −3.96 to 1.34%, i.e. the similar range of case C1 (diffusion induced surface segregation). As shown in Fig. 6(d.1)–(d.4), a diffusion-induced negative segregation layer at the top surface and a diffusion-induced positive segregation layer at the bottom are detectable, and they are in the same range of the weak flow-induced segregation.

3.4. Case C4

In Case C4 (Fig. 1(d)) we consider an alloy of Sn-10 wt.%Pb, which cooled from the top. This case is actually quite similar to case C2, just solidifies in the opposite direction. As shown in Fig. 7, both thermal and solutal buoyancy operate in the same direction, driving the flow. Therefore, the final segregation (c^{index}) range, from −58 to 156%, is stronger than the case C2. The dynamics of flow for both cases are not identical, but similar. The final segregation distribution patterns are quite similar as well. For the analysis of case C4 we can refer to Case C2.

4. Discussion

4.1. Macrosegregation intensity by different mechanisms

Calculated macrosegregation results of 4 cases are compared in Fig. 8. The segregation distribution is shown in color scale, but its intensity is analyzed by the c^{index} distribution range as labelled in the figures and by the so-called global macrosegregation intensity (GMI). GMI, as defined by Eq. (16), is used to evaluate the global average segregation intensity, while the c^{index} distribution range is used to quantify the macrosegregation extremes.

For the columnar solidification benchmark and alloys considered in this study, there exists three mechanisms responsible for the macrosegregation: thermal buoyancy flow, solutal buoyancy flow and species diffusion at the macroscopic scale. By comparison of the two flow mechanisms, the solutal buoyancy overweighs. That is the reason why only the solutal buoyancy force direction is marked in Figs. 1 and 8 (upper raw) indicating the dominant driving force for flow. The impact of thermal and solutal buoyancies on the flow depends on the solidification direction. Therefore, it is not surprising that the final segregation pattern and segregation intensity of each case depend on the alloy and solidification direction, as can be seen in Fig. 8. The diffusion induced macrosegregation falls in a very narrow range, i.e. undetectable in comparison with flow-induced segregation. This result confirms the work of Krane et al. [19]. In the case C3, the dominant solutal buoyancy is against the solidification direction (stabilizing the interdendritic flow), but it cannot (or not possible) fully suppress the thermal buoyancy. Therefore, there still exists a very weak flow, which leads to minor segregation (with the intensity similar to the diffusion-induced surface segregation). If the same color scale,

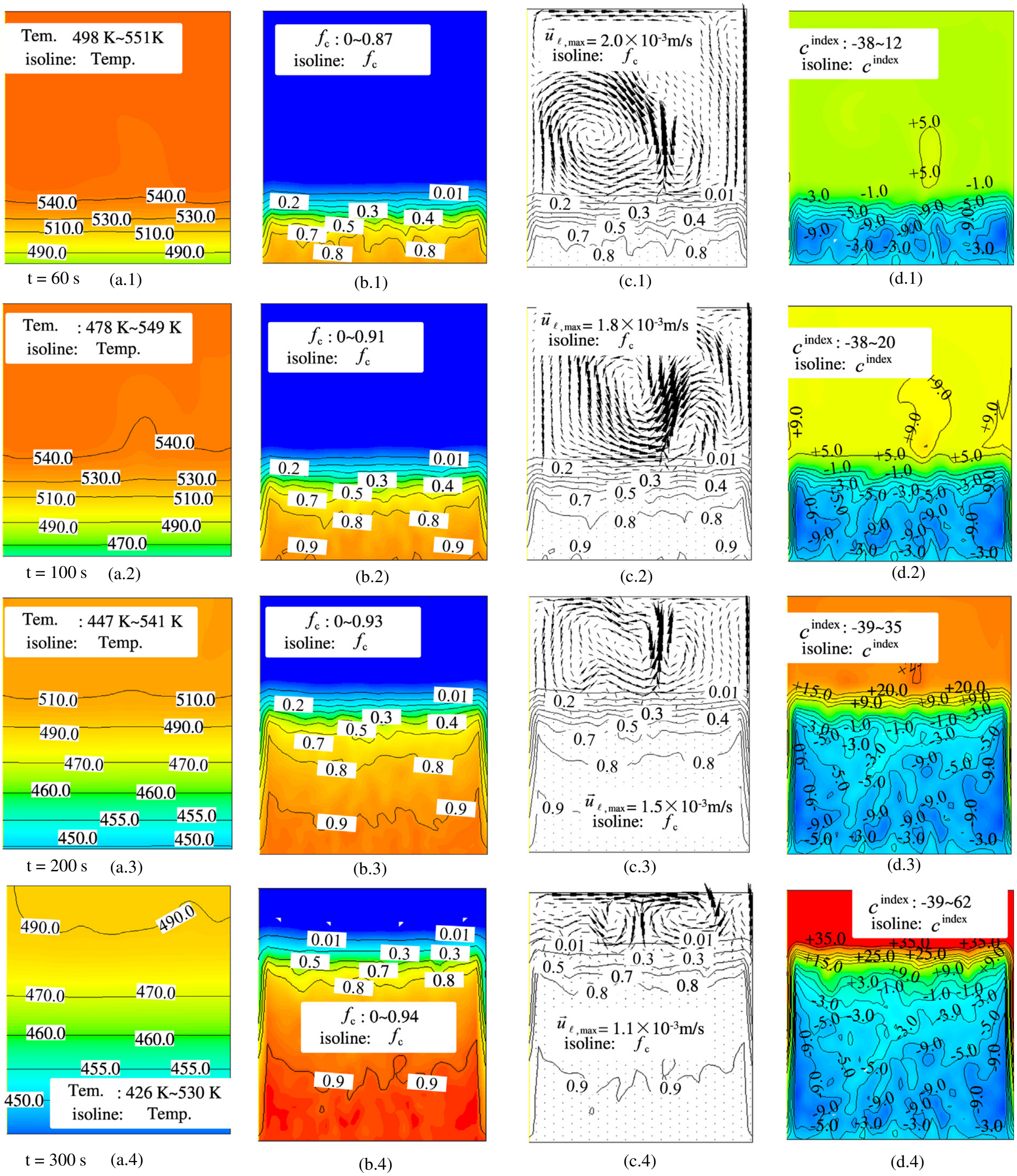

Fig. 5. Solidification sequence of Case C2 at 60, 100, 200 and 300 s. The column a.x shows the evolution of the temperature field in color scale overlaid with isolines; b.x shows contours of f_c in color scale and its isolines, and the columnar tip front position is represented by $f_c = 0.01$; c.x shows the liquid velocity ovelaid with f_c isolines; d.x shows the evolution of macrosegregation (c^{index} in %) in color scale and with isolines. The alloy is Pb-18 wt.%Sn. (For interpretation of the references to color in this figure legend, the reader is referred to the web version of this article.)

e.g. from −100 to +100 of c^{index}, were taken for all 4 cases, no segregation would be seen for the cases C1 and C3. In principle, the solutal convection induced segregation pattern can be estimated according to solutal buoyancy force in respect to the solidification direction, as from the cases C2 and C4.

Can one estimate the macrosegregation tendency based on the simple settings of each case (C1–C4) without performing any calculation? In principle, yes, one can. For example, no segregation or ignorable segregation would occur for C1 and C3; for the case C2, a positive segregation at the top and negative segregation at the bottom; for the case C4, a positive segregation at the bottom and negative segregation at the top. However, fine details of macrosegregation are hard to know. The thermo-solutal convection during solidification is highly transient (Figs. 5–7). Some vortexes evolve while others fall into decay. These transient behaviors of flow (number of vortexes, magnitude and direction of flow, lifetime of each vortex, etc.) determine the fine details of macrosegregation of Fig. 8(b)–(d). For example, in Case 2 and Case 4 the c^{index} distribution in the negative segregation region is not uniform, and some strip like macrosegregation structures are

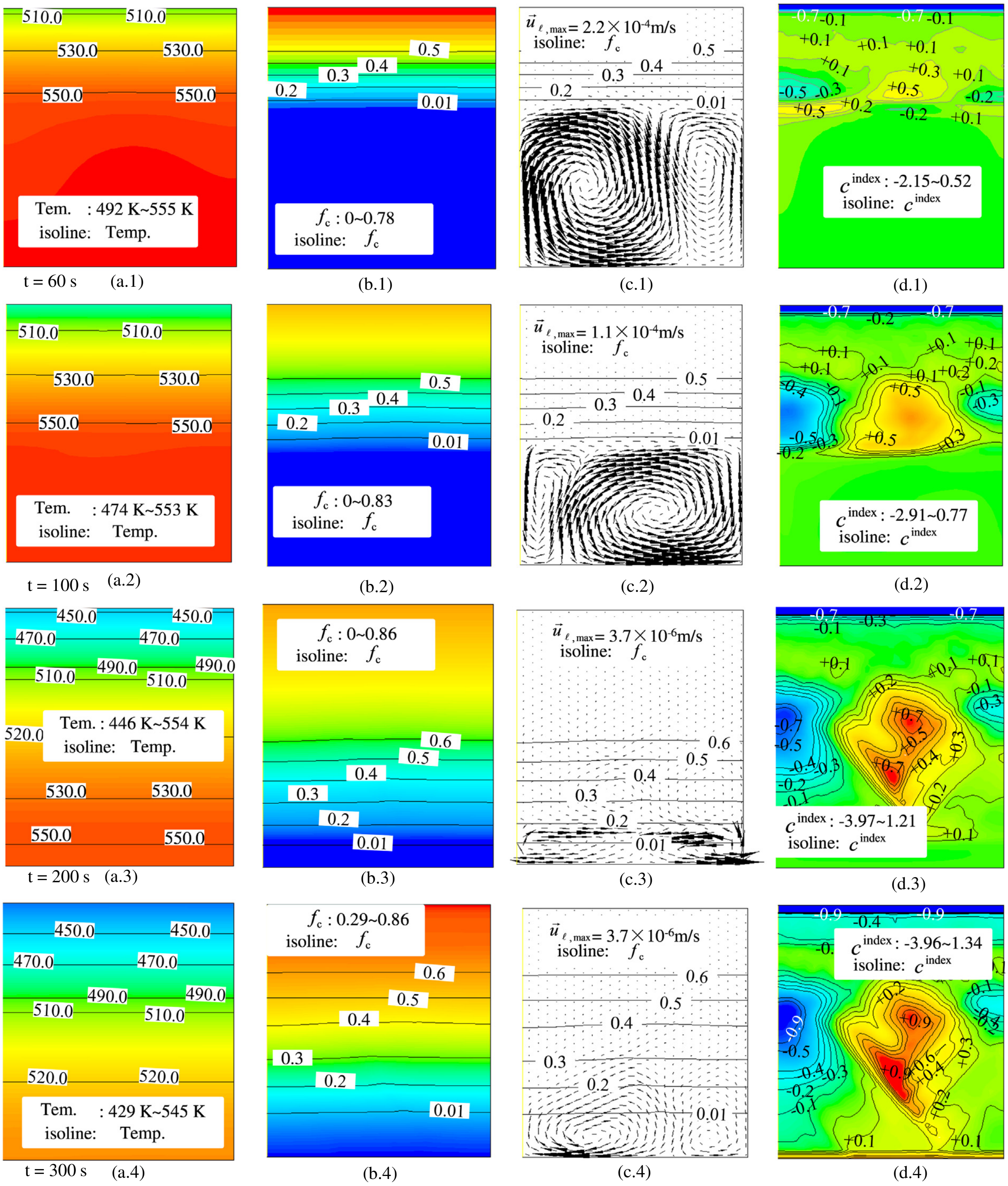

Fig. 6. Solidification sequence of Case C3 at 15, 100, 200 and 300 s. The column a.x shows the evolution of temperature field in color scale overlaid with its isolines; b.x shows contour of f_c in color scale and its isolines; c.x shows the liquid velocity ovelaid with f_c isolines, and the columnar tip front position is represented by $f_c = 0.01$; d.x shows the evolution of macrosegregation (c^{index} in %) in color scale and isolines. The alloy is Pb-18 wt.%Sn. (For interpretation of the references to color in this figure legend, the reader is referred to the web version of this article.)

observed in the negative-to-positive transition zone. In Case 3 there are an irregular shape of positive segregation zone in the middle and two negative segregation zones in both left and right sides of the test casting. The transient behaviours of flow depend not only on the solidification and buoyancy force directions, but also on many other factors such as the mushy zone thickness and morphology, cooling condition and material properties (thermal- and solutal expansion coefficients), etc.

In Case 2 and Case 3, positive segregation channels are predicted along both side boundaries, i.e. symmetry plane (left) and adiabatic wall (right). The flow is confined by the boundaries. The interdendritic melt near the side boundaries is difficult to be brought out of the mushy region, and the solidification is retarded, hence channels form there. This kind of channel segregation was often observed experimentally [52], and it was also predicted numerically by other models [53,54].

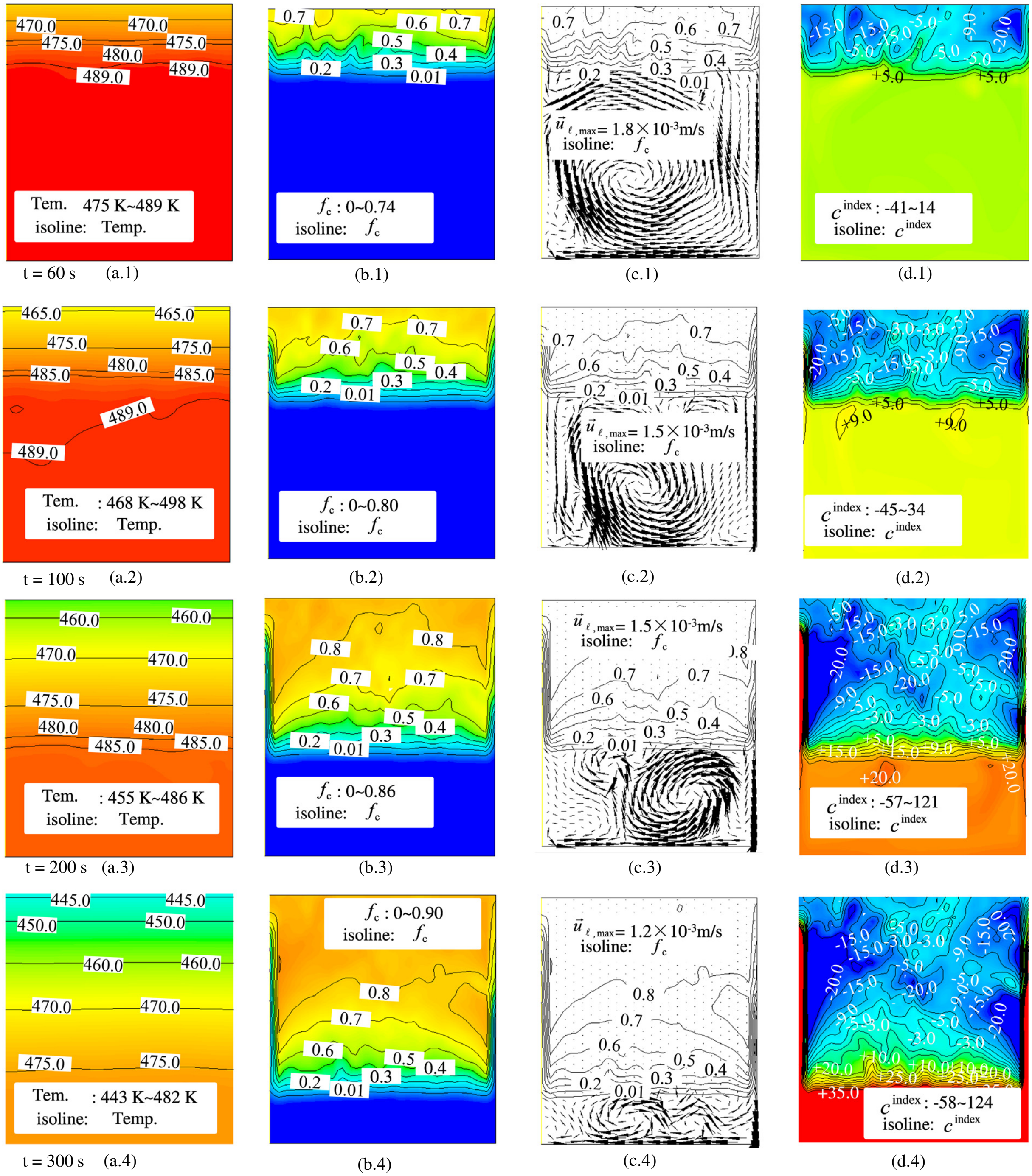

Fig. 7. Solidification sequence of Case C4 at 60, 100, 200 and 300 s. The column a.x shows the evolution of temperature field in color scale overlaid with its isolines; b.x shows contour of f_c in color scale and its isolines, and the columnar tip front position is represented by $f_c = 0.01$; c.x shows the liquid velocity ovelaid with f_c isolines; d.x shows the evolution of macrosegregation (c^{index} in %) in color scale and isolines. The alloy is Sn-10 wt.%Pb. (For interpretation of the references to color in this figure legend, the reader is referred to the web version of this article.)

The macrosegregation intensity (severity) is found to be closely related to the velocity magnitude of the flow. When the velocity is very small ($\sim 10^{-5}$ m/s), the macrosegregation will fall into the same range of diffusion-induced surface segregation, i.e. $|c^{\text{index}}| < 4$ or GMI < 0.1. Case 3 is one example for that. When the velocity magnitude is in the order of 10^{-2} m/s, such as in Case C2 and Case C4, the macrosegregation can reach as high as $|c^{\text{index}}| > 100$ (or GMI > 30).

4.2. Convection-induced macrosegregation

Convection-induced macrosegregation during columnar solidification can be analyzed according to the flow-solidification interaction [55]. It can be described by:

$$\frac{\partial}{\partial t} c_{\text{mix}} = -f_\ell \vec{u}_\ell \cdot \nabla c_\ell. \qquad (17)$$

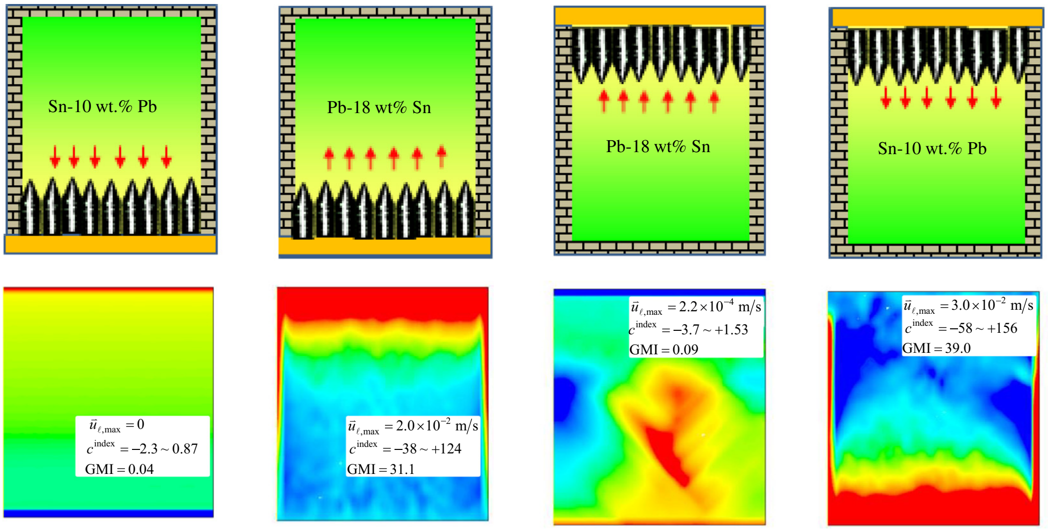

(a) Case C1 (b) Case C2 (c) Case C3 (d) Case C4

Fig. 8. Comparison of the final macrosegregation patterns among 4 cases. The segregation (c^{index} in %) contours are shown in color (low row) with different distribution ranges. The maximum flow velocity during solidification and the global macrosegregation intensity (GMI), are also given. The yellow walls indicate chilled walls, while the hatched ones are adiabatic. (For interpretation of the references to color in this figure legend, the reader is referred to the web version of this article.)

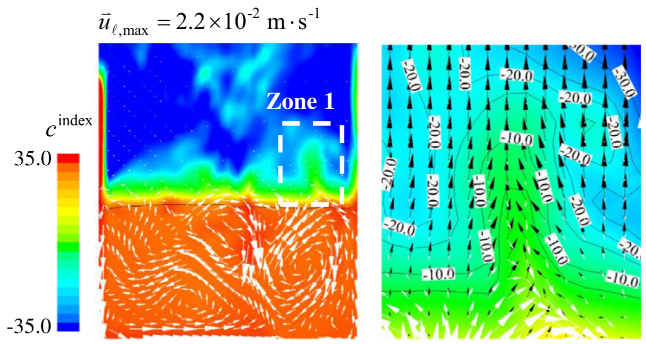

(a) (b)

Fig. 9. Solidification of Case C4 ($t = 50$ s): Sn-10 wt.%Pb cooling from top. (a) Macrosegregation contour (c^{index} in %) overlaid by liquid velocity vectors (white); (b) zoom-in view of Zone 1, where the direction of ∇c_ℓ is also shown by black vectors.

Variation of the local mixture concentration, c_{mix}, is caused by the flow, $\vec{u}_\ell$, of melt in a region where a solute concentration gradient, ∇c_ℓ, exists. In the solidifying mushy zone there exists a strong ∇c_ℓ which points against the solidification direction (for the case of solute partition coefficient k less than 1). According to Eq. (17), an interdendritic flow with its velocity direction pointing towards ∇c_ℓ direction (against the solidification direction) leads to a reduction of c_{mix}, i.e. formation of negative segregation. In another words, a flow against the solidification direction will transport the solute-lean melt to a region to replace the solute-rich melt, hence to cause the reduction of the mixture concentration c_{mix} of the region. Actually the local solidification will accelerate in this scenario. An opposite flow direction, i.e. flow in the solidification direction, leads to formation of positive segregation, and the local solidification will retard. Or to say, the flow in solidification direction will transport the solute-rich melt to a region to replace the solute-lean melt, hence to cause the increase of c_{mix}. Notice that Eq. (17) is derived from the Flemings' theory [56], but it is different from the original one ($\partial c_{\text{mix}}/\partial t = -mf_\ell \vec{u}_\ell \cdot \nabla T$). The current solidification model has considered the diffusion-governed growth kinetics, while the early Flemings' model took a simple microsegregation model based on Gulliver-Scheil assumption (interdendritic melt is infinite mixing). It has been confirmed that the infinite mixing kinetics as assumed by the Gulliver-Scheil or the lever rule, which cannot properly consider the solute distribution in the interdendritic at the early stage of dendrite growth, leads to error estimation of macrosegregation [57,58].

Eq. (17) can be applied to analyze the macrosegregation mechanisms of the current test cases. An example of solidification of Case 4 at 50 s is shown in Fig. 9. Solidification direction is downward. ∇c_ℓ is generally against the solidification direction. The flow is, however, quite transient and dynamic. Just near the solidification front, some flow is following the solidification direction while some flow in other regions is against the solidification direction. Therefore, the c_{mix} distribution at the solidification front is quite non-uniform. As shown in Fig. 9(b), a zoom-in view of a region near the solidification front, the flow $\vec{u}_\ell$ and liquid solute concentration gradient ∇c_ℓ have an opposite direction, leading to formation of a positive segregate. This kind of segregation is sometimes referred to as origin of channel segregation. If the flow keeps in the same direction, i.e. in the solidification direction, the channel will continue to grow and a stable channel will develop. In the current benchmark, no stable channel inside the domain could be seen, because the flow direction changes dynamically.

4.3. Mesh sensitivity

Mesh (grid) size is an important factor influencing the accuracy of segregation calculations. As example, calculations with different mesh size (0.5–2.0 mm) for Case 4 were performed, and the final macrosegregation distributions are compared in Fig. 10. About ¾ of upper region bears negative segregation, about ¼ of the bottom region bears severe positive segregation. The global c^{index} distribution tendencies are almost the same and consistent for all cases of mesh size. In this sense, a relative coarse mesh, e.g. 2 mm, seems to be sufficient to confirm the expectation for the macrosegregation tendency.

In order to perform the quantitative evaluation of the mesh sensitivity, the c^{index} distribution range (segregation extremes $c^{\text{index}}_{\text{min}}$, $c^{\text{index}}_{\text{max}}$) and the global macrosegregation intensity (GMI) are plotted in Fig. 11 against the mesh (grid) size. GMI varies between 30 and

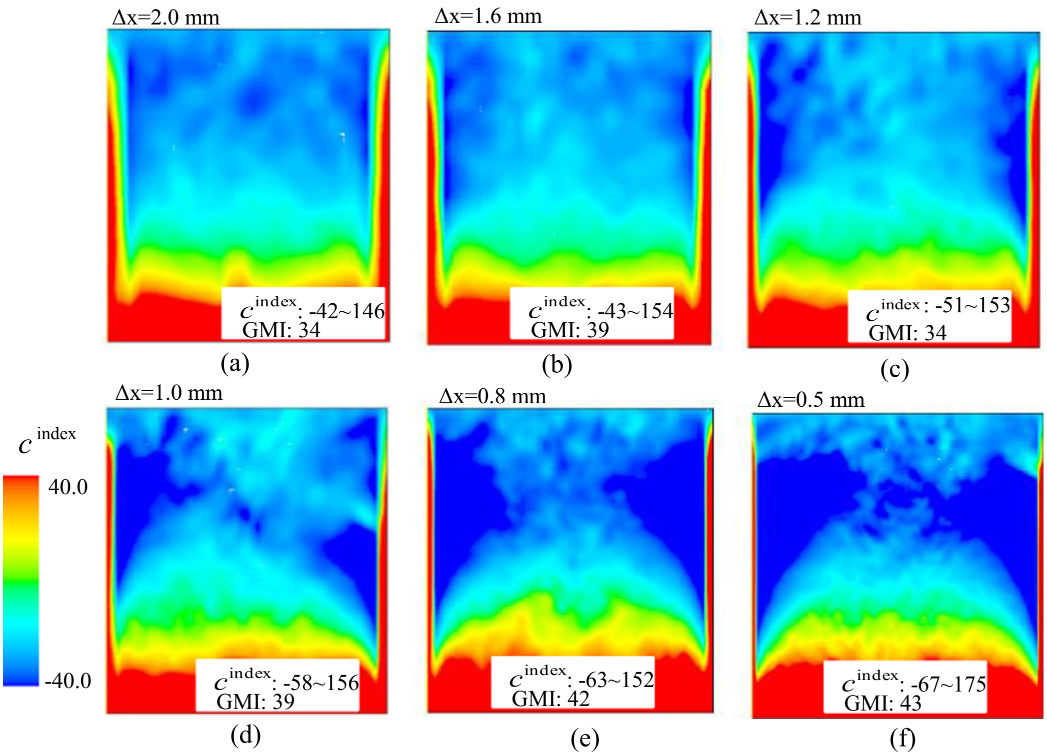

Fig. 10. Mesh sensitivity study of macrosegregation formation in Case C4. The macrosegregation contours (c^{index} in %) are shown in color scale for a mesh size of (a) 2.0 mm, (b) 1.6 mm, (c) 1.2 mm, (d) 1.0 mm, (e) 0.8 mm and (f) 0.5 mm. (For interpretation of the references to color in this figure legend, the reader is referred to the web version of this article.)

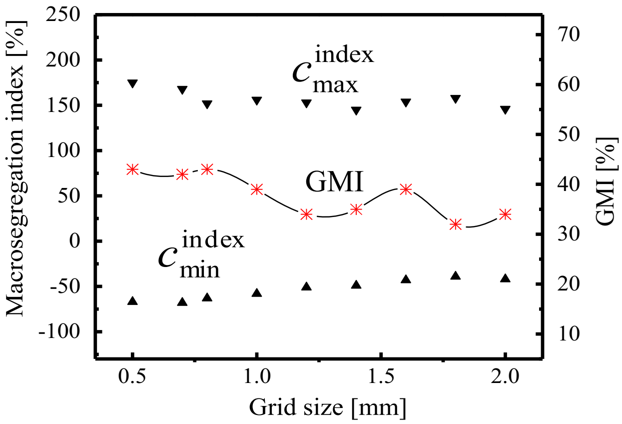

Fig. 11. Influence of mesh size on macrosegregation range (c_{min}^{index}, c_{max}^{index}) and global macrosegregation intensity (GMI) for Case C4.

40% when the mesh size is larger than 1 mm. As the mesh size is reduced to 0.8 mm, the variation range of GMI becomes significantly reduced. However, the c^{index} distribution range varies with the mesh size, even when the mesh size is reduced to as small as 0.5 mm.

From Fig. 10, fine details of the c^{index} distribution show some differences between the calculations of different mesh sizes: one difference is the c^{index} distribution in the negative-to-positive transition zone; one is the thickness of the channels along the side boundaries. The former difference in the fine details of c^{index} distribution is due to the inconsistent flow patterns which are calculated by different mesh sizes. The latter difference in the thickness of segregation channels along the side boundaries is obviously due to insufficient mesh resolution, especially in the boundary layer. The current modelling result shows that the channel thickness is almost linearly reduced with the mesh size. The channel thickness is in the magnitude of one mesh size. According to Kumar et al. [54], who modeled a test casting of the same geometry with an alloy of Sn-5 wt.% Pb as cooled laterally, the channels inside the middle domain of test casting were found to be in the range of 1.0–1.685 mm in thickness and they spanned 2–5 times of mesh sides. The smallest mesh size as used by Kumar et al. is 0.2 mm. The mesh size as used in the current paper is coarser than those as used in [54], but it is smaller than the channel thickness (1.0–1.685 mm) as predicted in [54]. As we discussed in Section 4.1, both side boundaries, i.e. symmetry plane and adiabatic wall, confine the flow. They provide favorite locations for the formation of channel segregates. The channels as formed along boundaries might be much thinner than those inside the middle domain of the test casting. Extreme fine mesh would be necessary to solve the flow in the boundary layer. Further study is needed.

The modelling results presented in previous sections are based on the mesh size of 1 mm. Key features of the predicted segregation patterns of different cases are valid, but the fine details of the c^{index} distribution do not converge to the precise results.

5. Summary

In order to provide exercise examples for metallurgical students to learn different macrosegregation mechanisms, a simple 2D casting with ideal configuration of pure columnar solidification was simulated by using a volume-average based solidification model. 4 test cases were calculated where solidification occur unidirectionally, either upwards or downwards. Two different alloys were considered: Sn-10 wt.%Pb with solute element Pb heavier than the solvent Sn; Pb-18 wt.%Sn with solute element Sn lighter than the solvent Pb. The final macrosegregation tendency in each test case should be estimated without any simulation according to the alloy and the predefined solidification direction. For example, a solute lighter alloy (Pb-18 wt.%Sn) solidifying upwards would lead to a positive segregation (enrichment of Sn) in the top region and negative segregation (poor in Sn) in the bottom region. That is true. However, the modelling results show that more complicated details of macrosegregation distribution can develop due to the complexity of the transient flow.

In the present test cases, 3 macrosegregation mechanisms operate: thermal buoyancy flow, solutal buoyancy flow and macroscopic diffusion in interdendritic melt. Diffusion-induced macrosegregation occurs only at the bottom and top surfaces in an extremely narrow range, and it is ignorable if the mechanism of thermo-solutal buoyancy flow operates. Solutal buoyancy dominates over the thermal buoyancy when both of them operate at the same time. Solidification shrinkage induced macrosegregation, which is also much stronger than the diffusion-induced macrosegregation [19], was not included in the test cases. Details of macrosegregation formation as induced by thermo-solutal convection during columnar solidification can be analyzed by the relation $\partial c_{\mathrm{mix}}/\partial t = -f_\ell \vec{u}_\ell \cdot \nabla c_\ell$.

Calculation of the formation of macrosegregation is sensitive to the mesh size. Although fine details of the c^{index} distribution have not converged to mesh-independent results with the current grid resolution, key features of the global segregation patterns as presented in this paper are valid.

Other 4 cases of equiaxed solidification will be presented as Part II in next paper.

Acknowledgements

The authors acknowledge the financial support from Austrian Research Promotion Agency (FFG) through the project of Bridge Early Stage (No. 842441), as well as the technical support from the industrial partner Primetals Technologies (former Siemens VAI).

References

[1] M.C. Flemings, ISIJ Int. 40 (2000) 833–841.
[2] A. Ludwig, M. Wu, A. Kharicha, Metall. Mater. Trans. A 46A (2015) 4854–4867.
[3] J.A. Dantzig, M. Rappaz, Solidification, EPFL Press, 2009.
[4] A. Ludwig, Lecture note on solidification course in Swiss Federal Institute of Technology of Lausanne (EPFL), Lausanne, 2015.
[5] M.C. Flemings, G.E. Nereo, Trans. Metall. Soc. AIME 239 (1967) 1449–1462.
[6] G. Lesoult, Mater. Sci. Eng. A 413–414 (2005) 19–29.
[7] E.J. Pickering, C. Chesman, S. Al-Bermani, M. Holland, P. Davies, J. Talamantes-Silva, Metall. Mater. Trans. B 46B (2015) 1860–1874.
[8] M. Wu, A. Kharicha, A. Ludwig, Mater. China 34 (2015) 640–651.
[9] C. Beckermann, Int. Mater. Rev. 47 (2002) 243–261.
[10] J. Ni, C. Beckermann, Metall. Mater. Trans. B 22 (1991) 349–361.
[11] A. Ludwig, M. Wu, Metall. Mater. Trans. A 33 (2002) 3673–3683.
[12] M. Wu, A. Ludwig, A. Buhrig-Polaczek, M. Fehlbier, P.R. Sahm, Int. J. Heat Mass Transfer 46 (2003) 2819–2832.
[13] M. Wu, A. Ludwig, J. Luo, Mater. Sci. Forum 475–479 (2005) 2725–2730.
[14] M. Wu, J. Domitner, A. Ludwig, Metall. Mater. Trans. A 43 (2012) 945–964.
[15] H.J. Thevik, A. Mo, Int. J. Heat Mass Transfer 40 (1997) 2055–2065.
[16] H.J. Thevik, A. Mo, T. Rusten, Metall. Mater. Trans. B 30 (1999) 135–142.
[17] M.C. Schneider, C. Beckermann, Int. J. Heat Mass Transfer 38 (1995) 3455–3473.
[18] H.J. Thevik, A. Mo, Metall. Mater. Trans. B 28 (1997) 665–669.
[19] M.J.M. Krane, F.P. Incropera, Metall. Mater. Trans. A 26 (1995) 2329–2339.
[20] W. Bennon, F. Incropera, Int. J. Heat Mass Transfer 30 (1987) 2161–2170.
[21] M.J.M. Krane, F.P. Incropera, D.R. Gaskell, Int. J. Heat Mass Transfer 40 (1997) 3827–3835.
[22] W. Bennon, F. Incropera, Metall. Mater. Trans. B 18 (1987) 611–616.
[23] V. Voller, A. Brent, C. Prakash, Int. J. Heat Mass Transfer 32 (1989) 1719–1731.
[24] M. Schneider, C. Beckermann, Metall. Mater. Trans. A 26 (1995) 2373–2388.
[25] J. Ni, C. Beckermann, Transport Phenomena in Material Processing, vol. 132, ASME HTD, New York, 1990.
[26] C. Beckermann, R. Viskanta, Appl. Mech. Rev. 46 (1993) 1–27.
[27] M. Wu, A. Ludwig, Adv. Eng. Mater. 5 (2003) 62–66.
[28] M. Wu, A. Ludwig, Metall. Mater. Trans. A 37 (2006) 1613–1631.
[29] M. Wu, A. Ludwig, Metall. Mater. Trans. A 38A (2007) 1465–1475.
[30] M. Wu, A. Ludwig, Acta Mater. 57 (2009) 5621–5631.
[31] M. Wu, A. Ludwig, Acta Mater. 57 (2009) 5632–5644.
[32] M. Wu, A. Fjeld, A. Ludwig, Comput. Mater. Sci. 50 (2010) 32–42.
[33] M. Wu, A. Ludwig, A. Fjeld, Comput. Mater. Sci. 50 (2010) 43–58.
[34] J. Li, M. Wu, A. Ludwig, A. Kharicha, Int. J. Heat Mass Transfer 72 (2014) 668–679.
[35] J. Li, M. Wu, J. Hao, A. Kharicha, A. Ludwig, Comput. Mater. Sci. 55 (2012) 419–429.
[36] J. Li, M. Wu, J. Hao, A. Ludwig, Comput. Mater. Sci. 55 (2012) 407–418.
[37] M. Wu, J. Li, A. Ludwig, A. Kharicha, Comput. Mater. Sci. 92 (2014) 267–285.
[38] M. Wu, J. Li, A. Ludwig, A. Kharicha, Comput. Mater. Sci. 79 (2013) 830–840.
[39] N. Leriche, H. Combeau, C.-A. Gandin, M. Založnik, IOP Conf. Series: Mater. Sci. Eng. 84 (2015) 012087.
[40] M. Bellet, H. Combeau, Y. Fautrelle, D. Gobin, M. Rady, E. Arquis, O. Budenkova, B. Dussoubs, Y. Duterrail, A. Kumar, Int. J. Therm. Sci. 48 (2009) 2013–2016.
[41] N. Ahmad, H. Combeau, J.-L. Desbiolles, T. Jalanti, G. Leosoult, J. Rappaz, M. Rappaz, C. Stomp, Metall. Mater. Trans. A 29 (1998) 617–630.
[42] H. Combeau et al., in: A. Ludwig, M. Wu, A. Abdellah (Eds.), Proceedings of 13th Modeling of Casting, Welding and Advanced Solidification Processes, IOP Conf. Series: Mater. Sci. Eng., vol. 33, 2012, http://dx.doi.org/10.1088/1757-899X/33/1/012086.
[43] D.J. Hebditch, J.D. Hunt, Metall. Trans. 5 (1974) 1557–1564.
[44] L. Hachani, K. Zaidat, Y. Fautrelle, Int. J. Heat Mass Transfer 85 (2015) 438–454.
[45] J. Lipton, M.E. Glicksman, W. Kurz, Mater. Sci. Eng. 65 (1984) 57–63.
[46] M.A. Martorano, C. Beckermann, C.A. Gandin, Metall. Mater. Trans. A 34 (2003) 1657–1674.
[47] D. Poirier, Metall. Mater. Trans. B 18 (1987) 245–255.
[48] M. Klassen, J. Cahoon, Metall. Mater. Trans. A 31 (2000) 1343–1352.
[49] J. Gu, C. Beckermann, Metall. Mater. Trans. A 30 (1999) 1357–1366.
[50] E. Cadirli, M. Gündüz, J. Mater. Sci. 35 (2000) 3837–3848.
[51] ANSYS Fluent – Release 14.5, Fluent Theory Guide, ANSYS Inc, <www.ansys.com>.
[52] D. Ma, Q. Wu, A. Bührig-Polaczek, Metall. Mater. Trans. B 43 (2012) 344–353.
[53] J. Guo, C. Beckermann, Numer. Heat Transfer: Part A: Appl. 44 (2003) 559–576.
[54] A. Kumar, B. Dussoubs, M. Zaloznik, H. Combeau, I. Phys. D: Appl. Phys. 42 (2009) 105503.
[55] M. Wu, L. Könözsy, A. Ludwig, W. Schützenhofer, R. Tanzer, Steel Res. Int. 79 (2008) 637–646.
[56] M.C. Flemings, G.E. Nereo, Trans. Met. Soc. AIME 239 (1967) 1449–1461.
[57] M. Zaloznik, H. Combeau, in: S.L. Cockcroft, D.M. Maijer (Eds.), Proceedings of 12th Modeling of Casting, Welding and Advanced Solidification Processes, TMS, 2009, pp. 253–260.
[58] M. Wu, A. Kharicha, A. Ludwig, Mater. Sci. Forum 790–791 (2014) 85–90.

Paper II

Numerical analysis of macrosegregation in vertically solidified Pb-Sn test castings – Part II: Equiaxed solidification

Yongjian Zheng, Menghuai Wu, Abdellah Kharicha, Andreas Ludwig,

Computational Materials Science, 2016, 124: 456-470.

Computational Materials Science 124 (2016) 456–470

Contents lists available at ScienceDirect

Computational Materials Science

journal homepage: www.elsevier.com/locate/commatsci

Numerical analysis of macrosegregation in vertically solidified Pb-Sn test castings – Part II: Equiaxed solidification

Y. Zheng [a], M. Wu [a,b,*], A. Kharicha [a,b], A. Ludwig [a]

[a] Chair of Modelling and Simulation of Metallurgical Processes, Montanuniversitaet Leoben, Austria
[b] Christian Doppler Laboratory for Advanced Simulation of Solidification and Melting, Montanuniversitaet Leoben, Austria

ARTICLE INFO

Article history:
Received 22 April 2016
Received in revised form 14 July 2016
Accepted 16 July 2016
Available online 5 August 2016

Keywords:
Macrosegregation
Equiaxed solidification
Nucleation
Crystal sedimentation
Equiaxed-to-columnar-transition (ECT)

ABSTRACT

In order to get basic understandings of the macrosegregation mechanisms, 8 test cases of a 2D casting ($50 \times 60\ \mathrm{mm}^2$) with unidirectional cooling from either top or bottom were simulated. Part I of this two-part study has presented 4 cases of pure columnar solidification. Part II will present the other 4 cases of equiaxed solidification. Two alloys were considered: Sn–10 wt%Pb with solute element Pb heavier than the solvent Sn; Pb–18 wt%Sn with solute element Sn lighter than the solvent Pb. The solidified equiaxed crystal is considered always heavier than the melt. With such simple configurations, it is believed that the macrosegregation tendency during equiaxed solidification can be estimated. However, the modeling results show that complicated macrosegregation patterns can develop due to the complexity of the event of equiaxed-to-columnar transition (ECT). Analysis of the segregation mechanisms for each case is made. The three-phase mixed columnar-equiaxed solidification model (Wu and Ludwig, MMTA, 2006, p. 1613) is modified and used for this study. One modification is to consider the heterogeneous nucleation of equiaxed crystals and transport of inoculants (embryos). The inoculants serve as heterogeneous nucleation sites for the equiaxed crystals, which can be transported as well. Another modification is to include the ECT. When all inoculants are consumed and the equiaxed crystals settle down in the bottom region, the remaining melt in the upper part can only solidify as columnar structure. Those columnar structures develop/grow from the packed equiaxed crystals by triggering the event of ECT.

1. Introduction

1.1. Motivation

In order to provide exercise examples for metallurgical students to learn different macrosegregation mechanisms, a simple 2D casting with ideal configuration of pure columnar solidification or equiaxed solidification was designed and taught in the annual "solidification course" of EPFL held in Les Diablerets, Switzerland [1,2]. As shown in Fig. 1, 8 simple test cases were configured. They were unidirectionally cooled from either top or bottom. Two different alloys were considered: Sn-10 wt%Pb with solute element Pb heavier than the solvent Sn; Pb-18 wt%Sn with solute element Sn lighter than the solvent Pb. It is believed that, based on our theoretical knowledge and experience which we had previously, we should be able to estimate the global macrosegregation tendency without performing any numerical simulation. The current work is to simulate these 8 test cases by using a three-phase mixed columnar-equiaxed solidification model [3]. One purpose is to test the theoretical knowledge and experience. A more important purpose is to demonstrate the potential complexity of the macrosegregation phenomena. The current study is divided into two parts. In part I the 4 test cases of pure columnar solidification have been presented [4]. This paper, as Part II, will present other 4 test cases of equiaxed solidification, i.e. the scenarios as shown schematically in cases E1 through E4 of Fig. 1.

1.2. Challenge of modeling equiaxed solidification

Understanding to the equiaxed solidification was significantly improved in the last decades [5,6], but most important knowledge about the crystal transport, i.e. one origin of macrosegregation, is missing [7]. Although the importance of that transport phenomenon has been addressed for decades [8], there is no mature theory to describe the relationship between the crystal transport and the resulting structural heterogeneity and macrosegregation until some numerical models were developed recently [9,10].

---

* Corresponding author at: Chair of Modelling and Simulation of Metallurgical Processes, Montanuniversitaet Leoben, Austria.

E-mail address: menghuai.wu@unileoben.ac.at (M. Wu).

http://dx.doi.org/10.1016/j.commatsci.2016.07.018

Nomenclature

c_0	initial concentration (1)
c_ℓ, c_e, c_c	species concentration (1)
c^{ref}	reference concentration (1)
c_{eu}	eutectic concentration (1)
$c_\ell^*,\ c_e^*,\ c_c^*$	equilibrium concentration at interface (1)
$C_{\ell e}^p$	species exchange between liquid and equiaxed ($\text{kg m}^{-3}\ \text{s}^{-1}$)
$C_{\ell c}^p$	species exchange between liquid and columnar ($\text{kg m}^{-3}\ \text{s}^{-1}$)
c^{index}	macrosegregation index (%)
c_{mix}	mix concentration (1)
$c_p^\ell,\ c_p^e,\ c_p^c$	specific heat ($\text{J kg}^{-1}\ \text{K}^{-1}$)
D_ℓ	diffusion coefficient ($\text{m}^2\ \text{s}^{-1}$)
d_e	equiaxed grain diameter (m)
d_c	columnar trunk diameter (m)
$f_\ell,\ f_e,\ f_c$	volume fraction of different phases (1)
f_{si}	dendrite to equiaxed volume ratio in the envelope (1)
f_c^{free}	critical f_c for free moving equiaxed phase (1)
f_e^{Env}	volume fraction of equiaxed grain envelope (1)
$f_{e,CET}$	critical equiaxed phase f_e under which the primary dendrite tip growth would be blocked (1)
$f_{e,packing}$	equiaxed grain packing limit (1)
$\vec{g}$	gravity (m s^{-2})
$\vec{g}_e',\ \vec{g}_\ell'$	reduced gravity (m s^{-2})
h	heat transfer coefficient ($\text{W m}^{-2}\ \text{K}^{-1}$)
H^*	volume heat transfer coefficient between phases ($\text{W m}^{-3}\ \text{K}^{-1}$)
$h_\ell,\ h_e,\ h_c$	enthalpy (J kg^{-1})
$h_\ell^{ref},\ h_e^{ref},\ h_c^{ref}$	reference enthalpy (J kg^{-1})
Δh	latent heat (J kg^{-1})
K	permeability of liquid in porous medium (m^2)
$K_{\ell e}(=-K_{e\ell})$	the drag force coefficient ($\text{kg m}^{-3}\ \text{s}^{-1}$)
k	solute partitioning coefficient at the liquid solid interface (1)
k_ℓ, k_e, k_c	thermal conductivity ($\text{W m}^{-1}\ \text{K}^{-1}$)
l	actual columnar length in tip cell (m)
$M_{\ell e}(=-M_{e\ell})$	liquid-equiaxed net mass transfer rate ($\text{kg m}^{-3}\ \text{s}^{-1}$)
$M_{\ell c}(=-M_{c\ell})$	liquid-columnar net mass transfer rate ($\text{kg m}^{-3}\ \text{s}^{-1}$)
m	slope of liquidus in phase diagram (K)
N_{nu}	equiaxed grain production rate by nucleation ($\text{m}^{-3}\ \text{s}^{-1}$)
n_{em}	inoculant number density (m^{-3})
n_{eq}	equiaxed grain number density (m^{-3})
n_c	columnar trunk number density (m^{-3})
n_{max}	maximum equiaxed grain volume density, or maximum available nucleation sites in simultaneous nucleation law (m^{-3})
p	pressure (N m^{-2})
$Q_{\ell e}(=-Q_{e\ell})$	total energy exchange between liquid and equiaxed phases ($\text{J m}^{-3}\ \text{s}^{-1}$)
$Q_{\ell e}^d(=-Q_{e\ell}^d)$	energy transfer between liquid and equiaxed phases ($\text{J m}^{-3}\ \text{s}^{-1}$)
$Q_{\ell e}^p(=-Q_{e\ell}^p)$	energy exchange due to phase change between liquid and equiaxed phases ($\text{J m}^{-3}\ \text{s}^{-1}$)
$Q_{\ell c}(=-Q_{c\ell})$	total energy exchange between liquid and columnar phases ($\text{J m}^{-3}\ \text{s}^{-1}$)
$Q_{\ell c}^d(=-Q_{c\ell}^d)$	energy transfer between liquid and columnar phases ($\text{J m}^{-3}\ \text{s}^{-1}$)
$Q_{\ell c}^p(=-Q_{c\ell}^p)$	energy exchange due to phase change between liquid and columnar phases ($\text{J m}^{-3}\ \text{s}^{-1}$)
$Q_{ec}(=-Q_{ce})$	total energy exchange between equiaxed and columnar phases ($\text{J m}^{-3}\ \text{s}^{-1}$)
$Q_{ec}^d(=-Q_{ce}^d)$	energy transfer between equiaxed and columnar phases ($\text{J m}^{-3}\ \text{s}^{-1}$)
$Q_{ec}^p(=-Q_{ce}^p)$	energy exchange due to phase change between equiaxed and columnar phases ($\text{J m}^{-3}\ \text{s}^{-1}$)
R_{tip}	primary dendrite tip radius (m)
$R\ (R_e, R_c)$	grain radius (equiaxed, columnar) (m)
$R_{f,e}$	maximum radius of equiaxed grain (m)
$R_{f,c}$	maximum radius of columnar trunk (m)
T_0	initial temperature (K)
T, T_ℓ, T_e, T_c	temperature (K)
T_f	melting point of solvent at $c_0 = 0$ (K)
T_{ref}	reference temperature for enthalpy definition (K)
T_{eu}	eutectic temperature (K)
T_{liq}	liquidus temperature (K)
T_{EXT}	external temperature (K)
ΔT	constitutional undercooling (K)
ΔT_N	undercooling for maximum grain production rate (K)
ΔT_σ	Gaussian distribution width of nucleation law (K)
t	time (s)
Δt	time step (s)
$\vec{U}_{\ell e}(=-\vec{U}_{e\ell})$	total liquid-equiaxed momentum exchange rate ($\text{kg m}^{-2}\ \text{s}^{-2}$)
$\vec{U}_{\ell e}^d(=-\vec{U}_{e\ell}^d)$	liquid-equiaxed momentum change due to drag force ($\text{kg m}^{-2}\ \text{s}^{-2}$)
$\vec{U}_{\ell e}^p(=-\vec{U}_{e\ell}^p)$	liquid-equiaxed momentum exchange due to phase change ($\text{kg m}^{-2}\ \text{s}^{-2}$)
$\vec{U}_{\ell c}(=-\vec{U}_{c\ell})$	total liquid-columnar momentum exchange rate ($\text{kg m}^{-2}\ \text{s}^{-2}$)
$\vec{U}_{\ell c}^d(=-\vec{U}_{c\ell}^d)$	liquid-columnar momentum change due to drag force ($\text{kg m}^{-2}\ \text{s}^{-2}$)
$\vec{U}_{\ell c}^p(=-\vec{U}_{c\ell}^p)$	liquid-columnar momentum exchange due to phase change ($\text{kg m}^{-2}\ \text{s}^{-2}$)
$\vec{U}_{ce}$	total columnar-equiaxed momentum exchange rate ($\text{kg m}^{-2}\ \text{s}^{-2}$)
$\vec{U}_{ce}^d$	columnar-equiaxed momentum exchange rate due to drag ($\text{kg m}^{-2}\ \text{s}^{-2}$)
$\vec{U}_{ce}^p$	columnar-equiaxed momentum exchange rate due to phase change ($\text{kg m}^{-2}\ \text{s}^{-2}$)
$\vec{u}_\ell, \vec{u}_e, \vec{u}_c$	velocity vector (m s^{-1})
$v_{Re},\ v_{Rc}$	grain growth speed in radius direction for equiaxed and columnar (m s^{-1})
v_{tip}	grain growth speed in tip direction (m s^{-1})
V_{domain}	volume of the calculated domain (m^3)
x, y	coordinate (m)
β_T	thermal expansion coefficient (K^{-1})
β_c	solutal expansion coefficient (1)
Γ	Gibbs Thomson coefficient (m K)
λ_1	primary columnar arm space (m)
μ_ℓ, μ_e	viscosity ($\text{kg m}^{-1}\ \text{s}^{-1}$)
$\rho_\ell,\ \rho_e,\ \rho_c$	density (kg m^{-3})
ρ_{ref}	reference density (kg m^{-3})
$\Delta\rho$	density difference between solid and liquid phase (kg m^{-3})
ρ_ℓ^b	density for buoyancy force (kg m^{-3})
$\bar{\bar{\tau}}_l,\ \bar{\bar{\tau}}_e$	stress-strain tensors ($\text{kg m}^{-1}\ \text{s}^{-1}$)

Subscripts

ℓ	mark liquid
e	equiaxed
c	columnar phases

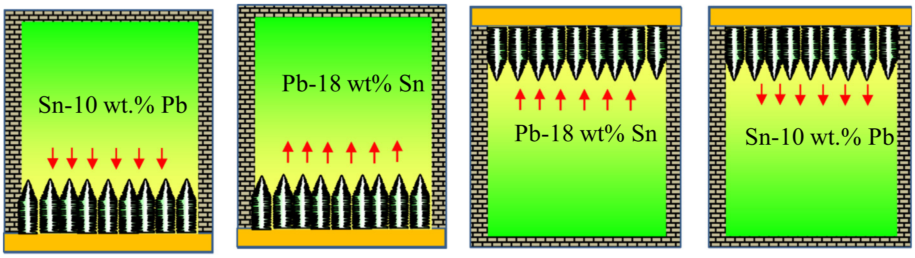

(a) Case C1 (b) Case C2 (c) Case C3 (d) Case C4

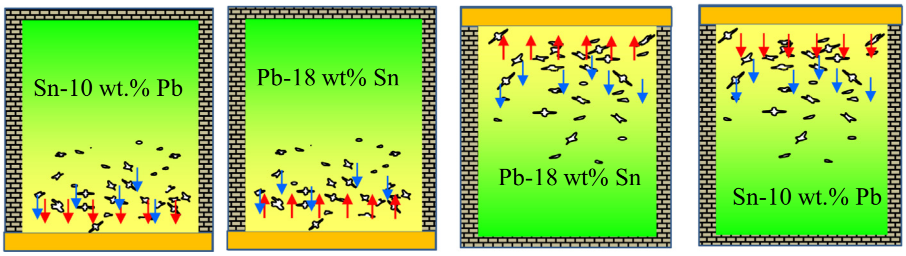

(e) Case E1 (f) Case E2 (g) Case E3 (h) Case E4

Fig. 1. Schematics of columnar (upper row) and equiaxed (lower row) solidification, solutal buoyancy force direction (red arrows) of the interdendritic/inter-granular melt, and crystal sedimentation direction (blue arrows) of the equiaxed grains. 8 cases were defined, where two different alloys were considered: Sn-10 wt%Pb with solute element Pb heavier than the solvent Sn; Pb-18 wt%Sn with solute element Sn lighter than the solvent Pb. The color gradients indicate the distribution of solute element in the melt: yellow for enrichment, green as the nominal composition. The yellow walls indicate chilled walls, while the hatched ones are adiabatic. Cases C1, C2, E1 and E2 were cooled from bottom, while the other 4 cases were cooled from top. (For interpretation of the references to color in this figure legend, the reader is referred to the web version of this article.)

A numerical model describing equiaxed solidification needs to consider nucleation, growth, sedimentation/flotation of equiaxed crystals, and melt flow. Therefore, a multiphase volume-average approach comes into favor [9,10]. The equiaxed crystals can be treated as a pseudo liquid phase (secondary fluid phase), interpenetrating and incorporating with the parent melt (primary fluid phase). The number density, grain size, moving velocity and other physical quantities of equiaxed crystals are volume-averaged and calculated by solving an additional set of conservation equations. Mass transfer due to solidification, momentum and energy transfer between the parent melt and the growing and moving equiaxed crystals are considered in closure laws. This approach was used by different authors to study the formation of macrosegregation during globular equiaxed solidification [11–14] and dendritic equiaxed solidification [15–19]. Recently, it was extended by Wu et al. for mixed columnar-equiaxed solidification, considering either non-dendritic [3,20–24] or dendritic growth of crystals [25–27]. To validate the numerical models, series of experiments based on various materials, e.g., NH_4Cl-H_2O [28,29], succinonitrile-acetone [30,31], Al-Cu alloy [32], and Sn-Pb alloy [33], were performed as well.

The volume-average based three-phase mixed columnar-equiaxed solidification model [3,34] with slight modifications is used in this paper. One modification is to consider the transport of inoculants (embryos). The inoculants serve as heterogeneous nucleation sites for the equiaxed crystals. Another modification is to include the equiaxed-to-columnar-transition (ECT). During equiaxed solidification, when all inoculants are consumed and the equiaxed crystals settle down in the bottom region, the remaining melt in the upper part can only solidify as columnar structure.

2. Numerical model and simulation settings

2.1. Model in brief

The three-phase mixed columnar-equiaxed solidification model was described previously [3,34]. Here, only a brief outline of the model assumptions is given. Conservation equations, source terms and exchange terms, and some auxiliary equations are summarized in Table 1.

(1) Three phases are the primary liquid melt, equiaxed and columnar phases. Their volume fractions are f_ℓ, f_e and f_c with $f_\ell + f_e + f_c = 1$. Both the liquid and equiaxed phases are moving phases, for which the corresponding Navier-Stokes equations are solved. The columnar phase is assumed to be rigid and stationary.
(2) Equiaxed crystals originate from heterogeneous nucleation [35]. The nucleation rate is a function of undercooling, $\Delta T = T_f + mc_\ell - T$. Transport of both inoculants (embryos) and equiaxed crystals is described in Section 2.3.
(3) The columnar structural growth is triggered by equiaxed-to-columnar transition (ECT), and it is described in Section 2.2.
(4) Simple crystal morphology is assumed for the diffusion-governed solidification kinetics: spheres for equiaxed grains and step-wise cylinders for columnar tree trunks. The solidification of both columnar trunk and equiaxed grain is governed by diffusion; the concentration difference $(c_\ell^* - c_\ell)$ is the driving force for the solidification. Back diffusion in solid is neglected $(D_c, D_e = 0)$.
(5) To deal with the hydrodynamic interaction between phases, a simplified dendritic morphology for the equiaxed phase is assumed, and the concept of "equiaxed grain envelope" is employed [36]. A dendritic equiaxed crystal is described by the equiaxed grain envelope, which includes the solid 'dendrite' and the inter-dendritic melt. The ratio of the volume of solid 'dendrite' to the volume of the equiaxed grain envelope is predefined: f_{si}. Therefore, the volume fraction of equiaxed grain envelopes (f_e^{Env}) is related to the volume fraction of the net solid phase of equiaxed crystals (f_e) by $f_e^{Env} = f_e / f_{si}$. In this study, f_{si} is set as a constant value (0.5).
(6) Volume-averaged concentrations (c_ℓ, c_e, c_c) are calculated by Eqs. (6)–(8). Thermodynamic equilibrium is assumed at the liquid-solid interface, which dictates the concentrations

Table 1
Conservation equations, sources and exchange terms, and auxiliary equations.

1. Conservation equations		
Mass:	$\frac{\partial}{\partial t}(f_\ell\rho_\ell)+\nabla\cdot(f_\ell\rho_\ell\vec{u}_\ell)=M_{e\ell}+M_{c\ell}$	(1)
	$\frac{\partial}{\partial t}(f_e\rho_e)+\nabla\cdot(f_e\rho_e\vec{u}_e)=M_{\ell e}$	(2)
	$\frac{\partial}{\partial t}(f_c\rho_c)=M_{\ell c}$	(3)
Momentum:	$\frac{\partial}{\partial t}(f_\ell\rho_\ell\vec{u}_\ell)+\nabla\cdot(f_\ell\rho_\ell\vec{u}_\ell\otimes\vec{u}_\ell)=-f_\ell\nabla p+\nabla\cdot\bar{\bar{\tau}}_\ell+f_\ell\rho_\ell\vec{g}'_\ell-\vec{U}_{\ell e}-\vec{U}_{\ell c}$ with $\vec{g}'_\ell=\frac{\rho^{b}_\ell(T,c)-\rho_\ell}{\rho_\ell}\vec{g}$, $\rho^{b}_\ell(T,c)=\rho_\ell\cdot[1+\beta_T\cdot(T^{ref}-T_\ell)+\beta_c\cdot(c^{ref}-c_\ell)]$, $\vec{U}_{\ell e}=\vec{U}^{p}_{\ell e}+\vec{U}^{d}_{\ell e}$, $\vec{U}_{\ell c}=\vec{U}^{p}_{\ell c}+\vec{U}^{d}_{\ell c}$	(4)
	$\frac{\partial}{\partial t}(f_e\rho_e\vec{u}_e)+\nabla\cdot(f_e\rho_e\vec{u}_e\otimes\vec{u}_e)=-f_e\nabla p+\nabla\cdot\bar{\bar{\tau}}_e+f_e\rho_e\vec{g}'_e+\vec{U}_{\ell e}+\vec{U}_{ce}$	(5)
	with $\vec{g}'_e=\frac{\Delta\rho}{\rho_e}\vec{g}$, $\vec{U}_{ce}=\vec{U}^{p}_{ce}+\vec{U}^{d}_{ce}$, $\Delta\rho=\rho_e-\rho_\ell$.	
Species:	$\frac{\partial}{\partial t}(f_\ell\rho_\ell c_\ell)+\nabla\cdot(f_\ell\rho_\ell\vec{u}_\ell c_\ell)=\nabla\cdot(f_\ell\rho_\ell D_\ell\nabla c_\ell)-C^{p}_{\ell c}-C^{p}_{\ell e}$	(6)
	$\frac{\partial}{\partial t}(f_e\rho_e c_e)+\nabla\cdot(f_e\rho_e\vec{u}_e c_e)=\nabla\cdot(f_e\rho_e D_e\nabla c_e)+C^{p}_{\ell e}$	(7)
	$\frac{\partial}{\partial t}(f_c\rho_c c_c)=\nabla\cdot(f_c\rho_c D_c\nabla c_c)+C^{p}_{\ell c}$	(8)
Enthalpy:	$\frac{\partial}{\partial t}(f_\ell\rho_\ell h_\ell)+\nabla\cdot(f_\ell\rho_\ell\vec{u}_\ell h_\ell)=\nabla\cdot(f_\ell k_\ell\nabla\cdot T_\ell)-Q_{\ell c}-Q_{\ell e}$	(9)
	$\frac{\partial}{\partial t}(f_e\rho_e h_e)+\nabla\cdot(f_e\rho_e\vec{u}_e h_e)=\nabla\cdot(f_e k_e\nabla\cdot T_e)+Q_{\ell e}+Q_{ce}$ with $Q_{\ell e}=Q^{p}_{\ell e}+Q^{d}_{\ell e}$, $Q_{ce}=Q^{p}_{ce}+Q^{d}_{ce}$, $Q^{d}_{ce}=0$	(10)
	$\frac{\partial}{\partial t}(f_c\rho_c h_c)=\nabla\cdot(f_c k_c\nabla\cdot T_c)+Q_{\ell c}-Q_{ce}$ with $Q_{\ell c}=Q^{p}_{\ell c}+Q^{d}_{\ell c}$, $h_\ell=\int_{T_{ref}}^{T_\ell}c^{\ell}_{p}dT+h^{ref}_\ell$, $h_e=h_c=\int_{T_{ref}}^{T_e}c^{e}_{p}dT+h^{ref}_e$, $L=h^{ref}_\ell-h^{ref}_e$	(11)

2. Nucleation and transport of the equiaxed grains				
Trans. equation:	$\frac{\partial}{\partial t}n_{em}+\nabla\cdot(\vec{u}_\ell n_{em})=-N_{nu}$	(12)	$\frac{\partial}{\partial t}n_{eq}+\nabla\cdot(\vec{u}_e n_{eq})=N_{nu}$	(13)
Nucleation:	$N_{nu}=\frac{n_{em}}{n_{max}}\cdot\frac{D(\Delta T)}{Dt}\cdot\frac{dn}{d(\Delta T)}$	$\frac{D(\Delta T)}{Dt}=\frac{\partial T}{\partial t}+u_\ell\cdot(m\cdot\frac{\partial c_\ell}{\partial x}-\frac{\partial T_\ell}{\partial x})+v_\ell\cdot(m\cdot\frac{\partial c_\ell}{\partial y}-\frac{\partial T_\ell}{\partial y})$	$\frac{dn}{d(\Delta T)}=\frac{n_{max}}{\sqrt{2\pi}\cdot\Delta T_\sigma}\cdot e^{-\frac{1}{2}\left(\frac{\Delta T-\Delta T_N}{\Delta T_\sigma}\right)^2}$	(14)

3. Mass transfer					
Equiaxed			**Columnar**		
Equi. grain growth velocity:	$v_{R_e}=\frac{dR_e}{dt}=\frac{D_\ell}{R_e(1-R_e/R_{f,e})}\cdot\frac{c^*_\ell-c_\ell}{c^*_\ell-c^*_e}$	(15)	Col. trunk growth velocity:	$v_{R_c}=\frac{dR_c}{dt}=\frac{D_\ell}{R_c}\cdot\frac{(c^*_\ell-c_\ell)}{(c^*_\ell-c^*_c)}\cdot\ln^{-1}\left(\frac{R_{f,c}}{R_c}\right)$	(16)
Mass transfer:	$M_{\ell e}=v_{R_e}\cdot(n_{eq}\cdot\pi d^2_e)\cdot\rho_e\cdot f_\ell$	(17)	Mass transfer for the trunks:	$M_{\ell c}=v_{R_c}\cdot(\pi d_c/\lambda^2_1)\cdot\rho_c\cdot\Phi_{imp}$	(18)
			Mass transfer incl. col. tips:	$M_{\ell c}=v_{R_c}\cdot n_c\cdot(\pi d_c\cdot l)\cdot\rho_\ell\cdot\Phi_{imp}+v_{tip}\cdot n_c\cdot(\pi R^2_{tip})\cdot\rho_\ell\cdot\Phi_{imp}$ with $\Phi_{imp}=\begin{cases}1 & d_c\le\lambda_1\\ 4f_\ell/(4-\pi) & d_c>\lambda_1\end{cases}$	(19)

4. Source and exchange terms				
Momentum transfer:	$\vec{U}^{p}_{\ell e}=\vec{u}_\ell\cdot M_{\ell e}$, $\vec{U}^{p}_{\ell c}=\vec{u}_\ell\cdot M_{\ell c}$, $\vec{U}^{p}_{ce}=0$.	(20)	$\vec{U}^{d}_{\ell e}=K_{\ell e}\cdot(\vec{u}_\ell-\vec{u}_e)$, $\vec{U}^{d}_{\ell c}=\frac{f^2_\ell\cdot\mu_\ell}{K}\cdot\vec{u}_\ell$ $\vec{U}^{d}_{ce}$ refers to [3], $K=6\times10^{-4}\cdot\lambda^2_1\cdot\frac{f^3_\ell}{(1-f_\ell)^2}$	(21)
Species transfer:	$C^{p}_{\ell e}=k\cdot c^*_\ell\cdot M_{\ell e}$, $C^{p}_{\ell c}=k\cdot c^*_\ell\cdot M_{\ell c}$	(22)		
Enthalpy transfer and latent heat:	$Q^{p}_{\ell e}=h_\ell\cdot M_{\ell e}$, $Q^{p}_{\ell c}=h_\ell\cdot M_{\ell c}$	(23)	$Q^{d}_{\ell e}=H^*\cdot(T_\ell-T_e)$, $Q^{d}_{\ell c}=H^*\cdot(T_\ell-T_c)$, $Q^{d}_{ce}=H^*\cdot(T_c-T_e)$, where $H^*=10^9\ \mathrm{W\cdot m^{-2}\cdot K^{-1}}$	(24)

5. Auxiliary equations					
Mixture concentration $c_{mix}=\frac{c_\ell\cdot\rho_\ell\cdot f_\ell+c_e\cdot\rho_e\cdot f_e+c_c\cdot\rho_c\cdot f_c}{\rho_\ell\cdot f_\ell+\rho_e\cdot f_e+\rho_c\cdot f_c}$	(25)	Macrosegregation index in % $c^{index}=\frac{c_{mix}-c_0}{c_0}\times100$	(26)	Global macrosegregation intensity $\mathrm{GMI}=\frac{1}{V_{domain}}\cdot\iiint_{V_{domain}}\lvert c^{index}\rvert dV$	(27)

at the interface (c_ℓ^*, c_e^*, c_c^*). A linearized Pb-Sn binary phase diagram is used, and a constant solute redistribution coefficient k and a constant liquidus slope m are assumed.

(7) The macrosegregation is usually evaluated by the mixture concentration c_mix, as defined by Eq. (25), but here two additional quantities are defined to quantify the macrosegregation: one is the macrosegregation index c^index, Eq. (26), and another one is the global macrosegregation intensity (GMI), Eq. (27). The quantities of them are presented in %.

(8) Resistance of the mushy zone (columnar phase) to interdendritic flow is calculated using a permeability law according to Blake-Kozeny [37]. The drag force coefficient $K_{\ell\mathrm{e}}$ for the melt-equiaxed interaction is treated according to Kozeny-Carman for $f_\mathrm{e} < 0.7$, and Blake-Kozeny for $f_\mathrm{e} \geqslant 0.7$ [37].

(9) The presence of equiaxed crystals influences the growth of primary dendrite tips. The critical volume fraction of equiaxed envelopes ($f_\mathrm{e,CET}$) to block the growth of the primary columnar dendrite tips is set as 0.49 [37]. When $f_\mathrm{e}^\mathrm{Env}$ ($=f_\mathrm{e}/f_\mathrm{si}$) reaches $f_\mathrm{e,CET}$ at the columnar tip front, the columnar-to-equiaxed transition (CET) occurs.

(10) The presence of the columnar structure influences the motion of equiaxed crystals. The equiaxed crystals can be captured by the columnar dendrite trunk when the local volume fraction of the columnar phase reaches a critical value of $f_\mathrm{c}^\mathrm{free} = 0.2$.

(11) The interactions between neighboring equiaxed crystals and their influence on the motion of equiaxed phase is modeled by a so-called effective viscosity (μ_e) [38], which increases with the volume fraction of the equiaxed phase. When the volume fraction of the grain envelope of equiaxed phase $f_\mathrm{e}^\mathrm{Env}$ ($=f_\mathrm{e}/f_\mathrm{si}$) reaches the packing limit $f_\mathrm{e,packing}$, μ_e increases to infinitive, and a rigid network of equiaxed crystals is built. Here $f_\mathrm{e,packing}$ is equal to 0.637.

2.2. Equiaxed-to-columnar transition (ECT) and columnar-to-equiaxed transition (CET)

The terms equiaxed-to-columnar transition (ECT) and columnar-to-equiaxed transition (CET) have been used to describe the crystal structural transition between equiaxed and columnar during solidification of an alloy casting. After nucleation of crystals in undercooled melt, e.g., near the casting surface, growth of the crystals is generally equiaxed. With the progress of solidification, when a temperature gradient is gradually established, the growth of the crystals becomes unidirectionally against the heat flux direction. Columnar structure develops. This crystal structural transition from equiaxed to columnar is called as ECT. During the late stage of solidification, when new equiaxed crystals nucleate and grow in the liquid ahead of columnar zone, the growth of columnar structure will be blocked by the equiaxed crystals and the transition from columnar to equiaxed, i.e. CET, occurs. When the motion of equiaxed crystals and mechanical interaction between the dendritic crystals occur, the aforementioned ECT and CET become much more complex. They might not be simply explained by cooling direction (unidirectional or homogenous cooling). In order to treat the ECT and CET considering the crystal transport and interaction phenomena, following modeling concept is suggested.

During equiaxed solidification, equiaxed crystals can coagulate with each other. When the local volume fraction of equiaxed envelope $\left(f_\mathrm{e}^\mathrm{Env} = f_\mathrm{e}/f_\mathrm{si}\right)$ becomes larger than a critical volume fraction ($f_\mathrm{e,packing}$), the equiaxed phase builds a rigid network. Here $f_\mathrm{e,packing}$ is called as packing limit, taking 0.637. As the equiaxed phase is arrested by the mold wall (stationary), the velocity of the equiaxed phase vanishes, and then the equiaxed phase is considered as rigid and stationary. Numerically, this rigid and stationary equiaxed phase region is marked. Columnar primary dendrite tips are allowed to initiate and grow from the outer contour of the marked region. The growth of the columnar primary dendrite tips is tracked explicitly. The numerical algorithm, as described previously to track the columnar tip front [34], is applied here. The growth velocity of the columnar primary dendrite tip is modeled according to LGK [39].

The solidification of the columnar phase region competes with the solidification of the equiaxed phase region. When the solidification of the columnar phase "overtakes" the solidification of equiaxed phase, the event of equiaxed-to-columnar transition (ECT) is triggered. Otherwise, the solidification of the columnar phase is suppressed, or the solidification of existing columnar primary tip front is blocked by equiaxed phase, i.e. columnar-to-equiaxed transition (CET) is triggered. In order to judge if the solidification of columnar phase can "overtake" the solidification of equiaxed phase, following algorithm is implemented. If the columnar primary dendrite tip front can grow out of the considered volume element before $f_\mathrm{e}^\mathrm{Env}$ reaches a so-called blocking limit ($f_\mathrm{e,CET}$), the growth of columnar primary tip front can continue into the neighboring cell or cells. In opposite, if the columnar primary dendrite tip front cannot grow out of the considered volume element before $f_\mathrm{e}^\mathrm{Env}$ reaches $f_\mathrm{e,CET}$, CET occurs. $f_\mathrm{e,CET}$ was suggested by Hunt to be 0.49 [37], but was recently modified to be 0.2 [38]. During the late stage of equiaxed solidification, the inoculants are consumed, i.e. no new equiaxed grain can nucleate, ECT event occurs and the rest domain of the casting solidifies as columnar structure. Therefore, the final ECT position is marked by the isoline of $f_\mathrm{e}^\mathrm{Env} = f_\mathrm{e,CET}$.

2.3. Heterogeneous nucleation and transport of inoculants and equiaxed crystals

Heterogeneous nucleation law is verified for most technical alloys. Inoculants, i.e. nucleation embryos, exist in the parent melt. The inoculants will be activated by undercooling. The activated inoculants develop as equiaxed nuclei and they can grow. The undercooling needed to activate an inoculant depends on the size of the inoculant [40]. Empirically, it was found that the nucleation event follows a Gaussian distribution function of undercooling [35], as described by Eq. (14), and it is widely used in different solidification models.

The inoculants and equiaxed crystals are quantified by their number densities: n_em and n_eq. The transport of inoculants n_em is calculated by Eq. (12) according to liquid melt velocity $\vec{u}_\ell$, while the transport of equiaxed crystals n_eq is calculated by Eq. (13) according to the velocity of equiaxed phase $\vec{u}_\mathrm{e}$. The source term N_nu determines the nucleation rate. The total number (volume integral) of inoculants and equiaxed crystals in the whole casting must be conserved: a certain number of inoculants consumed are identical to the number of newly-nucleated equiaxed crystals. Actually, the above idea is quite similar to that of Bedel et al. [41]. Please notice that different size groups of inoculants were treated by Bedel, and transport of each size group has to be calculated individually. In the current model, however, no size groups are distinguished. Only one transport equation for n_em is necessarily solved. Statistically, nucleation rate is estimated to be proportional to the local number density of inoculants (n_em).

2.4. Configuration of the test casting

The configuration of the 2D test casting is shown in Fig. 2. The geometry, alloys and most of material properties are taken from

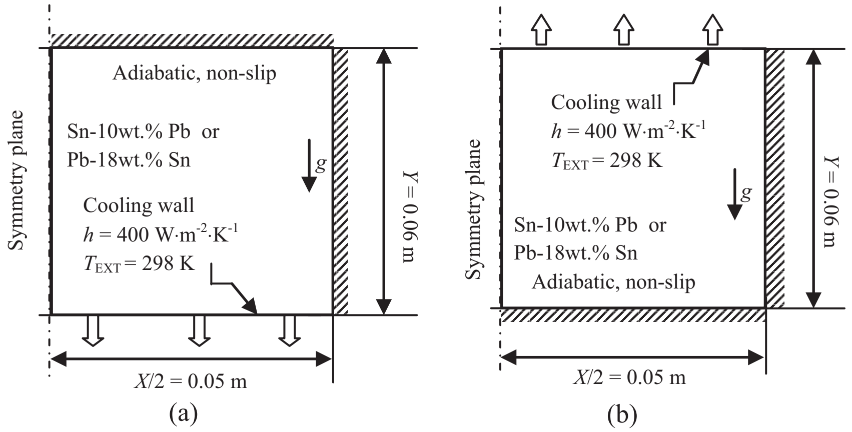

Fig. 2. Geometry of test cases with boundary and initial conditions.

Table 2
Material properties and other parameters.

	Symbol	Units	Sn-10 wt%Pb	Pb-18 wt%Sn	Ref.
Nominal concentration	c_0	–	10.0 wt%Pb	18.0 wt%Sn	
Liquidus temperature	T_{liq}	K	492.14	558.63	[42]
Melting point of solvent at $c_0 = 0$	T_f	K	505	600.65	[42]
Eutectic composition	c_{eu}	wt%	38.1	61.9	[42]
Eutectic temperature	T_{eu}	K	456	456	[35]
Liquidus slope	m	K (wt%)$^{-1}$	−1.286	−2.334	[42]
Equilibrium partition coefficient	k	–	0.0656	0.310	[42]
Reference density	ρ_{ref}	kg m^{-3}	7000	9250	[42]
Specific heat	$c_p^\ell,\ c_p^e,\ c_p^c$	J kg^{-1} K^{-1}	260	176	[42]
Thermal conductivity	$k_\ell,\ k_e,\ k_c$	W m^{-1} K^{-1}	55.0	17.9	[42]
Latent heat	Δh_f	J kg^{-1}	6.1×10^4	3.76×10^4	[42]
Viscosity	μ_ℓ	kg m^{-1} s^{-1}	1.0×10^{-3}	1.1×10^{-3}	[42]
Liquid thermal expansion coefficient	β_T	K^{-1}	6.0×10^{-5}	1.16×10^{-4}	[42]
Liquid solutal expansion coefficient	β_C	wt%$^{-1}$	-5.3×10^{-3}	4.9×10^{-3}	[42]
Primary dendritic arm spacing	λ_1	m	1.3×10^{-3}	1.85×10^{-3}	[42]
Second dendritic arm spacing	λ_2	m	0.65×10^{-4}	1.85×10^{-4}	[42]
Diffusion coefficient (liquid)	D_ℓ	m^2 s^{-1}	4.5×10^{-9}	4.5×10^{-9}	[43]
Initial temperature	$T_0 = T_{liq}$	K	492.14	558.64	[42]
Heat transfer coefficient	h	W m^{-2} K^{-1}	400	400	[42]
External temperature	T_{EXT}	K	298	298	[42]
Density difference of solid and liquid	$\Delta\rho$	kg m^{-3}	304	420	[44]
Gibbs Thomson coefficient	Γ	m K	6.5×10^{-8}	7.9×10^{-8}	[45]
Initial inoculant number density	n_{em}	m^{-3} s^{-1}	1.0×10^{10}	1.0×10^{10}	
Initial equiaxed number density	n_{eq}	m^{-3} s^{-1}	1.0×10^7	1.0×10^7	
Gaussian distribution width	ΔT_N	K	3.0	3.0	
Undercooling for maximum grain production rate	ΔT_σ	K	5.0	5.0	

a numerical benchmark as suggested by Bellet et al. [42]. Only half of the test casting is calculated by setting a symmetry plane at the left boundary. Two different alloys are considered: one is Sn-10 wt%Pb with solute element Pb heavier than the solvent Sn; the other is Pb-18 wt%Sn with solute element Sn lighter than the solvent Pb. The solidified equiaxed crystal is considered always heavier than the melt. Thermodynamic data and thermal physical properties of both alloys are listed in Table 2. The casting is cooled unidirectionally, either from the bottom or from the top. Therefore, 4 test cases of calculations are defined and they are correspondent to 4 cases in the bottom row of Fig. 1.

3. Modeling results

3.1. Case E1

Case E1 (Fig. 1(e)) considers the solidification of Sn-10 wt%Pb alloy from the bottom. Both thermal and solutal buoyancy forces of the melt act downwards, but the buoyancy force of the equiaxed phase, pointing downwards as well, is dominant over the thermal and solutal buoyancy forces of the melt. The solidification sequence is shown in Fig. 3.

Nucleation of equiaxed crystals and solidification start from the bottom wall, gradually extend to the upper region. The inoculants, as quantified by their number density n_{em} (Fig. 3(c.x) in color scale), begins to be activated as and transferred into equiaxed nuclei, which can grow as equiaxed grains. The number density of equiaxed grains n_{eq} is also shown in the same figure Fig. 3(c.x), but as isolines. The equiaxed phase has higher density than the melt; they tend to sink. Because the downward buoyancy force of the equiaxed phase overwhelms the thermal and solutal buoyancy forces of the melt. As shown in Fig. 3(b.x), the motion of equiaxed grains is mostly downwards. The velocity field of the melt (Fig. 3(a.x)) becomes very unstable. The sinking grains tend to drag the melt downwards on the one hand; sedimentation of equiaxed grains pushes the melt upwards on the other hand. During the early stage of solidification (Fig. 3(a.2)), some vortexes of

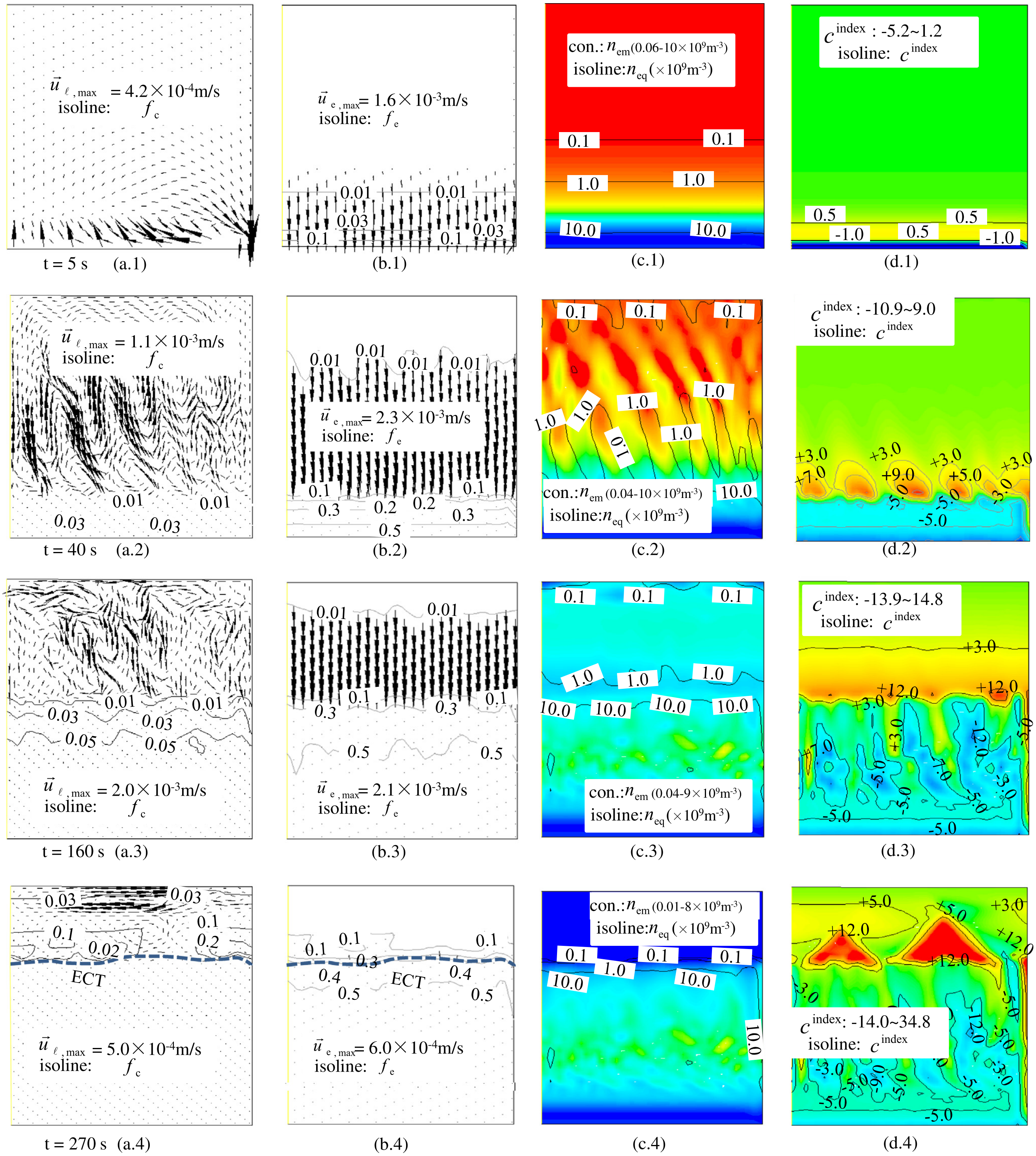

Fig. 3. Solidification sequence of Case E1. The column a.x shows the liquid velocity overlaid by f_c isolines, as well as the ECT (blue dash line in a.4); b.x shows the equiaxed velocity field overlaid by f_e isolines; c.x shows the evolution of n_{em} in color scale overlaid by n_{eq} isolines; d.x shows the evolution of macrosegregation index overlaid by its isolines. The alloy is Sn-10 wt%Pb. (For interpretation of the references to color in this figure legend, the reader is referred to the web version of this article.)

melt flow develop. With the progress of solidification, some vortexes merge together to form a few larger vortexes (Fig. 3(a.3)). Finally, a double diffusive convection cell is observed during the late stage of solidification (Fig. 3(a.4)).

The transport of n_{em} follows the melt flow, while the transport of n_{eq} follows the velocity of equiaxed phase. The sinking/sedimentation of equiaxed phase leads to the increase of both f_e (Fig. 3(b.x)) and n_{eq} (Fig. 3(c.x)) in the bottom region. The region of liquid-solid two phase mixture extends gradually to the upper part of the casting due to the continuous solidification and enhanced mixing by the crystal movement and melt flow. Nucleation event continues in the upper boarder of the two phase mixture region. During the late stage of solidification, almost all inoculants are consumed (Fig. 3(c.4)), and no further nucleation of equiaxed grains occurs. The remaining melt in the upper part of the casting can only solidify as columnar structure. The consumption of the inoculants stimulates the equiaxed-to-columnar transition (ECT).

The pile-up of equiaxed phase in the bottom region is shown in Fig. 3(b.x). As the amount of equiaxed phase increases to a certain limit at the bottom, i.e. $f_{\mathrm{e}}^{\mathrm{Env}}$ $(=f_{\mathrm{e}}/f_{\mathrm{si}}) \geqslant f_{\mathrm{e,packing}}$, the motion of the equiaxed phase stops. The equiaxed grains can continue to grow, but they are stationary. The stationary equiaxed phase region can develop into a columnar structure, if no sufficient equiaxed phase (competing with the growth of columnar structure) exists in the columnar tip front. However, during the early stage of solidification (Fig. 3(a.1–3) and (b.1–3)), due to the continuous nucleation and growth of the equiaxed grains ahead of the columnar tip front no visible columnar structure (less than 0.03 of the maximum f_{c}) can be seen. The solidification structure is dominantly equiaxed. The ECT event occurs at ca. 243 s, when most inoculants are consumed in the upper region and no sufficient equiaxed grains exist in front of columnar tip front. The ECT boarder is observed in Fig. 3 (a.4). Below the ECT line it is dominant by equiaxed structure, while above the ECT line there is only columnar structure.

Fig. 3(d.x) shows the formation of macrosegregation. During the early stage of solidification (before ECT) the macrosegregation is caused by the crystal sedimentation. The accumulation of equiaxed phase at the bottom region induces the negative segregation. The solute-enriched melt is pushed upwards, leading to formation of a layer of positively segregated melt in the front of the two-phase mixture region. This positive segregation layer is not uniform (Fig. 3(d.2)), because of the vortexes of the melt flow. This positive segregation layer is also not stable, because the subsequent solidification, crystal sedimentation and melt flow will adapt its distribution. With the progress of solidification, some weak positively-segregated bands form (Fig. 3(d.3)) in the packed equiaxed region. These weak positive segregation bands follow the traces of the quasi-steady vortexes in the melt flow. After ECT, the solidification structure is purely columnar, and the dominant mechanism of macrosegregation is the thermo-solutal convection. As we mentioned previously, both thermal and solutal buoyancy forces of the melt act downwards. The thermal and solutal buoyancy forces try to stabilize the melt, i.e. to minimize the flow. Therefore, the flow intensity at the late stage of solidification becomes very weak ($\sim 10^{-4}$ m/s), and the flow pattern is also adapted into a kind of double diffusive convection cell. Finally, two positively segregation regions are 'frozen' into the columnar structure just above the ECT line.

3.2. Case E2

Case E2 (Fig. 1(e)) considers the solidification of the alloy Pb-18 wt%Sn from the bottom. The settings of this case are the same as the Case E1 except for the alloy. In Case E2 the solute element (Sn) is now lighter than the solvent (Pb), i.e. the solutal buoyancy force of the melt points upwards, leading to much stronger solutal convection ($\sim 10^{-2}$ m/s) than for the Case E1. The solidification sequence is shown in Fig. 4.

Initially, nucleation and solidification start from the bottom. Inoculants (n_{em}) begin to be activated as equiaxed nuclei (n_{eq}), Fig. 4(c.x). The equiaxed grains tend to sink (Fig. 4(b.x)), while the melt rises. The velocity field of the melt (Fig. 4(a.x)) is also unstable (similar to E1), but the flow pattern looks quite different from that of E1. Less number of vortexes and larger magnitude of the melt velocity are found for the current Case E2. The velocity field of the equiaxed phase is more chaotic.

The crystal sedimentation leads to pile-up of equiaxed crystals in the bottom. The region of the liquid-solid two phase mixture extends gradually towards the upper region. Nucleation of new equiaxed crystals continues at the upper border of the two phase mixture region. During the late stage of solidification, inoculants are almost consumed (Fig. 4(c.4)). The ECT event occurs at around 110 s. The remaining melt in the upper part solidifies as columnar structure.

Fig. 4(d.x) shows the formation of macrosegregation. During the early stage of solidification (before ECT) sedimentation-induced negative segregation is observed at the bottom. The solute-enriched melt is pushed upwards, leading to a gradual enrichment of solute in the bulk melt (similar to Case E1). The significant differences between cases E2 and E1 are the flow patterns and their magnitudes of melt flow. The large velocity of the melt for the Case E2 due to solutal convection enhances the solute mixing in the bulk melt, rather than the concentrated positively-segregated band in front of the liquid-solid two phase mixture region of Case E1. After ECT (110 s) the solidification structure is pure columnar, and the dominant mechanism of macrosegregation is thermo-solutal convection. Again, the large velocity magnitude of the interdendritic and bulk melt leads to formation of a large positive segregation, which is concentrated in the top surface region of the test case (Section 4.1, Fig. 7). As what we learnt from the Case C2 of Part I (pure columnar solidification of Pb -18 wt% Sn from bottom) [4], two positive segregation channels develop along both side boundaries in the Case E2 during the late stage of columnar solidification.

3.3. Case E3

Case E3 (Fig. 1(g)) considers the solidification of the alloy Pb-18 wt%Sn from the top. The equiaxed grains, as nucleated from the top, will sink immediately downwards, while the melt, as enriched with solute element Sn, tries to stay in the top region. The solidification sequence of this case, as shown in Fig. 5, becomes more dynamic than the last two cases (E1 and E2).

Nucleation (Fig. 5(c.x)) and solidification start from the top surface. The sinking equiaxed grains (Fig. 5(b.x)) drag the surrounding melt with them, initializing a transient melt flow in the bulk (Fig. 5 (a.x)). This transient flow brings inoculants from lower region to upper cold region where nucleation continues. The sinking velocity of equiaxed phase is very large ($\sim$0.02 m/s), and the equiaxed phase piles up at the bottom. The further solidification process includes: (1) transport of inoculants by the melt flow to upper regions, where nucleation continues; (2) growth of equiaxed grains; (3) sinking of equiaxed grains and further pile-up of equiaxed phase at the bottom. An interesting phenomenon (Fig. 5(c.x)) is that the settling equiaxed crystals can entrap a part of rest melt in the inter-granular space. That means that a part of inoculants might also be entrapped there without being activated as equiaxed nuclei. In this case the ECT event occurs quite early, at around 70 s. The rest melt in the upper region solidifies as columnar structure.

Fig. 5(d.x) shows the formation of macrosegregation. In principle, the macrosegregation mechanism of equiaxed solidification (before ECT) is similar to the last two cases as cooled from the bottom, E1 and E2. The main difference is that the solute mixing is more effective for Case E3. Generally, one can see a similar segregation pattern as that of E1 and E2: i.e. sedimentation-induced negative segregation at the bottom region and a positive segregation in the top, but the transition zone from negative to positive segregation is wider. After ECT melt flow during columnar solidification adapts the distribution in the upper region. At the end of solidification a relatively strong positive segregation at the top surface region is observed.

3.4. Case E4

Case E4 (Fig. 1(h)) considers solidification of alloy Sn-10 wt%Pb from the top. The solidification sequence is shown in Fig. 6. Solidification of this case is quite similar to Case E3, especially

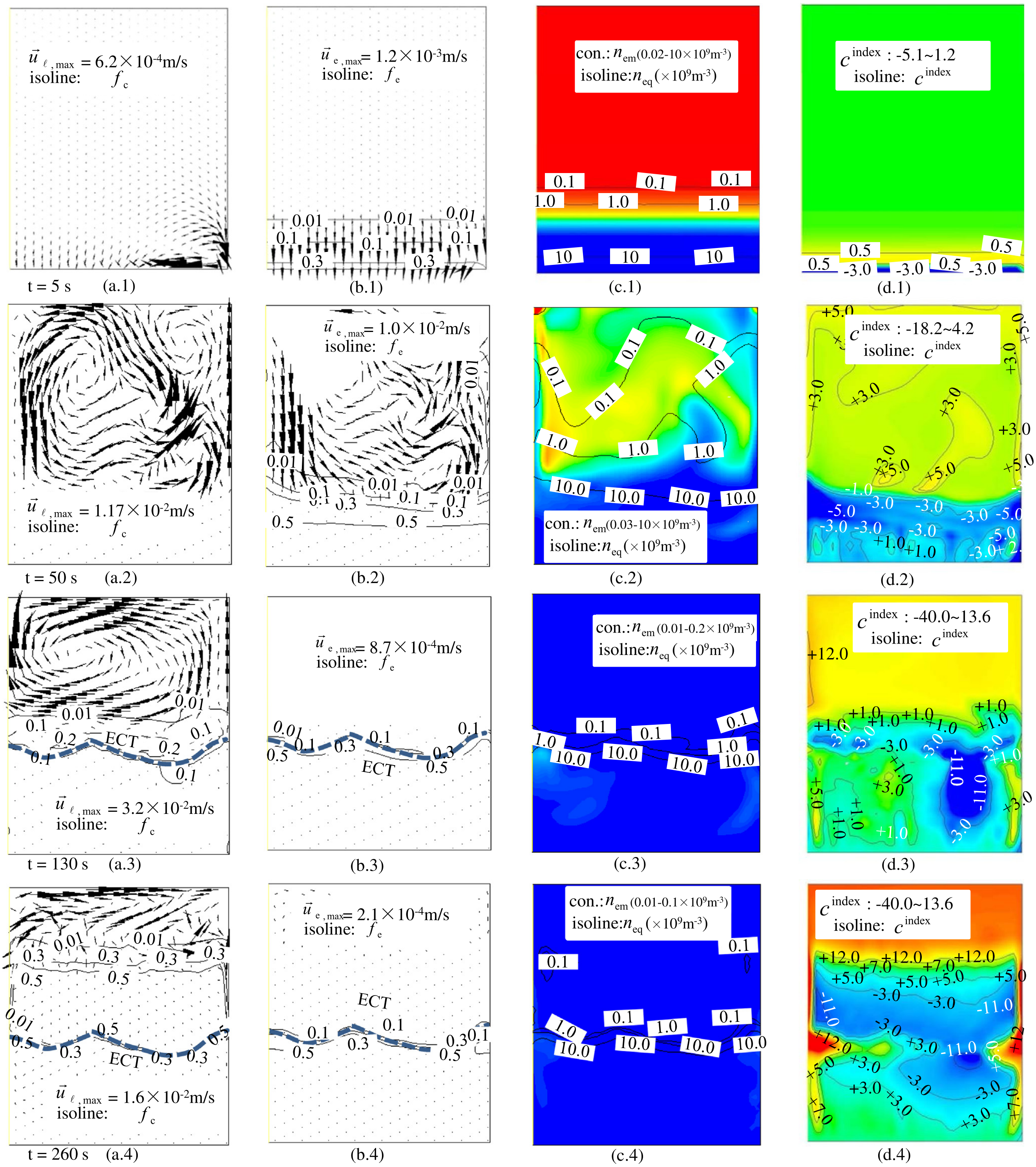

Fig. 4. Solidification sequence of Case E2. The column a.x shows the liquid velocity overlaid by f_c isolines, as well as the ECT (blue dash line in a.3, a.4); b.x shows the equiaxed velocity field overlaid by f_e isolines; c.x shows the evolution of n_{em} in color scale overlaid by n_{eq} isolines; d.x shows the evolution of macrosegregation index overlaid by its isolines. The considered alloy is Pb-18 wt%Sn. (For interpretation of the references to color in this figure legend, the reader is referred to the web version of this article.)

during the early stage. Analysis of the early stage equiaxed solidification can refer to that of Case E3. The major difference between this Case E4 and the Case E3 is the late stage of columnar solidification. ECT occurs at 125 s. After ECT the columnar primary tip front grows very fast, and the columnar structure spreads from the ECT line immediately into the entire upper region, leaving the remaining melt solidifying in the large inter-columnar region (mushy zone). As the casting is cooled continuously from the top surface, the upper surface is in favor of solidification. The upper surface solidifies faster than the inner region of the mushy zone. The thermo-solutal convection is still quite active in the mushy zone. The solutal buoyancy force of this alloy points downwards, in the same direction of the thermal buoyancy force. The last-to-solidify region of the Case E4 is located in the region close to ECT line. Therefore, the large area of positive segregation in the upper region, which has formed during the early stage equiaxed

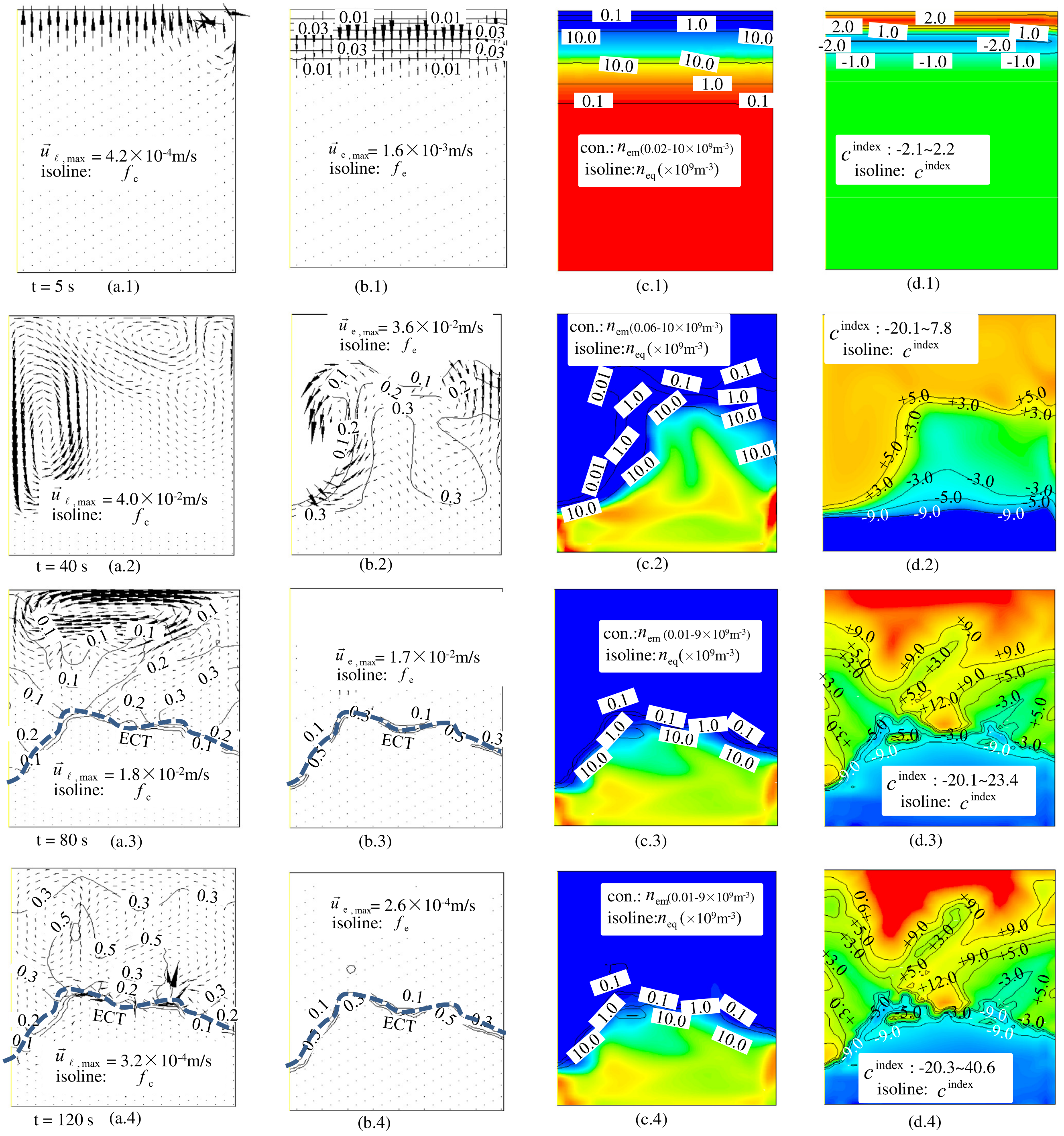

Fig. 5. Solidification sequence of Case E3. The column a.x shows the liquid velocity overlaid by f_c isolines, as well as the ECT (blue dash line in a.3, a.4); b.x shows the equiaxed velocity field overlaid by f_e isolines; c.x shows the evolution of n_{em} in color scale overlaid by n_{eq} isolines; d.x shows the evolution of macrosegregation index overlaid by its isolines. The considered alloy is Pb-18 wt%Sn. (For interpretation of the references to color in this figure legend, the reader is referred to the web version of this article.)

solidification, is gradually driven into the last-to-solidify region by the thermo-solutal convection. This leads to the formation of a large positive segregation band above the ECT line.

4. Discussion

4.1. Macrosegregation intensity by different mechanisms

The calculated macrosegregation results of the 4 test cases of equiaxed solidification are compared in Fig. 7. The segregation distribution is shown in color scale, but its intensity is analyzed by the c^{index} distribution range as labeled in the figures and by the global macrosegregation intensity (GMI). GMI is used to evaluate the global average segregation intensity, while the c^{index} distribution range is used to quantify the macrosegregation extremes.

During equiaxed solidification, there are four mechanisms which lead to the formation of macrosegregation: crystal sedimentation, thermal buoyancy flow, solutal buoyancy flow and species diffusion in the interdendritic/inter-granular melt. We learnt from Part I [4] that the diffusion-induced surface segregation falls into

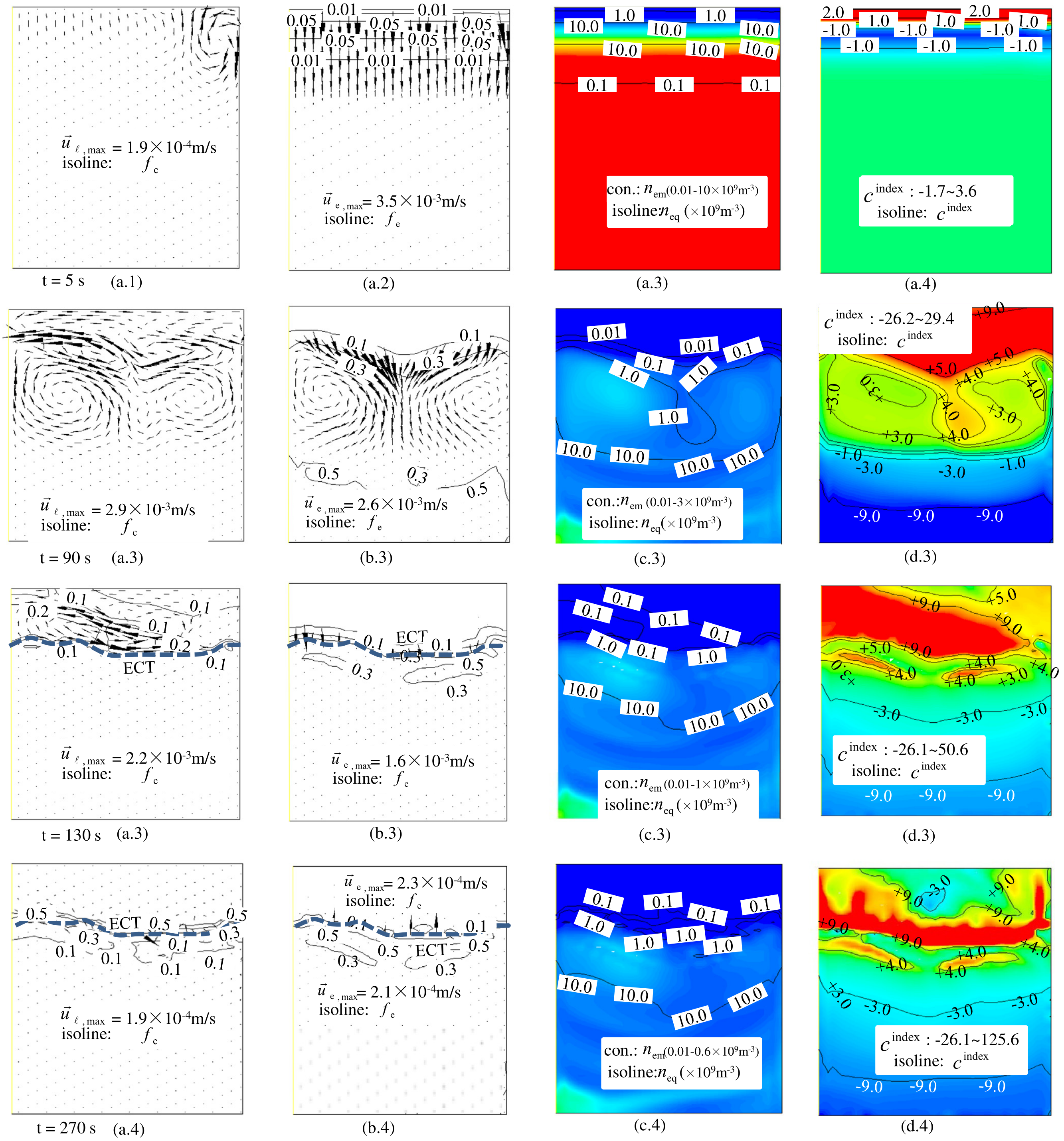

Fig. 6. Solidification sequence of Case E4. The column a.x shows the liquid velocity overlaid by f_c isolines, as well as the ECT (blue dash line in a.3, a.4); b.x shows the equiaxed velocity field overlaid by f_e isolines; c.x shows the evolution of n_{em} in color scale overlaid by n_{eq} isolines; d.x shows the evolution of macrosegregation index overlaid by its isolines. The considered alloy is Sn-10 wt%Pb. (For interpretation of the references to color in this figure legend, the reader is referred to the web version of this article.)

the range of $|c^{index}| < 4\%$ or GMI < 0.1. Thus, it is ignorable in comparison to the sedimentation-induced segregation (Fig. 7). Among the other three mechanisms, crystal sedimentation is dominant. Evidently, during early stage of solidification, a negative segregation zone develops at the bottom, and the bulk melt in the upper region is gradually enriched with solute (Figs. 3–6). No matter what alloy is considered and which cooling condition (cooling from top or from bottom) is applied, settling of equiaxed crystals at the bottom leads to negative segregation. Further theoretical analysis of the sedimentation-induced macrosegregation is carried out in Section 4.2. The intensity/strength of sedimentation-induced negative segregation at the bottom region is in the order of $c^{index} = -10\%$. For some special cases, c^{index} might reach extreme value of −32% at certain position. After ECT, only two flow mechanisms operate: thermal and solutal buoyancy. The concentration distribution in the upper region is then adapted by the thermo-solutal convection during columnar solidification. As mentioned above, the remaining melt in the upper part after ECT is normally enriched with solute, i.e. positively-segregated. The formation of the final positive segregation distribution depends on the alloy and cooling direction [4]. Therefore, different positive segregation patterns are observed for the cases, E1–E4.

Can one estimate the macrosegregation tendency based on the simple settings of each case (E1–E4) without performing any simulation? The answer is: difficult to estimate. Although we know that the start of equiaxed solidification leads to a negative segregation at the bottom, the occurrence of ECT and the final distribution of positive segregation in the upper region during columnar solidification governed by thermo-solutal convection cannot be estimated. If no ECT occurs, things become easier. With the ECT, the dominant macrosegregation mechanism is changed from crystal sedimentation to thermo-solutal convection. Furthermore, the macrosegregation as induced by thermo-solutal buoyancy depends on the alloy and cooling direction.

Can a technical alloy solidify as pure equiaxed structure without ECT? According to the classical heterogeneous nucleation theory, equiaxed nuclei originate from exogenous particles/inoculants which exist in the parent melt. The nucleation event creates new crystals, and in the meantime it consumes the inoculants. If all inoculants are consumed and the equiaxed crystals are transported away, the remaining melt has to solidify as columnar structure. We assume that no other nucleation mechanism operates, e.g., homogenous nucleation, crystal multiplication, or fragmentation of columnar dendrites. The modeling results of Fig. 7 show ECT for all cases. It implies the difficulty to get pure equiaxed structure in technical alloys by gravity casting techniques.

Notice that the assumed symmetry boundary condition for the left side of the test casting influences the calculation accuracy of macrosegregation. This symmetry boundary corresponds to an adiabatic and free-slip boundary, and no mass is allowed to cross the boundary. The reality might be different. Therefore, for engineering application of the macrosegregation model, special caution must be taken for the assumption of symmetry.

From the study of pure columnar solidification in Part 1 [4], we knew that the macrosegregation intensity is related to the velocity magnitude of flow. We anticipate that this relationship should apply for equiaxed solidification as well. The modeling results of Fig. 7, however, do not clearly show this relationship. The reason is that for all 4 test cases of equiaxed solidification, the velocity magnitude of crystal sedimentation and flow are in the similar range, i.e. 10^{-3}–10^{-2} m/s. The labeled maximum velocity in Fig. 7 is the value at a certain moment and at a certain position, it does not represent statistic average velocity magnitude during the solidification process. Generally, during equiaxed solidification the velocity magnitude of the crystal sedimentation and the flow is larger than that of thermo-solutal convection during pure columnar solidification. The difference of macrosegregation intensity among all 4 equiaxed solidification cases is not so large, and they are in the similar range, i.e. c^{index} from −25 to +180%, and GMI is from 5 to 33.

Another interesting phenomenon as observed is that the final area of equiaxed zone of test cases E1 and E4 (alloy Sn–10 wt% Pb) is evidently larger than that of test cases E2 and E3 (alloy Pb–18 wt%Sn). The modeling result (Fig. 7) implies that the final area of equiaxed zone is mostly dependent on the alloy rather than the cooling (solidification) direction. As the total number of nucleation inoculants are set equal for all test cases and most inoculants are eventually activated as equiaxed nuclei, the smaller area of equiaxed zone (E2 and E3) corresponds to the finer equiaxed grains. This kind of alloy-dependency of the equiaxed zone (or grain size) can be explained by the so-called "growth-restricting effect" GRE according to Hellawell and Maxwell [46,47], where $GRE = m(k-1)c_0$. The role of solute element in an alloy is to restrict the growth rate of the growing interface, which, in turn,

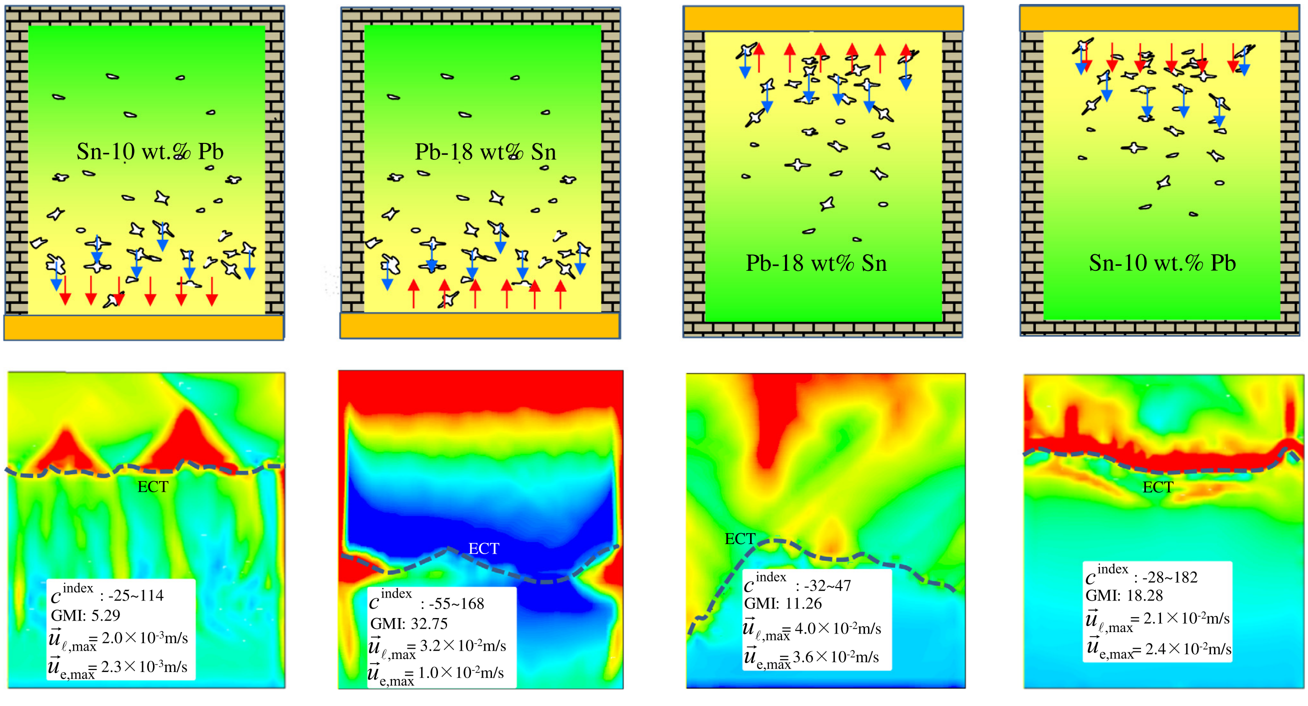

(a) Case E1 (b) Case E2 (c) Case E3 (d) Case E4

Fig. 7. Comparison of the final macrosegregation patterns for the 4 test cases of equiaxed solidification. The segregation (c^{index} in %) contours are shown in color scale, and they have different distribution ranges, as labeled in the figure. The maximum flow velocity and crystal sedimentation velocity during solidification and the global macrosegregation intensity (GMI) are also given. The yellow walls indicate chilled walls, while the hatched ones are adiabatic. (For interpretation of the references to color in this figure legend, the reader is referred to the web version of this article.)

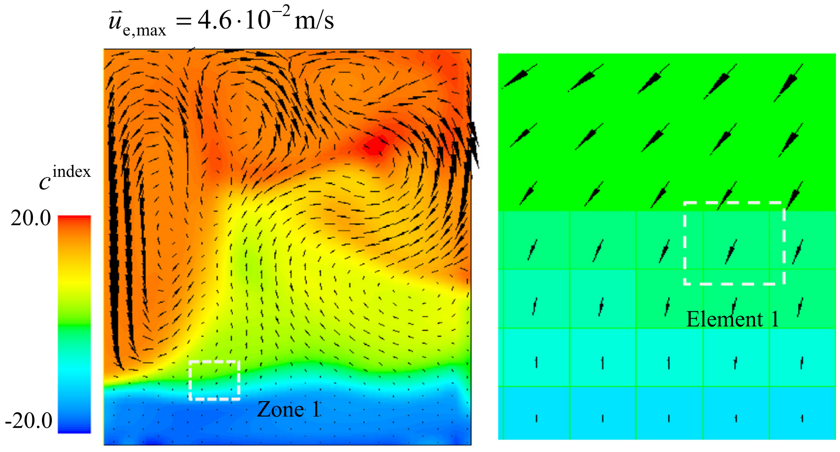

(a) (b)

Fig. 8. Solidification event in Case E3 (t = 30 s): Pb-18 wt%Sn cooling from the top. (a) Macrosegregation index overlaid by equiaxed velocity vectors; (b) zoom-in view of Zone 1.

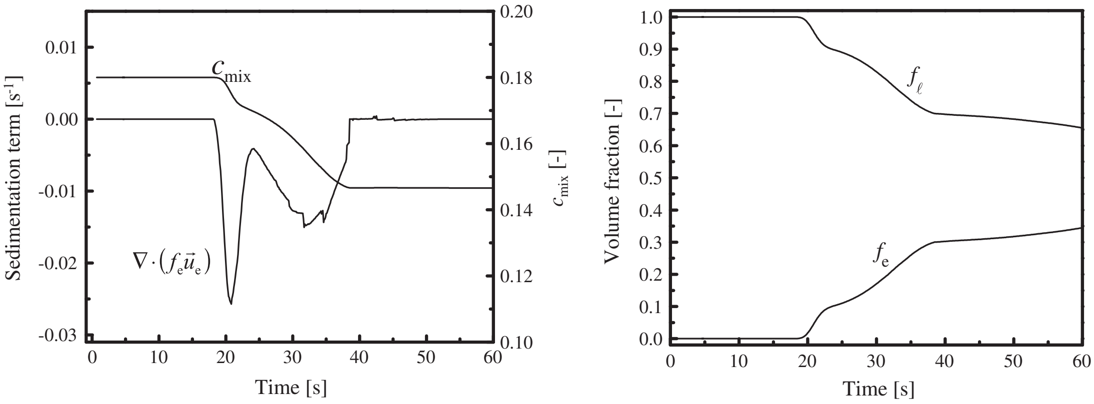

(a) (b)

Fig. 9. Analysis of c_{mix} evolution of in a reference element (element 1 as marked in Fig. 8(b)). (a) Sedimentation term and mixture concentration; (b) volume fractions of phases.

allows more time for further nucleation events to occur. Therefore, a large value of GRE can be related to a fine equiaxed structure, i.e. small area of equiaxed zone. The GRE values for alloy Sn–10 wt%Pb and Pb–18 wt%Sn are 12 and 29 correspondingly.

4.2. Sedimentation-induced macrosegregation

Sedimentation-induced macrosegregation during equiaxed solidification can be analyzed according to the transport of equiaxed phase, which is described by the following equation [21]:

$$\frac{\partial}{\partial t}(c_{\mathrm{mix}}) \approx (c_\ell - c_{\mathrm{e}}) \cdot \nabla \cdot \left(f_{\mathrm{e}}\vec{u}_{\mathrm{e}}\right) \tag{28}$$

Variation of the local mixture concentration, c_{mix}, depends on the concentration difference between the melt and the equiaxed phase, $c_\ell - c_{\mathrm{e}}$, and the divergence of the superficial velocity of the equiaxed phase, $\nabla\cdot(f_{\mathrm{e}}\vec{u}_{\mathrm{e}})$, which is also named as sedimentation term. $c_\ell - c_{\mathrm{e}}$ is always positive for alloys with partitioning coefficient k less than one. The sedimentation term, $\nabla\cdot(f_{\mathrm{e}}\vec{u}_{\mathrm{e}})$, gives an indication about the local depletion or accumulation of equiaxed crystals. For example, a negative value of $\nabla\cdot(f_{\mathrm{e}}\vec{u}_{\mathrm{e}})$ means accumulation of equiaxed crystals in the local volume element. According to Eq. (28), the accumulation of equiaxed crystals would lead to a negative value of $\partial c_{\mathrm{mix}}/\partial t$, i.e. the decrease of c_{mix}, and thus to the formation of negative segregation.

Eq. (28) can be applied to analyze the sedimentation-induced macrosegregation of the current benchmark. An example is shown in Figs. 8 and 9. In Zone 1 of Fig. 8, the equiaxed velocity slows down and equiaxed crystals settle. Taking one reference element (Element 1) in Zone 1, the evolution of quantities of c_{mix}, $\nabla\cdot(f_{\mathrm{e}}\vec{u}_{\mathrm{e}})$, f_{e} and f_ℓ are tracked. Between 23 and 50 s a strong negative sedimentation term $\nabla\cdot(f_{\mathrm{e}}\vec{u}_{\mathrm{e}})$ occurs, and f_{e} increases correspondingly. As consequence c_{mix} decreases and a negative segregation appears there.

Similar to the study in Part 1 [4], thermo-solutal convection induced macrosegregation during columnar solidification after ECT can be analyzed according to the flow-solidification interaction [21].

4.3. Mesh sensitivity

Calculations with 8 different mesh (grid) sizes for the Case E3 were performed, and the resulting segregation patterns are shown in Fig. 10. As the mesh size decreases from 2.0 mm to 0.8 mm, the global segregation tendencies are quite similar: a positive

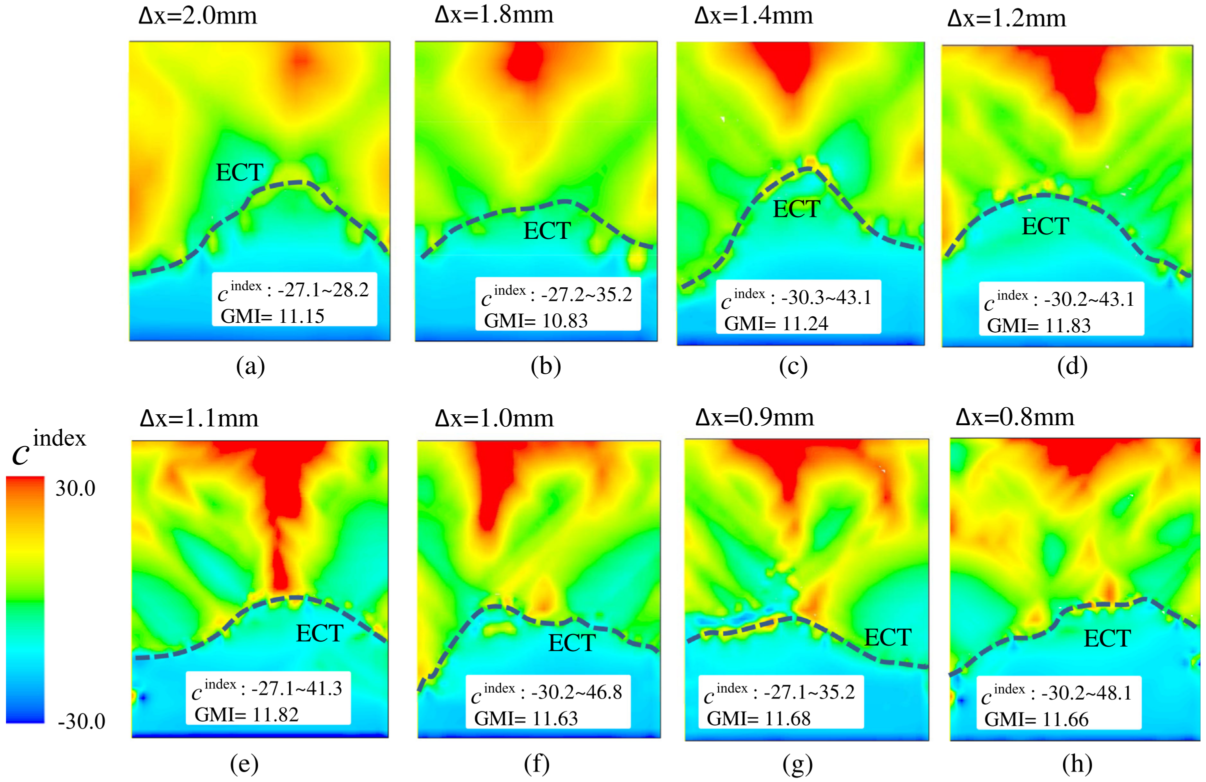

Fig. 10. Mesh sensitivity of macrosegregation predictions for Case E3. The macrosegregation contours are shown in color scale for mesh sizes of (a) 2.0 mm, (b) 1.8 mm, (c) 1.4 mm, (d) 1.2 mm, (e) 1.1 mm, (f) 1.0 mm, (g) 0.9 mm and (h) 0.8 mm.

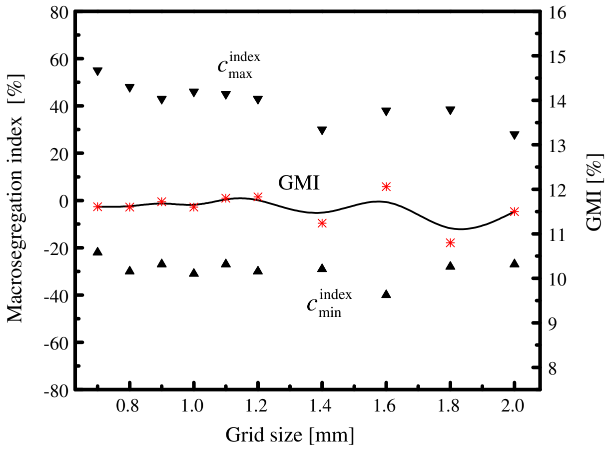

Fig. 11. Influence of mesh size on the macrosegregation extremes and GMI (Case E3).

macrosegregation zone in the upper region, a crystal sedimentation induced negative segregation zone in the bottom region, and a negative-to-positive transition zone is observed near the ECT line. In order to perform the evaluation of the mesh sensitivity more precisely, the c^{index} distribution range (segregation extremes $c_{\min}^{\text{index}}$, $c_{\max}^{\text{index}}$) and the global macrosegregation intensity (GMI) are plotted in Fig. 11 against the mesh (grid) size. The variation of GMI with different mesh sizes is quite small. As the mesh size is reduced to 1.2 mm, GMI seems to become stable at a value of 11.7. That means that a relative coarse mesh (1.2 mm) is sufficient for the prediction of the global macrosegregation intensity.

The distribution of c^{index} varies with the mesh size, even when the mesh size is reduced to as small as 0.8 mm (Fig. 10). The area of equiaxed zone (the negative segregation zone below the ECT line) seems to be similar for all calculations with different mesh sizes, but the shapes of the ECT line are different. The most significant difference between those calculations of different mesh sizes is the distribution of positive segregation in the upper pure columnar solidification region. Although a large positive segregation zone which mostly concentrates near the top surface is predicted by all calculations, the details of its distribution are different. The quantitative analysis of the segregation extremes ($c_{\min}^{\text{index}}$, $c_{\max}^{\text{index}}$) in Fig. 11 shows that no converged results are obtained, even when the mesh size is reduced to 0.8 mm. This kind of mesh dependency is understandable. In the early stage of equiaxed solidification, the details of crystal sedimentation and the induced melt flow are slightly mesh-dependent; hence the ECT line is also slightly influenced by the mesh size. In the late stage of columnar solidification, the interdendritic flow is also slightly mesh-dependent; hence the final distribution of the positive segregation is influenced by the mesh size. However, key features of the predicted global segregation patterns of different test cases are valid. The modeling results presented in this paper are based on the mesh size of 1 mm.

5. Conclusions

In order to provide exercise examples for metallurgical students to learn different macrosegregation mechanisms, a simple 2D casting with ideal configuration of equiaxed solidification was simulated by using a volume-average based solidification model [3]. The model was modified by (i) consideration of heterogeneous nucleation of equiaxed crystals and transport of inoculants and (ii) consideration of equiaxed-to-columnar transition (ECT). 4 test cases were calculated where cooling occur unidirectionally, either upwards or downwards. It was believed that the final macrosegregation tendency in each test case should be estimated without performing any simulation. However, the modeling results show that more complicated details of macrosegregation distribution can develop due to the complexity of the equiaxed-to-columnar transition (ECT). Following conclusions were drawn.

(1) Even for such simple case of equiaxed solidification, it is quite difficult to estimate the final macrosegregation tendency without performing any simulation. The main difficulty arises from the ECT. During the early stage of equiaxed solidification before ECT, the macrosegregation tendency is predictable: equiaxed sedimentation, i.e. the dominant macrosegregation mechanism, induces negative segregation in the bottom region; while solute-enriched melt is distributed in the upper region. After the ECT during the late stage of columnar solidification, the thermo-solutal convection becomes the dominant macrosegregation formation mechanism. The redistribution of the positive macrosegregation pattern in the upper region by thermo-solutal convection depends on the alloy and cooling direction.

(2) According to the classical heterogeneous nucleation theory [35,40] that equiaxed nuclei originate from exogenous particles/inoculants, it is difficult to get pure equiaxed structure in technical alloys by gravity casting technique. The modeling results show that an ECT event occurs during late stage of solidification when all inoculants are consumed. The remaining melt in the upper part of the test casting solidifies as columnar structure.

(3) Although we found that the macrosegregation intensity during pure columnar solidification increased with the velocity magnitude of melt flow, the modeling results did not clearly show this relationship in the 4 test cases of equiaxed solidification.

Calculation of macrosegregation is sensitive to the mesh size. The fine details of the c^{index} distribution should be interpreted with caution regarding mesh quality, but key features of the predicted segregation patterns of the 4 test cases of equiaxed solidification are valid.

Other 4 cases of pure columnar solidification were presented as Part I in a previous paper [4].

Acknowledgements

The authors acknowledge the financial support from Austrian Research Promotion Agency (FFG) through the project of Bridge Early Stage (No. 842441), as well as the technical support from the industrial partner Primetals Technologies (former Siemens VAI).

References

[1] J.A. Dantzig, M. Rappaz, Solidification, EPFL Press, 2009.
[2] A. Ludwig, Lecture note on solidification course in Swiss Federal Institute of Technology of Lausanne (EPFL), Lausanne, 2015.
[3] M. Wu, A. Ludwig, Metall. Mater. Trans. A 37 (2006) 1613–1631.
[4] M. Wu, Y. Zheng, A. Kharicha, A. Ludwig, Comput. Mater. Sci. 124 (2016) 444–455.
[5] W. Kurz, D.J. Fisher, Fundamentals of Solidification, third ed., Trans Tech Pub, Aedermannsdorf, Switzerland, 1992.
[6] M.C. Flemings, Solidification Processing, McGraw-Hill, 1974.
[7] M.C. Flemings, ISIJ Int. 40 (2000) 833–841.
[8] A. Ohno, Solidification: The Separation Theory and Its Practical Applications, Springer Science & Business Media, 1987.
[9] J. Ni, C. Beckermann, Metall. Mater. Trans. B 22 (1991) 349–361.
[10] C. Beckermann, R. Viskanta, Appl. Mech. Rev. 46 (1993) 1–27.
[11] J. Ni, C. Beckermann, J. Mater. Process. Manuf. Sci. 2 (1993) 217–231.
[12] M. Wu, A. Ludwig, J. Luo, Mater. Sci. Forum. 475–479 (2005) 2725–2730.
[13] M. Wu, A. Ludwig, L. Ratke, Model. Simul. Mater. Sci. 11 (2003) 755–769.
[14] R. Nadella, D. Eskin, Q. Du, L. Katgerman, Prog. Mater. Sci. 53 (2008) 421–480.
[15] C. Wang, C. Beckermann, Metall. Mater. Trans. A 27 (1996) 2754–2764.
[16] M. Wu, A. Ludwig, Acta Mater. 57 (2009) 5621–5631.
[17] M. Wu, A. Ludwig, Acta Mater. 57 (2009) 5632–5644.
[18] A. Ciobanas, Y. Fautrelle, J. Phys. D: Appl. Phys. 40 (2007) 3733–3741.
[19] Ø. Nielsen, A. Mo, B. Appolaire, H. Combeau, Metall. Mater. Trans. A 32 (2001) 2049–2060.
[20] N. Leriche, H. Combeau, C.-A. Gandin, M. Založnik, IOP Conf. Ser.: Mater. Sci. Eng. 84 (2015) 012087.
[21] M. Wu, L. Konozsy, A. Ludwig, W. Schutzenhofer, R. Tanzer, Steel Res. Int. 79 (2008) 637–644.
[22] A. Ludwig, M. Gruber-Pretzler, F. Mayer, A. Ishmurzin, M. Wu, Mater. Sci. Eng. A 413 (2005) 485–489.
[23] M. Wu, J. Li, A. Ludwig, A. Kharicha, Comput. Mater. Sci. 79 (2013) 830–840.
[24] M. Wu, J. Li, A. Ludwig, A. Kharicha, Comput. Mater. Sci. 92 (2014) 267–285.
[25] M. Wu, A. Fjeld, A. Ludwig, Comput. Mater. Sci. 50 (2010) 32–42.
[26] M. Ahmadein, M. Wu, J. Li, P. Schumacher, A. Ludwig, Metall. Mater. Trans. A 44 (2013) 2895–2903.
[27] M. Ahmadein, M. Wu, A. Ludwig, J. Cryst. Growth 417 (2015) 65–74.
[28] B. Appolaire, V. Albert, H. Combeau, G. Lesoult, Acta Mater. 46 (1998) 5851–5862.
[29] A. Kharicha, M. Stefan-Kharicha, A. Ludwig, M. Wu, Metall. Mater. Trans. A 44 (2013) 650–660.
[30] A. Badillo, D. Ceynar, C. Beckermann, J. Cryst. Growth 309 (2007) 216–224.
[31] A. Badillo, D. Ceynar, C. Beckermann, J. Cryst. Growth 309 (2007) 197–215.
[32] C.A. Gandin, S. Mosbah, T. Volkmann, D.M. Herlach, Acta Mater. 56 (2008) 3023–3035.
[33] L. Hachani, K. Zaidat, Y. Fautrelle, Int. J. Heat Mass Transfer 85 (2015) 438–454.
[34] M. Wu, A. Ludwig, Metall. Mater. Trans. A 38A (2007) 1465–1475.
[35] M. Rappaz, Int. Mater. Rev. 34 (1989) 93–123.
[36] J. Li, M.H. Wu, A. Ludwig, A. Kharicha, P. Schumacher, Mater. Sci. Forum 790 (2014) 121–126.
[37] R.B. Bird, W.E. Stewart, E.N. Lightfoot, Transport Phenomena, Wiley, 2006.
[38] A. Ludwig, M. Wu, Metall. Mater. Trans. A 33 (2002) 3673–3683.
[39] J. Lipton, M.E. Glicksman, W. Kurz, Mater. Sci. Eng. 65 (1984) 57–63.
[40] T. Quested, A. Greer, Acta Mater. 52 (2004) 3859–3868.
[41] M. Bedel, K. Tveito, M. Založnik, H. Combeau, M. M'Hamdi, Comp. Mater. Sci. 102 (2015) 95–109.
[42] M. Bellet, H. Combeau, Y. Fautrelle, D. Gobin, M. Rady, E. Arquis, O. Budenkova, B. Dussoubs, Y. Duterrail, A. Kumar, Int. J. Therm. Sci. 48 (2009) 2013–2016.
[43] M. Klassen, J. Cahoon, Metall. Mater. Trans. A 31 (2000) 1343–1352.
[44] J. Gu, C. Beckermann, Metall. Mater. Trans. A 30 (1999) 1357–1366.
[45] E. Cadirli, M. Gündüz, J. Mater. Sci. 35 (2000) 3837–3848.
[46] I. Maxwell, A. Hellawell, Acta Metall. 23 (1975) 229–237.
[47] M. Easton, D. Stjohn, Metall. Mater. Trans. A 30 (1999) 1613–1623.

Paper III

Incorporation of fragmentation into a volume average **solidification model**

Yongjian Zheng, Menghuai Wu, Abdellah Kharicha, Andreas Ludwig,

Modelling and Simulation in Materials Science and Engineering, 2018, 26 015004.

IOP Publishing Modelling and Simulation in Materials Science and Engineering

Modelling Simul. Mater. Sci. Eng. **26** (2018) 015004 (18pp) https://doi.org/10.1088/1361-651X/aa86c5

Incorporation of fragmentation into a volume average solidification model

Y Zheng[1], M Wu[1,2], A Kharicha[1,2] and A Ludwig[1]

[1] Chair of Modelling and Simulation of Metallurgical Processes, Montanuniversitaet Leoben, Austria
[2] Christian Doppler Laboratory for Advanced Simulation of Solidification and Melting, Montanuniversitaet Leoben, Austria

E-mail: menghuai.wu@unileoben.ac.at

Received 5 May 2017, revised 1 August 2017
Accepted for publication 17 August 2017
Published 5 December 2017

Abstract

In this study, a volume average solidification model was extended to consider fragmentation as a source of equiaxed crystals during mixed columnar-equiaxed solidification. The formulation suggested for fragmentation is based on two hypotheses: the solute-driven remelting is the dominant mechanism; and the transport of solute-enriched melt through an interdendritic flow in the columnar growth direction is favorable for solute-driven remelting and is the necessary condition for fragment transportation. Furthermore, a test case with Sn-10 wt% Pb melt solidifying vertically downward in a 2D domain ($50 \times 60\,\mathrm{mm}^2$) was calculated to demonstrate the model's features. Solidification started from the top boundary, and a columnar structure developed initially with its tip growing downward. Furthermore, thermo-solutal convection led to fragmentation in the mushy zone near the columnar tip front. The fragments transported out of the columnar region continued to grow and sink, and finally settled down and piled up in the bottom domain. The growing columnar structure from the top and pile-up of equiaxed crystals from the bottom finally led to a mixed columnar-equiaxed structure, in turn leading to a columnar-to-equiaxed transition (CET). A special macrosegregation pattern was also predicted, in which negative segregation occurred in both columnar and equiaxed regions and a relatively strong positive segregation occurred in the middle domain near the CET line. A parameter study was performed to verify the model capability, and the uncertainty of the model assumption and parameter was discussed.

Keywords: solidification, fragmentation, volume average model, macrosegregation, columnar-to-equiaxed transition

(Some figures may appear in colour only in the online journal)

0965-0393/18/015004+18$33.00

1. Introduction

Volume-average based multiphase solidification models were recently developed and applied to calculate the formation of as-cast structure and macrosegregation for industry castings [1–4]. The following solidification features are mostly considered: the progress of columnar tip front and evolution of columnar dendrite structure, nucleation and growth of equiaxed crystals, melt flow and equiaxed crystal sedimentation, solute partitioning at the solid/liquid interface, transport of the solute species and formation of macrosegregation, interaction or competition between growing columnar and equiaxed phases, and occurrence of columnar-to-equiaxed transition (CET). However, for most such models, the origin of the equiaxed crystals was simply treated as a continuous undercooling-dependent heterogeneous nucleation event [5, 6] or a simultaneous nucleation event at a certain undercooling [4]. The number of equiaxed crystals created through fragmentation was ignored or simplified, although many laboratory experiments [7–9] and industry practices [10] have confirmed its importance.

Fragmentation has been understood through two main mechanisms: the mechanism of the mechanical fracture of the crystal dendrites, and mechanism of dendrite remelting. As early as the 1960s, Chalmers and Williamson [11] observed the formation of ice crystals in the flowing and undercooled waters and determined that mechanical rupture (fracture) was responsible for their origin. By submerging bulk ice in flowing and slightly-undercooled (−0.2 °C) water, new ice crystals in the shape of small discs were observed to grow immediately from the ice substrate. As the connection of the ice discs with the substrate of the bulk ice was very weak, they were washed away from it by the flow. Based on these experimental observation, Chalmers and Williamson [11] anticipated that this type of ‘crystal multiplication’ mechanism through mechanical rupturing would occur in metal castings by the agitation of the melt during freezing. However, a later experiment conducted by Garabedian *et al* [12] with the same type of water showed that it was very difficult to produce the ‘crystal breeding,’ that is, crystal multiplication by pure fluid sheering. A growing ice crystal was rotated in the undercooled water to create a sheer force on the ice dendrites. By sheering the water with a velocity as high as $1.5\ \mathrm{m\ s^{-1}}$, the ice crystals could not be broken. In the late 1990s, Pilling and Hellawell [13] performed a theoretical calculation for the metal alloy, and determined that the maximum stress of a dendrite arm at its weakest point (connection with the primary dendrite) under the shear flow would only reach approximately 1% of the estimated yield strength of the material at its melting point. They concluded that the interdendritic flow does not contribute directly to the crystal multiplication because of dendrite fracturing. This conclusion was confirmed by Mullis *et al* [14] with a recent calculation, for which they stated that ‘under most conditions, the likelihood of dendrites experiencing mechanical damage due to flow of the parent melt is remote.’ The fragmentation caused by remelting the dendrite stem was first proposed by Jackson *et al* through an $NH_4Cl–H_2O$ solidification experiment [15]. Forced flow during solidification was introduced by stirring the melt by using a motor-driven propeller. It was suggested that fragmentation resulted from solute rejection during dendrite growth, producing favorable conditions for the remelting of a side branch at its base and leading to subsequent ‘pinch off.’ The heat and solute generated by the growth of side branches increases the local temperature and solute concentration; this is experienced by the base of the side branches leading to the occurrence of ‘constitutional’ remelting. Stirring was performed to create or enhance the interdendritic flow necessary for transporting the fragments out of the mushy zone. This remelting-induced fragmentation theory was later supported by many follow-up experiments, for example, by using similar $NH_4Cl–H_2O$

solutions [16–18], other model alloys (succinonitrile (SCN)-acetone) [19], and even metal alloys [9, 20–22]. The method of synchrotron x-ray radiography provided an opportunity to perform *in situ* observation of the fragmentation process of metal alloys during solidification at the elevated temperature. Solute-driven remelting seems to be the dominant mechanism for fragmentation, although many authors still believe that mechanical fractures cannot be ignored [18]. Regardless of the mechanism being operated, the importance of the flow is confirmed by almost all the above-mentioned studies: (1) the flow influences the transport of the fragments and (2) promotes or retards the remelting of the dendrite stems through solute transportation.

According to Hellawell *et al* [7], five steps are necessarily considered for evaluating the fragmentation event and its consequence on the as-cast structure formation: (1) dendrite arms are first fragmented/detached from the columnar dendrites; (2) fragments are transported through the mushy zone by interdendritic flow; (3) fragments during transport through the mushy zone survive the superheat; (4) fragments continue to grow in the bulk melt; and (5) equiaxed grains grow from those fragment sediments and interact with the columnar structure, and they might be entrapped into and block the columnar structure, leading to CET. In reality, some multiphase volume average models [2, 3] have already considered steps (2)–(5). Moreover, the treatment of step (1) can be decided by answering the following questions. What is the production rate of the fragments, and what is its correlation with the thermal or solutal fields, interdendritic flow, and dendrite morphology (fraction of solid, primary, and secondary spaces)? What is the (average) size of the fragments? This information is needed by the volume average solidification model for defining the source term for the transport equation of the number density of equiaxed crystals, for defining mass and energy transfers between the columnar structure phase and the newly formed fragments, as part of the equiaxed phase. In the multiphase transport system, 'fragmentation' implies that a certain number of detached dendrite arms from the columnar structure will be converted into equiaxed structure, and correspondingly a certain amount of mass and energy will be transferred into the equiaxed phase.

Experiments were also conducted for performing fragment count. For example, Paradies *et al* [19] performed a solidification experiment under forced flow condition based on a model alloy, that is, SCN-acetone. They attempted to count the number of detached fragments at the front of the mushy zone. Fragments that cannot be transported out of the mushy zone (fully remelted or locked into the dendrite network) were ignored. Based on this fragment count, they estimated the fragment production rate. The dimension of the field of view (in which the fragments were counted) seems large enough for performing statistical analysis. The original purpose of this study was to establish a correlation between the fragmentation rate and the experiment-controlling parameters, that is, the cooling rate, forced flow rate, and initial alloy composition; however, this attempt was unsuccessful. Although the velocity adjacent to the mushy zone appeared to correlate well with the fragmentation rate from the experiment of one alloy (SCN-1.3 wt% acetone), this correlation contradicted with the experiment of another alloy (SCN-6.1 wt% acetone). The size of fragments was not measured. Montgomery *et al* [18] performed another fragment count experiment based on the solidification of $NH_4Cl–H_2O$ solutions under natural convection conditions. The fragments were counted ahead of the mushy zone, and both the number and volume fraction of fragments were measured (from which average size of fragments can be estimated). Again, this study could only provide some information for understanding the production, development, and transport of crystal fragments but failed to establish a quantitative correlation of the fragmentation rate with the flow, thermal, and alloy composition parameters. By using the synchrotron x-ray radiography, Liotti *et al* attempted to count the fragmentation rate during solidification of metal alloys (Al-15 wt%Cu) [22]. A pulsed electromagnetic field was introduced to create a pulse flow in the interdendritic region, and the following valuable information was obtained. The introduced pulse flow enhances the fragmentation through the remelting mechanism; fragmentation is not a phenomenon confined to the front mushy region but is spread throughout a wide range of the mushy zone with high solid fraction. Unfortunately, owing to the limited dimensions of the specimen (200 μm) the transport of the fragments by flow through the mushy zone into the bulk melt region cannot be studied using this method. Fragments created in the deep mushy zone are not necessarily counted as active nuclei of equiaxed crystals because they cannot be transported into the bulk melt [7].

Lesoult [10] reported a very valuable study for steel based on a hypothesis that stirring of molten steel before the solidification of the front would result in seeding of the liquid with dendritic fragments. Presumably, those fragments were eroded from the columnar tip front. He determined that the fragment flux quantified by the number of crystals eroded per unit time and area of the columnar solidification front ($\mathrm{cm^{-2}\,s^{-1}}$) correlated with the tangential velocity of the liquid along the solidification front. For example, under intensity stirring (tangential liquid velocity up to $1\ \mathrm{m\,s^{-1}}$), the fragment flux reached as high as $10\text{–}100\ \mathrm{cm^{-2}\,s^{-1}}$. In addition, under natural convection condition (tangential liquid velocity of $1\ \mathrm{cm\,s^{-1}}$), the fragment flux would be reduced to approximately $1\ \mathrm{cm^{-2}\,s^{-1}}$. This concept was later implemented into a multiphase solidification model to calculate the fragmentation phenomenon during a mixed columnar-equiaxed solidification of steel [23]. As the size and shape of the newly eroded fragments were not available, they were assumed to be spheres with diameter of 1 μm. This numerical treatment seems reasonable for a solidification model but the experimentally determined relationship of the fragment flux with the tangential liquid velocity does not directly correlate with the solute-driven remelting mechanism of the fragmentation. According to the classical solidification theory [24], it is the flow in the growth direction of the primary columnar dendrites, rather than the tangential liquid velocity, that may promote the remelting of the dendrites.

Based on the Flemings' theory for local remelting of the mushy zone [24], Campanella *et al* derived an onset criterion for remelting-induced fragmentation [25]. That is, fragmentation occurs when the component of the fluid flow velocity in the thermal gradient direction, presumably coinciding with the growth direction of the primary columnar dendrites, becomes larger than the speed of the isotherms at a depth of 6–8 λ_2 (secondary dendrite arm space) in the mushy zone. This implies that the flow transports a solute-enriched melt from the deep interdendritic region into the front region of the mushy zone, reducing the melting point, and hence promoting the remelting of dendrite arms in that region. Additionally, the flow in the columnar growth direction is necessary for transporting fragments out of the mushy zone. The shortcoming of this onset criterion is that no quantitative information is provided about the production rate and size of the fragments.

Inspired by the work of Campanella *et al* [25], in this study, a local remelting-based formulation for the fragmentation is suggested and implemented in a three-phase mixed columnar-equiaxed solidification model [6, 26]. The test case was calculated to show the model features. A series of simulations were conducted to study the sensitivity of the modeling result to the numerical and modeling parameters.

2. The model

A three-phase mixed columnar-equiaxed solidification model has been described previously [6, 26]. As the columnar dendrite structure and the equiaxed grains (crystals) are treated as two separate solid phases, their evolutions through solidification are calculated explicitly. In addition, their amounts are quantified by their volume fractions, f_c and f_e, respectively. The columnar phase is stationary ($\vec{u}_c \equiv 0$), and the morphological parameters, such as the primary and secondary arm spaces, λ_1 and λ_2, are predefined (experimental data from literature). The equiaxed phase motion $\vec{u}_e$ is calculated by solving the corresponding momentum conservation equation. The transport of the number density of the equiaxed crystals n_{eq} must be calculated as

$$\frac{\partial}{\partial t} n_{eq} + \nabla \cdot (\vec{u}_e n_{eq}) = N, \tag{1}$$

by considering a source term N, which should include three parts [27]: the heterogeneous nucleation N_{nucl}, fragmentation N_{frag}, and death by dissolution (remelting) N_{remelt}. As soon as n_{eq} is determined, the average diameter of the equiaxed grains (d_e) can be calculated. For the globular equiaxed crystal, $d_e = \sqrt[3]{6 f_e / \pi n_{eq}}$. If the crystal is dendritic, a concept of the dendritic crystal envelop is employed; the fraction solid inside the dendritic crystal envelop, that is, f_{si} must be calculated [28, 29] or presumed [30], and then the diameter of the equiaxed grain envelope can be estimated by $d_e^{env} = d_e \big/ \sqrt[3]{f_{si}}$. In this study, a constant f_{si} value of 0.5 is used.

2.1. Remelting-induced fragmentation

It is known that the transport of the solute-enriched melt through the interdendritic flow in the columnar-growth direction would lead to remelting [24, 25]. Under normal diffusion-governed solidification/remelting condition, the driving force for the remelting is the constitutional supersaturation ($c_\ell - c_\ell^*$), where c_ℓ is the volume-averaged concentration of interdendritic melt; c_ℓ^* is the thermodynamic equilibrium concentration of the melt at the liquid–solid interface. If the curvature effect is considered, $c_\ell^* = \frac{T - T_f}{m} - \frac{\Gamma}{m}\left(\frac{1}{r_1} - \frac{1}{r_2}\right)$. A positive value of ($c_\ell - c_\ell^*$) results in remelting, or a process leading to an increase of c_ℓ promotes remelting. The influence of the interdendritic flow on c_ℓ^* is very limited. Furthermore, the curvature of the dendrite stem is independent from the flow, whose influence on the local temperature T is ignorable compared with its influence on solute concentration (because of large Lewis number of metal alloys). The interdendritic melt usually has a concentration gradient (∇c_ℓ) contradictory to the columnar growth direction of alloys with the solute partition coefficient (k) less than one (figure 1). An interdendritic flow in the columnar growth direction indicates $-(\vec{u}_\ell - \vec{u}_c) \cdot \nabla c_\ell > 0$. Here, $\vec{u}_\ell$ and $\vec{u}_c$ denote the liquid velocity and the columnar phase velocity, respectively. Therefore, the flow leads to a local increase in c_ℓ, promoting the remelting. Actually, the rate of remelting should be proportional to the value of $-(\vec{u}_\ell - \vec{u}_c) \cdot \nabla c_\ell$. Even if the local capillary effect, that is, the coarsening or ripening phenomenon is ignored, fragments can be produced by the 'homogenous' remelting. Based on the large number of experimental facts on the remelting-induced fragmentation [15–22] and the above-mentioned theoretical analysis, we assume that the rate of fragmentation is proportional to the value of $-(\vec{u}_\ell - \vec{u}_c) \cdot \nabla c_\ell$ by suggesting the following formulation for the fragmentation-induced mass transfer rate from the columnar to equiaxed phase:

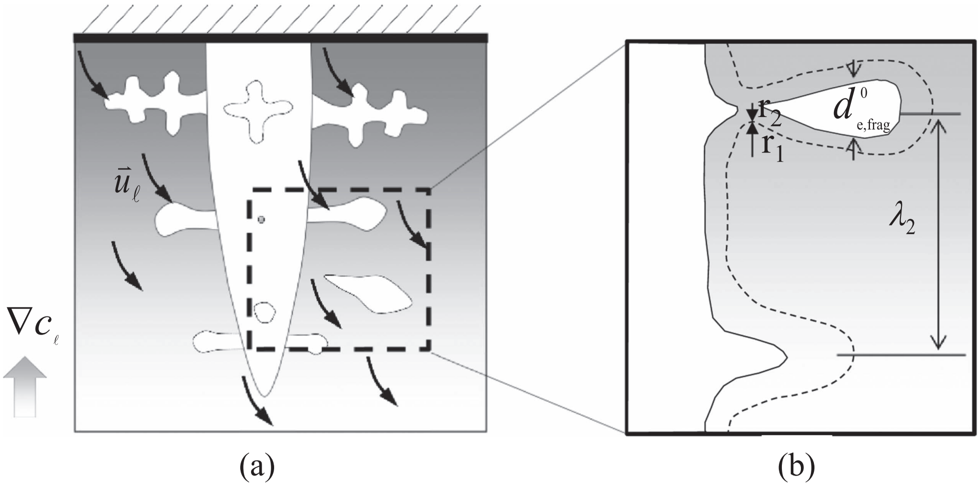

Figure 1. Schematic description of remelting-induced fragmentation: (a) transport of solute-enriched interdendritic melt through the flow, and (b) formation of a fragment by remelting of the side arm.

$$M_{\mathrm{ce}} = -\gamma \cdot (\vec{u}_\ell - \vec{u}_{\mathrm{c}}) \cdot \nabla c_\ell \cdot \rho_{\mathrm{e}}. \tag{2}$$

Note that fragmentation occurs only with remelting, that is, when $M_{\mathrm{ce}} > 0.0$. For solidification (calculated M_{ce} has a negative value), we set $M_{\mathrm{ce}} = 0.0$ to prevent the occurrence of fragmentation. The mass integral of all fragments as produced per time (kg $\mathrm{m}^{-3}\ \mathrm{s}^{-1}$) is proportional to the increase rate of constitutional supersaturation caused by the interdendritic flow. Here, a fragmentation coefficient γ was assigned to bridge the unknown correlation between M_{ce} and the increase rate of constitutional supersaturation. In other words, all other unknown contributing factors, such as the curvature effect of the dendrites, latent heat-induced thermal fluctuation, and diffusion in the interdendritic melt, for the remelting-induced fragmentation are included in the single coefficient γ. γ has a positive value for the alloy with the solute partition coefficient $k < 1$, a negative value for the alloy with $k > 1$. The coefficient must be determined experimentally, or estimated reversely from some available experimental information. Section 4.2 presents the parameter study on γ.

As shown in figure 1, we assume that the fragment is globular (spherical). The diameter of the fragment is proportional to the secondary dendrite arm spacing and the volume fraction of the columnar phase:

$$d^0_{\mathrm{e,frag}} = \lambda_2 f_{\mathrm{c}}. \tag{3}$$

Here, f_{c} indicates the columnar phase volume fraction. Hence, the rate of the fragment production can be calculated as follows:

$$N_{\mathrm{frag}} = \frac{M_{\mathrm{ce}}}{\rho_{\mathrm{e}} \cdot \frac{\pi}{6}(d^0_{\mathrm{e,frag}})^3}. \tag{4}$$

Correspondingly, the fragmentation-induced momentum transfer ($\vec{U}^{\mathrm{p}}_{\mathrm{ce}}$), energy transfer ($Q^{\mathrm{p}}_{\mathrm{ce}}$), and species transfer ($C^{\mathrm{p}}_{\mathrm{ce}}$) from the columnar to equiaxed phases are defined as follows:

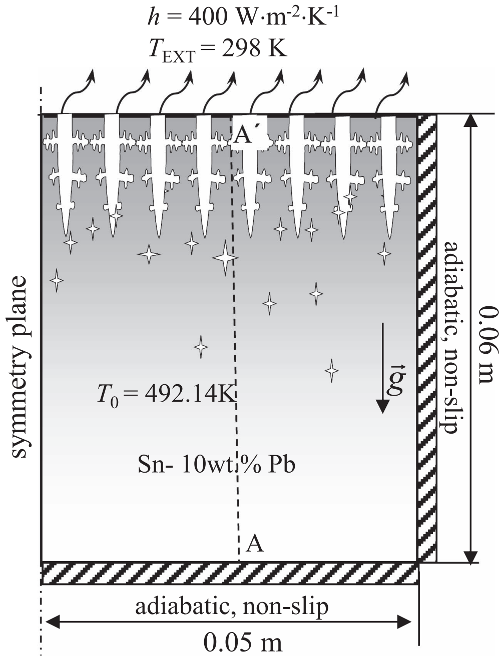

Figure 2. Configuration of the test case.

$$\vec{U}^{\mathrm{p}}_{\mathrm{ce}} = \vec{u}_{\mathrm{c}} \cdot M_{\mathrm{ce}}, \tag{5}$$

$$Q^{\mathrm{p}}_{\mathrm{ce}} = h_{\mathrm{c}} \cdot M_{\mathrm{ce}}, \tag{6}$$

$$C^{\mathrm{p}}_{\mathrm{ce}} = c_{\mathrm{c}} \cdot M_{\mathrm{ce}}, \tag{7}$$

where $\vec{u}_{\mathrm{c}}$, h_{c}, and c_{c} are respectively the moving velocity, enthalpy, and concentration of the columnar phase. Several auxiliary quantities, such as macrosegregation index $c^{\mathrm{index}} = (c_{\mathrm{mix}} - c_0) \times 100/c_0$, mixture concentration $c_{\mathrm{mix}} = (c_\ell \rho_\ell f_\ell + c_{\mathrm{c}} \rho_{\mathrm{c}} f_{\mathrm{c}} + c_{\mathrm{e}} \rho_{\mathrm{e}} f_{\mathrm{e}}) / (\rho_\ell f_\ell + \rho_{\mathrm{c}} f_{\mathrm{c}} + \rho_{\mathrm{e}} f_{\mathrm{e}})$, and global macrosegregation intensity $\mathrm{GMI} = \left(\iiint_{V_{\mathrm{domain}}} |c^{\mathrm{index}}| \, \mathrm{d}V \right) \Big/ V_{\mathrm{domain}}$, are used to analyze the macrosegregation [31, 32].

2.2. Test-case configuration and numerical implementation

Figure 2 shows the configuration of a 2D test case. The geometry is obtained from the benchmark defined by Bellet *et al* [33]; however, in this study, only half of the benchmark is calculated by setting a symmetry plane at the left boundary. Heat is only extracted through the top wall with a heat transfer coefficient $h = 400$ W m^{-2} K^{-1}, while other walls are set as adiabatic boundaries. Moreover, an alloy of Sn-10 wt%Pb is considered. The solute element Pb is heavier than the solvent Sn, and the solidified equiaxed crystal is assumed to always be heavier than the melt. As a closed domain is calculated and no volume shrinkage is considered, the Boussinesq approximation is conducted for the thermo-solutal convection and crystal sedimentation. The test-case domain is initially filled with the stationary melt of its liquidus temperature, that is, no superheat and motion. Solidification with a columnar

Table 1. Material properties and other parameters.

	Symbol	Units		References
Nominal concentration	c_0	1	0.1	
Liquidus temperature	T_{liq}	K	492.14	[33]
Melting point of solvent at $c_0 = 0$	T_{f}	K	505	[33]
Eutectic composition	c_{eu}	1	0.381	[33]
Eutectic temperature	T_{eu}	K	456	[34]
Liquidus slope	m	K	−128.6	[33]
Equilibrium partition coefficient	k	1	0.0656	[33]
Reference density	ρ_{ref}	kg m^{-3}	7000	[33]
Specific heat	c_{p}^{ℓ}, c_{p}^{e}, c_{p}^{c}	$\text{J kg}^{-1}\text{ K}^{-1}$	260	[33]
Thermal conductivity	k_ℓ, k_{e}, k_{c}	$\text{W m}^{-1}\text{ K}^{-1}$	55.0	[33]
Latent heat	L	J kg^{-1}	6.1×10^4	[33]
Viscosity	μ_ℓ	$\text{kg m}^{-1}\text{ s}^{-1}$	1.0×10^{-3}	[33]
Liquid thermal expansion coefficient	β_{T}	K^{-1}	6.0×10^{-5}	[33]
Liquid solutal expansion coefficient	β_{C}	$\text{wt\%}^{-1}$	-5.3×10^{-3}	[33]
Primary dendritic arm spacing	λ_1	m	1.3×10^{-3}	[33]
Second dendritic arm spacing	λ_2	m	0.65×10^{-4}	[33]
Diffusion coefficient (liquid)	D_ℓ	$\text{m}^2\text{ s}^{-1}$	4.5×10^{-9}	[35]
Diffusion coefficient (solid)	D_{c}, D_{e}	$\text{m}^2\text{ s}^{-1}$	1×10^{-12}	[35]
Initial temperature	T_0	K	492.14	[33]
Heat transfer coefficient	h	$\text{W m}^{-2}\text{ K}^{-1}$	400	[33]
External temperature	T_{EXT}	K	298	[33]
Solid–liquid density difference	$\Delta\rho$	kg m^{-3}	304	[36]
Gibbs Thomson coefficient	Γ	m K	6.5×10^{-8}	[37]
Fragmentation coefficient	γ	1	0.1 (0.01, 1.0, 10.0)	

structure initiates from the top unidirectionally. Equiaxed crystals could be produced near the columnar region through fragmentation. Table 1 shows the thermodynamic data and thermal physical properties of alloy Sn-10 wt%Pb. In this study, we considered only one source term for equation (1): the origin of equiaxed crystals through fragmentation. The parts due to the heterogeneous nucleation N_{nucl} and the death by dissolution (remelting) N_{remelt} were ignored.

The solidification model is developed within the framework of the CFD software ANSYS-Fluent version 14.5 [6, 26]. Calculations with maximum 30 iterations were set for each time step to decrease the residuals of continuity, momentum conservation, species transport, and user-defined scalar conservation equations to a value below the convergence criterion of 10^{-4} and the enthalpy conservation equations below that of 10^{-7}. Owing to the complexity of the multiphase coupling, the time step should be kept small (0.001–0.01 s) to satisfy the above-mentioned convergence criteria.

3. Simulation results

3.1. Solidification sequence

Figure 3 shows the solidification sequence of the test case. For this calculation, a constant fragmentation coefficient ($\gamma = 0.1$) was assumed. With the initiation of cooling, the growth of columnar trunks and thermo-solutal convection begin from the top. The velocity magnitude is calculated as 1.4 cm s^{-1}. At 5 s, as shown in figure 3(a.1), a columnar-liquid two-phase region

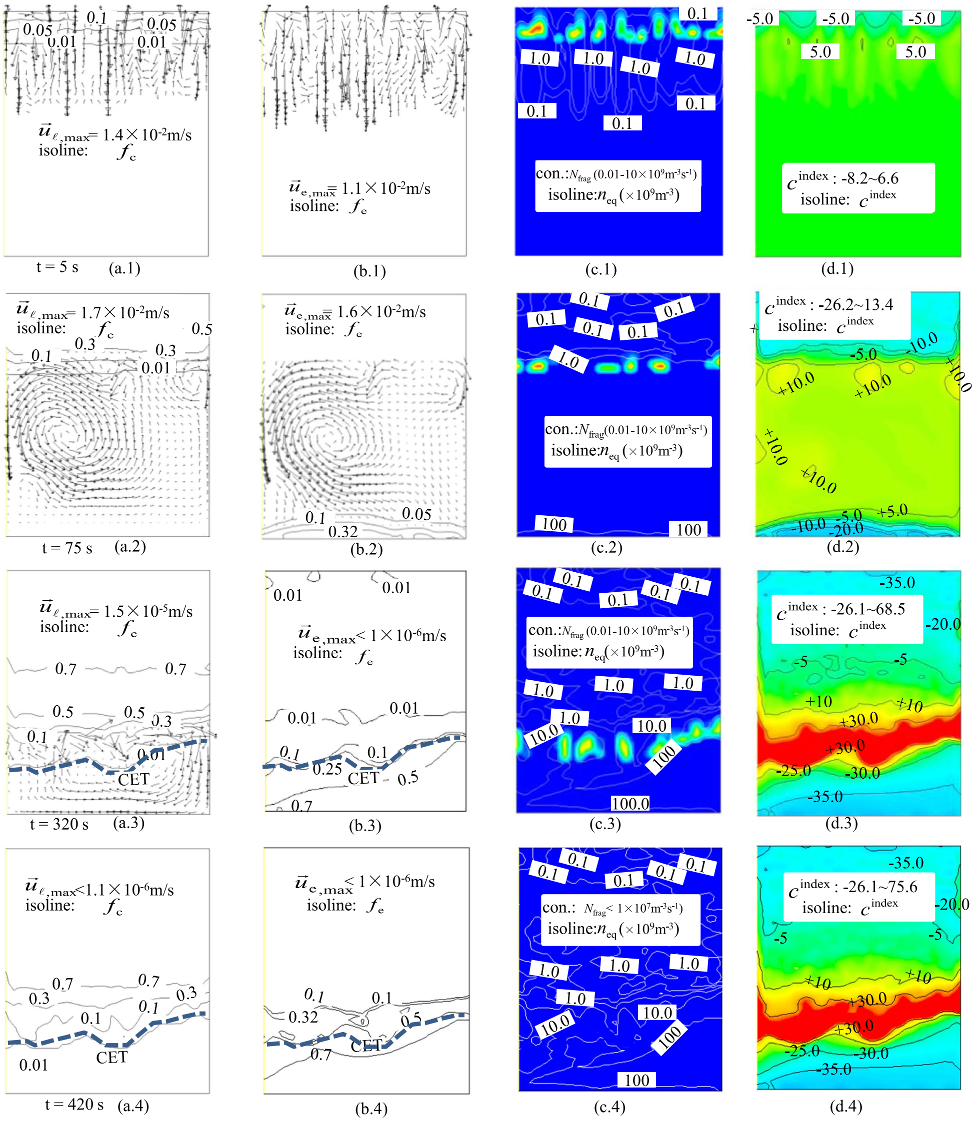

Figure 3. Solidification sequence of the test case: (a.*x*) show liquid velocity overlaid with f_c isoline; (b.*x*) show equiaxed velocity overlaid with f_e isoline; (c.*x*) show N_{frag} contour overlaid with n_{eq} isoline; and (d.*x*) show the contour of macrosegregation index (c^{index}). N_{frag} and c^{index} are represented in the color scales with blue for the minimum (or negative extreme), and red for the maximum (or positive extreme).

(mush) is developed. Some convection cells can penetrate into the mushy zone. Furthermore, fragmentation shown by the N_{frag} contour in figure 3(c.1) occurs in the mushy zone. The formation of the fragments seems nonuniform. Some 'islands' with local high fragmentation rate are found near the columnar tip front in the mushy zone; these fragments serve as nuclei for the equiaxed crystals. The number density N_{eq} achieves a magnitude of $10^9\ \text{m}^{-3}$. Moreover, the equiaxed crystals start growing and sinking; however, their motion is influenced by the melt flowing through the drag force. Figure 3(b.1) shows the motion of the equiaxed crystals, with similar velocity magnitude to the melt flow.

At 75 s, the top mushy zone (columnar) extends to approximately $1/3$ of the domain (figure 3(a.2)). A large vortex of melt flow and some small convection cells form in the bulk and near the columnar tip front regions, penetrating into the mushy zone (till $f_e \sim 0.3$). The melt flow has a significant impact on the velocity field of the equiaxed crystals (figure 3(b.2)). Both the melt flow and motion of equiaxed crystals have similar velocity magnitude: 1.7 and 1.6×10^{-2} m s^{-1}. The equiaxed crystals finally settle at the bottom of the domain. As f_e reaches the packing limit, the equiaxed phase stops moving. This phenomenon is known as equiaxed settlement or sedimentation. A second mushy zone with packed equiaxed crystals develops from the bottom. The fragmentation continues near the columnar tip front (figure 3(c.2)), supplying equiaxed nuclei continuously. The maximum number density can reach a magnitude of 10^{11} m^{-3}.

At 320 s, the extension of the columnar mushy zone and the pile-up of the equiaxed mushy zone meet at approximately one-third height of the domain, figures 3(a.3)–(b.3). The growth of the columnar tip front is blocked by the equiaxed grain envelope mechanically, that is, CET occurs, as represented by the blue dash line. The melt flow is confined in the mushy zone, and its velocity magnitude is reduced to 10^{-5} m s^{-1}. This slow interdendritic flow still causes fragmentation in the columnar mushy zone above the CET line (figure 3(c.3)). The motion of equiaxed crystals is ignorable. These newly formed fragments cannot be transported out of the columnar mushy region but they will grow as equiaxed phase, competing with the growth of the columnar phase. In addition, a mixed columnar-equiaxed phase region is obtained above the CET line. Figures 3(a.4)–(c.4) show the solidification results at 420 s. The entire solidification sequence ends at 580 s, and the remaining melt in the mushy zone solidifies as a eutectic phase below temperature T_{eu}.

Figures 3(d.1)–(d.4) present the evolution of macrosegregation during solidification. At 5 s, the macrosegregation is weak, and a negative segregation occurs in the columnar mushy zone. A slightly positive segregation, following the pattern of the melt convection cells, is obtained before the columnar tip front. At 75 s, with the extension of the columnar mushy zone, the negative segregation (both the strength and area) increases. The positive segregation in the bulk melt region due to the mixing effect of the melt flow and crystals sedimentation becomes relatively homogenous. The equiaxed mushy zone near the bottom bears negative segregation. This process continues until the CET occurs at 320 s. The region of the middle positive segregation is gradually reduced to a relatively narrow region between the top negatively-segregated columnar mushy zone and the bottom negatively-segregated equiaxed mushy zone. The intensity of the positive segregation increases there. The solidification process ends at 580 s. The location of the final solidification is near the CET line. After the CET event, the global segregation distribution patterns remain.

3.2. Formation and transport of fragments

Figure 4 shows fragmentation-induced mass transfer rate (M_{ce}) from the columnar to equiaxed phases in the solidifying domain at 3 s. The number of fragments newly produced (N_{frag}) is proportional to M_{ce}. Fragments are mainly located in the mushy zone near the columnar tip front, which is indicated by isoline $f_c = 0.01$. According to the model (equation (2)), the interdendritic flow in the direction against the liquid concentration gradient direction leads to local increase of c_ℓ, promoting remelting and fragmentation. This can be witnessed from the detailed view (Zone 1) of the liquid velocity $\vec{u}_\ell$ (white) and liquid concentration gradient ∇c_ℓ

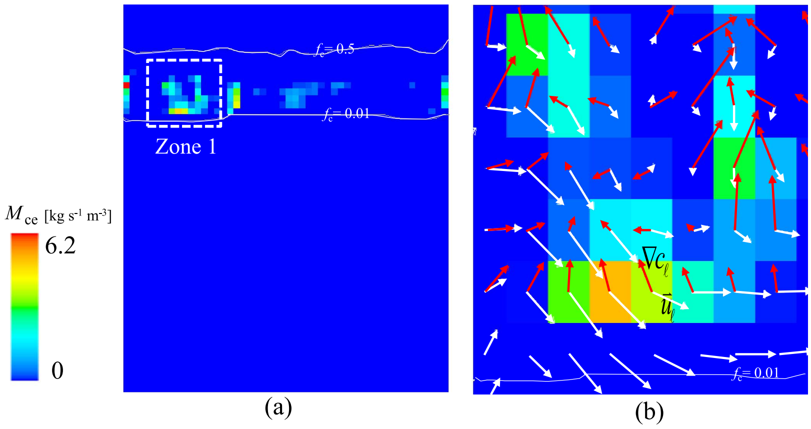

Figure 4. Fragmentation-induced columnar-to-equiaxed mass transfer at 3 s: (a) global view of M_{ce} contour and (b) zoom-in view of Zone 1 overlaid with liquid velocity $\vec{u}_\ell$ (white) and liquid concentration gradient ∇c_ℓ (red). Isolines of f_c are plotted in (a), indicating the position of columnar mushy zone.

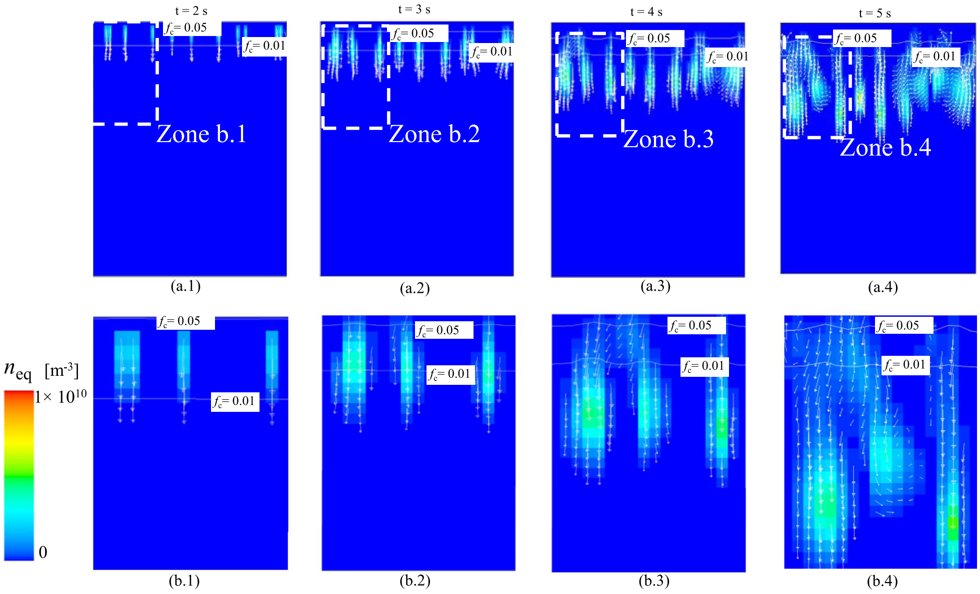

Figure 5. Evolution of equiaxed number density (n_{eq}) from 2 to 5 s: (a.x) show the global view of n_{eq} contour overlaid with liquid velocity $\vec{u}_e$ (white); (b.x) show the zoom-in view of Zone (b.x). Isolines of f_c are plotted in (a.x), indicating the position of columnar mushy zone.

(red) in figure 4(b). In the region where fragmentation-induced mass transfer occurs ($M_{ce} > 0.0$), the angle between the two vectors ($\vec{u}_\ell$, ∇c_ℓ) is larger than 90°.

As soon as new fragments are created in the columnar mushy zone, they act as nuclei of equiaxed crystals. The equiaxed number density (n_{eq}) increases locally, and they can be transported with the velocity of $\vec{u}_e$. Figure 5 shows the detailed analysis of the transport of n_{eq}

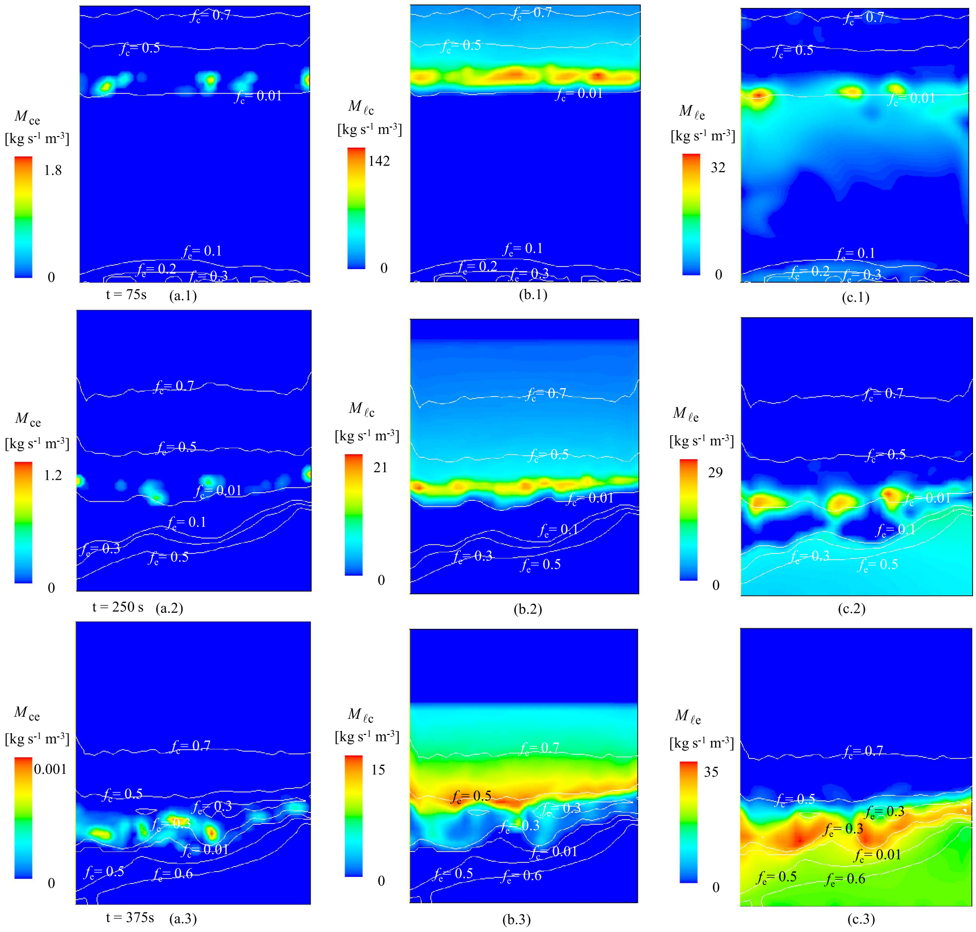

Figure 6. Balance of mass transfer among M_{ce}, $M_{\ell c}$, and $M_{\ell e}$ (75, 250 and 375 s). (a.x) contour of M_{ce} overlaid with f_e and f_c isolines; (b.x) contour of $M_{\ell c}$ overlaid with f_e and f_c isolines; (c.x) contour of $M_{\ell e}$ overlaid with f_e and f_c isolines.

by $\vec{u}_e$. With the solidification, equiaxed crystals, that is, n_{eq}, are gradually transported out of the columnar mushy zone into the bulk region. In addition, new fragments, as new nuclei of equiaxed crystals, are continuously produced in the mushy zone. Generally, the equiaxed velocity is pointed downward because of the larger density of solid than that of liquid; however, the motion of the equiaxed phase ($\vec{u}_e$) in the bulk region is significantly influenced by the melt convection.

The balance between the fragmentation-induced mass transfer (M_{ce}) and solidification-induced mass transfer ($M_{\ell c}$, $M_{\ell e}$) is analyzed in figure 6. At the early stage of solidification (75 s), solidification-induced mass transfer rate $M_{\ell c}$ (maximum 142 Kg m^{-3} s^{-1}) is much larger than fragmentation-induced mass transfer rate M_{ce} (maximum 1.8 Kg m^{-3} s^{-1}). The solidification rate of the columnar phase overweighs the fragmentation-induced mass transfer rate. Furthermore, $M_{\ell e}$ (maximum 32.0 Kg m^{-3} s^{-1}) is also much larger than M_{ce}. When the solidification proceeds to 250 s, M_{ce} is still at the magnitude of 1.2 Kg m^{-3} s^{-1}, while the maximal values of $M_{\ell c}$ and $M_{\ell e}$ are 40 and 71 Kg m^{-3} s^{-1}. During the late stage of

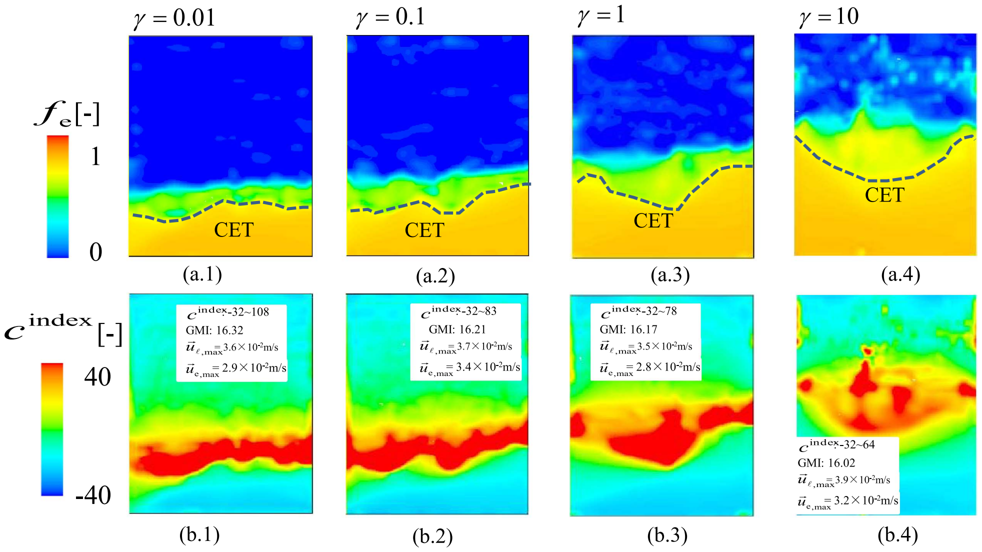

Figure 7. Influence of the chosen fragmentation coefficient γ on the as-cast structure and macrosegregation. (a.x) Distribution of equiaxed phase (the blue region above the CET line is dominated by the columnar phase). (b.x) Macrosegregation contour (c^{index}).

solidification (375 s), the columnar tip front is stopped by the pile of equiaxed crystals from the bottom, and CET occurs. At this moment, M_{ce} is insignificantly small (maximum 10^{-3} Kg m^{-3} s^{-1}), thus fragmentation is almost terminated. However, the solidification of columnar and equiaxed phases continues. The main function of fragmentation, i.e. the effect of, M_{ce} is to supply the sites of equiaxed nuclei rather than to form equiaxed phase directly. The formation of equiaxed phase is mainly due to the growth of those equiaxed crystals during the subsequent solidification. We find that M_{ce} is always smaller than $M_{\ell\text{c}}$ in the current test case. This correlation might apply for other alloys, but further study is needed to verify it. Note that fragmentation depends on the flow intensity, and in the current test case the thermal-solutal convection is weak (10^{-2} m s^{-1}).

4. Parameter study and discussion

4.1. Fragmentation coefficient γ and equiaxed sedimentation

It is well-accepted that the solute-driven remelting is the key mechanism for fragmentation; however, there is no theoretical model available for the fragmentation. In this study, a fragmentation coefficient γ was introduced (equation (2)) to bridge the unknown correlation between M_{ce}, N_{frag}, and the possible contributing factors for the remelting-induced fragmentation, such as the curvature effect of the dendrites, thermal fluctuation induced by the release of latent heat, and solute diffusion in the interdendritic melt. This coefficient should be determined experimentally. To determine the influence of γ on the solidification, four cases with different values of γ (0.01, 0.1, 1.0, and 10) were calculated. The end solidification results of these cases are compared in figure 7. For each case, a CET line separates two regions: the upper columnar region and the lower equiaxed region. Obviously, the equiaxed region increases with the influence of the chosen γ. Owing to equiaxed crystal sedimentation,

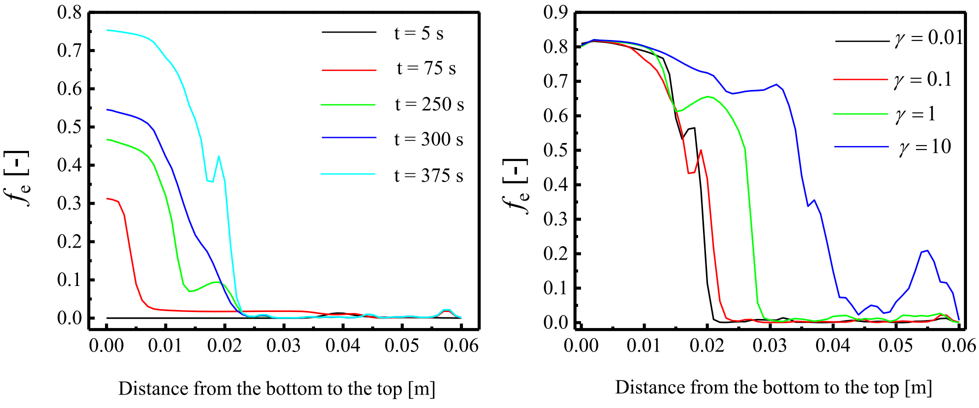

(a) (b)

Figure 8. (a) Evolution of f_e along the vertical line A-A′, as marked in figure 2 during solidification when $\gamma = 0.1$; (b) Influence of γ on f_e distribution along the vertical line A-A′ at the end solidification.

a strong macrosegregation occurs for each case: negative segregations in both the upper columnar region and lower equiaxed region, and a positive segregation region sandwiched between the two just above the CET line. The macrosegregation range (c^{index}) and global macrosegregation index (GMI) are labeled in figures 7(b.1)–(b.4). The segregation intensity is correlated to the relative motion between the liquid and the settling equiaxed crystals [31, 32]; hence, the maximal liquid velocity $\vec{u}_{\ell.\max}$ and equiaxed velocity $\vec{u}_{\text{e}.\max}$ are also labeled. It is found that the influence of γ on $\vec{u}_{\ell.\max}$ and $\vec{u}_{\text{e}.\max}$ is not significant, and hence the influence of γ on segregation intensity is not significant. The major influence of γ is on the as-cast structure distribution.

Quantitative analyses were conducted for the equiaxed sedimentation along the vertical line A-A′ marked in figure 2. Figure 8(a) presents the evolution of f_e. At 5 s, only a small amount of equiaxed phase is detected. In addition, at 75 s, an equiaxed layer exists in the bottom region with the maximal f_e reaching 0.32; the equiaxed packing limit ($0.637 \times f_{\text{si}}$). With the continuation of solidification, the equiaxed region's thickness increases to approximately 23 mm at the end of solidification, and the maximal f_e reaches 0.8. Figure 8(b) shows the influence of γ on f_e distribution along the vertical line A-A′. The thickness of the equiaxed zone increases with γ.

4.2. Grid sensitivity study

Calculations with four mesh sizes (0.8, 1.0, 1.5 and 2.0 mm) were performed. Figure 9 shows the phase distribution and macrosegregation at the end of solidification. A CET line at about a one-third height from the bottom separates the columnar and equiaxed regions (figure 9(a.x)). It does not seem possible to possess a grid-independent shape of the equiaxed zone but the areas of equiaxed zone for all cases are similar. Macrosegregation distributions of the four cases are shown in figure 9(b.x). According to the figure, the decrease of the grid size from 2.0 to 0.8 mm causes the macrosegregation distribution and segregation intensity to become closer. The case with grid size of 2.0 mm is quite different from other cases. Macrosegregation index range c^{index} and GMI are also labeled in this figure. The c^{index} value for all cases ranges from −32 to 85. The range does not significantly change when the mesh size decreases more than $\Delta x = 1.5$ mm.

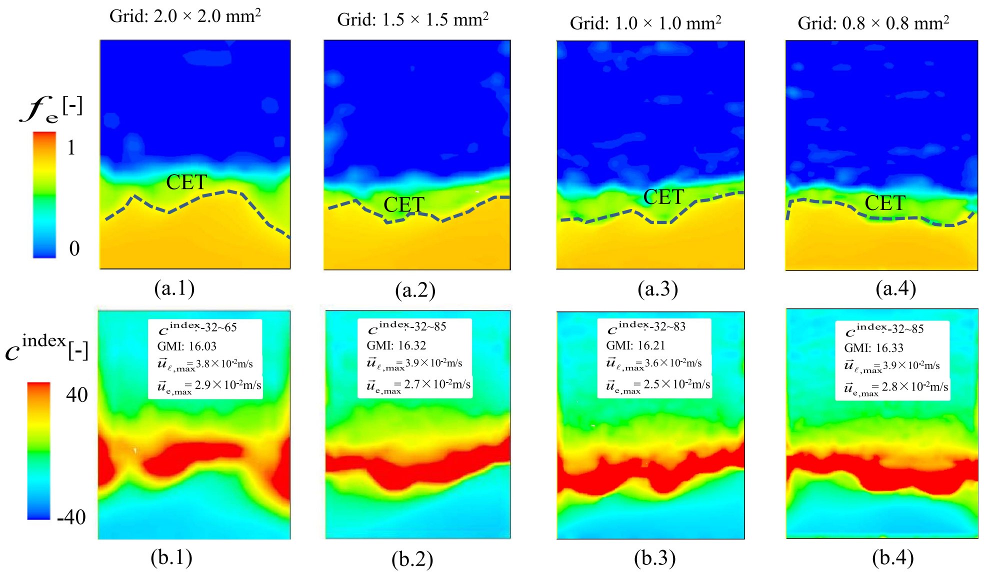

Figure 9. Influence of mesh size on the as-cast structure and macrosegregation. (a.x) Distribution of equiaxed phase (the blue region above the CET line is dominated by the columnar phase); (b.x) macrosegregation contour (c^{index}).

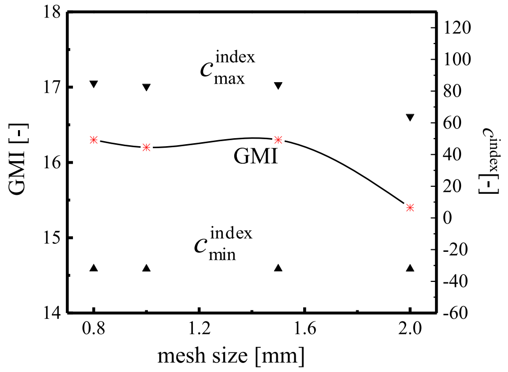

Figure 10. Influence of mesh size on the macrosegregation range and GMI.

Although the macrosegregation patterns for the cases with mesh size smaller than 1.5 mm look rather similar, they cannot converge to a grid-independent result. The macrosegregation is relatively sensitive to the melt convection and crystal sedimentation during the solidification. However, the melt convection greatly interacts with the movement of equiaxed crystals, which are randomly produced through fragmentation. In addition, the velocities of both liquid melt and solid crystals are very sensitive to mesh size. However, the GMI, which can reflect the overall macrosegregation intensity in the domain, can obtain a relatively convergent result (figure 10) when the mesh size is below 1.5 mm.

5. Conclusions

In this study, a fragmentation formulation was proposed and implemented in a volume average model for the mixed columnar-equiaxed solidification. A test case with Sn-10 wt%Pb melt solidifying downward in a 2D domain ($50 \times 60\,\text{mm}^2$) was simulated by assuming that fragmentation is the only source of equiaxed crystals. A reasonable solidification sequence was calculated. The interdendritic flow in the columnar tip growth direction led to the local increase of c_ℓ, promoting remelting and fragmentation. Fragments were produced in the mushy zone near the columnar tip front. These fragments were transported out of the columnar region and continued to grow and sink, and finally settled down and piled up in the bottom domain. The columnar structure, growing from the top, and the pile-up of equiaxed crystals from the bottom finally led to a mixed columnar-equiaxed structure and the occurrence of a CET. A special macrosegregation pattern was predicted, according to which negative segregation occurred in both columnar and equiaxed regions, and a relatively strong positive segregation occurred near the CET line.

The current formulation for the fragmentation considered that transport of a solute-enriched melt through interdendritic flow in the columnar growth direction is in favor of the solute-driven remelting, and hence in favor of fragmentation. One modeling parameter was introduced: the fragmentation coefficient γ. For the fragmentation, the unknown contributing factors, such as the curvature effect of the dendrites, latent heat-induced thermal fluctuation, and diffusion in the interdendritic melt, were included in the single coefficient γ. This coefficient must be determined experimentally or require another theoretical model. The numerical parameter study showed that the influence of γ on the intensity of the flow and equiaxed motion is not significant, and hence its influence on segregation intensity is not significant. The major influence of γ is on the as-cast structure distribution, that is, the larger the γ, the larger the equiaxed zone.

A general issue for the calculation of the multiphase transport phenomena during solidification is the grid size sensitivity. The parameter study showed that the global as-cast structure, that is, the area of equiaxed zone, and the macrosegregation pattern and intensity become insensitive to the grid size when it is smaller than 1.5 mm. Fine details of the structural and compositional distributions are not quantitatively solvable with the current grid resolution.

Acknowledgments

The authors acknowledge the financial support from Austrian Research Promotion Agency (FFG) through the project of Bridge Early Stage (No. 842441), as well as the technical support of the industrial partner Primetals (former Siemens VAI).

ORCID iDs

M Wu https://orcid.org/0000-0003-0321-412X

References

[1] Beckermann C and Viskanta R 1993 Mathematical modeling of transport phenomena during alloy solidification *Appl. Mech. Rev.* **46** 1–27

[2] Wu M, Li J, Ludwig A and Kharicha A 2013 Modeling diffusion-governed solidification of ternary alloys: I. Coupling solidification kinetics with thermodynamics *Comput. Mater. Sci.* **79** 830–40

[3] Wu M, Li J, Ludwig A and Kharicha A 2014 Modeling diffusion-governed solidification of ternary alloys: II. Macroscopic transport phenomena and macrosegregation *Comput. Mater. Sci.* **92** 267–85

[4] Combeau H, Založnik M, Hans S and Richy P E 2009 Prediction of macrosegregation in steel ingots: influence of the motion and the morphology of equiaxed grains *Metall. Mater. Trans.* B **40** 289–304

[5] Rappaz M 1989 Modelling of microstructure formation in solidification processes *Int. Mater. Rev.* **34** 93–124

[6] Wu M and Ludwig A 2006 A three-phase model for mixed columnar-equiaxed solidification *Metall. Mater. Trans.* A **37** 1613–31

[7] Hellawell A, Liu S and Lu S 1997 Dendrite fragmentation and the effects of fluid flow in castings *JOM* **49** 18–20

[8] Su Z J, Chen J, Nakajima K and He J C 2009 Criterion for dendrite fragmentation of carbon steel under imposition of linear travelling EMS *Steel Res. Int.* **80** 824–33

[9] Yasuda H, Yamamoto Y, Nakatsuka N, Nagira T, Yoshiya M, Sugiyama A, Ohnaka I, Umetani K and Uesugi K 2008 *In situ* observation of nucleation, fragmentation and microstructure evolution in Sn–Bi and Al–Cu alloys *Int. J. Cast Met. Res.* **21** 125–8

[10] Lesoult G 2005 Macrosegregation in steel strands and ingots: characterisation, formation and consequences *Mater. Sci. Eng.* A **413–414** 19–29

[11] Chalmers B and Williamson R 1965 Crystal multiplication without nucleation *Science* **148** 1717–8

[12] Garabedian H and Strickland-Constable R 1974 Collision breeding of ice crystals *J. Cryst. Growth* **22** 188–92

[13] Pilling J and Hellawell A 1996 Mechanical deformation of dendrites by fluid flow *Metall. Mater. Trans.* A **27** 229–32

[14] Mullis A M, Walker D J, Battersby S E and Cochrane R F 2001 Deformation of dendrites by fluid flow during rapid solidification *Mater. Sci. Eng.* A **304** 245–9

[15] Jackson K, Hunt J, Uhlmann D and Seward T 1966 On origin of equiaxed zone in castings *Trans. Metall. Soc. AIME* **236** 149–58

[16] Christenson M and Incropera F 1989 Solidification of an aqueous ammonium chloride solution in a rectangular cavity: I. Experimental study *Int. J. Heat Mass Transfer* **32** 47–68

[17] Christenson M, Bennon W and Incropera F 1989 Solidification of an aqueous ammonium chloride solution in a rectangular cavity: II. Comparison of predicted and measured results *Int. J. Heat Mass Transfer* **32** 69–79

[18] Montgomery W and Incropera F 1998 Fragmentation of dendritic crystals during solidification of aqueous ammonium chloride *Exp. Heat Transfer* **11** 59–86

[19] Paradies C, Smith R and Glicksman M 1997 The influence of convection during solidification on fragmentation of the mushy zone of a model alloy *Metall. Mater. Trans.* A **28** 875–83

[20] Mathiesen R, Arnberg L, Bleuet P and Somogyi A 2006 Crystal fragmentation and columnar-to-equiaxed transitions in Al–Cu studied by synchrotron x-ray video microscopy *Metall. Mater. Trans.* A **37** 2515–24

[21] Jung H, Mangelinck-Noel N, Nguyen-Thi H, Bergeon N, Billia B, Buffet A, Reinhart G, Schenk T and Baruchel J 2009 Fragmentation in an Al–7 wt% Si alloy studied in real time by x-ray synchrotron techniques *Int. J. Cast Met. Res.* **22** 208–11

[22] Liotti E, Lui A, Vincent R, Kumar S, Guo Z, Connolley T, Dolbnya I, Hart M, Arnberg L and Mathiesen R 2014 A synchrotron x-ray radiography study of dendrite fragmentation induced by a pulsed electromagnetic field in an Al–15Cu alloy *Acta Mater.* **70** 228–39

[23] Leriche N, Combeau H, Gandin C-A and Založnik M 2015 *IOP Conf. Ser.: Mater. Sci. Eng.* **84** 012087

[24] Flemings M C and Nereo G E 1967 Macrosegregation: I *Trans. Metall. Soc. AIME* **239** 1449–62

[25] Campanella T, Charbon C and Rappaz M 2004 Grain refinement induced by electromagnetic stirring: a dendrite fragmentation criterion *Metall. Mater. Trans.* A **35** 3201–10

[26] Wu M and Ludwig A 2007 Using a three-phase deterministic model for the columnar-to-equiaxed transition *Metall. Mater. Trans.* A **38** 1465–75

[27] Beckermann C 1997 Modeling segregation and grain structure development in equiaxed solidification with convection *JOM* **49** 13–7

[28] Wu M and Ludwig A 2009 Modeling equiaxed solidification with melt convection and grain sedimentation: II. Model verification *Acta Mater.* **57** 5632–44

[29] Wu M and Ludwig A 2009 Modeling equiaxed solidification with melt convection and grain sedimentation: I. Model description *Acta Mater.* **57** 5621–31

[30] Wu M, Ludwig A and Kharicha A 2017 A four phase model for the macrosegregation and shrinkage cavity during solidification of steel ingot *Appl. Math. Modelling* **41** 102–20

[31] Zheng Y, Wu M, Kharicha A and Ludwig A 2016 Numerical analysis of macrosegregation in vertically solidified Pb–Sn test castings: II. Equiaxed solidification *Comput. Mater. Sci.* **124** 456–70

[32] Wu M, Zheng Y, Kharicha A and Ludwig A 2016 Numerical analysis of macrosegregation in vertically solidified Pb–Sn test castings: I. Columnar solidification *Comput. Mater. Sci.* **124** 444–55

[33] Bellet M, Combeau H, Fautrelle Y, Gobin D, Rady M, Arquis E, Budenkova O, Dussoubs B, Duterrail Y and Kumar A 2009 Call for contributions to a numerical benchmark problem for 2D columnar solidification of binary alloys *Int. J. Therm. Sci.* **48** 2013–6

[34] Ahmad N, Rappaz J, Desbiolles J-L, Jalanti T, Rappaz M, Combeau H, Lesoult G and Stomp C 1998 Numerical simulation of macrosegregation: a comparison between finite volume method and finite element method predictions and a confrontation with experiments *Metall. Mater. Trans.* A **29** 617–30

[35] Klassen M and Cahoon J 2000 Interdiffusion of Sn and Pb in liquid Pb–Sn alloys *Metall. Mater. Trans.* A **31** 1343–52

[36] Rocha O L, Siqueira C A and Garcia A 2003 Heat flow parameters affecting dendrite spacings during unsteady-state solidification of Sn–Pb and Al–Cu alloys *Metall. Mater. Trans.* A **34** 995–1006

[37] Cadirli E and Gündüz M 2000 The directional solidification of Pb–Sn alloys *J. Mater. Sci.* **35** 3837–48

Paper IV

Use of a mixed columnar-equiaxed solidification model to analyse the formation of as-cast structure and macrosegregation in a Sn-10 wt% Pb benchmark experiment

Yongjian Zheng, Menghuai Wu, Ebrahim Karimi-sibaki, Abdellah Kharicha, Andreas Ludwig

International Journal of Heat and Mass Transfer, 2018, 122, 939-953

International Journal of Heat and Mass Transfer 122 (2018) 939–953

Contents lists available at ScienceDirect

International Journal of Heat and Mass Transfer

journal homepage: www.elsevier.com/locate/ijhmt

Use of a mixed columnar-equiaxed solidification model to analyse the formation of as-cast structure and macrosegregation in a Sn-10 wt% Pb benchmark experiment

Y Zheng [a], M Wu [a,b,*], E Karimi-Sibaki [a,b], A Kharicha [a,b], A Ludwig [a]

[a] Chair of Modelling and Simulation of Metallurgical Processes, Montanuniversitaet Leoben, Austria
[b] Christian Doppler Laboratory for Advanced Simulation of Solidification and Melting, Montanuniversitaet Leoben, Austria

ARTICLE INFO

Article history:
Received 28 November 2017
Received in revised form 22 January 2018
Accepted 5 February 2018

Keywords:
Macrosegregation
As-cast structure
Fragmentation
Crystal sedimentation
Columnar-to-equiaxed transition (CET)
Channel segregation

ABSTRACT

A solidification benchmark experiment based on a Sn-10 wt% Pb alloy was performed at the SIMAP Laboratory in Grenoble, France, to investigate the formation of as-cast structure and macro- and mesosegregation (Wang et al., 2009; Hachani et al., 2015). The current study simulated this benchmark using a mixed columnar-equiaxed solidification model. This model was developed by the current authors (Wu et al., 2006), and recently extended to consider the crystal fragmentation of columnar dendrites as the source of equiaxed grains. A satisfactory experiment-simulation agreement in the temperature evolution, the as-cast structure, and the distribution of macro- and mesosegregation, was obtained. By analysis of the modelling results, new knowledge regarding the formation of the as-cast structure (mixed columnar-equiaxed) was obtained: The fragmentation-induced equiaxed crystals are transported away from the front region of the columnar zone by the melt flow; those crystals continue to grow or re-melt depending on the condition of local constitutional undercooling or supersaturation; the density of the melt varies with the Pb enrichment in the melt, and the equiaxed crystals can settle down or float up through the balance of the flow-induced drag force and the gravity-driven sedimentation; it is the motion of equiaxed crystals that determines the final distribution of the equiaxed zone in this benchmark experiment; the interdendritic flow and its interaction with the solidification in the front region of the columnar zone lead to the formation of segregation channels.

1. Introduction

Laboratory solidification experiments with Pb-Sn and Pb-Zn alloys, following the configuration of Hebditch and Hunt [1], were widely used to investigate the formation of as-cast structure and macrosegregation [2–4]. Recently, a sophisticated AFRODITE setup with precise control of cooling rate and temperature gradient was designed, and a series of solidification experiments and post-mortem metallographic and compositional analyses of as-solidified samples were performed at the SIMAP Laboratory in Grenoble, France [5–8]. Fig. 1 shows the configuration of the AFRODITE setup. Hachani et al. [7] presented comprehensive results regarding the temperature measurement, as-cast structure, and macro- and mesosegregation. Sn-10 wt% Pb alloy was considered. The current study simulated this benchmark using a mixed columnar-equiaxed solidification model, as developed by the authors [9]. In the original experiments of Hachani et al. [7], both solidification experiments under forced convection (with electromagnetic stirring) and under natural convection (gravity only) were performed. In the current study, however, only the experiment under natural convection was numerically investigated.

Previously, simulation studies with different numerical methods were reported for these benchmark experiments [6,10–12]. The cellular automaton and finite element method (CAFE) was successfully used to simulate the equiaxed distribution and the global macrosegregation [10,11]. The drawback of this stochastic method is that, in additional to the high computational cost due to the vast number of equiaxed crystals, the mesosegregation (segregation channels) and the equiaxed crystals as created by fragmentation have not been resolved. The multiphase volume or ensemble averaging technique was proposed to model the dendritic solidification of columnar or/and equiaxed structure [12–16]. By introducing a concept of grain envelope, the extra- and interdendritic melts, whose concentrations are significantly different, can be considered

---

[*] Corresponding author at: Chair of Modelling and Simulation of Metallurgical Processes, Montanuniversitaet Leoben, Austria.

E-mail address: menghuai.wu@unileoben.ac.at (M Wu).

https://doi.org/10.1016/j.ijheatmasstransfer.2018.02.012
0017-9310/

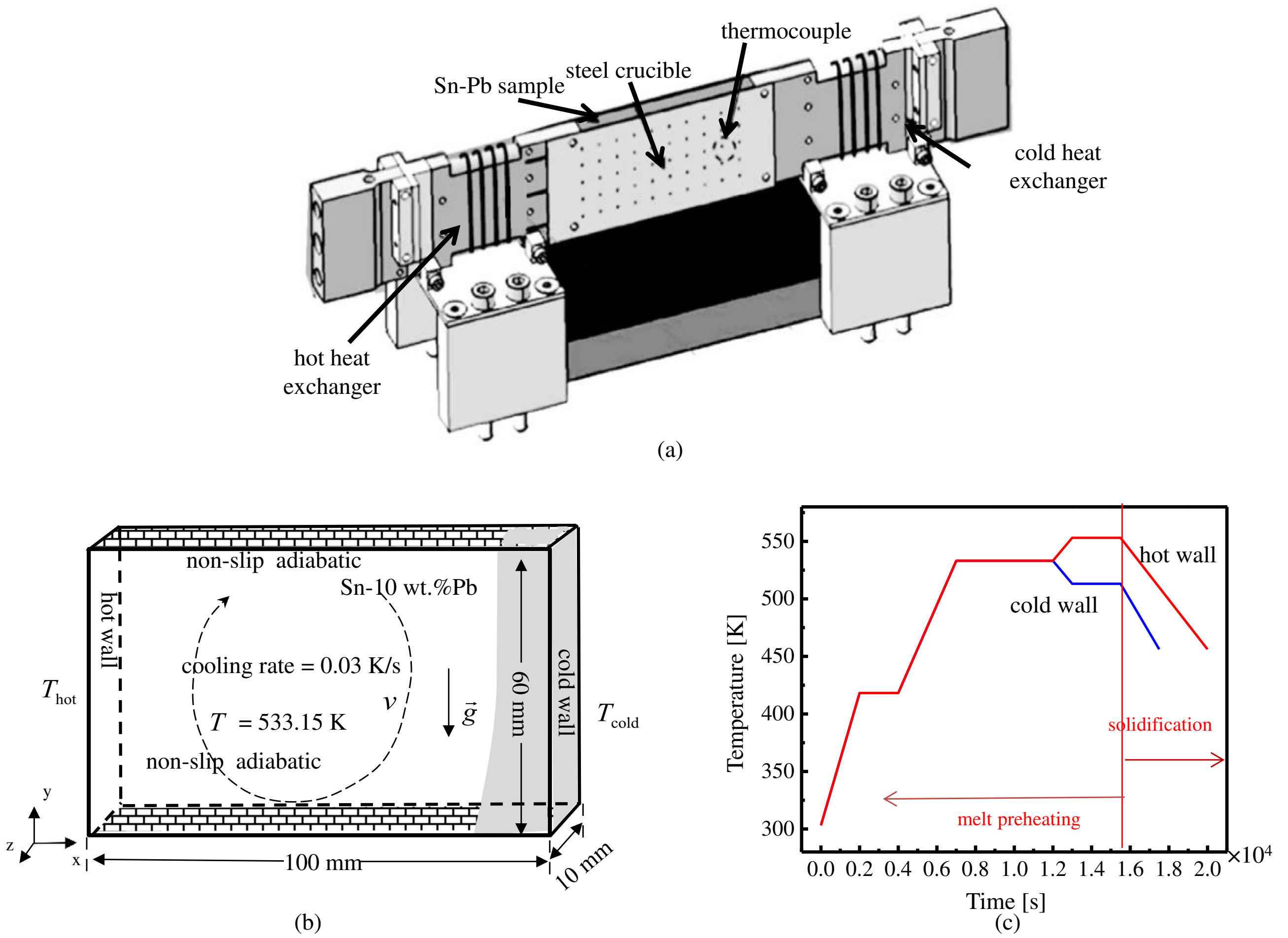

Fig. 1. Configuration of the AFRODITE setup [7]: (a) Schematic view of the experimental facility, (b) geometry and boundary conditions of the benchmark casting, and (c) temperature history experimentally applied at the boundaries of the hot and cold walls. (b) and (c) are reprinted from publication [7], with permission from Elsevier.

as different phases or phase regions. However, the more the phase regions, the larger the computation resource is demanded. To treat the mixed columnar-equiaxed solidification with dendritic morphology, five phase region are necessarily considered [14,15]. Therefore, some people used a mixture continuum solidification model [6,17] to calculate the macro- and mesosegregation. A drawback of the continuum solidification model is that it fails to distinguish the free-moving equiaxed crystals from the stationary columnar structure. A three-phase volume-average-based model was proposed by Wu et al. [9,18] to simulate the mixed columnar-equiaxed solidification. The tracking of the columnar tip front, the formation of equiaxed crystals based on the heterogeneous nucleation and the motion of equiaxed crystals, were considered.

This model has been satisfactorily applied to investigate the formation of as-cast structure (mixed columnar-equiaxed) and macrosegregation in steel and aluminium alloy ingots [19,20], and it was also applied to study the macrosegregation as observed in the Hebditch-Hunt benchmark experiments [21,22].

Unfortunately, the previous volume-average-based model has ignored the fragmentation phenomenon, which was believed to be the most important source of equiaxed crystals in the Sn-10 wt% Pb benchmark solidification experiment [7]. Therefore, the three-phase mixed columnar-equiaxed solidification model was recently extended by incorporating the crystal fragmentation of columnar dendrites as a source of equiaxed crystals [23]. It is this extended model that is used for the current study.

One goal of this work is to further validate the mixed columnar-equiaxed solidification model by 'reproducing' the benchmark experiment. The ultimate goal is to explain the formation of the special pattern of as-cast structure and the macro- and mesosegregation. According to Hachani et al. [7], no comprehensive explanation to them has yet been achieved.

2. Model description

A three-phase mixed columnar-equiaxed solidification model [9] was adopted. The key features and assumptions are:

(1) The three phases are the primary melt, equiaxed, and columnar phases. Their volume fractions are quantified by f_ℓ, f_e and f_c, and $f_\ell + f_e + f_c = 1$. Both the liquid and equiaxed phases are moving phases, and the corresponding Navier-Stokes equations are solved. The columnar phase is assumed to be rigid and stationary.

(2) Columnar trunks (morphology) are approximated by step-wise cylinders, originating from the mould wall. Equiaxed crystals originate from fragmentation (see further description herein). To calculate the growth of equiaxed grains, a globular (spherical) morphology is assumed. However, to calculate the drag force and other hydrodynamic interactions, a simplified dendritic morphology of equiaxed crystal is considered. This simplified dendritic morphology is described by an equiaxed grain envelope, which includes

the solid 'dendrite' and the inter-dendritic melt. The volume ratio of the solid 'dendrite' to the equiaxed grain envelope is predefined: f_{si}. In this study, f_{si} is set as a constant value (0.5).

(3) When the volume fraction of the equiaxed grain envelope ($f_{\mathrm{e}}^{\mathrm{Env}}$ = $f_{\mathrm{e}}/f_{\mathrm{si}}$) reaches the blocking criterion $f_{\mathrm{e,CET}}$ (=0.49) at the columnar tip front, the columnar-to-equiaxed transition (CET) occurs [24]. In the opposite scenario, the columnar phase can also grow from the packed equiaxed zone, and equiaxed-to-columnar transition (ECT) occurs [25].

(4) The interactions between neighbouring equiaxed crystals and their influence on the motion of the equiaxed phase is modelled by a so-called effective viscosity (μ_{e}) [26], which increases with the volume fraction of the equiaxed phase. When the volume fraction of the equiaxed phase grain envelope $f_{\mathrm{e}}^{\mathrm{Env}}$ reaches the packing limit $f_{\mathrm{e,packing}}$ (=0.637), μ_{e} increases to infinity, and a rigid network of equiaxed crystals is built.

(5) The presence of the columnar structure influences the motion of equiaxed crystals. The equiaxed crystals can be captured by the columnar dendrite trunk when the local volume fraction of the columnar phase reaches a critical value of $f_{\mathrm{c}}^{\mathrm{free}} = 0.2$.

(6) Resistance of the mushy zone (columnar phase) to interdendritic flow is calculated using a permeability law according to Blake-Kozeny [27]. The drag force coefficient $K_{\ell \mathrm{c}}$ for the liquid-equiaxed interaction is treated according to Kozeny-Carman for $f_{\mathrm{e}}^{\mathrm{Env}} < 0.7$, and Blake-Kozeny for $f_{\mathrm{e}}^{\mathrm{Env}} \geqslant 0.7$ [27].

(7) The solidification of the columnar phase competes with that of the equiaxed crystals. The solidification of both columnar trunk and equiaxed crystals is governed by diffusion; the difference between equilibrium and volume-averaged melt concentrations ($c_{\ell}^{*} - c_{\ell}$) is the driving force for the solidification. If the driving force ($c_{\ell}^{*} - c_{\ell}$) < 0, remelting would occur.

(8) In this study, fragmentation of columnar dendrites is considered as the only source of equiaxed crystals. Following the consideration that solute-driven remelting of secondary or high-order dendrites is the key mechanism for fragmentation [27–32], a new formula was proposed for the fragmentation-induced mass transfer rate [23]: $M_{\mathrm{ce}} = -\gamma \cdot \vec{u}_{\ell} \cdot \nabla c_{\ell} \cdot \rho_{\mathrm{e}}$. This means that an interdendritic flow in the columnar zone $\vec{u}_{\ell}$ against the direction of the melt concentration gradient ($-\nabla c_{\ell}$) increases the local constitutional supersaturation, hence promoting remelting-induced fragmentation. Here, a fragmentation coefficient, γ, is assigned to bridge the unknown correlation between M_{ce} and the increase rate of constitutional supersaturation. The details can be found in Appendix A.

3. Benchmark configuration

The dimension of the casting sample (calculation domain), the boundary, and initial conditions were rigidly derived from the benchmark experiment [7], as shown in Fig. 1. The experiment used two lateral heat exchangers, allowing input/extraction of the heat into/from two vertical sides of the sample. The geometry of the sample was a quasi-two-dimensional rectangular ingot with size 100 × 60 × 10 mm^3. The stage of melt preheating (homogenization of the melt temperature), which was necessary during experiment, was ignored in the numerical simulation. Thus, the melt was assumed to be homogeneous in temperature before solidification. As solidification started, the imposed temperatures were applied at both lateral side walls (Fig. 1(c)). The temperature difference between the two lateral walls was 40 K, and the cooling rate (CR) was 0.03 K/s. The front/back and top/bottom walls were treated as adiabatic.

The alloy was Sn-10 wt% Pb. A linearized Pb-Sn binary phase diagram, with a constant solute partition coefficient k and a constant liquidus slope m, was used. Other thermodynamic and thermal physical data/properties are listed in Table 1 The transport of equiaxed crystals due to sedimentation played an essential role in this benchmark experiment. The density of solid equiaxed dendrites was reasonably assumed constant (7950 kg m^{-3}), but the liquid density was strongly dependent on the solute (Pb) mass fraction [33,34], as is shown in Fig. 2.

Several auxiliary quantities were used to analyse the macrosegregation [35,36]: the mixture concentration, $c_{\mathrm{mix}} = (c_{\ell}\rho_{\ell}f_{\ell} + c_{\mathrm{c}}\rho_{\mathrm{c}}f_{\mathrm{c}} + c_{\mathrm{e}}\rho_{\mathrm{e}}f_{\mathrm{e}})/(\rho_{\ell}f_{\ell} + \rho_{\mathrm{c}}f_{\mathrm{c}} + \rho_{\mathrm{e}}f_{\mathrm{e}})$; macrosegregation index, $c^{\mathrm{index}} = (c_{\mathrm{mix}} - c_0) \times 100/c_0$; and the global macrosegregation intensity, GMI = $(\iint_{\mathrm{V_{domain}}} |C^{\mathrm{index}}| dv)/\mathrm{V_{domain}}$. The model was implemented within the framework of the CFD software, ANSYS-Fluent, Version 14.5. All simulations were performed in parallel

Table 1
Material properties and other parameters.

	Symbol	Units		Ref.
Nominal concentration of alloy (Pb)	c_0	1	0.1	
Liquidus temperature	T_{liq}	K	492.14	[33]
Melting point of solvent (Sn)	T_{f}	K	505	[33]
Eutectic composition	c_{eu}	1	0.381	[33]
Eutectic temperature	T_{eu}	K	456	[37]
Liquidus slope	m	K	−128.6	[33]
Equilibrium partition coefficient	k	1	0.0656	[33]
Reference density	ρ_{ref}	kg m^{-3}	7000	[33]
Solid density	ρ_{e}, ρ_{c}	kg m^{-3}	7950	[34]
Specific heat	c_{p}^{ℓ}, $c_{\mathrm{p}}^{\mathrm{e}}$, $c_{\mathrm{p}}^{\mathrm{c}}$	J kg^{-1} K^{-1}	260	[33]
Thermal conductivity	k_{ℓ}, k_{e}, k_{c}	W m^{-1} K^{-1}	55.0	[33]
Latent heat	L	J kg^{-1}	6.1×10^{4}	[33]
Viscosity	μ_{ℓ}	kg m^{-1} s^{-1}	1.0×10^{-3}	[33]
Liquid thermal expansion coefficient	β_{T}	K^{-1}	6.0×10^{-5}	[33]
Primary dendritic arm spacing	λ_1	M	2.25×10^{-4}	[38]
Secondary dendritic arm spacing	λ_2	M	6.5×10^{-5}	[33]
Diffusion coefficient (liquid)	D_{ℓ}	m^2 s^{-1}	4.5×10^{-9}	[39]
Diffusion coefficient (solid)	D_{c}, D_{e}	m^2 s^{-1}	1×10^{-12}	[39]
Initial temperature	T_0	K	492.14	[33]
Gibbs-Thomson coefficient	Γ	m K	6.5×10^{-8}	[38]
Fragmentation coefficient	γ	1	0.1	

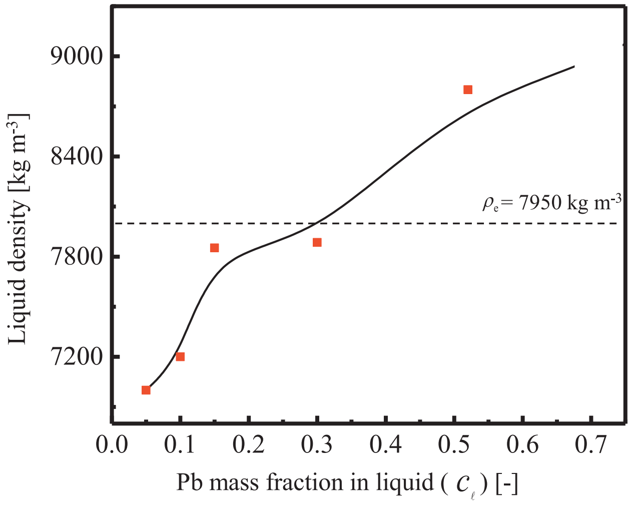

Fig. 2. Melt density as function of solute (Pb) mass fraction in the Sn-Pb alloy [33,34].

on a high-performance cluster (2.6 GHz, 12 cores). It takes approximately 30 days for a three-dimensional (3D) simulation and approximately 10 days for a 2D case.

4. Results

4.1. Solidification sequence

The calculated solidification sequence is shown in Fig. 3. To assist in the result description, the global solidification and melt flow patterns are schematically drawn in Fig. 3(a.x). A full 3D calculation was performed, but here only the result on a vertical section at z = 0.003 m is presented. The reason for showing the result on this section rather than on the symmetry section z = 0.0 m is that no obvious segregation channel appears on the symmetry section. Although the casting configuration is quasi-two-dimensional, the calculated mesosegregation (channel segregation) has the nature of full 3D, i.e. the main channel does not appear in the casting centre, but quite close to the casting surface. The time is accounted from the start of the cooling stage (Fig. 1(c)).

At 30 s, a clockwise thermal convection with maximum velocity 3.7×10^{-2} m/s developed (Fig. 3(b.1)). As the superheat of the melt

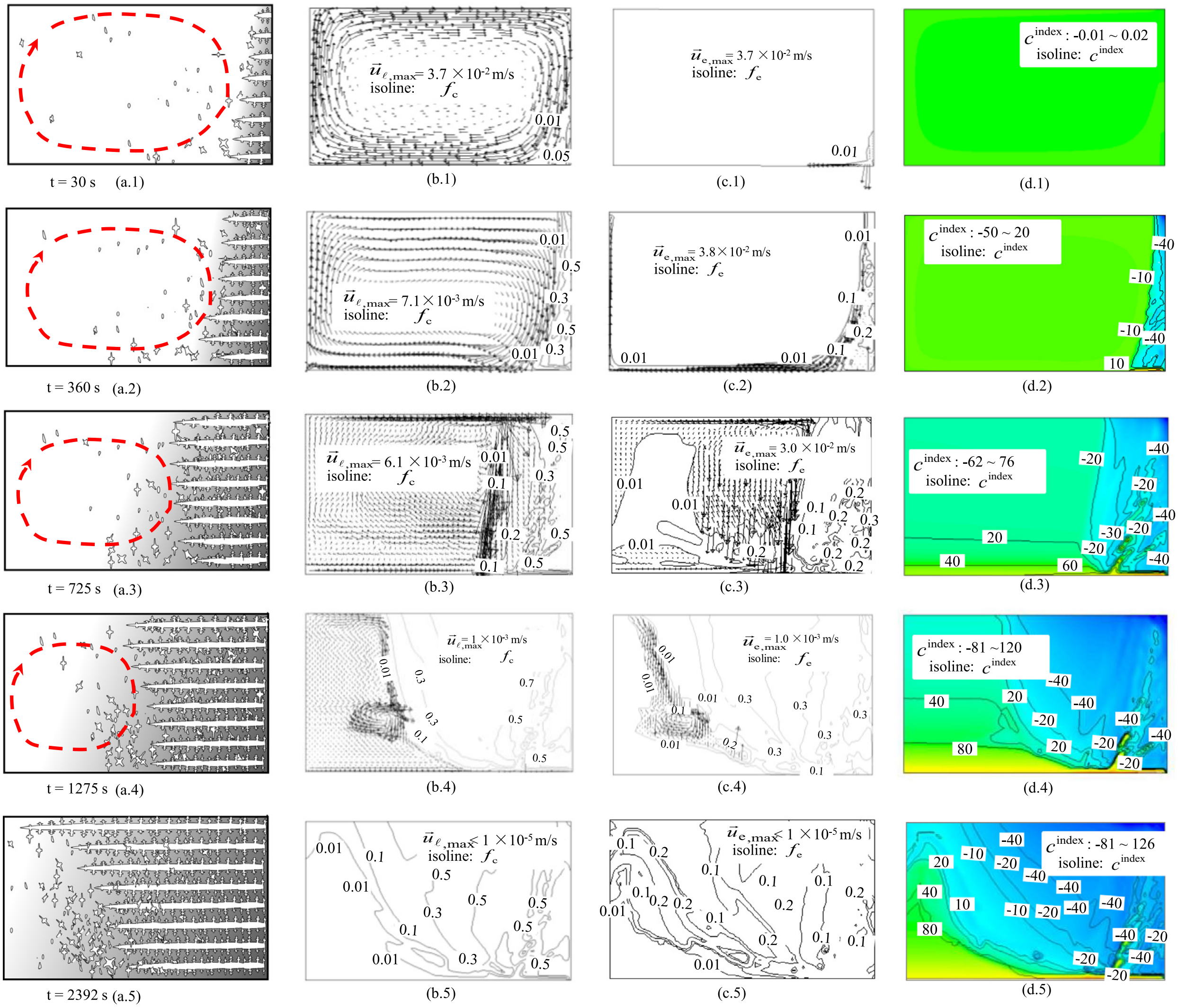

Fig. 3. Solidification sequence of the benchmark (on the plane z = 0.003 m): (a.x.) Schematic of solidification regions and global melt flow pattern, (b.x.) liquid velocity overlaid with f_c isoline, (c.x.) equiaxed velocity overlaid with f_e isoline (d.x.) contour of the macrosegregation index (c^{index}). c^{index} are shown in the colour scales with blue for the minimum (or negative extreme), and red for the maximum (or positive extreme).

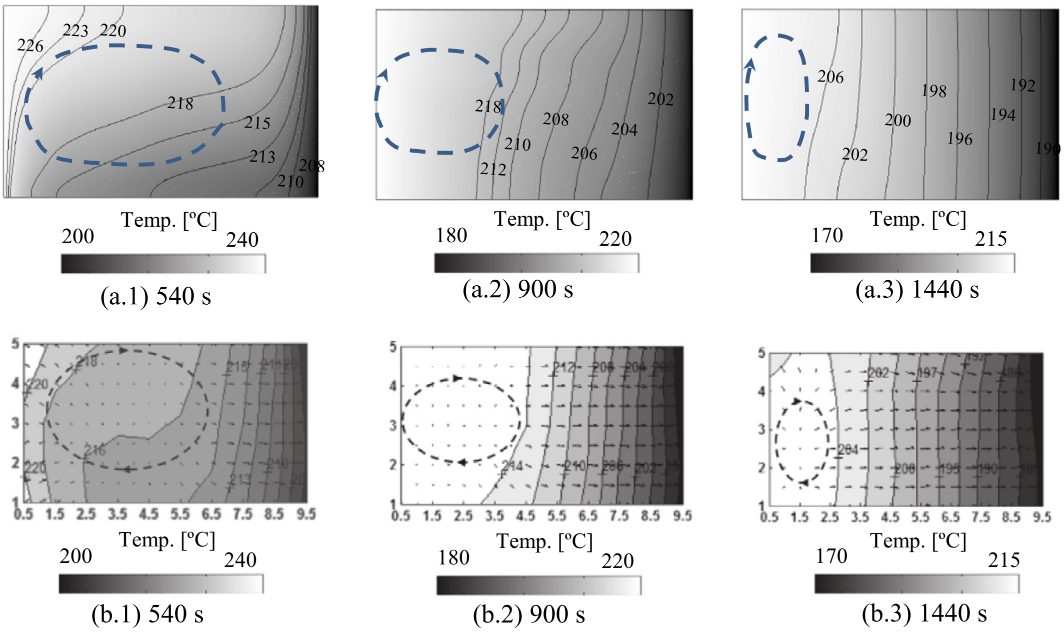

Fig. 4. Comparison of the temperature field on the symmetry plane z = 0.0 at *t* = 540, 900, and 1440 s from the beginning of solidification between simulation (a.x) and experiment (b.x). (b.x) are reprinted from publication [7], with permission from Elsevier.

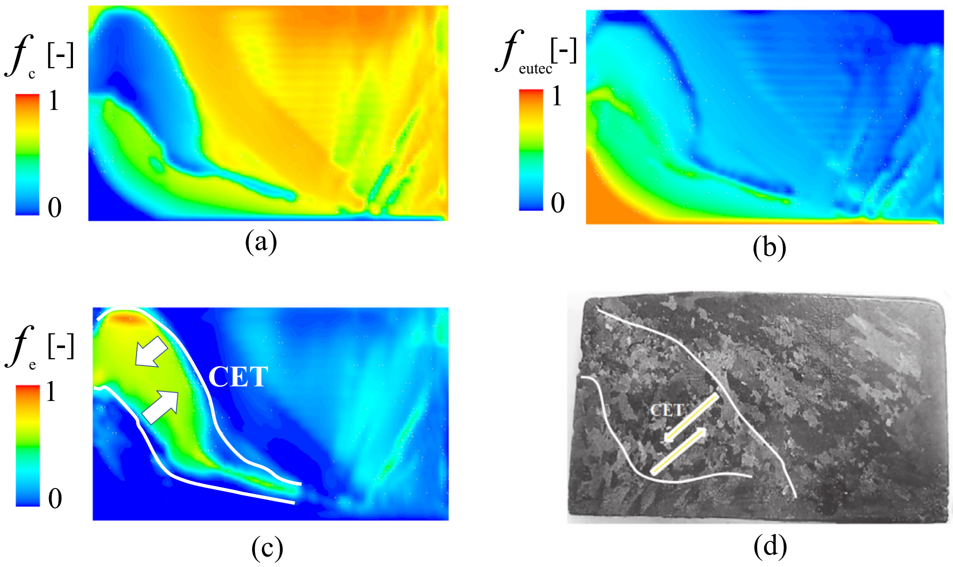

Fig. 5. As-cast structure: simulation results of volume fractions of (a) columnar, (b) rest eutectic, and (c) equiaxed phases; (d) metallography of the as-cast structure. (d) is reprinted from publication [7], with permission from Elsevier.

is extracted from the cold wall (right side) and the temperature there drops gradually below the liquidus temperature, the columnar trunks start to grow. A columnar-liquid mushy zone forms, and in the mushy zone, equiaxed crystals are produced because of the fragmentation. Equiaxed crystals have the tendency to sediment on the bottom because the density of the equiaxed phase is larger than that of the liquid. The lower-right corner is the place where equiaxed crystals first accumulate (Fig. 3(c.1)). At this early stage of solidification, the macrosegregation over the domain is negligibly small (Fig. 3(d.1)).

At 360 s, the columnar phase region on the right side of the benchmark extends leftwards (Fig. 3(a.2)–(b.2)). The velocity of the liquid decreases dramatically, and its maximum value is approximately 7.1×10^{-3} m/s. In the mushy zone, the liquid can flow through the columnar dendrites, initializing the segregation channels (Fig. 3(b.2) and (d.2)). Equiaxed crystals are produced continuously near the columnar front by fragmentation, but they are brought into the bulk region. The maximum velocity of the equiaxed crystals is approximately 3.8×10^{-2} m/s. It is larger than that of the liquid, and the region with high velocity is located near the columnar front. The accumulated equiaxed region is spread along the bottom surface of the benchmark (Fig. 3(c.2)).

From 360 s to 725 s, the liquid velocity deceases gradually. More segregation channels are observed in the columnar region (Fig. 3(b.3) and (d.3)). More equiaxed crystals are produced in the region near the columnar tip front (Fig. 3(a.3)). In the middle bottom region of the benchmark, the equiaxed phase forms a packed zone. In the bulk region near the hot wall, equiaxed crystals float up, or sink down to the lower-left region where remelting of the crystals occurs (Fig. 3(c.3)).

As solidification proceeds to 1275 s, the columnar front continues to grow (Fig. 3(a.4)), and more segregation channels form in the columnar region (right) (Fig. 3(d.4)). Solute (Pb) enrichment in the liquid phase increases the liquid density, hence decreasing the density difference between the liquid and equiaxed phase. It becomes easier for liquid to sweep the equiaxed crystals with the upward melt flow. A portion of equiaxed crystals is even brought upwards by a vortex (Fig. 3(b.4)–(c.4)). Some small equiaxed crystals are brought upwards to the upper-left corner region. They grow, and then settle down. One can also see that some newly formed crystals by dendrite fragmentation attach to the packed equiaxed network in the bottom near the vortex (Fig. 3(c.4)). The solute enriched melt, which becomes denser and heavier, starts to accumulate in the bottom-left region of the benchmark, resulting in a positive macrosegregation in the lower-left corner (Fig. 3(d.4)).

At 2392 s, the velocities for both liquid and equiaxed phases vanish. The right part of the benchmark is composed of the columnar phase with negative macrosegregation and positive segregation channels. The lower-left part is dominated by a solute-enriched phase (rest eutectic) with positive macrosegregation. There is an equiaxed region on the upper-left corner (Fig. 3(c.5)), which extends to the middle bottom region. The solidification does not end yet, and the final as-cast structure and macrosegregation remain nearly unchanged during the rest solidification.

4.2. Comparisons with the experimental measurements

4.2.1. Temperature field

The calculated temperature field is compared with the experimental measurement (Fig. 4). As the temperature gradient builds up during the early stage of solidification (Fig. 4(a.1)), a clockwise convection forms and distorts the isotherms. Afterwards, as the solidification front advances and the flow magnitude decreases, the isotherms gradually become vertical (Fig. 4(a.2) and (a.3). The simulation results agree well with the experimental measurement (Fig. 4(b.1)–(b.3)). However, the global temperature, especially near the hot side wall, is slightly overestimated by the simulation. The reason may be the heat loss through the front/back and top/bottom walls, which is ignored by the numerical simulation. In the experiment, minor heat loss from those walls would occur [5,40].

4.2.2. As-cast structure

Comparison of the as-cast structure between simulation and experiment is shown in Fig. 5. The general appearance of them is quite similar. The upwind tiled columnar structure region is located in the left side. A small second columnar structure region is observed in the lower-left corner, where the volume fraction of rest eutectic is predicted quite high by the simulation. The equiaxed structure is located in the upper-left region, which extends to the middle bottom. The equiaxed zone is enclosed between two lines, which indicate the CET.

4.2.3. Macrosegregation

The macrosegregation between simulation and experiment is compared in Fig. 6. Numerically, the most positive macrosegregation (up to 25 wt% Pb) is located near the left side wall where the melt solidifies at the late stage, and the negative macrosegregation is located in the upper- right side of the benchmark. Near the lower-right corner, several segregation channels are observed in Fig. 6(a). Pb concentration in the segregation channels reaches 16 wt%. The numerically predicted segregation map (Fig. 6(a)) agrees qualitatively with the experimental results, as measured by two different methods. Fig. 6(b) shows the Pb distribution as measured by chemical analysis with technical inductively coupled plasma (ICP). It is mapped on the basis of 50 discrete measurements over the longitudinal section of the benchmark. Fig. 6(c) shows X-radiography of the as-solidified benchmark. Mesosegregation (channel segregates) can be clearly observed. The contrast of the X-radiography can provide only a qualitative evaluation of the relative Pb concentration. A quantitative segregation map (Fig. 6(d)) is made through digital processing of the X-radiography, and then calibrated by the chemically analysed quantities from Fig. 6(b).

A 3D view of segregation channels is presented by the iso-surface of 12 wt% Pb (Fig. 7). The channels form preferentially along the mould walls. Only some small discontinuous channel

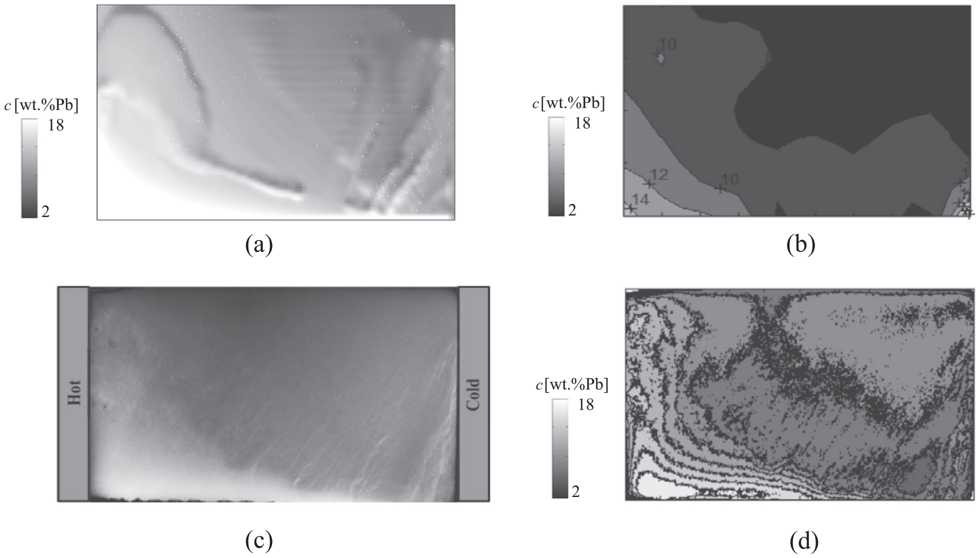

Fig. 6. Macrosegregation: (a) simulated macrosegregation (wt.% Pb) on the plane z = 0.003 m, (b) Pb concentration map measured by the chemical method coupled with technical inductively coupled plasma, (c) X-radiography of the as-solidified benchmark, and (d) Pb concentration map digitally processed from (c), and calibrated by the concentration value in (b). (b), (c) and (d) are reprinted from publication [7], with permission from Elsevier.

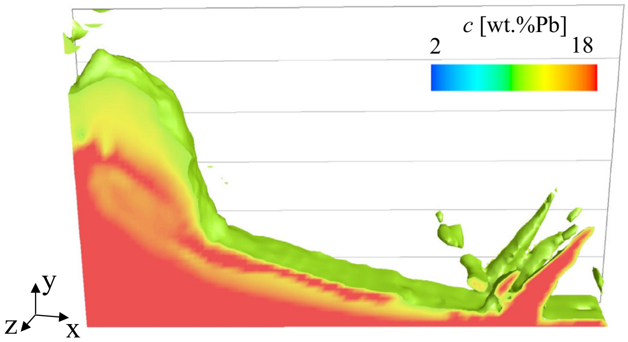

Fig. 7. 3D view of iso-surface of 12 wt% Pb, coloured by Pb-concentration from 2 wt% (blue) to 18 wt% (red). (For interpretation of the references to colour in this figure legend, the reader is referred to the web version of this article.)

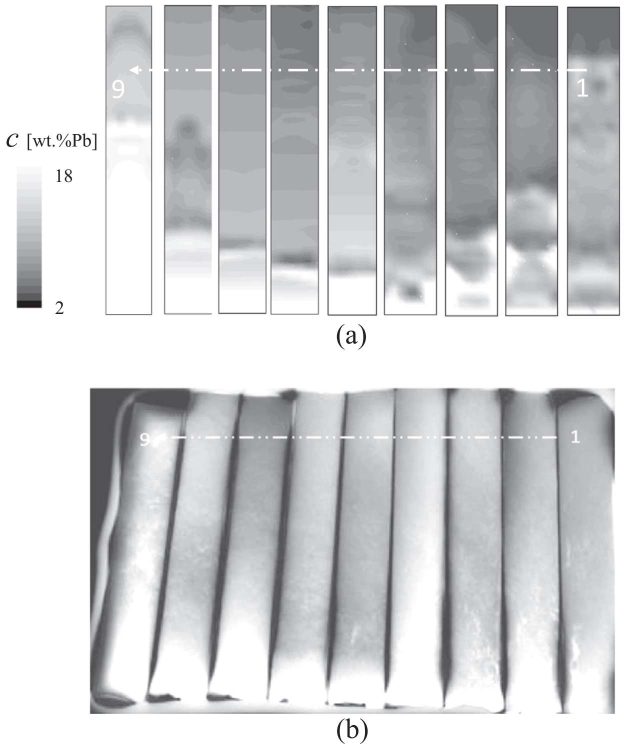

Fig. 8. Views of macrosegregation in slices perpendicular to the front (or back) side wall at positions 1–9, corresponding to 10, 20, 30, 40, 50, 60, 70, 80, and 90 mm from the cold wall: (a) Contours of Pb concentration predicted by simulation, and (b) X-ray photographs of the slices centred on the abovementioned positions (lighter colours correspond to Pb-rich zones). (b) is reprinted from publication [7], with permission from Elsevier.

pieces in the casting centre are found. Most channels are in the form of tubular structures. There are also some lamellar-structured channels, which connect the bottom Pb-enriched zone.

Views of macrosegregation in slices perpendicular to the front/back walls at nine positions, corresponding to 10, 20, 30, 40, 50, 60, 70, 80, and 90 mm from the cold wall of the as-solidified benchmark, are shown in Fig. 8. X-radiographs of the nine transverse-cut slices were made, and compared with the numerical simulation. The experimental slices were made perpendicularly to the front/back walls, but the views of X-radiographs were turned by 90°. Note that this comparison can be made only qualitatively, because each X-radiograph represents an integration of the X-ray signal through the thickness of each slice (5–6 mm), whereas the numerical result is the segregation map on the section. The contrast intensity of the X-radiographs is attenuated by the averaging over the thickness, probably resulting in the ignorance of the mini channels there. Generally, the simulation-experiment agreement is good. The global locations of the intensive Pb-enriched areas as predicted by simulation coincide with lighter areas as detected by the X-radiographs. The fact of the occurrence of channel segregates and their locations seem to agree with each other as well. The main differences between the simulation and the experiment are as follows. The concentrated positive segregation of Pb in the lower-left corner region seems to be overestimated by the simulation, and the transition from the high Pb-enriched region to the lower Pb-enriched region is numerically calculated more clearly than the experimental result (X-radiographs show a smoother transition from the very light region to the grey region). Exact locations of the segregation channels do not match the experimental results, and the average size (diameter) of the channels is also overestimated by the numerical simulation. It is known that one reason for this mismatch is the mesh size, which was discussed in previous reports [21,22].

Quantitative comparison of the macrosegregation profiles along horizontal lines (x direction) were made between the simulation and experiment (Fig. 9). Experimental measurements of Pb concentrations were made by the chemical method coupled with ICP. Fifty samples were extracted by drilling holes from the as-cast benchmark, at height y = 0.05, 0.04, 0.03, 0.02, and 0.01 m. This means that for each height, ten samples were drilled with equal intervals along the x direction. The mass used for chemical analysis was approximately 200 mg from each drilled sample. It is assumed that the measured Pb-concentration represents the mean value of the drilled sample, i.e. the mean Pb-concentration through the sample thickness (z direction). In order to make the simulation-experiment comparison meaningful, the simulation curves of Fig. 9 were also made by averaging the values through the sample thickness. In principle, the experimental points (data) and the simulation curves show a similar distribution tendency, but the numerical simulation seems to have overestimated the macrosegregation intensity. The calculated maximum positive segregation in the lower-left region (Fig. 9(e)) and the maximum negative segregation in the upper-right region of the benchmark (Fig. 9(a)) are larger than the experimental results. Additionally, some simulation curves (e.g. Fig. 9(e)) show clear fluctuation, sometimes varying between local minimum and maximum, indicating the line crossing the CET border or crossing the segregation channels; however, this kind of fluctuation cannot be seen experimentally. There is only one experimental point (close to the cold wall in Fig. 9(e)) that reaches a concentration of 20 wt% Pb, indicating probable channel segregation. From the X-radiographs (Fig. 6(c) and (d)), a few more channels can be identified. Those channels were obviously missed by the chemical analysis in Fig. 9.

5. Discussion

To understand the formation of the as-cast structure and macrosegregation, analyses of the numerical results and numerical parameter studies were made. In the previous section, a 3D simulation result was presented. This section is mostly based on the 2D calculations for purposes of enhancing the computational efficiency. Numerical factors, including the dimension (2D/3D) and mesh size, would influence the calculation accuracy [41]. A comparison between 3D and 2D calculations is shown in Fig. 10. Details about the distribution of the equiaxed phase, and the number and shape of the segregation channels, are slightly different between the 3D and 2D calculations. However, the global distribution of the as-cast structure, macrosegregation, and occurrence and location of segregation channels are quite similar. Sensitivity of the simulation result to the grid size is further analysed in §5.4.

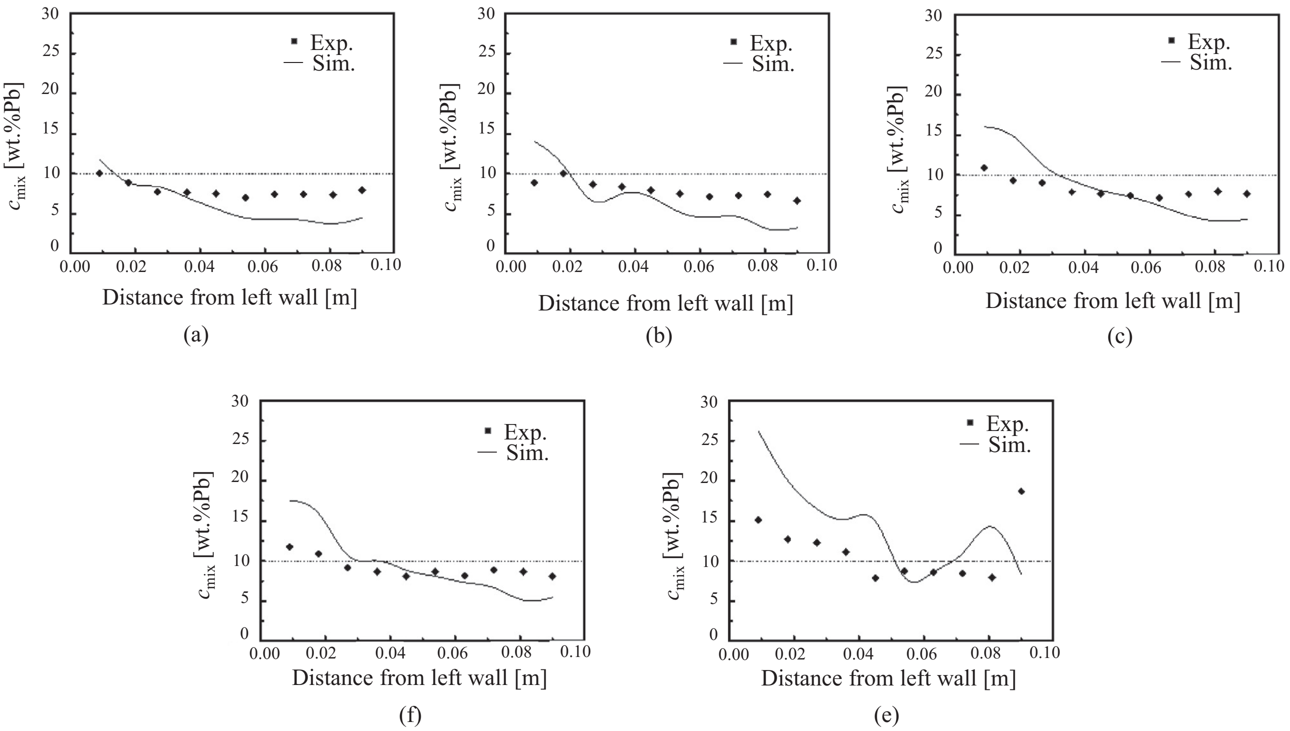

Fig. 9. Comparison of Pb-concentration obtained by ICP analysis (squares) with the simulation along the horizontal lines (x direction): (a)–(f) correspond to five different heights at y = 0.05, 0.04, 0.03, 0.02, 0.01 m. The simulation curves are post-processed by averaging the values through the thickness (z direction).

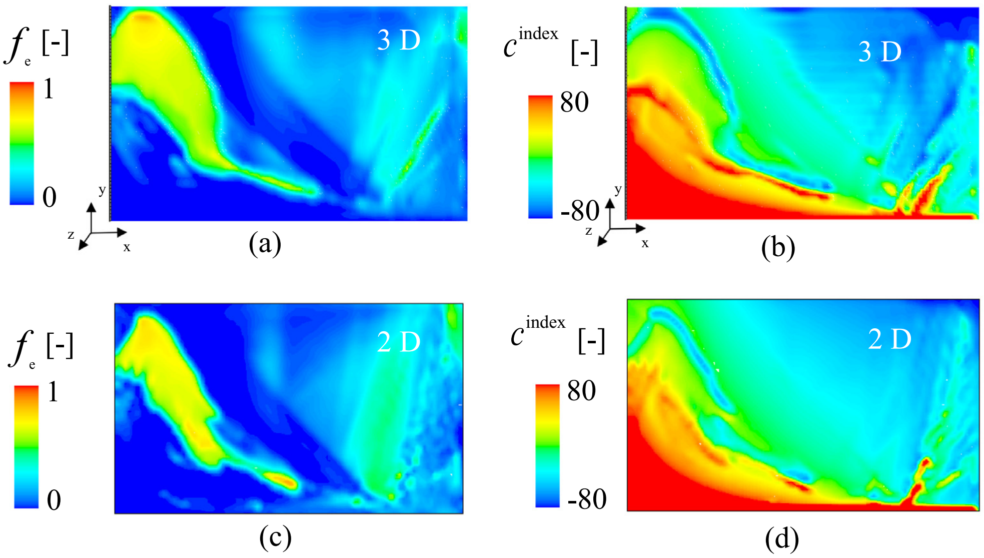

Fig. 10. Comparison of 3D and 2D simulations: (a) f_e and (b) c^{index} contours on the plane z = 0.003 m of the 3D simulation, and (c) f_e and (d) c^{index} contours of 2D simulation. Mesh sizes for both simulations are the same (1 mm).

5.1. Origin of equiaxed crystals by fragmentation

The production rate of fragments is quantified by N_{frag}, which is derived from the fragmentation-induced columnar-to-equiaxed mass transfer rate [23], as calculated by the formula $M_{ce} = -\gamma \cdot \vec{u}_\ell \cdot \nabla c_\ell \cdot \rho_e$, with an assumption of the size of newly created fragments ($d^0_{e,frag}$) equal to $\lambda_2 f_c$. Details about the fragmentation model, i.e. formula precisely, are described in Appendix A. This formula is suggested on the concept that the solute-driven remelting is the dominant mechanism for fragmentation [28–32], and transport of the solute-enriched melt by the interdendritic flow in the columnar-growth direction (or against the ∇c_ℓ direction) enhances the remelting. Additionally, the flow in the columnar-growth direction is a necessary condition to transport fragments out of the mush zone [42].

A detailed analysis of $\vec{u}_\ell$, ∇c_ℓ and the production rate of fragments N_{frag} is made in Fig. 11. The dendrite fragments are mostly produced near the columnar tip front. A global flow pattern is in the clockwise direction and it has the largest velocity near the columnar tip front (Fig. 11(a) and (b)). The columnar tip front is approximated by $f_c = 0.02$. Along the columnar tip front, the flow direction ($\vec{u}_\ell$) is slightly tilted outwards from the columnar mushy

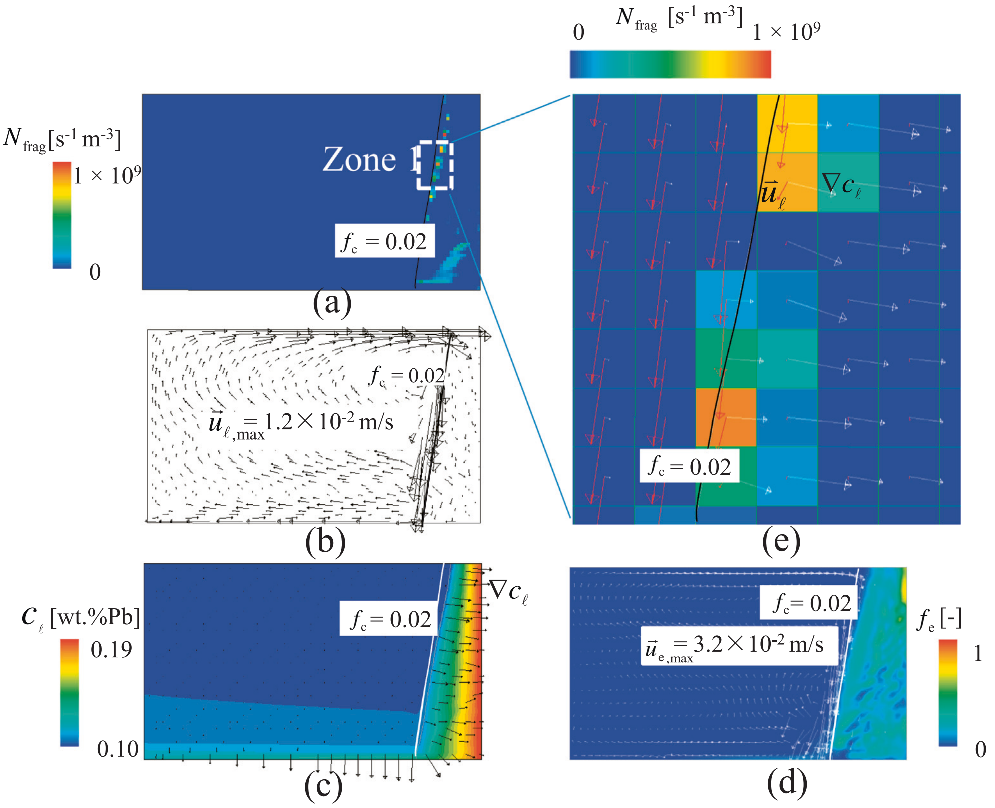

Fig. 11. Formation of equiaxed crystals by fragmentation (at 600 s). (a) Distribution of production rate of fragments N_{frag} with columnar tip front approximated by $f_c = 0.02$; (b) liquid velocity $\vec{u}_\ell$; (c) liquid concentration(c_ℓ) overlaid with vector ∇c_ℓ; (d) equiaxed volume fraction f_e and its velocity $\vec{u}_e$; (e) zoomed-in view of N_{frag} in Zone 1 overlaid with the liquid velocity $\vec{u}_\ell$ (red) and liquid concentration gradient ∇c_ℓ (white). (For interpretation of the references to colour in this figure legend, the reader is referred to the web version of this article.)

zone (Fig. 11(e)). The direction of ∇c_ℓ is always towards the columnar mushy zone, i.e. against the columnar tip growth direction (Fig. 11(c)). This kind of flow favours the fragmentation. A zoomed-in view (Zone 1) of the fragmentation region (Fig. 11(e)) provides more details about the distribution of N_{frag}. The liquid velocity and liquid concentration gradient are shown in vectors: $\vec{u}_\ell$ in red and ∇c_ℓ in white. The angle between the two vectors indicates the possibility of fragmentation. When it is larger than 90°, fragmentation may occur. No fragments can be produced when it is smaller than 90°. The non-homogenous distribution of N_{frag} is caused mainly by the instable flow along the columnar tip front. Both the velocity magnitude and flow direction oscillate along the columnar tip front, causing the non-homogenous distribution of N_{frag}. Note that one modelling parameter is introduced: the fragmentation coefficient γ. All unknown factors contributing to fragmentation, such as the curvature effect of the dendrites, latent heat-induced thermal fluctuation, and diffusion in the interdendritic melt, were included in the single γ. This parameter should be determined experimentally. The previous numerical parameter study [23] by varying γ (from 0.01 to 10.0) suggested a constant value (0.1) for the alloy Sn-10 wt% Pb. The simulation-experiment agreement for the current benchmark verifies that the value of 0.1 for γ is a reasonable choice for this alloy.

5.2. Formation of the equiaxed zone

As shown in Fig. 5(d), an accumulated equiaxed zone was obtained in the upper-left corner region of the as-solidified benchmark casting, and this region extends to the middle bottom. Similar results are predicted numerically (Fig. 5(a)–(c)). This is due to the transport of the equiaxed crystals. As shown in Figs. 3 and 11, all equiaxed crystals originate by fragmentation near the columnar tip front. The fragmentation-induced crystal fragments, i.e. equiaxed crystals, are transported out of the columnar mushy zone. They tend to sink down along the columnar tip front because its density is higher than that of the liquid melt, but in the meantime the melt flow also tries to bring them into the bulk region (left side). Because the density of the melt is strongly dependent on the solute enrichment of the melt (Fig. 2), the equiaxed crystals can settle down or float up through the balance of the flow-induced drag force and the gravity-driven sedimentation. In the early stage of solidification, the density of the solid (ρ_e) is much larger than that of the melt (ρ_ℓ); hence, the equiaxed crystals are prone to accumulate in the bottom region. In the late stage, however, with the gradual enrichment of Pb in the melt, the density difference ($\Delta\rho_{e\ell} = \rho_e - \rho_\ell$) becomes sufficiently small so that the drag force by melt flow can easily overwhelm the buoyancy force.

A detailed analysis of the crystal movement and the melt flow in the period from 1100 s to 1540 s is shown in Fig. 12. The newly formed fragments/equiaxed crystals along the columnar tip front sink downwards, driving a clockwise melt flow in the bulk melt pool. Both liquid and equiaxed phases are coupled by the drag force, which is according to Wang et al. [43]. As the downward melt stream along the columnar tip front meets the bottom region, it is 'forced' to change the direction. This sharp change of the flow direction causes to form a small clockwise vortex (Fig. 12(a.x)). This vortex is located in the low-right corner of the bulk melt pool. It is this vortex that carries a certain amount of equiaxed crystals away from the columnar tip front (Fig. 12(b.x)). In the 'eye' of the vortex, a relatively high volume fraction of equiaxed phase is distributed. As time proceeds, the whole area of the melt pool

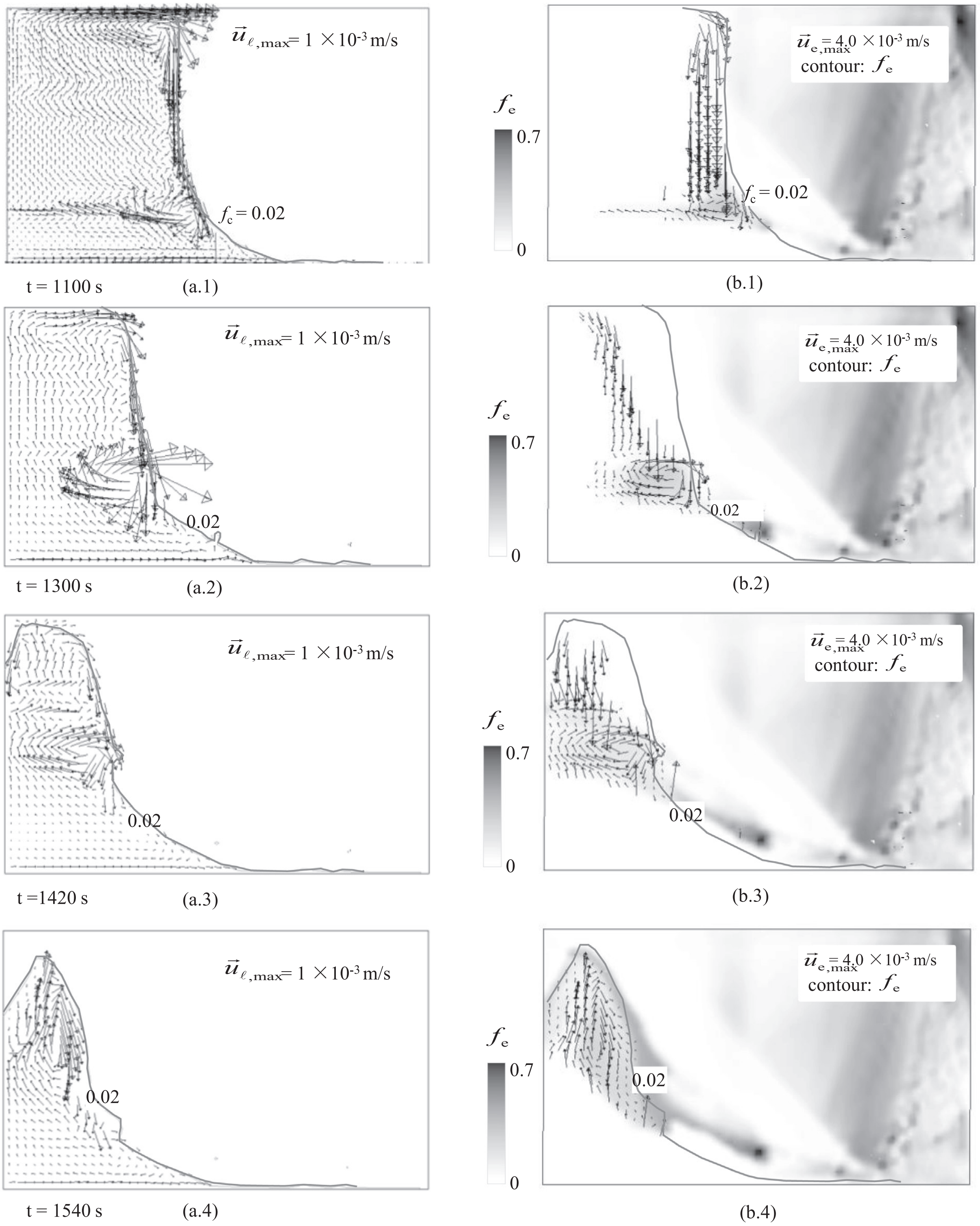

Fig. 12. Transport of crystal crystals during solidification in the period from 1100 s to 1540 s: (a.x) liquid velocity $\vec{u}_\ell$ overlaid with the isoline $f_c = 0.02$. Liquid velocity is shown in the region where the liquid volume fraction f_ℓ is between 0.1 and 1; (b.x) distribution of f_e overlaid with equiaxed velocity $\vec{u}_e$ and isoline $f_c = 0.02$. Equiaxed velocity is shown only in the region where f_e is between 0.001 and 1.

shrinks gradually (Fig. 12(a.2)–(a.4)). Correspondingly, the small vortex moves from the middle bottom region towards upper-left part of the benchmark, leaving a trail of distribution band of equiaxed phase (Fig. 12(b.2)–(b.4)). It can be anticipated that the crystal-carry vortex contributes significantly to the accumulated equiaxed zone of Fig. 5.

To demonstrate the role of the crystal movement in the formation of the as-cast structure, two extreme cases were calculated. Case (a) assumed a constant $\Delta\rho_{e\ell} = -150\ \text{kg/m}^3$, i.e. the equiaxed is slightly lighter than the melt; Case (b) assumed a constant $\Delta\rho_{e\ell}$ = 950 kg/m^3, i.e. the equiaxed is significantly heavier than the melt. Both cases ignored the density change of the melt with the Pb enrichment. Calculation results are shown in Fig. 13. Although the melt flow patterns for both cases are quite similar, the movements of the equiaxed crystals are completely different; hence, different as-cast structures are predicted. In Case (a), fragmentation-induced equiaxed crystals are first brought out of the columnar mushy zone, and then most of them float up to the top of the benchmark. In Case (b), fragmentation-induced equiaxed crystals try to settle down immediately, but most of them are captured in the columnar phase region. Only a small portion of them are brought out of the columnar mushy zone, and then are transported and accumulate in the left corner region of the benchmark. Obviously, none of these cases with a constant $\Delta\rho_{e\ell}$ can 'reproduce' the as-cast structure (Fig. 5(d)) as obtained experimentally.

5.3. Channel segregates (mesosegregation)

Channel segregates, also called mesosegregation or segregation channels, start and grow in the region of the columnar tip front (Fig. 3). In the as-solidified benchmark, those channel segregates are located in the lower part of the columnar structure (Figs. 5 and 6). A previous study by the current authors [21,22] found that channel segregates develop in two steps, i.e. the onset and the channel growth. Onset of the channel is caused by the mush (or convection) instability, which can be analysed in terms of the mush zone Rayleigh number (*R*a) [44,45]. If *R*a is larger than a critical value (0.12–0.24), a channel would initialize. However, the *R*a criterion alone is not a sufficient condition to predict the channel formation. The onset channel must continue to grow into a stable channel by the resulting interdendritic flow-solidification interaction. This flow-solidification interaction can be analysed by the interaction term, $\vec{u}_\ell \cdot \nabla c_\ell$. The sign of this term, $\vec{u}_\ell \cdot \nabla c_\ell$, can be used to distinguish two solidification regions: a suppressed solidification region, where the sign of the flow-solidification interaction term is negative (flow is in the opposite direction of the liquid concentration gradient); and an accelerated solidification region, where the sign of the flow-solidification interaction term is positive (flow is in the same direction of the liquid concentration gradient). Channels can occur only in the suppressed solidification region, where an increase in local flow caused by a flow perturbation is reinforced by the resulting suppressed solidification. This scenario occurs in the lower part of the columnar tip front region. In this situation, the flow becomes unstable and channels continue to grow. Channels do not form in the accelerated solidification region, where an increase in local flow intensity due to flow perturbation is throttled by the resulting accelerated solidification. In this latter case, flow perturbation is stabilized by flow-solidification interactions, and it does not matter whether the *R*a criterion for the onset of channels is fulfilled. For example, in the upper part of the columnar tip front region, the *R*a criterion could also be fulfilled, but no channel would occur there.

This paper will not repeat the analysis of the previous work [21,22], but a suppressed solidification region, where channels develop, is shown with more detail (Fig. 14). Channels are characterized by the lower solid fraction region, corresponding to the region of high c^{index}. The positive direction of∇c_ℓduring this stage of solidification is always rightward (Fig. 11(c)); the flow in the channel is left-downward, as shown in Fig. 14(a.2). The sign of $\vec{u}_\ell \cdot \nabla c_\ell$ in the channel is negative, i.e. the solidification is suppressed. In the neighbouring region (channel wall), however, the flow is conducted towards the channel, which is much more permeable. The sign of $\vec{u}_\ell \cdot \nabla c_\ell$ in the neighbouring region (channel wall) is no more negative, i.e. solidification might be accelerated there. With this kind of flow-solidification interaction, the channel becomes stable.

The view of the transverse section (Fig. 14(a.3)–(b.3)) shows that the channels occur preferentially near the wall, which coincides with other numerical studies [6,46] as well as with the current benchmark (Fig. 8(b)) and other experiments [47].

5.4. Grid sensitivity

Calculations with four mesh sizes (0.8, 1.0, 1.5, and 2.0 mm) were performed. Fig. 15 shows the equiaxed phase distribution and macrosegregation at the end of solidification. A CET line

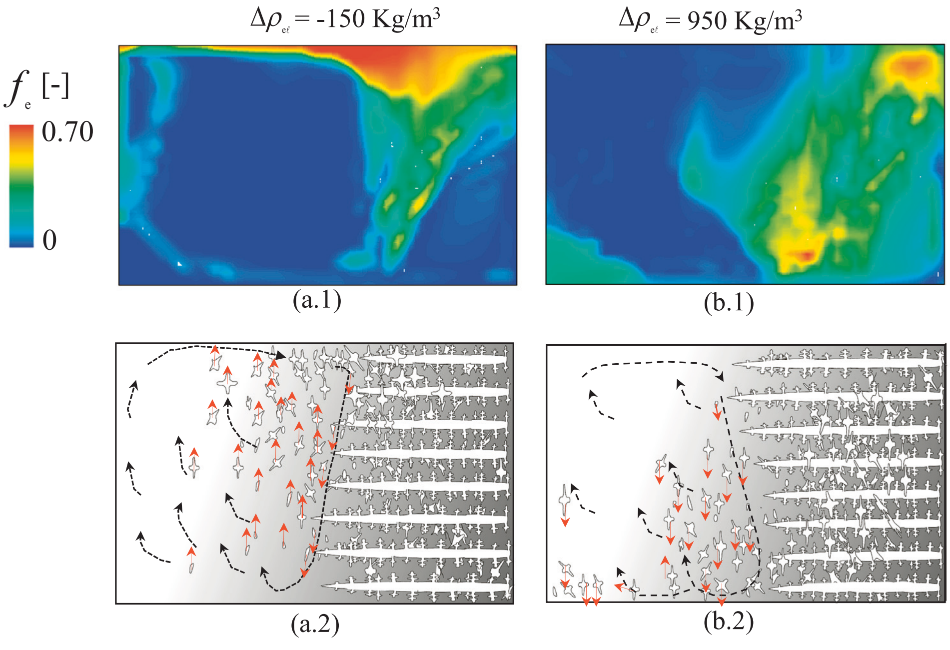

Fig. 13. Influence of density difference between equiaxed phase and melt ($\Delta\rho_{e\ell}$) on the formation of as-cast structure. Two cases are calculated: (a.x) with $\Delta\rho_{e\ell} = -150$ kg m^{-3}; (b.x) with $\Delta\rho_{e\ell} = 950$ kg m^{-3}. The upper row (a.1) and (b.1) are the simulation results of the f_e distribution in the as-solidified benchmark; the lower row (a.2) and (b.2) are schematics of the melt flow and equiaxed movement (black dashed lines indicate the circulation of melt flow and red arrows indicate the moving direction of equiaxed crystals).

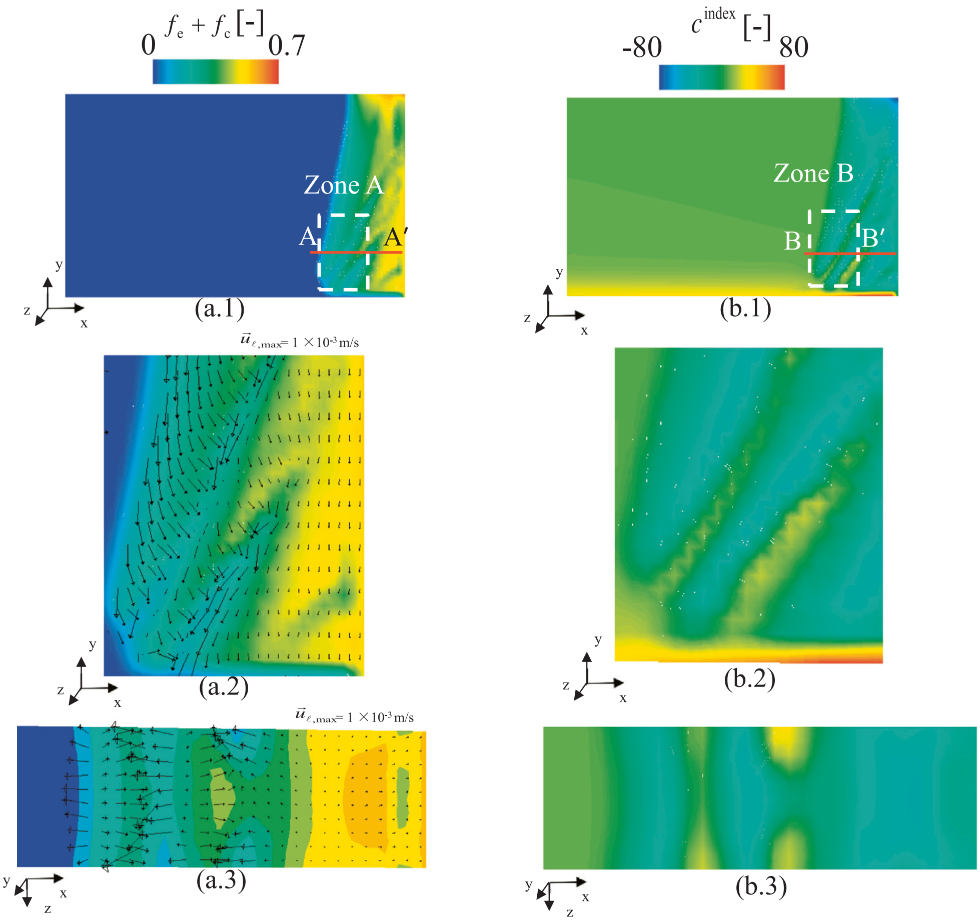

Fig. 14. Analysis of channel segregation during the early stage of solidification (at 700 s): (a.1) solid fraction ($f_e + f_c$) on the plane z = 0.003 m; (a.2) zoomed-in view (Zone A), superimposed with liquid velocity; (a.3) solid fraction on the transversal section contour along A–A′; (b.1) macrosegregation (c^{index}) on the plane z = 0.003 m; (b.2) zoomed-in view (Zone B); (b.3) macrosegregation on the transversal section along B-B’. This result is taken from the 3D calculation.

separates the columnar and equiaxed regions (Fig. 15(a.x)). Macrosegregation distributions are compared in Fig. 15(b.x). It does not seem possible to possess a grid-independent result, especially regarding to the distribution of equiaxed area and the details of the channel segregates (mesosegregation), but the global as-cast structure and macrosegregation pattern are similar for all cases. The area of the equiaxed zone, as bordered by the CET line, remains nearly unchanged when the mesh size is smaller than Δx = 1.5 mm. All cases have predicted the occurrence of channel segregates in the lower-right corner of the benchmark (columnar structure region). A tendency is clear, that with the decrease in grid size from 2.0 to 0.8 mm, the modelling results of the macrosegregation distribution and segregation intensity tend to converge. The c^{index} value for all cases ranges from -86 to 230. The c^{index} range does not significantly change when the mesh size decreases to smaller than Δx = 1.0 mm. The global macrosegregation intensity (GMI) reflects the overall macrosegregation intensity in the domain, and it seems to approach a convergent result (60.7) when the mesh size is smaller than 1.0 mm.

One can safely conclude that the mesh size of 1 mm, as used for this study, can reliably resolve the global as-cast structure and macrosegregation pattern, and even predict the occurrence (or probability/risk of occurrence) of channel segregates. Fine details of the channel segregates, i.e. the number of channels and segregation intensity in the channels, are not solvable with the current mesh resolution. A similar conclusion was also drawn in other studies [21,22,48]. One origin of this mesh sensitivity of the channel segregates might be the flow in the high liquid volume fraction (in the front of the columnar mushy zone), which is highly sensitive to the mesh size [17].

6. Conclusions

A solidification benchmark experiment based on Sn-10 wt% Pb alloy as performed at the SIMAP Laboratory in Grenoble, France [7] was numerically ‘reproduced’ by a mixed columnar-equiaxed solidification model [9]. The experiment-simulation agreement in the temperature evolution, as-cast structure, and macro- and mesosegregation further verified the numerical model. By analysis of the modelling results, the following knowledge/conclusions were obtained:

(1) Understanding of the formation of the as-cast structure (mixed columnar-equiaxed), as observed experimentally, was improved. The columnar structure developed first from the cold wall. The fragmentation-induced equiaxed crystals are transported away from the front region of the columnar zone by the melt flow. Those crystals can grow or re-melt during the movement. The equiaxed crystals settle down and float up through the balance of the flow-induced drag force and the gravity-driven sedimentation. The equiaxed crystals, interacting with the growing columnar structure, lead to CET and form the final as-cast structure.

(2) For the alloy (Sn-10 wt% Pb) considered in this benchmark experiment, the density variation of the melt with the Pb enrichment plays a critical role in the movement (transport)

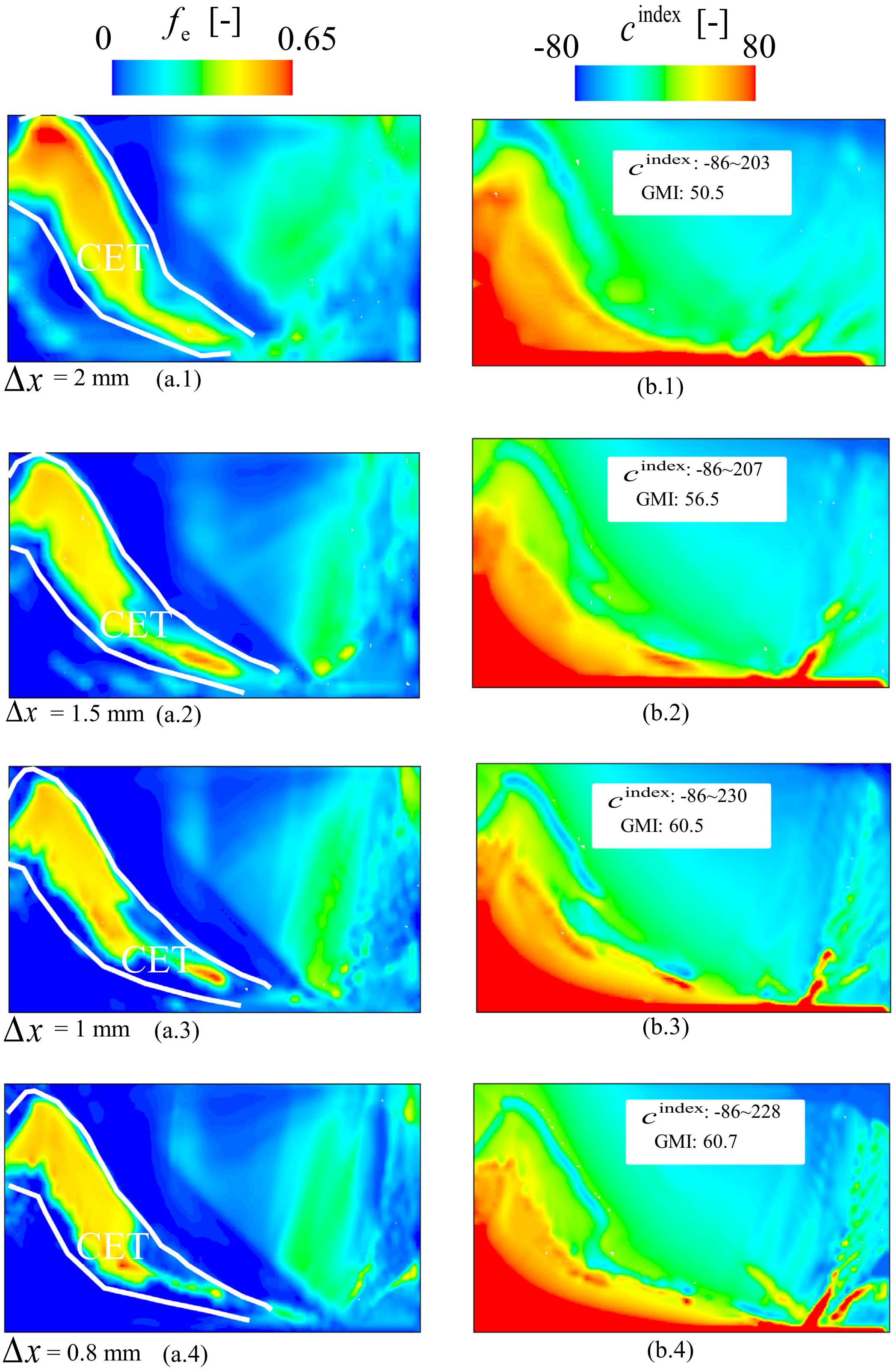

Fig. 15. Influence of mesh size (0.8, 1.0, 1.5, 2.0 mm) on the as-cast structure and macrosegregation: (a.x) f_e distribution with bold lines for the CET; (b.x) c^{index} map and global macrosegregation intensity (GMI) value.

of equiaxed crystals. The equiaxed crystals are normally denser than the melt, and tend to settle downwards. With the Pb-enrichment during solidification, however, the melt becomes gradually denser as well. The reduced density difference between the solid and the Pb-enriched melt favours the upward motion of the crystals, because of the drag force as imposed by the upward melt flow. If this Pb concentration-dependent density variation of the melt were ignored, the experimentally observed as-cast structure would not be ‘reproducible’ numerically.

(3) Because crystal fragmentation was found to play a critical role in the origin of equiaxed crystals in this benchmark experiment [7], the mixed columnar-equiaxed model was extended for fragmentation [23]. The modelling concept for fragmentation is that solute-driven remelting is the dominant mechanism for fragmentation [28–32], and transport of the solute-enriched melt by the interdendritic flow in the columnar-growth direction (or against the ∇c_ℓdirection) enhances remelting. Although further experimental evaluations are desirable, the first simulation-experiment comparison with a satisfactory agreement, concerning the result of as-cast structure and global macrosegregation pattern, provides convincing evidence for this modelling concept.

(4) The numerical model also predicted mesosegregation, i.e. channel segregates (or segregation channels), which qualitatively agrees with the experiment. Similar to many other numerical [6,46] and experimental studies [47], the segregation channels were predicted to occur preferentially near the wall. It must also be stated that the current modelling results can be used only to evaluate the occurrence (or probability/risk of occurrence) of channel segregates. Details of the channel segregates, e.g. the channel quantity and size, are still mesh-size-dependent.

Conflict of interest

The authors declared that there is no conflict of interest.

Acknowledgements

The authors acknowledge the financial support from the Austrian Research Promotion Agency (FFG) through the Bridge Early Stage project (No. 842441), as well as the technical support of industrial partner Primetals (formerly Siemens VAI).

Appendix A. Production of equiaxed crystals by fragmentation

Transport of the number density of the equiaxed crystals, n_{eq}, is described by

$$\frac{\partial}{\partial t} n_{\mathrm{eq}} + \nabla \cdot (\vec{u}_{\mathrm{e}} n_{\mathrm{eq}}) = N_{\mathrm{frag}}, \tag{A.1}$$

where N_{frag} is the source term of equiaxed crystals by fragmentation [49].

It is known that transport of the solute-enriched melt by the interdendritic flow in the columnar-growth direction would lead to remelting [32,50]. Under normal diffusion-governed solidification condition, the driving force for the remelting is the constitutional supersaturation, $(c_\ell - c_\ell^*)$, where c_ℓ and c_ℓ^* are the volume-averaged concentration of interdendritic melt and the thermodynamic equilibrium concentration of the melt at the liquid-solid interface. A positive value of $(c_\ell - c_\ell^*)$ results in remelting, or a process leading to an increase of c_ℓ promotes remelting. The interdendritic melt has usually a concentration gradient (∇c_ℓ) in opposite to the columnar-growth direction for alloys with the solute partition coefficient (k) less than one (Fig. A.1). An interdendritic flow in the columnar-growth direction means $-(\vec{u}_\ell - \vec{u}_{\mathrm{c}}) \cdot \nabla c_\ell > 0$; therefore, the flow leads to local increase of c_ℓ, promoting the remelting. Actually, the rate of remelting should be somehow related to the value of $-(\vec{u}_\ell - \vec{u}_{\mathrm{c}}) \cdot \nabla c_\ell$. Even the local capillary effect, i.e. coarsening or ripening phenomenon, is ignored, fragments can be produced by the ‘homogenous’ remelting. Based on the large number of experimental facts on the remelting-induced fragmentation [28–30,42,51,52] and the above theoretical analysis, we assume that the rate of fragmentation is proportional to the value of $-(\vec{u}_\ell - \vec{u}_{\mathrm{c}}) \cdot \nabla c_\ell$, by suggesting following formulation for the fragmentation-induced mass transfer rate from the columnar phase to the equiaxed phase:

$$M_{\mathrm{ce}} = -\gamma \cdot (\vec{u}_\ell - \vec{u}_{\mathrm{c}}) \cdot \nabla c_\ell \cdot \rho_{\mathrm{e}}. \tag{A.2}$$

The mass integral of all fragments as produced per time, $\mathrm{kg \cdot m^{-3} \cdot s^{-1}}$, is proportional to the increase rate of constitutional supersaturation as caused by the interdendritic flow.’ Here a fragmentation coefficient’ γ is assigned to bridge the unknown correlation between M_{ce} and the increase rate of constitutional supersaturation. In other words, all other unknown contributing factors for the remelting-induced fragmentation such as the curvature effect of the dendrites, latent heat induced thermal fluctuation, diffusion in the interdendritic melt, etc. are included in the single coefficient γ. It must be determined experimentally, or estimated reversely from some available experimental information. As shown in Fig. A.1, we assume that the fragment is globular (spherical) with a diameter proportional to the secondary dendrite arm and the volume fraction of the melt:

$$d^0_{\mathrm{e,frag}} = \lambda_2 f_{\mathrm{c}}. \tag{A.3}$$

Hence the rate of the fragment production can be calculated as:

$$N_{\mathrm{frag}} = \frac{M_{\mathrm{ce}}}{\rho_{\mathrm{e}} \cdot \frac{\pi}{6} \left(d^0_{\mathrm{e,frag}}\right)^3} \tag{A.4}$$

Correspondingly, the fragmentation induced momentum transfer $(\vec{U}^{\mathrm{p}}_{\mathrm{ce}})$, energy transfer $(Q^{\mathrm{p}}_{\mathrm{ce}})$ and species transfer $(C^{\mathrm{p}}_{\mathrm{ce}})$ from the columnar to equiaxed phases are:

$$\vec{U}^{\mathrm{p}}_{\mathrm{ce}} = \vec{u}_{\mathrm{c}} \cdot M_{\mathrm{ce}}, \tag{A.5}$$

$$Q^{\mathrm{p}}_{\mathrm{ce}} = h_{\mathrm{c}} \cdot M_{\mathrm{ce}}, \tag{A.6}$$

$$C^{\mathrm{p}}_{\mathrm{ce}} = c_{\mathrm{c}} \cdot M_{\mathrm{ce}}, \tag{A.7}$$

with $\vec{u}_{\mathrm{c}}$, h_{c}, c_{c} being the moving velocity, the enthalpy and the concentration of the columnar phase. Accordingly, the diameter of equiaxed crystals are shown as

$$d_{\mathrm{e}} = (6 f_{\mathrm{e}} / \pi \cdot n_{\mathrm{e}})^{1/3}. \tag{A.8}$$

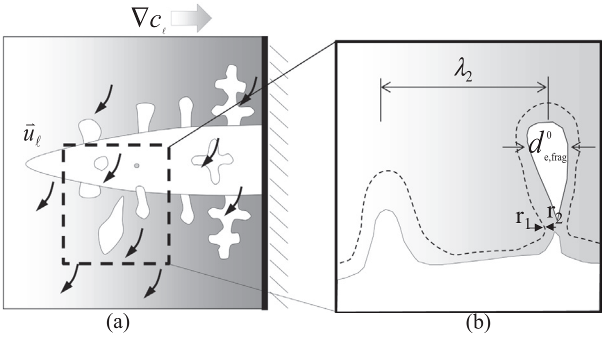

(a) (b)

Fig. A.1. Schematic description of remelting-induced fragmentation: (a) transport of solute-enriched interdendritic melt by the flow, and (b) formation of a fragment by remelting of the side arm.

References

[1] D. Hebditch, J. Hunt, Observations of ingot macrosegregation on model systems, Metall. Mater. Trans. 5 (1974) 1557–1564.
[2] C. Gau, R. Viskanta, Melting and solidification of a metal system in a rectangular cavity, Int. J. Heat Mass Transfer 27 (1984) 113–123.
[3] J. Sarazin, A. Hellawell, Channel formation in Pb-Sn, Pb-Sb, and Pb-Sn-Sb alloy ingots and comparison with the system NH_4Cl-H_2O, Metall. Mater. Trans. A 19 (1988) 1861–1871.
[4] M.I. Bergman, D.R. Fearn, J. Bloxham, M.C. Shannon, Convection and channel formation in solidifying Pb-Sn alloys, Metall. Mater. Trans. A 28 (1997) 859–866.
[5] X. Wang, Y. Fautrelle, An investigation of the influence of natural convection on tin solidification using a quasi two-dimensional experimental benchmark, Int. Heat Mass Transfer 52 (2009) 5624–5633.
[6] R. Boussaa, L. Hachani, O. Budenkova, V. Botton, D. Henry, K. Zaidat, H.B. Hadid, Y. Fautrelle, Macrosegregations in Sn-3wt% Pb alloy solidification: experimental and 3D numerical simulation investigations, Int. J. Heat Mass Transfer 100 (2016) 680–690.
[7] L. Hachani, K. Zaidat, Y. Fautrelle, Experimental study of the solidification of Sn-10 wt.%Pb alloy under different forced convection in benchmark experiment, Int. J. Heat Mass Transfer 85 (2015) 438–454.
[8] L. Hachani, B. Saadi, X.D. Wang, A. Nouri, K. Zaidat, A. Belgacem-Bouzida, L. Ayouni-Derouiche, G. Raimondi, Y. Fautrelle, Int. J. Heat Mass Transfer 55 (2012) 1986–1996.
[9] M. Wu, A. Ludwig, A three-phase model for mixed columnar-equiaxed solidification, Metall. Mater. Trans. A 37A (2006) 1613–1631.
[10] C.-A. Gandin, T. Carozzani, H. Digonnet, S. Chen, G. Guillemot, Direct Modeling of structures and segregations Up to industrial casting scales, JOM 65 (2013) 1122–1130.
[11] T. Carozzani, C.-A. Gandin, H. Digonnet, M. Bellet, K. Zaidat, Y. Fautrelle, Direct simulation of a solidification benchmark experiment, Metall. Mater. Trans. A 44 (2013) 873–887.
[12] A. Ciobanas, Y. Fautrelle, Ensemble averaged multiphase Eulerian model for columnar/equiaxed solidification of a binary alloy: I. The mathematical model, J. Phys. D: Appl. Phys. 40 (2007) 3733–3741.
[13] A. Ciobanas, Y. Fautrelle, Ensemble averaged multi-phase Eulerian model for columnar/equiaxed solidification of a binary alloy: II. Simulation of the columnar-to-equiaxed transition (CET), J. Phys. D: Appl. Phys. 40 (2007) 4310–4336.
[14] M. Wu, A. Fjeld, A. Ludwig, Modelling mixed columnar-equiaxed solidification with melt convection and grain sedimentation–Part I: Model description, Comp. Mater. Sci. 50 (2010) 32–42.
[15] M. Wu, A. Ludwig, A. Fjeld, Modelling mixed columnar-equiaxed solidification with melt convection and grain sedimentation–Part II: Illustrative modelling results and parameter studies, Comp. Mater. Sci. 2010 (50) (2010) 43–58.
[16] C. Wang, C. Beckermann, Equiaxed dendritic solidification with convection: Part I. Multiscale/multiphase modeling, Metall. Mater. Trans. A 27 (1996) 2754–2764.
[17] H. Combeau, M. Bellet, Y. Fautrelle, D. Gobin, E. Arquis, O. Budenkova, B. Dussoubs, Y. Du Terrail, A. Kumar, C.-A. Gandin, Analysis of a numerical benchmark for columnar solidification of binary alloys, IOP Conf. Series: Mate. Sci. Eng. 33 (2012) 012086.
[18] M. Wu, A. Ludwig, Using a three-phase deterministic model for the columnar-to-equiaxed transition, Metall. Mater. Trans. A 38A (2007) 1465–1475.
[19] J. Li, M. Wu, A. Ludwig, A. Kharicha, Simulation of macrosegregation in a 2.45-ton steel ingot using a three-phase mixed columnar-equiaxed model, Int. J. Heat Mass Transfer 72 (2014) 668–679.
[20] M. Ahmadein, M. Wu, J. Li, P. Schumacher, A. Ludwig, Prediction of the As-Cast Structure of Al-4.0 Wt Pct Cu Ingots, Metall. Mater. Trans. A 44 (2013) 2895–2903.
[21] J. Li, M. Wu, J. Hao, A. Ludwig, Simulation of channel segregation using a two-phase columnar solidification model–Part I: Model description and verification, Comp. Mater. Sci. 55 (2012) 407–418.
[22] J. Li, M. Wu, J. Hao, A. Kharicha, A. Ludwig, Simulation of channel segregation using a two-phase columnar solidification model–Part II: Mechanism and parameter study, Comp. Mater. Sci. 55 (2012) 419–429.
[23] Y. Zheng, M. Wu, A. Kharicha, A. Ludwig, An attempt to incorporate fragmentation into a volume average solidification model, Model. Simul. Mater. Sci. Eng. 26 (2018) 015004.
[24] J. Hunt, Steady state columnar and equiaxed growth of dendrites and eutectic, Mater. Sci. Eng. 65 (1984) 75–83.
[25] Y. Zheng, M. Wu, A. Kharicha, A. Ludwig, Numerical analysis of macrosegregation in vertically solidified Pb-Sn test castings–Part II: Equiaxed solidification, Comp. Mater. Sci. 124 (2016) 456–470.
[26] A. Ludwig, M. Wu, Modeling of globular equiaxed solidification with a two-phase approach Metall, Mater. Trans. A 33 (2002) 3673–3683.
[27] R.B. Bird, W.E. Stewart, E.N. Lightfoot, Transport Phenomena, Wiley, 2006.
[28] K. Jackson, J. Hunt, D. Uhlmann, T. Seward, On the origin of the equiaxed zone in castings, Trans. Metall. Soc. Aime 236 (1966) 149–158.
[29] W. Montgomery, F. Incropera, Fragmentation of dendritic crystals during solidification of aqueous ammonium chloride, Exp. Heat Transfer 11 (1998) 59–86.
[30] R. Mathiesen, L. Arnberg, P. Bleuet, A. Somogyi, Crystal fragmentation and columnar-to-equiaxed transitions in Al-Cu studied by synchrotron X-ray video microscopy, Metall. Mater. Trans. A 37 (2006) 2515–2524.
[31] E. Liotti, A. Lui, R. Vincent, S. Kumar, Z. Guo, T. Connolley, I. Dolbnya, M. Hart, L. Arnberg, R. Mathiesen, A synchrotron X-ray radiography study of dendrite fragmentation induced by a pulsed electromagnetic field in an Al–15Cu alloy, Acta Mater. 70 (2014) 228–239.
[32] T. Campanella, C. Charbon, M. Rappaz, Grain refinement induced by electromagnetic stirring: a dendrite fragmentation criterion, Metall. Mater. Trans. A 35 (2004) 3201–3210.
[33] M. Bellet, H. Combeau, Y. Fautrelle, D. Gobin, M. Rady, E. Arquis, O. Budenkova, B. Dussoubs, Y. Duterrail, A. Kumar, Call for contributions to a numerical benchmark problem for 2D columnar solidification of binary alloys, Int. J. Therm. Sci. 48 (2009) 2013–2016.
[34] O.L. Rocha, C.A. Siqueira, A. Garcia, Heat flow parameters affecting dendrite spacings during unsteady-state solidification of Sn-Pb and Al-Cu alloys, Metall. Mater. Trans. A 34 (2003) 995–1006.
[35] M. Wu, J. Li, A. Ludwig, A. Kharicha, Modeling diffusion-governed solidification of ternary alloys–Part 1: Coupling solidification kinetics with thermodynamics, Comp. Mater. Sci. 79 (2013) 830–840.
[36] M. Wu, J. Li, A. Ludwig, A. Kharicha, Modeling diffusion-governed solidification of ternary alloys–Part 2: Macroscopic transport phenomena and macrosegregation, Comp. Mater. Sci. 92 (2014) 267–285.
[37] N. Ahmad, J. Rappaz, J.-L. Desbiolles, T. Jalanti, M. Rappaz, H. Combeau, G. Lesoult, C. Stomp, Numerical simulation of macrosegregation: a comparison between finite volume method and finite element method predictions and a confrontation with experiments, Metall. Mater. Trans. A 29 (1998) 617–630.
[38] E. Cadirli, M. Gündüz, The directional solidification of Pb-Sn alloys, J. Mater. Sci. 35 (2000) 3837–3848.
[39] M. Klassen, J. Cahoon, Interdiffusion of Sn and Pb in liquid Pb-Sn alloys, Metall. Mater. Trans. A 31 (2000) 1343–1352.
[40] X.D. Wang, P. Petitpas, C. Garnier, J.-P. Paulin, Y. Fautrelle, A quasi two-dimensional benchmark experiment for the solidification of a tin–lead binary alloy, Comptes Rendus Mécanique 335 (2007) 336–341.
[41] M. Rappaz, Modeling and characterization of grain structures and defects in solidification, Curr. Opin. Solid State Mater. Sci. 20 (2016) 37–45.
[42] A. Hellawell, S. Liu, S. Lu, Dendrite fragmentation and the effects of fluid flow in castings, JOM 49 (1997) 18–20.
[43] C. Wang, S. Ahuja, C. Beckermann, H. De Groh, Multiparticle interfacial drag in equiaxed solidification, Metall. Mater. Trans. B 26 (1995) 111–119.
[44] C. Beckermann, J. Gu, W. Boettinger, Development of a freckle predictor via rayleigh number method for single-crystal nickel-base superalloy castings, Metall. Mater. Trans. A 31 (2000) 2545–2557.
[45] M. Worster, J. Wettlaufer, Natural convection, solute trapping, and channel formation during solidification of saltwater, J. Phys. Chem. B 101 (1997) 6132–6136.
[46] J. Guo, C. Beckermann, Three-dimensional simulation of freckle formation during binary alloy solidification: effect of mesh spacing, Numer. Heat Transfer: Part A: Appl. 44 (2003) 559–576.
[47] D. Ma, Q. Wu, A. Bührig-Polaczek, Some new observations on freckle formation in directionally solidified superalloy components, Metall. Mater. Trans. B 43 (2011) 344–353.
[48] A. Kumar, B. Dussoubs, M. Založnik, H. Combeau, Effect of discretization of permeability term and mesh size on macro-and meso-segregation predictions, J. Phys. D: Appl. Phys. 42 (2009) 105503–105515.
[49] C. Beckermann, Modeling segregation and grain structure development in equiaxed solidification with convection, JOM 49 (1997) 13–17.
[50] M.C. Flemings, G.E. Nereo, Macrosegregation: Part I, Trans. Metall. Soc. Aime 239 (1967) 1449–1462.
[51] M. Christenson, W. Bennon, F. Incropera, Solidification of an aqueous ammonium chloride solution in a rectangular cavity—II. Comparison of predicted and measured results, Int. J. Heat Mass Transfer 32 (1989) 69–79.
[52] M. Christenson, F. Incropera, Solidification of an aqueous ammonium chloride solution in a rectangular cavity—I. Experimental study, Int. J. Heat Mass Transfer 32 (1989) 47–68.

Paper V

Role of fragmentation in ascast structure: numerical study and experimental validation

Yongjian Zheng, Menghuai Wu, Abdellah Kharicha, Andreas Ludwig

China Foundry, 2017, 14: 321-326.

Role of fragmentation in as-cast structure: numerical study and experimental validation

Yong-jian Zheng[1], ***Meng-huai Wu**[1,2], **A. Kharicha**[1,2], **and A. Ludwig**[1]

1. Chair of Simulation and Modelling of Metallurgical Processes, Montanuniversitaet Leoben, Leoben, Austria

2. Christian Doppler Laboratory for Advanced Process Simulation of Solidification and Melting, Department of Metallurgy, University of Leoben, Leoben, Austria

Abstract: A volume average solidification model is extended to incorporate fragmentation as the source of equiaxed crystals during mixed columnar-equiaxed solidification. This study is to use this model to analyze the role of fragmentation in the formation of as-cast structure. Test simulations are made for the solidification of a model alloy (Sn-10wt.%Pb) with two different geometries. The first one is a 2D rectangular domain (50 × 60 mm^2) as cooled from the top boundary. Solidification starts unidirectionally as columnar structure from the top. The solute (Pb) enriched interdendritic melt is heavier than the bulk melt, and sinks downwards, hence leads to solutal convection. Fragmentation phenomenon occurs near the columnar tip front. The fragments are transported out of the columnar region, and they continue to grow and sink, and finally settle down and pile up at the bottom. The growing columnar structure from the top and pile-up of equiaxed crystals from the bottom finally lead to a mixed columnar-equiaxed structure, in turn leading to a columnar-to-equiaxed transition (CET). The second geometry is a 3D plate, 100 × 60 ×10 mm^3, as cooled laterally from one side. It was cast experimentally and analyzed for the as-cast structure. The equiaxed fragments are produced in the solidification front and transported into the bulk melt, leading to a special pattern of as-cast structure: columnar structure in the cool wall side and equiaxed structure in the upper left corner near the hot wall side, extending downwards to the middle bottom region. Numerically calculated as-cast structures agree with the experiment results.

Key words: macrostructure; interdendritic fluid flow; fragmentation

CLC numbers: TP391.99 **Document code:** A **Article ID:** 1672-6421(2017)05-321-06

More and more evidence has shown that the interdendritic fluid flow can facilitate the fragmentation by the mechanism of solute-driven remelting of dendrite arms[1-4]. On this base, a dendrite fragmentation criterion was proposed[5]. Additionally, the interdendritic flow is also a necessary condition for transport of the fragments out of the (columnar structure) mushy zone, and those fragments act as nuclei of equiaxed crystals[6]. The current authors proposed a formula to incorporate fragmentation into a volume average model[7]. This work is to use this model to investigate the role of fragmentation in the formation of as-cast structure.

Two simulation examples are investigated. The first one takes the similar configuration of the experiment as performed by Cao et al.[8]. A 2D cavity, as initially filled with aqueous ammonium chloride (NH_4Cl-H_2O), is cooled from top unidirectionally. The columnar structure grows from the top; the thermal-solutal convection causes the fragmentation; equiaxed crystals as grown from the fragments sediment at the bottom; finally a mixed columnar (top region) and equiaxed (bottom region) structure is developed. The second simulation example is based on a laboratory benchmark[9, 10]. A plate casting of Sn-10wt.%Pb alloy is cooled laterally. The columnar structure grows initially from the cool side; fragmentation occurs in the front of the columnar structure; the thermal-solutal convection transports from fragments to the other side, leading to a special pattern of mixed columnar (cool side) and equiaxed structure.

1 Fragmentation formulation

A three-phase mixed columnar-equiaxed solidification

***Prof. Meng-huai Wu**

He got his Ph.D degree in 2000 at the Foundry Institute, RWTH Aachen in Germany, and Habilitation (professorial certificate) in 2008 at Montanuniversitaet Leoben in Austria, and became the head of Christian Doppler Laboratory for "Advanced Process Simulation of Solidification and Melting" in 2010. His main research interests are the modeling and simulation of solidification and related phenomena during different casting processes.

E-mail: menghuai.wu@unileoben.ac.at

Received: 2017-08-15; Accepted: 2017-09-04

model was described previously[11, 12]. The so-called three phases are the liquid, equiaxed and columnar. Their volume fractions are f_l, f_e and f_c with $f_\mathrm{l} + f_\mathrm{e} + f_\mathrm{c} = 1$. Both the liquid and equiaxed phases are moving phases, while the columnar phase is assumed to be rigid and stationary. A dendritic equiaxed crystal is presumed and it is described by an equiaxed grain envelope, which includes the solid 'dendrite' and the inter-dendritic melt. The ratio of the volume of solid 'dendrite' to the volume of the equiaxed grain envelope is predefined f_si. In this study, f_si is set as a constant value (0.5). When $f_\mathrm{e}^\mathrm{Env}$ ($= f_\mathrm{e}/f_\mathrm{si}$) reaches the hard blocking criterion, which is set as 0.49 at the columnar tip front, the columnar-to-equiaxed transition (CET) occurs. Once $f_\mathrm{e}^\mathrm{Env}$ exceeds the packing limit (0.637), equiaxed crystals will build a stationary network.

Fragments can be produced by the 'homogenous' remelting. Based on idea on the remelting-induced fragmentation[7], following formulation for the fragmentation-induced mass transfer rate from the columnar phase to the equiaxed phase is suggested:

$$M_{\mathrm{ce}} = -\gamma \cdot \left(\vec{u}_\ell - \vec{u}_\mathrm{c}\right) \cdot \nabla c_\ell \cdot \rho_\mathrm{e} \tag{1}$$

$\vec{u}_\ell$ and $\vec{u}_\mathrm{c}$ are velocities of the melt and columnar structure; ρ_e is the density of equiaxed crystals. Fragmentation occurs only with remelting, i.e. for the case of $M_{\mathrm{ce}} > 0.0$. For the case of solidification (calculated M_{ce} has a negative value), we set $M_{\mathrm{ce}} = 0.0$, i.e. no fragmentation should occur. Here a fragmentation coefficient, γ, is assigned to bridge the unknown correlation between fragmentation induced mass transfer rate and the increase rate of constitutional supersaturation caused by the interdendritic flow. All other unknown contributing factors for the remelting-induced fragmentation such as the curvature effect of the dendrites, latent heat induced thermal fluctuation, diffusion in the interdendritic melt, etc. are included in the single coefficient γ.

It is assumed that the fragment is globular (spherical). The diameter of the fragment is proportional to the secondary dendrite arm space and the volume fraction of the columnar phase: $d^0_{\mathrm{e\,frag}} = \lambda_2 f_\mathrm{c}$. Hence the rate of the fragment production can be calculated as:

$$N_{\mathrm{frag}} = M_{\mathrm{ce}} / \left[\rho_\mathrm{e} \cdot \frac{\pi}{6} \left(d^0_{\mathrm{e,frag}}\right)^3\right] \tag{2}$$

Transport of the number density of the equiaxed crystals, n_{eq}, must be calculated with

$$\frac{\partial}{\partial t} n_{\mathrm{eq}} + \nabla \cdot \left(\vec{u}_\mathrm{e} n_{\mathrm{eq}}\right) = N_{\mathrm{frag}} \tag{3}$$

by considering a source term N_{frag}, which refers to the source of equiaxed crystals by fragmentation. Heterogeneous nucleation and the death of equiaxed crystals by dissolution (remelting) are here ignored.

A model alloy Sn-10wt.%Pb is chosen for this study. Thermodynamic data and thermal physical properties of alloy Sn-10wt.%Pb are available, as listed in Table 1. A linearized Pb-Sn binary phase diagram, with a constant solute redistribution coefficient k and a constant liquidus slope m, is used. The solidification model is developed within the framework of the CFD software ANSYS-Fluent version 14.5.

Table 1: Material properties/data for alloy Sn-10wt.%Pb

Properties	Symbol	Units	Value	Ref.
Nominal concentration	c_0	1	0.1	
Liquidus temperature	T_{liq}	K	492.14	[13]
Melting point of solvent at c_0=0	T_f	K	505	[13]
Eutectic composition	c_{eu}	1	0.381	[13]
Eutectic temperature	T_{eu}	K	456	[14]
Liquidus slope	m	K	-128.6	[13]
Equilibrium partition coefficient	m	1	0.0656	[13]
Reference density	ρ_{ref}	$\mathrm{kg \bullet m^{-3}}$	7000	[13]
Equiaxed density	ρ_e	$\mathrm{kg \bullet m^{-3}}$	7304	[17]
Specific heat	c^l_p c^e_p c^c_p	$\mathrm{J \bullet kg^{-1} \bullet K^{-1}}$	260	[13]
Thermal conductivity	k_l k_e k_c	$\mathrm{W \bullet m^{-1} \bullet K^{-1}}$	55.0	[13]
Latent heat	L	$\mathrm{J \bullet kg^{-1}}$	6.1×10^4	[13]
Viscosity	μ	$\mathrm{kg \bullet m^{-1} \bullet s^{-1}}$	1.0×10^{-3}	[13]
Liquid thermal expansion coefficient	β_T	$\mathrm{K^{-1}}$	6.0×10^{-5}	[13]
Liquid solutal expansion coefficient	β_C	$\mathrm{wt.\%^{-1}}$	-5.3×10^{-3}	[13]
Primary dendritic arm spacing	λ_1	m	1.3×10^{-3}	[13]
Second dendritic arm spacing	λ_2	m	0.65×10^{-4}	[13]
Diffusion coefficient (liquid)	D	$\mathrm{m^2 \bullet s^{-1}}$	4.5×10^{-9}	[13]
Diffusion coefficient (solid)	$D_\mathrm{c}D_\mathrm{e}$	$\mathrm{m^2 \bullet s^{-1}}$	1×10^{-12}	[13]
Initial temperature	T_0	K	492.14	[13]
Heat transfer coefficient	h	$\mathrm{W \bullet m^{-2} \bullet K^{-1}}$	400	[13]
External temperature	T_{EXT}	K	298	[13]
Gibbs Thomson coefficient	Γ	$\mathrm{m \bullet K}$	6.5×10^{-8}	[13]
Fragmentation coefficient	γ	1	0.1	

2 Results and discussion

2.1 Simulation of a 2D test case

A 2D cavity is configured in Fig. 1. The configuration is similar to the experiment of Cao et al.[8], but a different alloy (Sn-10 wt.%Pb) is considered. Density difference between equiaxed crystals and liquid is set as 304 $\mathrm{kg \bullet m^{-3}}$ [17]. Heat is only extracted through the top wall with a heat transfer coefficient, h = 400 $\mathrm{W \bullet m^{-2} \bullet K^{-1}}$, while other walls are set as adiabatic boundary. As a closed domain is calculated and no volume shrinkage is considered, the Boussinesq approximation is made for the thermo-solutal convection and crystal sedimentation. The cavity is initially filled with the stationary melt of its liquidus temperature.

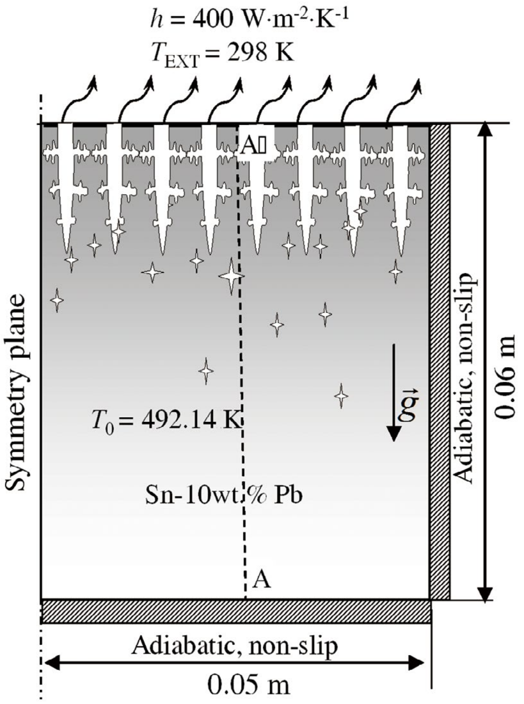

Fig. 1: Configuration of 2D cavity

Figure 2 shows the solidification sequence at a 75 s for the cavity. Here a constant fragmentation coefficient (γ= 0.1) is taken following a parameter study [7]. With the initiation of cooling, the growth of columnar trunks and thermal-solutal convection begin from the top. The bulk melt begins to move due to solutal or thermal buoyancy. Some convection cells can penetrate into the mushy zone. Furthermore, fragmentation is shown by the N_{frag} contouroccurs in the mushy zone. Equiaxed crystals start growing and sinking; however, their motion is influenced by the melt flow through the drag force, as seen schematically in Fig. 2(a). The top mushy zone (columnar) extends to approximately 1/3 of the domain [Fig. 2(b)]. A large vortex of melt flow and some small convection cells form in the bulk and near the columnar tip front regions, penetrating into the mushy zone (till $f_e \sim 0.3$). The melt flow has a significant impact on the velocity field of the equiaxed crystals. Both the melt flow and motion of equiaxed crystals have similar velocity magnitude. As f_e reaches the packing limit in the bottom region, the equiaxed phase stops moving. A second mushy zone with packed equiaxed crystals develops from the bottom [Fig. 2(c)]. Once the equiaxed is fixed, columnar phase has the possibility to grow, competing with the growth of the equiaxed phase. The fragmentation continues near the columnar tip front [Fig. 2(d)], supplying equiaxed nuclei continuously. The maximum number density can reach a magnitude of 10^{11} m^{-3}.

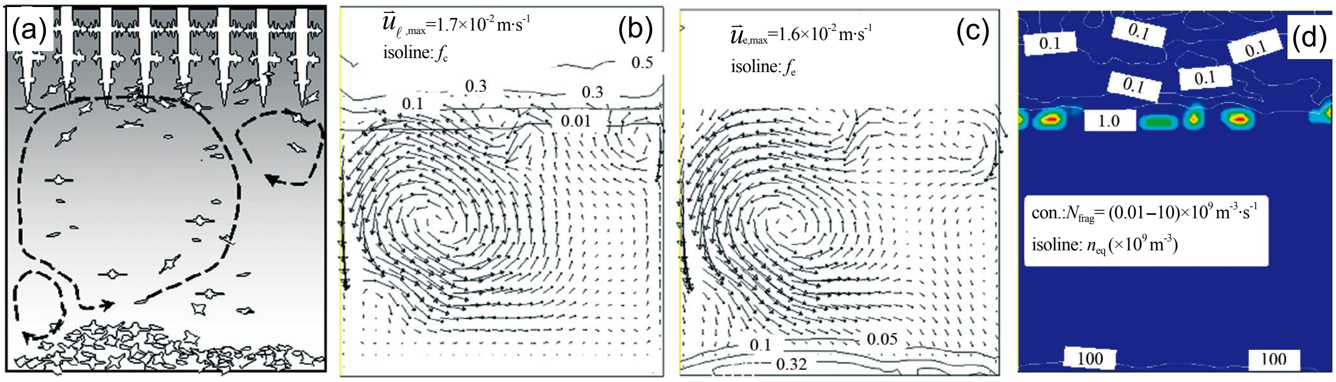

Fig. 2: Solidification sequence at 75 s for cavity: (a) schematic of different solidification regions and flow pattern, (b) calculated liquid velocity overlaid with f_c isoline, (c) equiaxed velocity overlaid with f_e isoline, and (d) contour of production rate of fragments (N_{frag}) overlaid with isoline of number density of equiaxed crystals (n_{eq}). N_{frag} is presented in color scale with blue for minimum (1×10^7 m^{-3}), and red for maximum (1×10^{10} m^{-3})

The extension of the upper columnar mushy zone and the pile-up of the equiaxed mushy zone meet at approximately one-third height of the domain. The growth of the columnar tip front is blocked by the equiaxed grain mechanically, that is, columnar-to-equiaxed transition (CET) occurs. The entire solidification sequence ends at 580 s, and the remaining melt in the mushy zone solidifies as eutectic phases below temperature T_{eu}. The final as-cast structure is shown in Fig. 3. The downward movement of fragments/equiaxed crystals leads to an equiaxed zone in the lower part of the cavity. In the upper part of the benchmark is mainly composed of columnar phase. There is a clear CET in the middle of the cavity; near the CET there is the location where the solidification ends with most amount of eutectic phases. The CET occurs at about 300 s, when the tip of columnar dendrite is blocked by the equiaxed crystals.

The numerically calculated solidification sequence and as-cast structure agrees qualitatively with the aqueous ammonium chloride experiment [8]. It was experimentally observed that the equiaxed crystals moved away from the front of the columnar mushy zone and settled to form an equiaxed region at the bottom, leading to CET in the middle of the cavity.

2.2 Simulation of a laboratory benchmark in 3D

The dimensions, boundary, initial and other process conditions for the simulation taken from the experiment performed in the SIMAP/EPM laboratory [10], are shown in Fig. 4. The calculation domain in 3D and boundary conditions are shown Fig. 4(a). The melt is assumed to be homogeneous before solidification. The temperature difference between the two lateral sides is 40 K, and the cooling rate CR = 0.03 K•s^{-1} for both cool and hot walls [Fig.

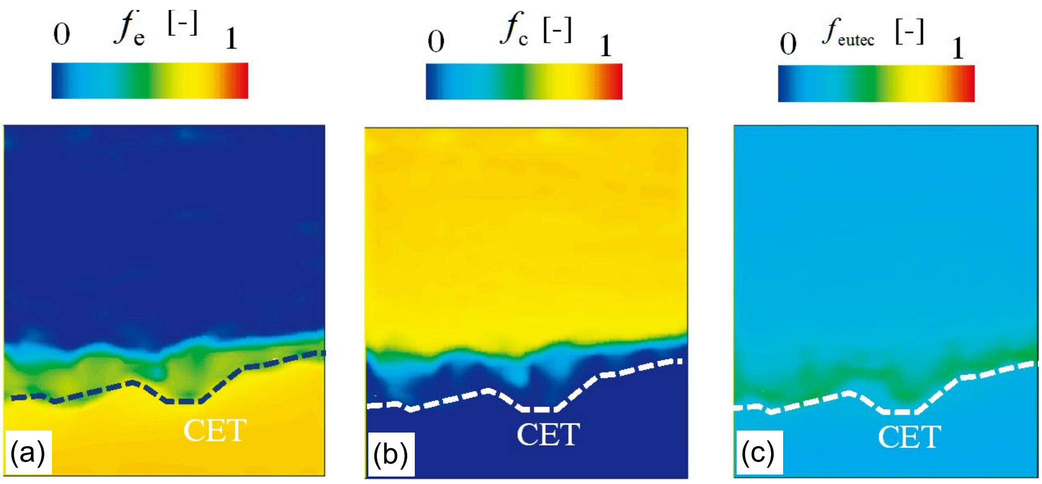

Fig. 3: Numerically calculated as-cast structure: contours of equiaxed volume fraction (a), columnar volume fraction (b) and eutectic volume fraction (c)

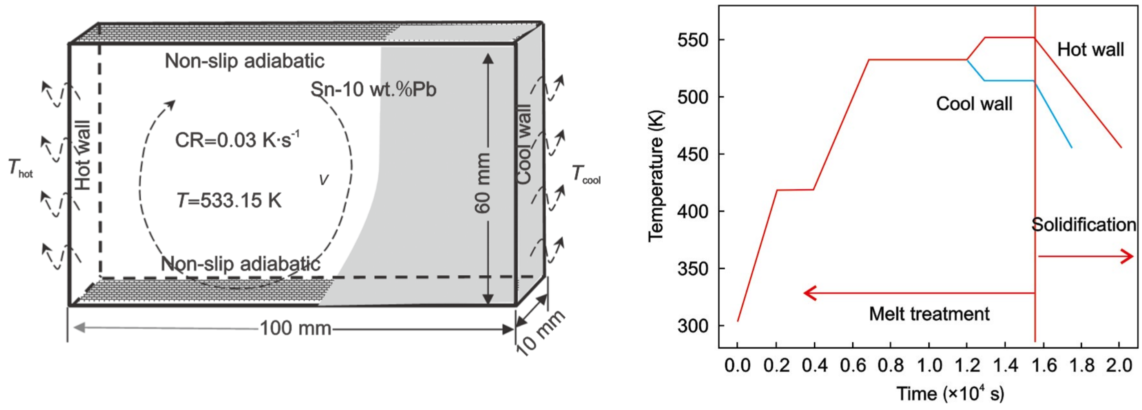

Fig. 4: Configuration of laboratory benchmark (a) and temperature history of hot wall and cool wall (b)

4(b)]. The liquid density is considered to be a function of the melt concentration[13, 17]. Permeability in the mushy zone is set to be anisotropic[18].

Figure 5 shows the solidification sequence at 1,135 s for the benchmark. The fragmentation of dendrite is considered as the only source of equiaxed crystals, therefore the presence of columnar is the precondition of equiaxed crystals. Equiaxed crystals are produced near the solidification front from cool wall (right). There is a clockwise circulation during solidification [Fig. 5(a)-(b)]. The newly-born fragments will float into the bulk-melt region. When the bulk melt temperature is higher than liquidus temperature, those crystals are melted. When the bulk melt is cooled to below liquidus temperature, those crystals survive and grow into the equiaxed structure. Another interesting point is that the melt is gradually enriched with solute (Pb) during the late stage of solidification, and when the density of the melt becomes larger than the solid equiaxed crystals, the equiaxed crystals float upwards [Fig. 5(c)-(d)].

The as-cast macrostructure on the center plane is shown in Fig. 6. Figure 7 shows the spatial distribution of different phases in the as-solidified plate. Simulation results show that the right side of the plate is dominantly occupied by columnar phase [Fig. 6(a)], and some eutectic phases are located in left-bottom region near the hot wall [Fig. 6(b)]. There is also little fraction of eutectic phase embedded in columnar phases. The equiaxed crystals are concentrated in the upper left corner and this region extends to the middle-bottom region of the plate [Fig. 6(c)]. The equiaxed zone is indicated by the space between bold line and dashed line. The bold line is the boundary of columnar and equiaxed phase i.e. CET. The dashed line indicated the boundary between equiaxed phase and eutectic. Figure 6(d) shows the experiment result of the as-cast structure. The general appearance is similar to the simulation one. Columnar dendrites exist in the right side and equiaxed crystals in the upper right region. However, a small second columnar region is observed in the left-bottom corner region near the hot wall but the simulation result show eutectic phases there. The simulation may overestimate Pb concentration in the rest melt during late stage of solidification. It requires further validation from the metallography analysis.

3 Conclusions

A fragmentation formulation by the mechanism of solute-driven remelting of the dendrite arms is integrated into a mixed columnar-equiaxed solidification model. Demonstratively, this model is used to simulate the solidification process of two test cases.

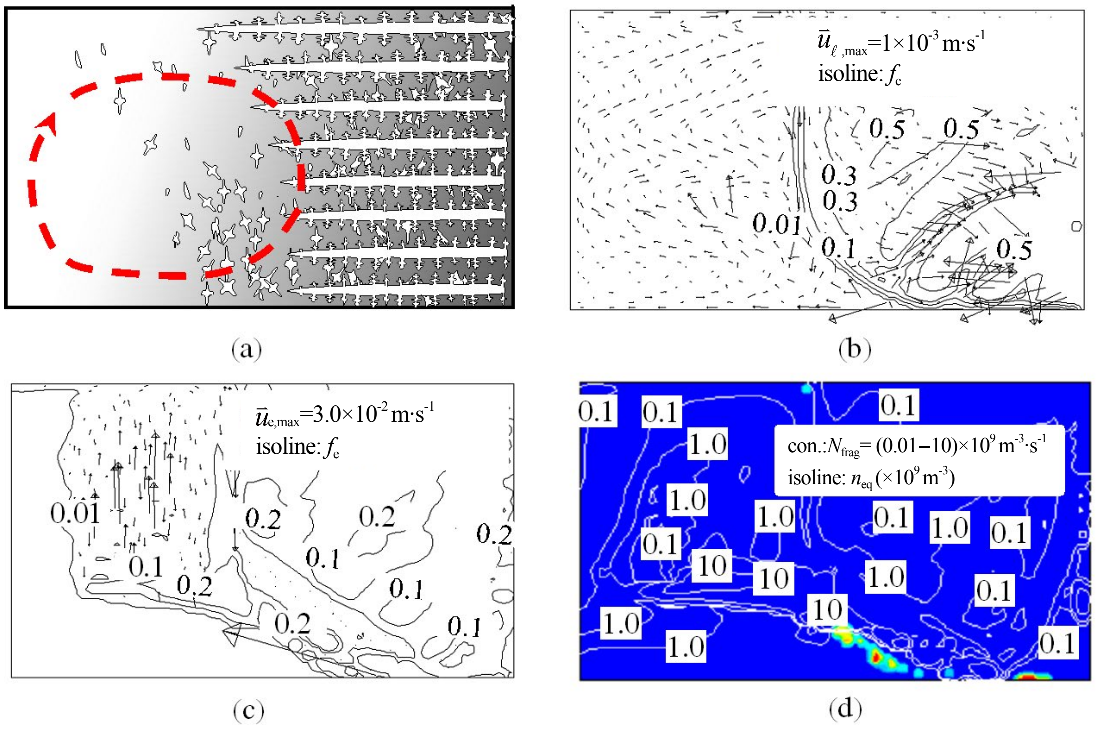

Fig. 5: Solidification sequence at 1,135 s for laboratory benchmark: (a) schematic of different solidification regions and flow pattern, (b) calculated liquid velocity overlaid with f_c isoline, (c) equiaxed velocity overlaid with f_e isoline, and (d) contour of production rate of fragments (N_{frag}) overlaid with isoline of number density of equiaxed crystals (n_{eq}). N_{frag} is presented in color scale with blue for minimum (1×10^{7} m^{-3}), and red for maximum (1×10^{10} m^{-3})

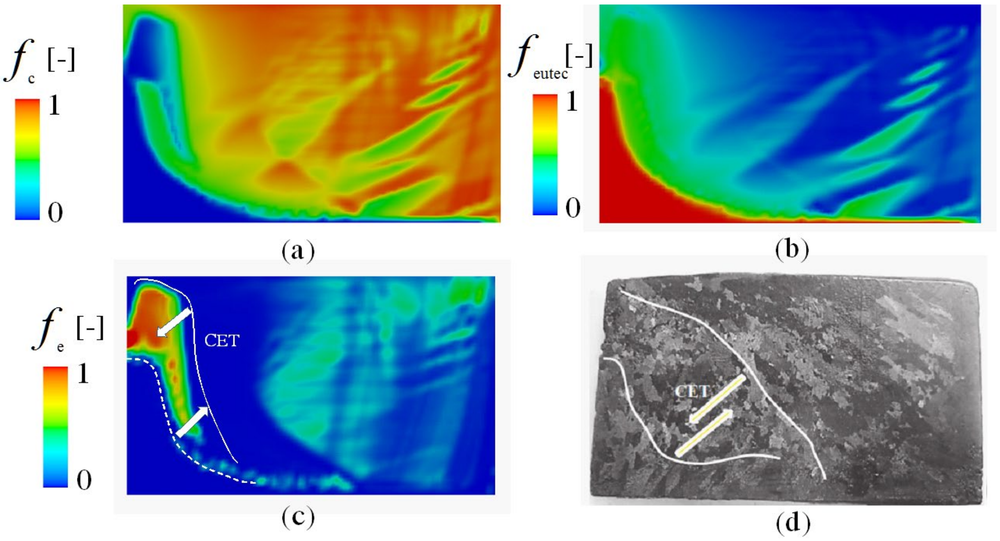

Fig. 6: Macrostructure on central cross section of as-solidified plate: simulation results of columnar volume fraction distribution (a), eutectic volume fraction (b), equiaxed volume fraction (c); and experimental result of as-cast structure (d)

The first case with Sn-10wt.%Pb melt solidifying downwards in a 2D domain (50×60 mm^2) is simulated. A reasonable solidification sequence is calculated. Solidification starts unidirectionally as columnar structure from the top; fragmentation as caused by the thermal-solutal convection occurs near the columnar tip front; the equiaxed crystals as grown from the fragments finally settle down and pile up at the bottom, leading to a mixed equiaxed (bottom region) and columnar (top) structure. The simulation result agrees qualitatively with what was observed experimentally by Cao et al.[8]. This test case demonstrates that the improved mixed columnar-equiaxed solidification model is able to calculate the phenomena such as dendrite fragmentation, transport of the fragments and the equiaxed crystals, formation of columnar-to-equiaxed transition (CET) and the final as-cast structure.

The second case takes the same configuration of a laboratory benchmark [10], i.e. a plate casting of the Sn-10wt.% Pb alloy as cooled laterally. Solidification as columnar structure starts from the mold wall of cool side; fragmentation occurs near the columnar tip front; the equiaxed fragments as produced in the solidification front are transported into the bulk melt, leading to a special pattern of as-cast structure: columnar structure in the cool

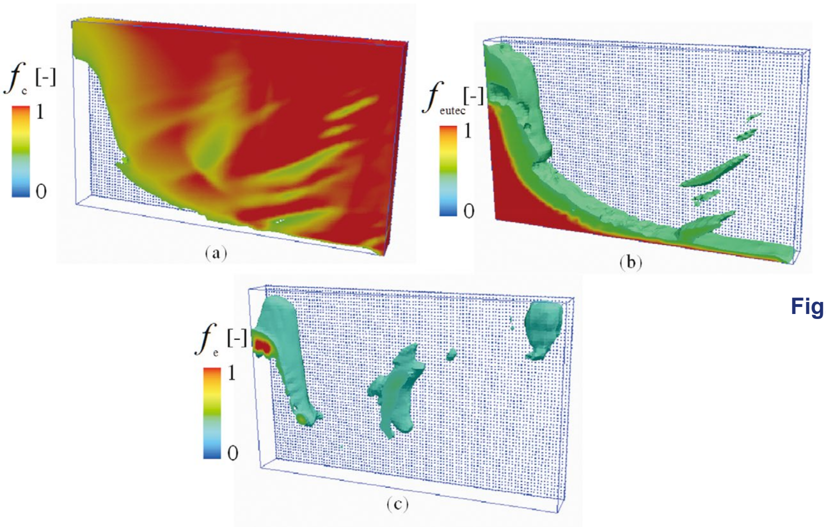

Fig. 7: Spatial distribution of as-cast structure (simulation result): (a) columnar volume fraction, (b) eutectic volume fraction and (c) equiaxed volume fraction. Distributions for different phase regions are presented by their isosurface of volume fraction *f* = 0.25

wall side and equiaxed structure in the upper left corner near the hot wall side, extending downwards to the middle bottom region. Numerically calculated phase distribution agrees satisfactorily with the postmortem analysis of the as-cast structure of the laboratory benchmark. This simulation-experiment agreement has partially verified the numerical model.

The numerical model provides a valuable tool to analyze the process of mixed columnar-equiaxed solidification, where the equiaxed crystals originate from fragmentation.

References

[1] Kattamis T Z, Coughlin J and Flemings M C. Influence of coarsening on dendrite arm spacing of aluminum-copper alloys. Transactions of the Metallurgical Society of Aime, 1967, 239(10): 1504–1511.

[2] Mathiesen R, Arnberg L, Bleuet P, et al. Crystal fragmentation and columnar-to-equiaxed transitions in Al-Cu studied by synchrotron X-ray video microscopy. Metallurgical and Materials Transactions A, 2006, 37(8): 2515–2524.

[3] Montgomery W and Incropera F. Fragmentation of dendritic crystals during solidification of aqueous ammonium chloride. Experimental Heat Transfer, 1998, 11(1): 59–86.

[4] Yasuda H, Yamamoto Y, Nakatsuka N, et al. In situ observation of nucleation, fragmentation and microstructure evolution in Sn-Bi and Al-Cu alloys. International Journal of Cast Metals Research, 2008, 21(1–4): 125–128.

[5] Campanella T, Charbon C and Rappaz M. Grain refinement induced by electromagnetic stirring: A dendrite fragmentation criterion. Metallurgical and Materials Transactions A, 2004, 35(10): 3201–3210.

[6] Pilling J and Hellawell A. Mechanical deformation of dendrites by fluid flow. Metallurgical and Materials Transactions A, 1996, 27(1): 229–232.

[7] Zheng Y, Wu M, Kharicha A, Ludwig A. Incorperation of fragmentation into a volume average solidification model. Modelling and Simulation In Materials Science and Engineering, 2017, in press: http://doi.org/10.1088/1361-651X/aa86c5.

[8] Gao J W and Wang C Y. Effects of grain transport on columnar to equiaxed transition in dendritic alloy solidification. Modeling of Casting, Welding and Advanced Solidification Processes VIII, 1998: 425–432.

[9] Boussaa R, Hachani L, Budenkova O, et al. Macrosegregations in Sn-3wt% Pb alloy solidification: Experimental and 3D numerical simulation investigations. International Journal of Heat and Mass Transfer, 2016, 100: 680–690.

[10] Hachani L, Zaidat K and Fautrelle Y. Experimental study of the solidification of Sn-10 wt.%Pb alloy under different forced convection in benchmark experiment. International Journal of Heat and Mass Transfer, 2015, 85(0): 438–454.

[11] Wu M and Ludwig A. A three-phase model for mixed columnar-equiaxed solidification. Metallurgical and Materials Transactions A, 2006, 37A(5): 1613–1631.

[12] Wu M and Ludwig A. Using a three-phase deterministic model for the columnar-to-equiaxed transition. Metallurgical and Materials Transactions A, 2007, 38A(7): 1465–1475.

[13] Bellet M, Combeau H, Fautrelle Y, et al. Call for contributions to a numerical benchmark problem for 2D columnar solidification of binary alloys. International Journal of Thermal Sciences, 2009, 48(11): 2013–2016.

[14] Ahmad N, Rappaz J, Desbiolles J L, et al. Numerical simulation of macrosegregation: a comparison between finite volume method and finite element method predictions and a confrontation with experiments. Metallurgical and Materials Transactions A, 1998, 29(2): 617–630.

[15] Klassen M and Cahoon J. Interdiffusion of Sn and Pb in liquid Pb-Sn alloys. Metallurgical and Materials Transactions A, 2000, 31(5): 1343–1352.

[16] Cadirli E and Gündüz M. The directional solidification of Pb-Sn alloys. Journal of Materials Science, 2000, 35(15): 3837–3848.

[17] Rocha O L, Siqueira C A and Garcia A. Heat flow parameters affecting dendrite spacings during unsteady-state solidification of Sn-Pb and Al-Cu alloys. Metallurgical and Materials Transactions A, 2003, 34(4): 995–1006.

[18] Schneider M and Beckermann C. A numerical study of the combined effects of microsegregation, mushy zone permeability and fllow, caused by volume contraction and thermosolutal convection, on macrosegregation and eutectic formation in binary alloy solidification. International Journal of Heat and Mass Transfer, 1995, 38(18): 3455–3473.

This study was financially supported by the Austrian Research Promotion Agency (FFG) through the project of Bridge Early Stage (No. 842441), and technically supported by the industrial partner Primetals (former Siemens VAI).